Development of a portable multi-channel broadband near-infrared spectroscopy instrument to measure brain tissue oxygenation and metabolism during functional activation and seizures

Janet Isabel de Roever

A thesis submitted to University College London
for the Degree of Doctor of Philosophy (Ph.D)
December 2019

University College London (UCL)
Department of Medical Physics and Biomedical Engineering

Supervisors: Dr Ilias Tachtsidis
Dr Judith Meek

Declaration

I, J.I de Roever, confirm that the work presented in this thesis is my own. Where information has been derived from other sources, I confirm that this has been indicated in the thesis.

Abstract

Epilepsy is a common neurological disorder often developed during childhood, characterised by abnormal neuronal discharges. These spontaneous recurrent seizures can be associated with poor long-term neurological development. Near-infrared spectroscopy (NIRS) is a non-invasive technique able to monitor cerebral concentration changes in oxygenated- ($\Delta[HbO_2]$) and deoxygenated- (Δ[HHb]) haemoglobin. However, current commercial NIRS systems use only a few wavelengths, limiting their use to haemodynamic monitoring. Broadband NIRS (bNIRS) systems use a larger number of wavelengths enabling changes in concentration of the oxidation state of cytochrome-c-oxidase (Δ[oxCCO]) to be determined, a marker of cellular metabolism.

This thesis describes the development and miniaturisation of an existing bNIRS system to monitor haemodynamic and metabolic changes in children with epilepsy. Using the latest technological advancements, the bulk and complexity of the system was reduced while increasing the number of measurement channels. Two miniature tungsten halogen light sources were utilised with time-multiplexing capabilities implemented (0.5Hz). Bifurcated optical fibre bundles (2.8mm diameter) connected to each light source and twelve detector fibre bundles (1mm diameter) arranged linearly into a ferrule (25mm diameter); modification of the interface between the detectors and lens-based spectrograph ensured compatibility with the increased detector number. Light was collimated to a diffraction grating with a wider 308nm bandwidth and the largest CCD image sensor available (1340x1300 array, 26.8x26mm) was integrated into the system. LabVIEW software was updated to enable simultaneous, real-time collection and display of intensity and concentration changes.

Extensive testing of the system was performed; in-vivo testing in healthy adults using a Stroop task demonstrated a typical haemodynamic response with regional variation in metabolism. Simultaneous bNIRS and electroencephalography data were collected from 12 children with epilepsy in the Neurology Unit. One patient case study is presented in detail, with temporal data from 17 seizures collected. A large decrease in metabolism was observed in the left posterior region, corresponding to a region of cortical malformation, suggesting an energetic deficiency in this region. This indicates the potential for Δ[oxCCO] as an investigative marker in monitoring seizures, providing localised information about cellular oxygen utilisation.

Impact Statement

The multi-channel broadband near-infrared spectroscopy (bNIRS) system developed as part of this thesis utilises the latest technology to deliver the next-generation system able to monitor cerebral changes in oxygenation and metabolism continuously. This miniaturised system combines an increased capacity and a reduced complexity compared with previous systems to deliver a bedside monitoring tool for use in the clinic in young children and infants with epilepsy. The device is able to monitor regional variations across the cortex; its portable, non-invasive capabilities are advantageous in this particular patient population, who are generally less tolerant to uncomfortable and complicated neuromonitoring techniques. bNIRS has applications in both neuroscience research, where brain function and the neural pathways in the developing brain are of interest, and in the clinic, where impairment to cerebral oxygen utilisation may be able to inform on brain injury and predict neurodevelopmental outcome.

bNIRS can be used to indirectly measure brain activity due to the coupling between neuronal activity and cerebral blood flow; this neurovascular coupling haemodynamic response is well-established in the healthy brain. This work has validated the capacity of the system to monitor not only spatial changes in haemodynamics during brain activity but also the heterogeneous changes in metabolism across the prefrontal cortex in the healthy brain. Investigation of the metabolic changes during neuronal activity enables a more comprehensive overview of the physiological response of the brain during periods of activation, a non-trivial task due to the interplay between multiple complex and competing processes.

In terms of clinical practice, this work has demonstrated the capabilities of the system to monitor neuronal activation triggered during seizures in children with epilepsy, providing an opportunity to examine the neurovascular coupling response in brain injury. Monitoring with bNIRS was performed in conjunction with electroencephalography, enabling complementary vasculature, cellular and electrophysiological measurements to be collected during seizures. Through careful patient selection, it was demonstrated that it is possible to use this multi-modal set-up to capture seizure events. Measurements of the regional variation in oxygen delivery to the cerebral tissue, as estimated by the difference between oxygenated and deoxygenated haemoglobin, coupled with measurements of the change in oxidation state of cytochrome-c-oxidase, an enzyme in the mitochondria of cells informing on cellular oxygen uptake, can provide an insight into localised regions where oxygen delivery and utilisation may be abnormal and inform on regions of the brain that are impaired.

In the future, this work can be extended to investigate a larger cohort of epilepsy patients to enable comparison of the cerebral response to seizures across patients. Furthermore, the system can be utilised in other clinical cohorts of interest, such as neonates with hypoxic ischaemic encephalopathy, where a restriction of blood and therefore oxygen to the brain during birth can lead to brain injury. A measure of metabolic changes across the newborn cortex during a functional task may provide an indicator of neurodevelopment in these patients.

This non-invasive, bedside monitoring tool has great potential in providing clinicians with real-time, localised information about cerebral metabolism.

Acknowledgements

First, I would like to thank my supervisors: Ilias Tachtsidis, who has overseen my journey over the last 6 years, introduced me to the world of NIRS and always been available for discussion; and Judith Meek, who has always been supportive, encouraging and a constant source of wisdom. I am indebted to Katerina Vezyroglou, who has been my clinical partner and who this project would not have been successful without. My thanks also go to all the people who have helped me along the way and contributed to this thesis: Helen Cross, Rachel Thornton, Mariana Alves, Emma Dean, Alan Worley, Subha Mitra, Nicola Robertson, Robert Cooper, Sarah Lloyd-Fox, Laura Pirazzoli and Maheen Siddiqui. I must also thank the families of the children recruited.

I have been fortunate to undertake this PhD in the Biomedical Optics Laboratory at UCL – the office has been a pleasure to come in to everyday thanks to everyone's friendliness, enthusiasm and smiling faces. I have made some great friends from the department. Thank you to all the Cornwall crew – where else would holidaying with your colleagues several times a year be a joy! Also a special shout-out to Fred, for introducing me to Normandy, Phong, for always smiling and Gemma, who I'm glad to have finally met – thank you for sitting next to me for 3 years and making me laugh everyday. I also want to thank everyone else in the Multimodal Spectroscopy group: Pardis Kaynezhad, Paola Pinti, Suzi Kovacsova, Luca Giannoni, Nico Chen and Josh Russell-Buckland.

I am grateful to my parents for always supporting me. And thank you to Alex, for bankrolling me the last few years and for understanding, and to Fern, for being just the best dog.

Publications and presentations resulting from this work

Peer-reviewed journal papers

de Roever I, Bale G, Mitra S, Meek J, Robertson NJ, Tachtsidis I. 'Investigation of the pattern of the hemodynamic response as measured by functional near-infrared spectroscopy (fNIRS) studies in newborns, less than a month old: A systematic review' *Frontiers in Human Neuroscience* 2018

Russell-Buckland J, Bale G, **de Roever I**, Tachtsidis I. 'ABroAD: A machine learning based approach to detect broadband NIRS artefacts' *Advances in Experimental Medicine and Biology* 2018

Kovacsova Z, Bale G, Mitra S, **de Roever I**, Meek J, Robertson N, Tachtsidis I. 'Investigation of confounding factors in measuring tissue saturation with NIRS spatially resolved spectroscopy' *Advances in Experimental Medicine and Biology* 2018

Bale G, Mitra S, **de Roever I**, Sokolska M, Price D, Bainbridge A, Gunny R, Uria-Avellanal C, Kendall G. S, Meek J, Robertson N, Tachtsidis I. 'Oxygen dependency of mitochondrial metabolism indicates outcome of newborn brain injury' *Journal of Cerebral Blood Flow and Metabolism* 2018

de Roever I, Bale G, Cooper RJ, Tachtsidis I. 'Functional NIRS Measurement of Cytochrome-C-Oxidase Demonstrates a More Brain-Specific Marker of Frontal Lobe Activation Compared to the Haemoglobins' *Advances in Experimental Medicine and Biology* 2017

Bale G, Mitra S, **de Roever I**, Chan M, Caicedo-Dorado A, Meek J, Robertson N, Tachtsidis I. 'Interrelationship Between Broadband NIRS Measurements of Cerebral Cytochrome C Oxidase and Systemic Changes Indicates Injury Severity in Neonatal Encephalopathy' *Advances in Experimental Medicine and Biology* 2016

Conference presentations

- **Oral presentation** 'A new multi-channel broadband NIRS system for quantitative monitoring of brain haemodynamics and metabolism during seizures' *ECBO, Munich, Germany 2019*
- **Poster presentation** 'Investigation of the pattern of the haemodynamic response as measured by fNIRS in newborns (less than a month old)' *fNIRS, Tokyo, Japan 2018*
- **Poster presentation** 'Investigation of cytochrome-c-oxidase as a more robust marker of frontal lobe activation' *fNIRS, Paris, France 2016*
- **Oral presentation** 'Functional NIRS measurement of cytochrome-c-oxidase demonstrates a more depth-resolved marker of frontal lobe activation compared to the haemoglobins' *International Society on Oxygen Transport to Tissue (ISOTT), Chicago, USA 2016*
- **Oral presentation** 'Cytochrome-C-Oxidase Exhibits Higher Brain-Specificity than Haemoglobin in Functional Activation' *BMLA, Darlington, UK 2016*
- **Oral presentation** 'Cytochrome-C-Oxidase Exhibits Higher Brain-Specificity than Haemoglobin in Functional Activation' *OSA Biomedical Optics, Miami, USA 2016*
- **Poster presentation** 'Near-infrared Spectroscopy Measurements of Cerebral Cytochrome-C-Oxidase and Tissue Oxygenation in Neonatal Brain Injury' *Optics in Clinical Practice III, University of Nottingham, UK 2015*

Prizes

ISOTT Duane F Bruley Award, July 2016

Contents

List of Figures

List of Tables

Abbreviations

$\Delta[]$	change in concentration
ATP	adenosine triphosphate
bNIRS	broadband near-infrared spectroscopy
BOLD	blood oxygen level dependent
CAD	computer aided design
CBF	cerebral blood flow
CBV	cerebral blood volume
CCD	charge-coupled device
CCO	cytochrome-c-oxidase
CuA	copper A
CW	continuous wave
CYRIL	cytochrome research instrument and application
DPF	differential pathlength factor
EEG	electroencephalography
ETC	electron transport chain
FD	frequency domain
HbD	haemoglobin difference
HbT	haemoglobin total
HHb	deoxygenated haemoglobin
HIE	hypoxic ischaemic encephalopathy
HbO_2	oxygenated haemoglobin
fNIRS	functional near-infrared spectroscopy
fMRI	functional magnetic resonance imaging
MBLL	modified Beer-Lamber law
NADH	nicotinamide adenine dinucleotide
MEG	magnetoencephalography
MRI	magnetic resonance imaging
MRS	magnetic resonance spectroscopy
NIRS	near-infrared spectroscopy
NVC	neurovascular coupling
oxCCO	oxidised cytochrome-c-oxidase
PET	positron emission tomography
TR	time-resolved

CHAPTER 1

Introduction

This chapter introduces the technique of near-infrared spectroscopy and its clinical applications in monitoring oxygenation and metabolism in the brain. The motivation behind this thesis is the application of this technique in the clinic to look at cerebral changes in brain injury, especially in neonates and young children where a non-invasive, bedside monitoring technique of cerebral metabolism is desirable. A system capable of monitoring across multiple regions of the head will enable regional variations in the cerebral response in brain injury to be observed, which may provide clinically relevant information to guide treatment.

1.1 Broadband near-infrared spectroscopy introduction

Near-infrared spectroscopy (NIRS) is a non-invasive technique that relies on the transparency of tissue in the NIR region to monitor changes in concentration of oxygenated- ($\Delta[\mathrm{HbO_2}]$) and deoxygenation- ($\Delta[\mathrm{HHb}]$) haemoglobin. Functional NIRS (fNIRS) is a technique that is widely used as an indirect monitor of brain activity, where changes in haemodynamics associated with neuronal activity can be detected. Current commercial NIRS and fNIRS instruments use just a few wavelengths of light to differentiate between the two haemoglobin states; however, this small number of wavelengths limit their use to monitoring only haemodynamic changes.

By using a bandwidth of at least 100 nm between 770 to 1000 nm, with a spectral resolution of 5 nm, it is possible to also resolve for changes in concentration of the oxidation state of cytochrome-c-oxidase ($\Delta[\mathrm{oxCCO}]$), a marker of oxygen utilisation at the cellular level. Hence, additional information about cellular metabolism is also available as well as the oxygenation state in tissue.

Unlike previous commercial NIRS systems that are prone to noise and cross-talk due to using only three or four wavelengths to resolve for changes in oxCCO, these broadband systems have been shown to accurately resolve for changes due to oxCCO and provide a reliable measure of this parameter (Bale et al. (2016)).

There has been a number of broadband NIRS (bNIRS) systems that have been developed at UCL over the last few years. The basic components of these systems is the same, comprising a light source, optical fibre bundles, spectrograph and CCD. However, the capabilities and hence applications of these systems differ greatly. This thesis presents the latest iteration in bNIRS system specifically designed for younger children and infants, able to utilise a larger CCD imaging area than previous iterations and providing a multi-channel, robust measure of cerebral metabolism.

1.2 Clinical introduction

NIRS is a versatile technique that can non-invasively monitor physiological changes at the bedside. This makes it a suitable technique for monitoring neonates and young children, where other techniques such as magnetic resonance imaging (MRI), are more difficult to use in this cohort due to the bulky nature, requirement for the patient to be moved to the machine and susceptibility to movement artifacts.

There are various clinical applications where bNIRS may be a useful tool in monitoring regional haemodynamic and metabolic variations in this age range. It has been shown that neuronal activity is closely related to haemodynamic changes through a process known as neurovascular coupling, with these changes able to be monitored using fNIRS. An increase in $\Delta[HbO_2]$ and decrease in $\Delta[HHb]$ is typically observed during periods of mental stimulation This neurovascular coupling response has been well-established in the adult brain; however, studies in neonates have shown a heterogeneous response. Understanding the interaction between neuronal activity, and blood supply and metabolism in the healthy, developing brain may provide a useful paradigm to investigate brain injury in this vulnerable age group.

Neuronal activity in response to a functional stimulus is not the only factor that can induce a haemodynamic and metabolic cerebral response. For example, seizures are a result of spontaneous, uncontrollable neuronal discharges and are associated with corresponding cerebral physiological changes in haemodynamics. This makes bNIRS a potentially useful tool in infants and children with epilepsy where it is unclear whether individual seizures are harmful to the brain and how recurrent seizures affect brain development in each individual. Some patients experience severe neurodevelopmental impairment, although it is difficult to predict outcome in patients. Further understanding in the capacity of the brain to buffer against these spontaneous neuronal events is needed; investigation of oxygenation to the brain and cellular oxygen uptake may provide useful insight.

1.3 Motivation and objectives

This work was motivated by both the research into the latest bNIRS technology to develop a multi-channel broadband NIRS device as well as the clinical potential of such a device to monitor brain injury in children. An insight into the heterogeneity of cellular metabolism in the injured brain of epilepsy patients may help localise areas of the brain that are not functioning properly and guide treatment for individual patients. This work builds on previous bNIRS systems to deliver the latest generation system; the aim of this thesis is to develop a portable, multi-channel bNIRS device capable of measuring brain oxygenation, haemodynamics and metabolism across multiple regions of the head, with a specific focus on infants and young children, where there is a clinical need for a non-invasive bedside monitoring tool revealing the cerebral physiological changes in brain injury.

The specific objectives of this thesis are therefore to:

- develop a next-generation bNIRS device using the latest advances in technology that is portable and is able to monitor changes in concentration of $\Delta[\mathrm{HbO_2}]$, $\Delta[\mathrm{HHb}]$ and $\Delta[\mathrm{oxCCO}]$ across multiple locations of the head;
- validate the functioning of the system through extensive laboratory tests and test the capacity and limitations of the system using a functional task in healthy adults;
- demonstrate the use of the system in a clinical setting simultaneously with EEG to collect data from children with epilepsy;
- investigate the electrophysiological and haemodynamic and metabolic cerebral response of the brain during seizures and the relationship between the bNIRS and EEG data.

1.4 Thesis overview

This thesis begins with an overview of the brain, discussed in Chapter 2 including how different types of cells mediate cerebral blood flow and the coupling of this with neural activity. The typical haemodynamic response to functional activation is discussed, and a literature review of the variability of this neurovascular coupling response in term neonates less than 1 month of age is presented. This chapter provides a background of the functioning of the brain and the neuromonitoring techniques currently available and provides context for where NIRS fits in.

Chapter 3 introduces the concept of NIRS and presents the typical components that comprise a bNIRS system, including the measurement of metabolic marker, CCO. A timeline of the most recent bNIRS systems is provided and the need and novelty of the next-generation system is presented.

Chapter 4 presents the bNIRS device developed as part of this thesis including the upgrade of the hardware and software from previous versions and validation of the functioning of the system in the laboratory.

This system is then used in a functional experiment in healthy adults, as presented in Chapter 5, where two functional tasks were used to test the capacity and limitations of the system. The system is finally deployed in a clinical setting at Great Ormond Street Hospital (GOSH) to monitor young children with epilepsy with daily seizures. Chapter 6 describes the set-up of the clinical experiments, where simultaneous EEG and bNIRS monitoring was performed, and the data from 10 patients are presented.

A case study is further discussed in Chapter 7, where data from a 3 year old patient are analysed in more depth. Various analysis methods are used on this dataset to investigate the bNIRS and EEG changes during seizures and how these complementary neuromonitoring modalities may be used to provide an overall picture of the brain response to seizures in this patient.

The thesis concludes with a brief summary of the work presented here and the future clinical experiments utilising the capabilities of this system that are planned.

1.5 Personal statement

The work presented here can be separated into three parts: the development of the instrumentation, design of the functional experiments in the healthy adult and the clinical application including integration of the bNIRS and EEG, and the analysis of this combined dataset in a case study. This work encompasses a collaboration with colleagues across both UCL and GOSH; here, I outline the work that was carried out by myself and acknowledge the help of my colleagues.

The development of this instrumentation was carried out by myself with supervision and advice from my colleagues and supervisors. This involved upgrading the hardware components to the latest and most suitable components available as well as upgrading the software to fully integrate the hardware components into a fully functioning system. Design of the headgear to hold the multiple optical fibre bundles was a large part of the process, where good optical coupling with the tissue is vital to ensure high quality data collection. A variety of headgear was developed both by myself and in collaboration with colleagues at Babylab, Birkbeck who have extensive experience with infant headgear, enabling flexibility in the application of the system across patients of different ages.

The functional activation experiment was done by myself while the collection of the clinical data collection was done in collaboration with my clinical colleague, Dr Katerina Vezyroglou. As well as the data collection, I was responsible for the quality of the optical data, synchronisation of the bNIRS data with the EEG and the analysis of the data presented in this thesis.

Some of this thesis has been published in peer-reviewed journals. I have written one paper from work directly produced for this thesis and another paper from work that was carried out during this thesis but is not relevant here, looking at the depth-dependent response of CCO. I have contributed to another 4 published papers where I appear as a co-author.

CHAPTER 2

Monitoring functional brain activity: from neonates to adults

This chapter provides an overview of the physiology of the healthy brain and discusses various neural imaging techniques able to monitor brain activity. This background is essential to develop understanding of NIRS as a neuromonitoring technique in the context of other techniques. There is a more specific focus on functional monitoring of brain activity in neonates as this is a potential application of the system developed in this thesis, before discussion about extending this to monitoring the adult brain.

2.1 Brain physiology of functional activation

2.1.1 Brain activity

Brain activity is associated with a complex series of cellular, metabolic and vascular processes (Pasley and Freeman (2008)), the mechanisms of which are still under investigation. The brain is made of two types of cells: nerve cells (neurons), which transmit electrical signals across the brain and glia cells, which provide neurons with structural support and nourishment.

Neurons

The brain comprises around 86 billion neurons (Azevedo et al. (2009)); these electrically excitable cells connect to each other to form neural networks in the brain, through which information can be processed and transmitted via electrical impulses. There are several types of specialised neurons, including sensory neurons, responding to sensory organs such as sound and light, motor neurons, causing muscle contractions and interneurons, connecting neurons to other neurons.

Figure 2.1 shows the structure of a typical neuron. Neurons communicate with each other through a series of electrical and chemical signals. Electrical impulses travel down the length of a neuron; at the junction, known as the synapse, connecting one neuron to another, chemical neurotransmitters are released across the gap towards the receiving neuron in order to continue propagation of the electrical signal.

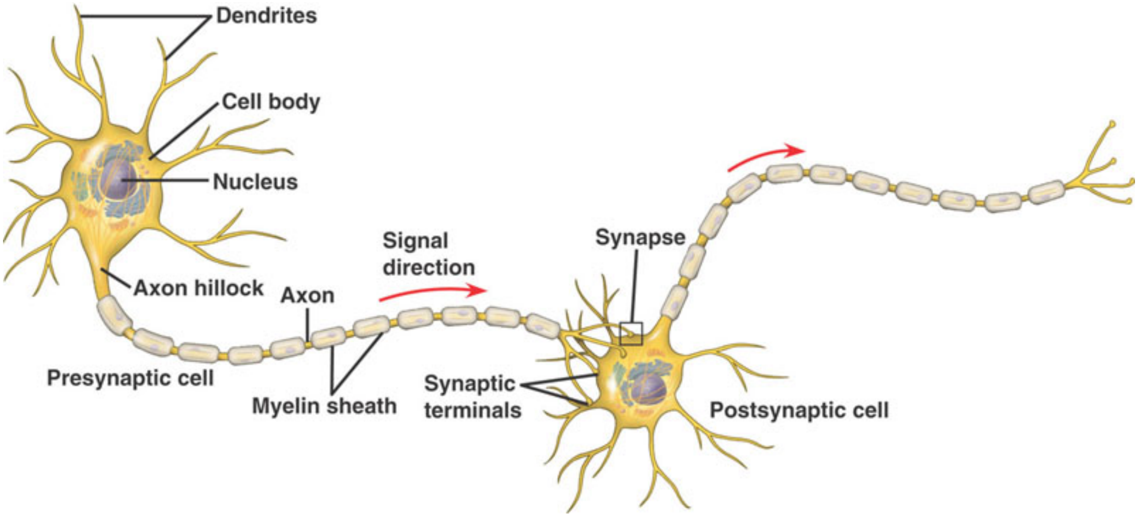

Figure 2.1: Diagram of a typical neuron cell (from Cheung (2011))

The three main parts of a neuron are the cell body, the dendrites and the axon. The cell body contains the nucleus of the cell which controls the function of the cell, and connects the dendrites to the axon. Dendrites are typically branched in order to receive synaptic transmissions from other neurons via neurotransmitters. The signal is propagated along the axon of the cell in the form of action potentials until it reaches the end of the cell at the axon terminal (also known as the synaptic terminal). Myelin sheaths around the axon speed up propagation of the signal.

Glia cells

There are various type of glia cells that are involved with the vasculature response to brain activity. The relationship between electrical activity and blood flow is closely related, as discussed later in Section 2.1.4, and it is the cerebral blood flow changes that enable detection of brain activity with NIRS.

Astrocytes are a specialised glial cell; there are around five times more astrocytes in the brain than neurons (Sofroniew and Vinters (2010)). Astrocytes have a characteristic star shape structure with a number of branched processes extending from the cell. The end foot processes envelop synapses and cerebral blood vessels providing a connection between neurons and blood vessels and it has recently been shown that astrocytes play an important role in mediating the vascular response to functional brain activity (Macvicar and Newman (2015)). Since the metabolic demand of the brain is high compared with other regions of the body, the oxygen supply and glucose delivery to brain cells via regulation of cerebral blood flow is vital for healthy brain function, highlighting the important role of astrocytes in a healthy brain.

Similarly, there is evidence to show that pericytes can regulate blood flow at the capillary level, including during neuronal activation where pericytes dilate capillaries to increase blood flow (Hall et al. (2014)). Pericytes wrap around edothelial cells in the capillary wall with long, branched extensions. Most neurons are closer to capillaries than arterioles, suggesting that capillaries are initially dilated before arterioles during brain activity, as demonstrated by Hall et al. (2014).

Vascular endothelial cells line the circulatory system and have a central role in the regulation of cerebral blood flow. As well as forming the blood brain barrier, restricting the transport of pathogens, cerebral endothelial cells also produce several vasoactive factors that regulate cerebral blood flow (Peterson et al. (2011)).

Action potentials

Action potentials are the electrical signals that enables neurons to communicate with each other and they occur when the electrical potential of a cell rapidly rises and falls. Neurons have a resting membrane potential of around -40 to -90 mV, with a larger concentration of Na^+ ions in the extracellular fluid outside the cell compared with inside, and a higher concentration of K^+ ions inside the cell compared with outside (Chudler (2015)).

Action potentials are caused by a reversal of the neuron's resting membrane potential, through an influx of sodium ions (causing depolarisation) and outflux of potassium ions (causing repolarisation), facilitating the propagation of the electrical signal. Voltage-gated channels allow a redistribution of ions within the neuron in order to generate a potential difference across the neuron membrane.

Depolarisation occurs after a triggering event, such as the binding of neurotransmitters to a voltage-gated channel, triggering other voltage-gated channels. These channels open to allow an influx of positively charged Na^+ into the cell, shifting the membrane potential closer to 0 mV. The membrane potential actually overshoots equilibrium during depolarisation to form a positive potential.

Repolarisation restores the cell to its resting membrane potential. Sodium channels close whilst potassium channels open, causing an outflux of K^+ from inside the cell to the extracellular fluid outside the cell. Hence, the cell loses the positive charge it gained during depolarisation. The potassium channels stay open long enough for the potential to become more negative than its resting potential, termed hyperpolarisation, and subsequently sodium and potassium channels pump Na$^+$ ions back to outside the cell and K$^+$ to inside the cell until the resting membrane potential is restored.

The signal propagates along the axon where, at the terminal end, the synapses transmit the signal chemically via neurotransmitters to motor cells or receiving dendrites of another neuron to continue propagation of the signal. A diagram showing the transmission of an action potential along an axon is shown in Figure 2.2.

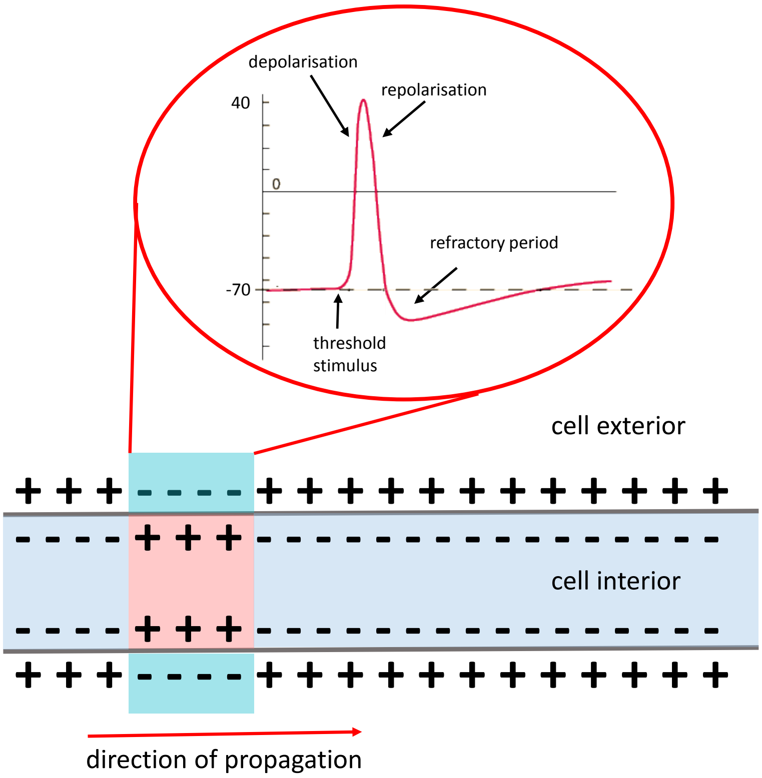

Figure 2.2: Diagram showing propagation of an action potential along an axon (adapted from https://en.wikipedia.org/wiki/Action_potential)

Dendrites are either pre-synaptic or post-synaptic, depending on whether they are transmitting or receiving a signal. At the pre-synaptic terminal, vesicles containing neurotransmitters are released and bind to receptors in the post-synaptic terminal, triggering voltage-gated channels. Neurotransmitters are excitatory or inhibitory, causing either a flux of positive ions into the postsynaptic cell to depolarise it and trigger an action potential, or a flux of negative ions into the cell or positive ions out of the cell to hyperpolarise it and inhibit an action potential.

2.1.2 Brain anatomy

The central nervous system is made up of the brain and spinal cord. The brain is encased in the skull and can be divided into four main sections, as shown in Figure 2.3: brain stem, cerebrum, cerebellum and diencephalon. The cerebrum forms the largest portion of the brain and can be divided further into different lobes: frontal, temporal, parietal and occipital. These various anatomical regions, shown in Figure 2.4, have been associated with different brain functions. For example, the frontal lobe is associated with emotions and concentration, the parietal lobe is associated with processing language and sensory information, the temporal lobe is associated with memory and hearing and the occipital lobe is associated with vision.

The brain is composed of two main types of matter: white and grey matter. White matter contains mainly axons whereas grey matter contains the cell bodies, dendrites and synapses of neurons. The outer cortex consists of grey matter with inner white matter and it is from the superficial layers of the brain consisting of grey matter that most neural information processing takes place.

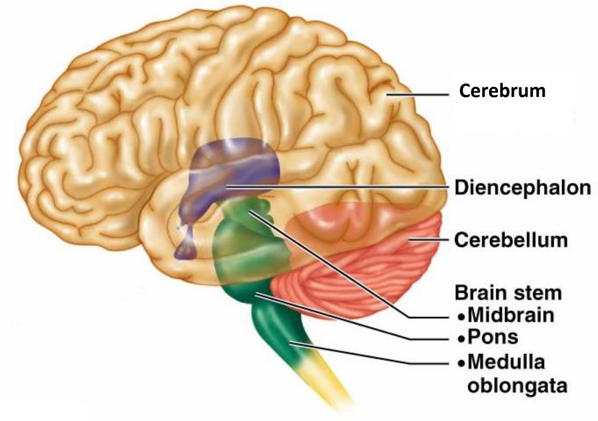

Figure 2.3: Diagram showing the structure of the human brain (from Rod (2015))

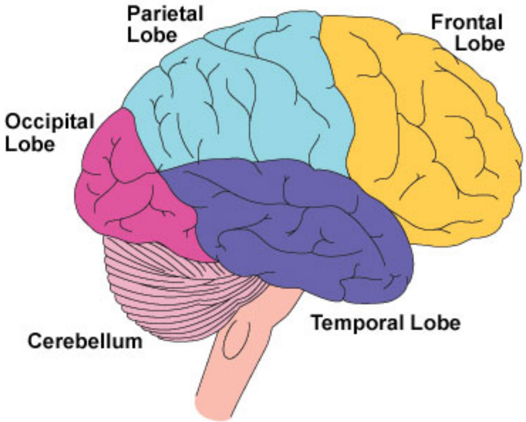

Figure 2.4: Diagram showing the four lobes of the brain (from Igou (2014))

Surrounding the brain are the extracerebral layers, as shown in Figure 2.5; the subarachnoid space is filled with cerebrospinal fluid (CSF) which provides cushioning, the meninges consisting of three protective layers, pia, arachnoid and dura mater, the skull which provides protection and the skin.

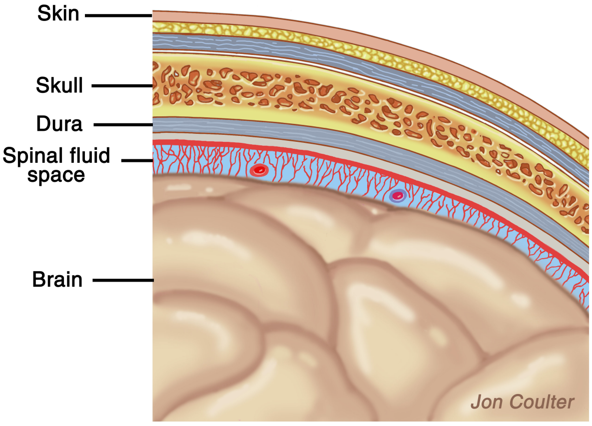

Figure 2.5: Diagram showing the extracerebral layers surrounding the brain (from Coulter (2017))

2.1.3 Energy

The brain has a high demand for energy to support its function. Cellular processes such as return of the ionic gradient of the cell after an action potential and recycling of neurotransmitters requires energy (Pasley and Freeman (2008)). This energy is provided in the form of adenosine triphosphate (ATP), which arises from several major pathways: glycolysis, tricarboxylic acid cycle (TCA) and oxidative phosphorylation. The former two processes produce a small amount of ATP but are linked to the final process, which produces the majority of ATP. Knowledge of the pathway for ATP production is needed to understand the origin of monitoring metabolism with NIRS.

Glycolysis

Glycolysis is the method of breaking down glucose into pyruvate to extract energy for cellular metabolism. It is an anaerobic process so does not require oxygen and it occurs in the cytoplasm of cells.

Glucose, which contains six carbons, is broken down into two three-carbon molecules; this process requires the use of two ATPs. The two three-carbon molecules are then converted into two pyruvates, creating two NADHs and four ATPs. NAD^+ is an electron carrier responsible for shuttling electrons around; when NAD^+ is reduced (i.e. when it has gained an electron), it is known as NADH. Hence, there is a net gain of two ATPs for every glucose molecule that undergoes glycolysis (Khan (2016)). The reaction is shown in Equation 2.1

$$glucose\ +\ 2\,ADP\ +\ 2\,NAD^{+}\ =\ 2\,pyruvate\ +\ 2\,ATP\ +\ 2\,NADH \tag{2.1}$$

where ADP is adenosine diphosphate.

Pyruvate oxidation

Pyruvate from glycolysis can then enter the mitochondria in cells; it is in the mitochondria where the majority of ATP is produced. Pyruvate oxidation links glycolysis to the remaining processes in cellular respiration: firstly, the TCA cycle, producing two more ATPs, then oxidative phosphorylation, producing 32 ATPs.

The first step before the TCA cycle is pyruvate oxidation, which occurs in the mitochondrion. This occurs when the three-carbon molecule, pyruvate, is converted to acetyl CoA, a two-carbon molecule attached to coenzyme A, which acts as the fuel for the TCA cycle. From the two pyruvate molecules, this process produces two acetyl CoA, two NADH and two carbons (in the form of CO_2) (Courtney et al. (2013)). The overall reaction is given by:

$$2\,pyruvate\ +\ 2\,NAD^{+}\ +\ 2\,CoA\ \rightarrow\ 2\,acetyl\ CoA\ +\ 2\,NADH\ +\ 2\,H^{+}\ +\ 2\,CO_2 \tag{2.2}$$

Tricarboxylic acid cycle

The TCA cycle, also known as the Kreb's cycle or citric acid cycle, takes the acetyl CoA produced from pyruvate oxidation and combines it with a four-carbon acceptor, known as oxaloacetate, to form a six-carbon molecule called citrate. Removal and then addition of a water molecule converts the citrate to isocitrate, which is then oxidised, releasing carbon in the form of CO_2 and leaving behind a five-carbon molecule. During this step, NAD^+ is reduced, producing NADH. The five-carbon molecule is also oxidised, reducing NAD^+ to NADH and releasing a carbon dioxide molecule. Hence, for every acetyl CoA utilised, two CO_2 molecules and 2 NADHs are produced.

The remaining four-carbon molecule combines with CoA forming succinyl-CoA. The CoA group is replaced by a phosphate, which is transferred to ADP to make ATP. The remaining four-carbon molecule is oxidised, where two hydrogen atoms are transferred to FAD^+, another electron carrier, producing $FADH_2$. In the final steps, water is added to the four-carbon molecule and oxidised to re-form oxaloacetate, and the process can start again. NAD^+ is reduced to NADH in this final step.

The overall reaction for the TCA cycle is (Courtney et al. (2013)):

$$\begin{aligned} oxaloacetate\ +\ acetyl\ CoA\ +\ ADP\ +\ P_{\mathrm{i}}\ +\ 3\ NAD^{+}\ +\ FAD^{+} \\ \rightarrow CoA\ +\ ATP\ +\ 3\ NADH\ +\ 3\ H^{+}\ +\ FADH_2\ +\ 2\ CO_2\ +\ oxaloacetate \end{aligned} \tag{2.3}$$

where $\mathrm{P_i}$ is an inorganic phosphate.

The TCA cycle provides the electron carriers, NADH and $\mathrm{FADH_2}$, required for the next step, oxidative phosphorylation, which produces the majority of ATP.

Oxidative phosphorylation

Oxidative phosphorylation is the final stage in cellular respiration and involves the electron transport chain (ETC). This process occurs in the inner membrane of the mitochondria, where electrons are passed from one part of the chain to the next in a series of redox reactions. NADH and $\mathrm{FADH_2}$ transfer electrons to molecules at the beginning of the ETC, oxidising back into $\mathrm{NAD^+}$ and FAD+ to be recycled in the process. As electrons pass down the chain, they release energy, some of which is used to pump $\mathrm{H^+}$ from the extracellular matrix into the intermembrane space; this forms an electrochemical gradient. The stored energy formed from this gradient drives the synthesis of ATP, a process known as chemiosmosis. An overview of the process is shown in Figure 2.6.

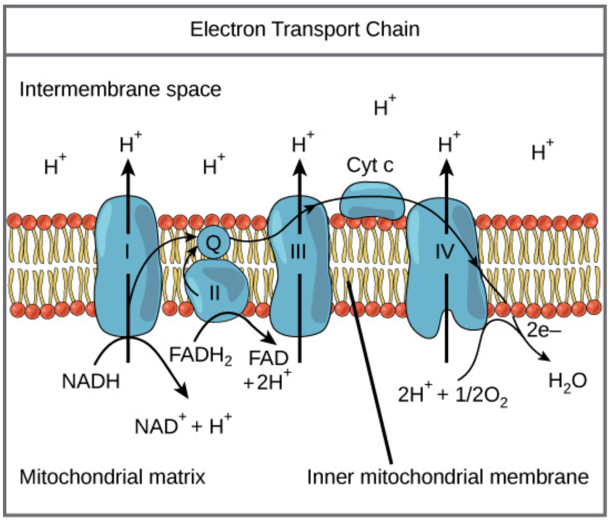

Figure 2.6: Schematic showing the stages of the electron transport chain (from Remsen (2013))

The ETC is made of a collection of membrane-embedded proteins and organic molecules, organised into four large complexes. NADH passes its electrons to complex I at the beginning of the ETC; protons are subsequently pumped into the intermembrane space. $\mathrm{FADH_2}$ passes its electrons to complex II (no protons are pumped in this complex). Electrons from complex I and complex II are then passed along to complex III via electron carriers, ubiquinone (Q), where more protons are pumped against the gradient. Finally, electrons are passed onto a mobile carrier called cytochrome c (cyt c). Cyt c carries the electrons to the final complex, complex IV; protons are again pumped against the electrochemical gradient here. The electrons from complex IV are passed onto O_2 which splits and combines with protons in the matrix to form H_2O.

Complex IV is also known as cytochrome-c-oxidase (CCO). CCO is the last enzyme in the ETC and is responsible for oxidising cyt c (i.e. cyt c loses an electron). This change in oxidation state of CCO causes a change in its absorption spectrum, which can be detected using NIRS. This is discussed further in Section 3.1.

Oxygen is crucial for the synthesis of ATP, where it is needed at the end of the electron transport chain to accept electrons, and complete the transfer of electrons along the ETC to continue the process of chemiosmosis.

2.1.4 Neurovascular coupling

Since the brain does not have internal reserves of energy but rather derives its energy from cellular processes, as described in Section 2.1.3, a supply of oxygen is required for cellular metabolism. This supply of oxygen comes from the blood where oxygen is transported from the lungs to around the body. Red blood cells contain millions of haemoglobins, an iron-containing protein with four binding sites (Natzke (1998)). Each haemoglobin can bind four oxygen molecules (one at each site); when this occurs, it is known as oxygenated haemoglobin (HbO_2), and this oxygen can then be passed onto cells during cellular respiration.

When a region of the brain is stimulated, there is a change in local neural activity which requires energy; hence, a corresponding local change in cerebral blood flow occurs to supply the oxygen required to generate energy in the form of ATP. This tight coupling between neural activity and cerebral blood flow is known as neurovascular coupling. The underlying process driving this mechanism is not clearly understood; better understanding of this mechanism is important in order to interpret neural imaging of blood flow. However, there is evidence that astrocytes, pericytes and endothelial cells are all involved with mediating cerebral blood flow, as discussed in Section 2.1.1.

Monitoring of the change in cerebral blood flow can thus be used to infer neural activity, as discussed further in Section 2.2. A typical haemodynamic response to functional activation for adults is shown in Figure 2.7, where there is an increase in $\Delta[HbO_2]$ and a corresponding decrease in concentration of deoxygenated haemoglobin $\Delta[HHb]$, with a small increase in concentration of total haemoglobin ($\Delta[HbT] = \Delta[HbO_2] + \Delta[HHb]$) during presence of a stimulus.

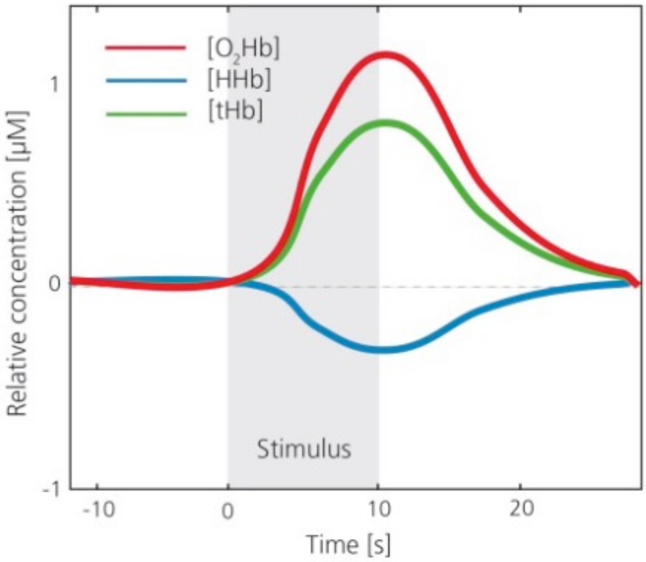

Figure 2.7: Typical haemodynamic response to functional activation in adult brain, with changes in HbO_2 *shown in red, HHb shown in blue and HbT shown in green (from Scholkmann et al. (2014))*

During presentation of a stimulus to the subject, known as functional activation, two conflicting processes are competing: oxygen consumption and oxygen supply. An increase in oxygen consumption occurs as the cells generate more energy via ATP production, corresponding to an increase in HHb and decrease in HbO_2. At the same time, there is an increase in oxygen delivery, corresponding to an increase in cerebral blood flow; hence, there is a decrease in HHb and increase in HbO_2, as HHb is flushed away and HbO_2 flows in. This balance between oxygen consumption and oxygen delivery has been shown in adults to display a disproportionate increase of oxygen delivery compared to oxygen consumption, resulting in the response shown in Figure 2.7. Studies on neonates have demonstrated a mixed response compared with adult studies, and this neonatal brain response will be discussed further in Section 2.3.

This haemodynamic response that is typical of functional activation occurs over the period of a few seconds after neuronal activity, with a delay caused by factors such as dilation of the blood vessels. The inference of neuronal activity from haemodynamic changes relies on a complex interaction involving cerebral blood flow, cerebral blood volume and cerebral metabolic rate of oxygen (Irani et al. (2007)), hence there is no simple relationship between the magnitude of the haemodynamic response and any physiological parameter.

2.2 Neuromonitoring techniques of functional activation

Neuroimaging techniques can be separated into two broad categories: structural imaging and functional imaging and monitoring. The latter is the focus of this chapter; it provides information about the relationship between mental function and location of brain activity, and can be used to investigate neural connections in the healthy brain as well as impairments in the pathologic brain.

There are several neuromonitoring techniques that can be used to investigate brain function, which can be categorised into two types: direct monitoring of brain activity via measurements of electrical activity and indirect monitoring via measurements of changes in blood flow, which infer brain activity based on the principle of neurovascular coupling. Direct measures of electrical activity are very fast, with the signal arising milliseconds after brain stimulation. Indirect measures of the haemodynamic signal are much slower, with a changes occurring a few seconds after the onset of stimulation. Figure 2.8 shows a schematic overview of the neuroimaging techniques and below, a brief summary of each technique is discussed.

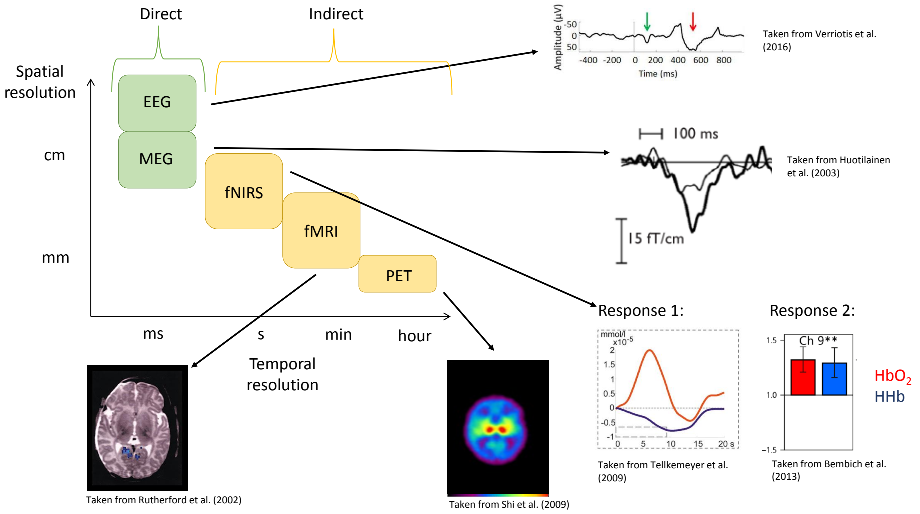

Figure 2.8: Overview of neuromonitoring techniques and their spatial and temporal resolution (adapted using images from Rutherford (2002),Shi et al. (2009),Telkemeyer et al. (2009),Bembich et al. (2013),Huotilainen et al. (2003) and Verriotis et al. (2016))

2.2.1 Electroencephalography (EEG)

Electroencephalography (EEG) is a direct measure of brain activity that monitors voltage fluctuations arising from spontaneous electrical activity in the brain. This activity comes from ionic currents that arise from activating neurons within brain tissue, due to the movement of ions across the cell membrane at the dendrites of post-synaptic terminals. The ionic fluxes generated from this causes a change in the electrical field; when summed across a large number of synchronously firing neurons, this can be detected using electrodes attached to the scalp. Only the net potential difference of many neurons orientated parallel to each other is detected (otherwise the potentials are cancelled out) (Jackson and Bolger (2014)).

There are a few different applications of EEG in monitoring brain activity; an example of a patient being monitored using EEG is shown in Figure 2.9. Amplitude-integrated EEG (aEEG) is a method of monitoring cortical activity, first developed by Maynard et al. (1969). The first studies in neonates were performed in the 1980s (Verma et al. (1984)), and recently this technique has been considered important in monitoring neonatal brain function in the clinic. aEEG monitoring on neonates with HIE has been widely used to assess brain function in this cohort and detect seizures in the first few days of life (van Rooij et al. (2010)).

Figure 2.9: Example of a patient being monitored with EEG (image from `shorturl.at/eGTY6`*)*

Event-related potentials (ERP) are a measure of the brain response as a result of a sensory, cognitive, or motor events. ERPs are small voltage changes that are time-locked to the event and selected from ongoing EEG activity by averaging epochs of EEG following repeated exposure to a stimulus (Blackwood and Muir (1990)). ERPs have been used to investigate cognitive development in infants using tasks such as auditory and visual stimuli (Hoehl and Wahl (2012)).

EEG is also routinely used to monitor children and adults in the clinic, although clear differences are seen due to the many maturational changes unfolding during growth and development. This results in changes to observed frequencies in factors such as background frequencies and the emergence of beta frequency activity in the healthy developing brain (St. Louis et al. (2016)). Patients with seizures are referred an EEG as part of routine diagnosis.

EEG is a non-invasive monitoring technique, which has the advantage of being cheap and practical; application of electrodes to the head is relatively easy and the technique can be used on awake neonates. Furthermore, EEG has a high temporal resolution (∼1000 Hz). The disadvantage is that there is poor spatial resolution due to uncertainty in the location of the electrical activity.

2.2.2 Magnetoencephalography (MEG)

Magnetoencephalography (MEG) is a neuromonitoring technique similar to EEG, but rather than detecting the electrical fields associated with ionic currents in dendrites, it detects the magnetic fields. Due to the small magnitude of this signal compared with ambient magnetic background noise, the detectable region is limited to the cortical surface of the brain.

MEG is a useful tool in studying fetal brain activity (Blum et al. (1985), Schneider et al. (2001), Dunn et al. (2015)) but its use in neonates is less apparent and it has only recently been utilised as a functional monitoring technique in newborns. MEG studies have been performed, with work mainly focused on auditory evoked responses, for example, Huotilainen et al. (2003) and Kujala et al. (2004). However, techniques such as EEG are preferred in neonatal studies due to the high susceptibility of MEG to movement artefacts. The most well-established clinical application of MEG is in presurgical evaluation in epilepsy where there is growing evidence that in some cases it can identify epileptogenic lesions not visible in structural scans (Braeutigam (2013)). More recently, a wearable MEG device has been developed using integrated quantum sensors, enabling potentially more accessible measurements across many populations, including infants and children (Boto et al. (2018)). Figure 2.10 shows an example of a typical MEG device and the smaller, wearable device.

Functional activity can also be monitored by looking at event-related fields. These are the equivalent of ERPs in EEG. Research includes investigation into age-related changes in sensorimotor stimuli (Bardouille et al. (2019)) and auditory processing in epilepsy patients (Nishitani et al. (1999)).

Advantages of the technique include a high temporal resolution due to the direct method of detecting neuronal signals as well as better spatial localisation compared with EEG due to less distortion of magnetic fields by the skull compared with electric fields; however, spatial resolution is still relatively low compared with other neuroimaging techniques such as fMRI, and monitoring of different regions of the brain is limited due to the weak signal and tangential requirement of the signal.

Figure 2.10: Example of MEG devices. a) Example of a patient being monitored with a typical MEG device. b) Example of a patient being monitored with the recently presented wearable MEG device (images from Boto et al. (2018) and `commons.wikimedia.org/wiki/File:NIMH_MEG.jpg`*)*

2.2.3 Positron emission tomography (PET)

Positron emission tomography (PET) is a functional imaging technique that detects emitted gamma rays from a radioactive tracer introduced into the bloodstream. Typical tracers used for neuroimaging are oxygen-15 which accumulates in regions of high blood flow, associated with brain activity, as well as fludeoxyglucose, which accumulates in regions of glucose uptake, indicating tissue metabolic activity. The technique was first proposed in 1975 and has since become a widely used neuromonitoring technique (Phelps et al. (1975)).

Some of the first PET studies on newborns were performed by Volpe et al. (1983) to measure regional CBF in premature infants with intraventricular haemorrhage, and Doyle et al. (1983) who assessed regional cerebral glucose metabolism in newborns with structural brain abnormalities. Shi et al. (2009) were the first to perform a PET study on clinically normal newborn infants to investigate the brain glucose metabolism. Early studies of PET were also used to investigate brain functional development, for example by Chugani et al. (1987) in children aged 5 to 21 years. Clinical applications include monitoring glucose and oxygen metabolism, and cerebral blood flow in epilepsy patients and in oncology. Figure 2.11 shows an example of PET device.

Advantages of PET include its lower susceptibility to movement artifacts compared with techniques such as functional MRI (fMRI). Disadvantages are that the technique requires the introduction of a radioactive tracer and monitoring periods are limited by the half-life of the tracer. The procedure is also expensive compared with techniques such as EEG, as a cyclotron is needed to produce the radioactive tracers; this limits the availability of this monitoring device.

Figure 2.11: Example of a PET device (image from `shorturl.at/blsLQ`*)*

2.2.4 Functional magnetic resonance imaging (fMRI)

Functional MRI is a functional neuroimaging technique that uses MRI technology to measure brain activity via associated changes in blood flow. It relies on the concept of neurovascular coupling to infer changes in neural activity and hence is an indirect measure of brain activity.

The main fMRI technique is blood oxygen level dependent (BOLD), where the presence of HHb in blood, a paramagnetic molecule, changes the proton signal from the surrounding water molecules and causes local dephasing of these protons thereby reducing the signal; this difference in magnetic susceptibility between the blood vessels and surrounding tissue provides a natural contrast agent to form an image (Ogawa and Lee (1990)). During neuronal activation in adults, an increase in oxygen consumption by cells leads to a higher concentration of HHb. This is shortly followed by an increase in the CBF providing a surplus of HbO_2, washing away the paramagnetic HHb and hence causing an increase in the MRI signal indicative of functional activation. This is known as a positive BOLD response, corresponding to a decrease in HHb. Studies in neonates have shown a mixed BOLD response to functional activation compared with adults; Table 2.1 shows a few examples of BOLD fMRI studies including neonates under a month old, and their functional response.

Table 2.1: Table showing some examples of BOLD fMRI studies and the direction of the BOLD response in neonates under a month old

First Author (Year)	**Title**	**Participants**	**Sedation**	**Stimuli**	**BOLD responses**
Yamada et al. (1997)	A rapid brain metabolic change in infants detected by fMRI	15 infants, 1 – 54 weeks	Sedated with pentobarbital	Visual	Neonates <5 weeks: +
Born et al. (1998)	Visual Activation in Infants and Young Children Studied by Functional Magnetic Resonance Imaging	17 infants, 3 days – 48 months	No sedation	Visual	+ (1/3) - (1/3) No response (1/3)
Anderson et al. (2001)	Neonatal auditory activation detected by functional magnetic resonance imaging	Included 13 term infants (1– 7 days)	No sedation	Auditory	- (7/9)+ (2/9)
Muramoto et al. (2002)	Age-Dependent Change in Metabolic Response to Photic Stimulation of the Primary Visual Cortex in Infants: Functional Magnetic Resonance Imaging Study	Included 15 infants <1 month (2 – 31 days)	Sedated with pentobarbital	Visual	-
Arichi et al. (2009)	Somatosensory cortical activation identified by functional MRI in preterm and term infants	Included six term infants (median 40 weeks + 3 days GA)	1 subject sedated	Somatosensory	+
Goksan et al. (2015)	fMRI reveals neural activity overlap between adult and infant pain	Includes 10 healthy term infants (1 – 6 days)	No sedation	Pain	+

Early BOLD studies on newborns were first performed by Born et al. (1996), who studied seven infants between 6 weeks and 3 years. A negative BOLD response was seen in the infants; however, for the two neonates included in the study, no response was observed. Their later study (Born et al. (1998)) studied seventeen infants, 3 of whom were 4 weeks age or less. These subjects showed a mixed response to visual stimulation, with the 4 week-old subject demonstrating a positive BOLD response as is typical with adults, the 5-day old subject demonstrating a negative BOLD-response, and the 3 day-old subject showing no stimulus-related change.

A study by Anderson et al. (2001) observed a mainly negative BOLD response as well. Thirteen term infants aged between 1 − 7 days were studied during auditory activation; a BOLD signal decrease was observed in seven out of nine term infants with the remainder displaying an increase in signal. This negative response seen in infants in response to a stimulus has been reported in several fMRI studies on activation in neonates, and suggests that the coupling between neural activity and vascular response is different in neonates compared with adults.

Some groups, however, have observed similar, positive BOLD responses in neonates in-line with a typical adult response. Yamada et al. (1997) studied fifteen infants between 1 − 54 weeks old, sedated with pentobarbital, and found that neonates less than 5 weeks old showed a positive BOLD response to visual stimulation. Positive responses were also observed in a somatosensory study by studies by Arichi et al. (2009), who studied six term infants, with only one sedated.

The mixed responses seen in the neonate population could be due to several factors. It is common for these infants to be sedated during imaging; this could have an effect on the neural responsivity observed to a stimulus. Furthermore, evolving structural and functional brain development in newborns could cause a difference in response compared to the well-studied response in the fully-developed adult brain.

BOLD fMRI has also been utilised in functional studies in children as well although the lower tolerance level of younger children to lie still in an MRI scanner is a major hindrance to effective functional imaging in this age group. Studies in young children include looking at working memory (Klingberg et al. (2002)) and language development (Holland et al. (2001)). Figure 2.12 shows an example of a patient being monitored using MRI.

Advantages of the technique are that it is non-ionising and non-invasive, does not require introduction of external contrast agents and has a high spatial sensitivity, in the order of mm. Disadvantages are that it is expensive and therefore not readily available, and requires neonates to be sedated before imaging to prevent movement artifacts. Furthermore, fMRI has a relatively poor temporal resolution (∼1 Hz) compared with other techniques, such as EEG. It is also only able to monitor changes arising from changes in concentration of HHb, due to its paramagnetic properties, whereas

Figure 2.12: Example of a patient being monitored with MRI (image from `commons.wikimedia.org/wiki/File:Siemens_Magnetom_Aera_MRI_scanner.jpg`)

a technique such as functional NIRS is able to monitor both changes in concentration of HHb and HbO_2, and hence provide more information about the physiological changes occurring during brain activation.

2.2.5 Functional NIRS (fNIRS)

Functional near-infrared spectroscopy (fNIRS) is a non-invasive neuroimaging technique able to monitor changes in concentration of HbO_2 and HHb in the brain. Monitoring these variables reveals the haemodnamic changes occurring in the brain and this can be related to changes associated with functional activation. It is a relatively inexpensive, non-invasive monitoring technique, able to monitor brain activity by introduction of near-infrared light into the tissue; attenuation changes associated with scattering and absorption within the tissue can be spectroscopically related to concentration changes of HbO_2 and HHb via the modified Beer Lambert law. This technique is described in more detail in the next chapter and Chapter 4. Figure 2.13 shows an example of a patient being monitored using fNIRS.

Advantages of the technique include its low cost and portability, allowing readily available access of this technique in a diverse range of settings. The temporal resolution is much higher than that of fMRI and, unlike fMRI, it has the ability to differentiate between changes in concentration of HbO_2 and HHb. Disadvantages are the poor spatial resolution (∼cm) compared with other techniques such as fMRI, the limited penetration depth of the signal allowing only the cerebral cortex to be monitored, and the contamination of extracerebral effects on the signal, which have to be accounted for. Previous BOLD studies on adults suggests a similar measured vascular response to a stimulus compared with fNIRS (Cui et al. (2012).)

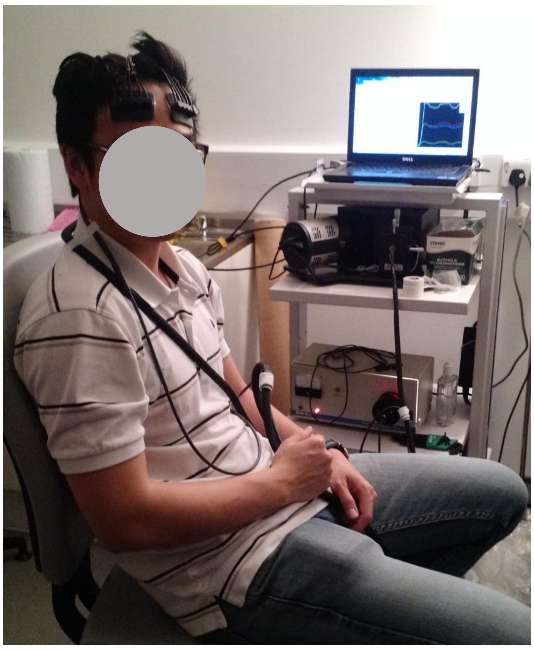

Figure 2.13: Example of a patient being monitored with fNIRS (own image)

2.3 Functional activation in term neonates aged 1 day to 1 month

One of the advantages of fNIRS is its suitability for monitoring neonates and children, as well as adults due to its portable size enabling bedside monitoring. This section focuses on use of fNIRS in neonates under 1 month of age as a potential use for the system developed in this thesis is in this cohort of subjects. There are many advantages to using fNIRS in the study of neonatal brain activity. Compared with adults, neonates have a smaller thickness of skull, allowing better transmission of light and hence a stronger signal originating from the brain. The technique is non-invasive and portable, allowing for flexible monitoring in a variety of settings. This is especially useful for neonates as measurements can be made with the baby on the mother's lap, measurements can be made relatively quickly and no sedation is required, all enabling a less stressful process.

2.3.1 Haemodynamic response to functional activation in neonates

This section is based on a review paper previously published (de Roever et al. (2018b)) and includes some extracts from this paper.

The typical haemodynamic response to a stimulus was discussed in Section 2.1.4; many studies have demonstrated this response in the healthy adult brain, where an increase in $\Delta[\text{HbO}_2]$ and decrease in $\Delta[\text{HHb}]$ relates to the dominant effect of increased oxygen supply compared with oxygen consumption. However, studies of functional activation in neonates have revealed a mixed haemodynamic response, often in contradiction with the typical adult response. An increase in $\Delta[\text{HbO}_2]$ and increase in $\Delta[\text{HHb}]$ is commonly seen, suggesting the balance between oxygen delivery and consumption may be different for neonates compared with adults.

There have been many fNIRS studies on neonates, including preterm neonates; however, since a premature newborn will be at a very different state of neurodevelopment that will affect how the brain responds, functional studies of preterm neonates falls outside the scope of this work. Instead, the focus is on term neonates within the first month of life.

The purpose of this review is to investigate the pattern of the haemodynamic response of healthy, term newborns to a stimulus, within a tightly controlled age range from birth to 1 month of age. This is a sensitive age range, where rapid growth and developmental changes are occurring in the brain, and is also an age of particular interest as it is a period when the newborn is at risk of significant brain injury. For example, HIE occurs in 1–2 per 1,000 live births (James and Patel (2014)) and is associated with neurodevelopmental impairment and mortality, and is an active area of research. It is therefore important to understand the typical response of the healthy newborn brain such that future work is able to identify abnormal response patterns associated with brain injury in this cohort.

2.3.2 Methods

The focus of the review was to look at whether the fNIRS-measured haemodynamic response of healthy newborns <1 month of age compared with the expected haemodynamic response of an increase in $\Delta[\text{HbO}_2]$ and decrease in $\Delta[\text{HHb}]$ and, if not, whether the variability of the haemodynamic response can be explained. Therefore, papers were identified using PubMed and Scopus, searching for a combination of keywords including (near-infrared spectroscopy | near infrared | optical | tomography) and (neonate | newborn) and (functional activation | activation | evoked response | response). The PRISMA chart for the selection of papers included in this review is shown in Figure 2.14. Papers were rejected if different parameters to $\Delta[\text{HbO}_2]$, $\Delta[\text{HHb}]$, and ΔHbT were reported, if results from term newborns <30 days old could not be extracted from a larger cohort outside this target range, or if studies were performed on newborns with suspected brain injury, such as HIE.

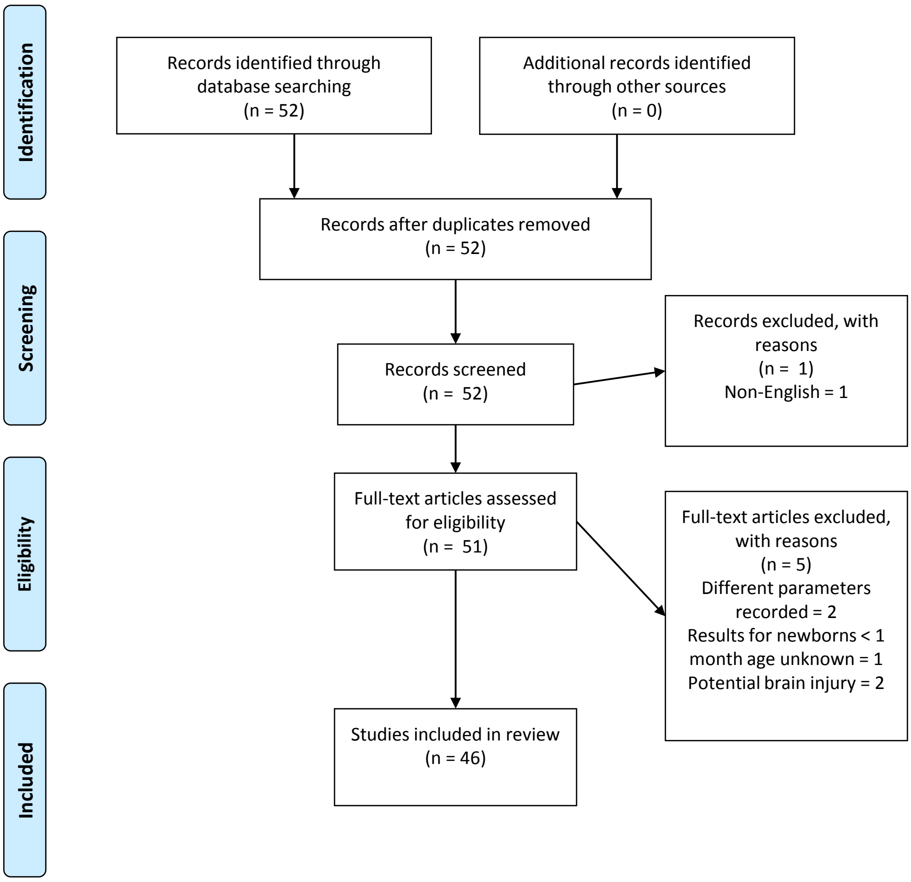

Figure 2.14: PRISMA chart showing papers identified, eligibility, and inclusion in this review paper (from de Roever et al. (2018a)). Note, two papers (Abboub et al. (2016), Ferry et al. (2016)) were later identified that were not flagged using the defined search criteria. These are cited here but not included in the final analysis

2.3.3 Results

A total of 46 studies using fNIRS in neonates were identified, with a total of 51 sets of results arising from some studies investigating more than one stimulus type. Table 2.2 presents a summary of the literature of functional activation studies with NIRS on term neonates less than 1 month old. The majority of studies were on healthy newborns. Some studies monitored newborns with potential pathology (marked with an asterisk in Table 2.2); however, these studies only included newborns with pathological conditions unrelated to cerebral function and with no congenital abnormalities. One study investigated newborns with HIE alongside a control group (Chen et al. (2002)); only the results from the control group are presented here. Similarly, some studies looked at both term and preterm newborns (Isobe et al. (2001), Ozawa et al. (2011b), Naoi et al. (2013), Carlier-Torres et al. (2014), Frie et al. (2017), Arimitsu et al. (2018)) or included subjects older than 30 days (Meek et al. (1998)); the results presented here only include the responses from the term infants <30 days old. It should be noted that not all papers reported all three NIRS parameters, $\Delta[\mathrm{HbO_2}]$, $\Delta[\mathrm{HHb}]$ and $\Delta[\mathrm{HbT}]$. In some papers, the measurement of $\Delta[\mathrm{HHb}]$ was reported in graphs or tables but the direction of the response was not explicitly analysed and discussed, with discussion often centered around the direction of $\Delta[\mathrm{HbO_2}]$.

Table 2.2: Table of literature review of fNIRS studies on healthy term newborns < 1 month old

First Author (Year)	**Participants**	**Instrumentation**	**Cortical Area of Interest**	**Experimental Protocol**	**Significant Results**		
					HbO_2	**HHb**	**HbT**
Meek et al. (1998)	Includes 3 awake term newborns, 3 days - 3 weeks	NIRO 500, Hamamatsu	Occipital	Visual. Checkerboard 5 Hz pattern reversal, 10 s on, 10 s off	+	+	+
Sakatani et al. (1999)	28 newborns, mean 3.1 days	NIRO 500, Hamamatsu	Frontal	Auditory. 60 dB piano music, 10 min on, 10 min off	+	Varied	+
Hoshi et al. (2000)	7 asleep newborns, 4 - 5 days	OMM-100, Shimadzu	Occipital	Visual. 10 Hz flashing light, 30 s on, off until baseline	+	Varied	+
Bartocci et al. (2000)	23 awake newborns, 1 - 8 days	NIRO 300, Hamamatsu	Frontal	Olfactory. Two odours: vanilla and mother's colostrum. Control: distilled water. 30 s on, 2 mins baseline	+	Not reported	+

Continued on next page

Table 2.2 – continued from previous page

First Author (Year)	**Participants**	**Instrumentation**	**Cortical Area of Interest**	**Experimental Protocol**	**Significant Results**		
					HbO_2	**HHb**	**HbT**
Isobe et al. (2001)	Included 2 sedated term newborns, 5 days and 9 days	Hitachi	Parieto-temporal	Motor. Passive knee movement, 15 s on, 30 s off	+	-	Not reported
Chen et al. (2002)	Included 20 healthy term newborns, 1 - 3 days	NIRO 500, Hamamatsu	Frontal	Auditory. 60 dB piano music, 10 min on, 10 min off	+	Varied	+
Peña et al. (2003)	12 asleep newborns, 2 - 5 days	ETG-100, Hitachi	Temporal, fronto-parietal	Auditory. Normal speech, backwards speech, silence. 15 s on, 25 - 35 s off	Not reported	Not reported	+

Continued on next page

Table 2.2 – continued from previous page

First Author (Year)	Participants	Instrumentation	Cortical Area of Interest	Experimental Protocol	Significant Results		
					HbO_2	**HHb**	**HbT**
Taga et al. (2003)	25 newborns - good data from 16 asleep newborns, GA 38 - 42 weeks	Hitachi	Occipital and frontal	Visual. 14 Hz flashing light, 3 s on, 20 s off	+	Varied	Not reported
Nissilä et al. (2003)	10 newborns, 0.5 - 4 days	In-house built, Helsinki	Temporal and parietal	Auditory. 1 kHz tone, 30 s on, 30 s off. Somatosensory.Touching heel, 30 s on, 30 s off	Tactile: +; Auditory: Not discussed but shown	Tactile: Not discussed but shown; Auditory: Not discussed but shown	Not reported

Continued on next page

Table 2.2 – continued from previous page

First Author (Year)	**Participants**	**Instrumentation**	**Cortical Area of Interest**	**Experimental Protocol**	**Significant Results**		
					HbO_2	**HHb**	**HbT**
Nissila et al. (2004)	10 asleep and awake newborns, mean 1.4 days	In-house built, Helsinki	Temporal	Auditory. Sinusoidal tones . 100 ms on, 25 s off	+	- or no change	Not reported
Haensse et al. (2005)	1 newborn, GA 38 weeks	In-house built, Zurich	Parietal	Sensory. Vibration to palm, 20 s on, 10 s rest	+	-	Not reported
Kotilahti et al. (2005)	20 awake and asleep newborns, 1 - 3 days	In-house built, Helsinki	Temporal	Auditory. Sinusoidal tones , 60 dB. 5 s on, 25 s off	+	Not discussed but shown	Not reported
Kusaka et al. (2005)	5 asleep newborns, 9 days - 16 weeks	OMM-2000, Shimadzu	Occipital	Visual. Stroboscopic white flashing light, 8 Hz onto eyelids. 15 s on, 45 s off	-	+	-

Continued on next page

Table 2.2 – continued from previous page

First Author (Year)	**Participants**	**Instrumentation**	**Cortical Area of Interest**	**Experimental Protocol**	**Significant Results**		
					HbO_2	**HHb**	**HbT**
Saito et al. (2007a)	20 asleep newborns, 2 - 9 days	NIRO 200, Hamamatsu	Frontal	Auditory. Infant-directed and adult-directed speech, 15 - 28 s on, off until return to baseline	+	Not reported	Not reported
Saito et al. (2007b)	20 asleep newborns, 1 - 9 days	NIRO 200, Hamamatsu	Frontal	Auditory. 60 - 70 dB normal, pitched and flat speech, 30 s on, 60 s off	+	Not reported	Not reported
Karen et al. (2008)	20 asleep newborns, median age 5.5 days	In-house built, MCP-II	Occipital	Visual. Flashing red LEDs, 0.5 - 1 Hz, 20 s on, 20 s off	+	-	+

Continued on next page

Table 2.2 – continued from previous page

First Author (Year)	Participants	Instrumentation	Cortical Area of Interest	Experimental Protocol	Significant Results		
					HbO_2	**HHb**	**HbT**
Gervain et al. (2008)	22 newborns, mean age 3.14 days 22 newborns, mean age 2.86 days	ETG-4000, Hitachi	Frontal, temporal	Auditory. Language repetition sequences. 18 s on, 25 - 35 s off	+	Not discussed but shown	Not reported
Telkemeyer et al. (2009)	34 newborns, 2 - 6 days	Omniat Tissue Oxymeter, ISS	Frontotemporal to tempoparietal	Auditory. Tonal recording 70 dB, 9 s on, 1 - 12 s off (mean 4.1 s)	+	-	Not reported
Aoyama et al. (2010)	34 asleep newborns, 2 - 9 days	NIRO-200, Hamamatsu	Frontal	Olfactory. Two odours: breast milk, artificial milk. 30 s on, 60 s off	+	Not reported	Not reported
Kotilahti et al. (2010)	13 asleep newborns, 1 - 4 days	In-house built, Helsinki 2	Temporal	Auditory. Infant-directed speech and piano music, 60 dB. 5 s on, 15 s off	Varied	For positive HbO_2, HHb -	Varied

Continued on next page

Table 2.2 – continued from previous page

First Author (Year)	**Participants**	**Instrumentation**	**Cortical Area of Interest**	**Experimental Protocol**	**Significant Results**		
					HbO_2	**HHb**	**HbT**
Liao et al. (2010)	11 newborns, 1 - 3 days	In-house built, Washington	Occipital	Visual. Counterphase checkerboard pattern, 10 s on, 20 s off	+	-	+
Benavides-Varela et al. (2011)	12 newborns, 1 - 5 days	ETG-4000, Hitachi	Frontal, parietal, temporal	Auditory. Consonant (C) Vowel (V) CVCV speech, 70 dB. 10 s on, 25 - 35 s off	+	Not discussed but shown	Not reported
Arimitsu et al. (2011)	17 asleep newborns, 3 - 8 days	ETG-4000, Hitachi	Frontal, parietal, temporal	Auditory. Phonemic and prosodic speech, 67 dB, 15 s on, 15 s off	+	Not discussed but shown	Not reported
May et al. (2011)	20 newborns, 1 - 3 days	ETG-4000, Hitachi	Frontal, parietal, temporal	Auditory. Forwards and backwards speech, 70 - 75 dB, 18 - 20 s on, 25 - 35 s off	+	Not discussed but shown	Not reported

Continued on next page

Table 2.2 – continued from previous page

First Author (Year)	**Participants**	**Instrumentation**	**Cortical Area of Interest**	**Experimental Protocol**	**Significant Results**		
					HbO_2	**HHb**	**HbT**
Minagawa-Kawai et al. (2011)	38 asleep newborns, 1 - 5 days	NTS Optical Imaging System, UCL	Temporal, frontal	Auditory. Tone patterns 80 dB, 10 s on, 8 - 14 s off	+	Not discussed but shown	Not reported
Ozawa et al. (2011a)	40 newborns, 4 - 6 days	NIRO 200, Hamamatsu	Frontal	Pain. Blood sampling on dorsum of hand, monitoring 5 minutes before, then during blood sampling procedure	+	Not reported	Not reported
Ozawa et al. (2011b)	Includes 50 term newborns, 4 - 6 days	NIRO 200, Hamamatsu	Frontal	Pain. Skin-breaking, monitoring 5 mins baseline and during procedure	+	Not reported	Not reported

Continued on next page

Table 2.2 – continued from previous page

First Author (Year)	**Participants**	**Instrumentation**	**Cortical Area of Interest**	**Experimental Protocol**	**Significant Results**		
					HbO_2	**HHb**	**HbT**
Benavides-Varela et al. (2012)	44 newborns, mean 2.5 days	ETG-4000, Hitachi	Frontal, temporal, parietal	Auditory. Consonant (C)/Vowel (V) CVCV words, 70 dB, 10 s on, 25 - 35 s off	+	No change	Not reported
Biallas et al. (2012)	14 asleep newborns, mean age 2.1 days	In-house built, Zurich 2	Occipital	Visual. Light flashing 0.5 Hz, 20 s on, 12 - 32 s off	Varied	Not reported	Not reported
Gervain et al. (2012)	22 newborns, 1 - 3 days	ETG-4000, Hitachi	Frontal, temporal	Auditory. Short repetition sequences (speech), 18 s on, 25 - 35 s off	+	-	Not reported
Liao et al. (2012)	11 newborns, 1 - 2 days	In-house built, Washington	Occipital	Visual. Counterphase checkerboard pattern, 10 s on, 20 s off	+	-	+

Continued on next page

Table 2.2 – continued from previous page

First Author (Year)	Participants	Instrumentation	Cortical Area of Interest	Experimental Protocol	Significant Results		
					HbO_2	**HHb**	**HbT**
Sato et al. (2012)	17 newborns, 1 - 7 days	Modified ETG-7000, Hitachi	Whole-head	Auditory. Forwards and backwards speech, 62 - 65 dB, 10 s on, 20 - 30 s off	+	-	+
Shibata et al. (2012)	10 asleep newborns, 2 - 9 days	Modified FOIRE-3000/16, Shimadzu	Parietal, temporal, occipital	Tactile. Vibration to palm, 10 s on, 25 - 30 s off. Auditory. Speech and music audio, 5 s on, 25 - 30 s off. Visual. Flashing light at 8 and 20 Hz, 5 s on, 25 - 30 s off	Tactile: + Auditory: + Visual: +	Not reported	Not reported
Bembich et al. (2013)	30 newborns, 3 days	ETG-4000, Hitachi	Parietal, temporal, frontal	Pain. 10 s before, during stimulus, 25 s after	+	Not discussed but shown	Not reported

Continued on next page

Table 2.2 – continued from previous page

First Author (Year)	Participants	Instrumentation	Cortical Area of Interest	Experimental Protocol	Significant Results		
					HbO_2	HHb	HbT
Naoi et al. (2013)	Included 29 asleep term newborns, mean 4.7 days	ETG-7000, Hitachi	Frontal, temporal, parietal, occipital	Infant-directed speech, adult-directed speech and pink noise (control), 62 dB. 20 s on, 20 s off	+	Not discussed but shown	Not reported
Carlier-Torres et al. (2014)	13 asleep newborns, mean age GA 38 ± 1 week	ETG-4000, Hitachi	Temporal	Auditory. Speech (consonant, vowel sounds), 76 dB, 15 s on, 20 - 30 s off	+	-	Not reported
Cristia et al. (2014)	40 newborns, 1 - 6 days	NTS Optical Imaging System, UCL	Temporal, frontal, temporoparietal	Auditory. Native and non-native speech and macaque sounds, 75 dB, 10 s on, 8 - 16 s off	+	Not discussed but shown	Not reported

Continued on next page

Table 2.2 – continued from previous page

First Author (Year)	**Participants**	**Instrumentation**	**Cortical Area of Interest**	**Experimental Protocol**	**Significant Results**		
					HbO_2	**HHb**	**HbT**
Bouchon et al. (2015)	24 asleep newborns, 1 - 3 days	NIRScout 816, NIRx	Temporal, frontal	Auditory. Speech (repetitive consonant vowel sounds). 9.9 - 10.9 s on, 20 - 25 s off	+	Not discussed but shown	Not reported
Gervain et al. (2016)	22 newborns, 1 - 3 days	ETG-4000, Hitachi	Temporal	Auditory. Water sounds. 18 s on, 25 - 35 s off	+	-	Not reported
Vannasing et al. (2016)	27 asleep newborns, day 1	Imagent Oxymeter, ISS	Temporal	Auditory. Forwards and backwards speech. 64 - 76 dB, 20 s on, 40 s off	+	Not discussed but shown	Not reported

Continued on next page

Table 2.2 – continued from previous page

First Author (Year)	Participants	Instrumentation	Cortical Area of Interest	Experimental Protocol	Significant Results		
					HbO_2	HHb	HbT
Verriotis et al. (2016)	36 newborns, 2 - 9 days	NIRO 200NX, Hamamatsu	Occipito-parietal	Somatosensory. Noxious: heel lance, innocuous: tactile. Auditory: click of lancet. 30 s baseline, stimuli, 30 s baseline	Tactile: + Pain: + Auditory: +	Tactile: no change Pain: Varied Auditory: no change	Pain: +
Frie et al. (2017)	Included 17 term newborns, 1 - 3 days	NIRScout, NIRx	Frontal, parietal	Olfactory. Three odours soaked in cotton bud held 1 cm below nose: pure handcleaner, diluted handcleaner, adhesive remover. Control: water. 10 s on, 2 min off	+	-	Not reported

Continued on next page

Table 2.2 – continued from previous page

First Author (Year)	**Participants**	**Instrumentation**	**Cortical Area of Interest**	**Experimental Protocol**	**Significant Results**		
					HbO_2	**HHb**	**HbT**
Issard and Gervain (2017)	59 newborns, 1 - 4 days	NIRScout 816, NIRx	Fronto-temporal, temporal, tempero-parietal	Auditory. Infant-directed speech (combination of syllables, compressed and non-compressed). 17 – 19 s on, 26 – 35 s off	+	Not discussed but shown	Not reported
Zhang et al. (2017)	18 newborns, 2 - 6 days	NIRScout 1624, NIRx	Frontal, temporal	Auditory. Four emotions presented through speech: fear, anger, happiness and neutral. 55 - 60 dB. 15 s on, 14 – 16 s off	+	Not discussed but shown	Not reported
Arimitsu et al. (2018)	Included 20 asleep term newborns, median 9 days	ETG-4000, Hitachi	Temporal	Auditory. Three words with prosodic and phonemic distinctions , 67 dB. 15 s on, 15 s off	+	-	Not reported

Continued on next page

Table 2.2 – continued from previous page

First Author (Year)	**Participants**	**Instrumentation**	**Cortical Area of Interest**	**Experimental Protocol**	**Significant Results**		
					HbO_2	**HHb**	**HbT**
May et al. (2018)	24 newborns, 0 - 3 days	ETG-4000, Hitachi	Temporal	Auditory. Forwards and backwards speech. 15 s on, 25 - 35 s off.	+	Reported but not discussed	Not reported

Figure 2.15 shows the percentage of studies that reported the different NIRS parameters, and of those parameters that were reported, what the observed response was (this does not include responses where only the measurements are presented but not explicitly discussed). From the 51 results reported, 49 discussed $\Delta[\mathrm{HbO_2}]$, 24 discussed $\Delta[\mathrm{HHb}]$, and 13 discussed $\Delta[\mathrm{HbT}]$.

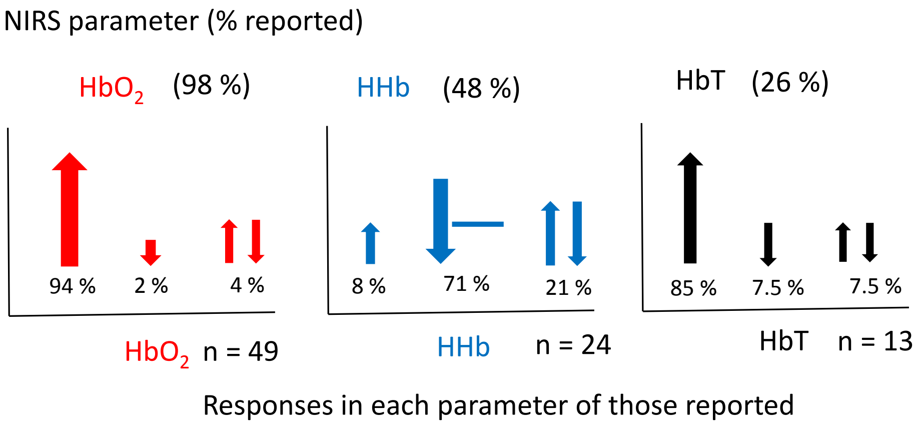

Figure 2.15: Graphs showing the percentage of NIRS parameters reported in fNIRS studies on newborns (above) (a total set of 51 responses from 46 studies were identified) and the corresponding responses of those reported (below). Changes in $[\mathrm{HbO_2}]$ *shown in red,* $[\mathrm{HHb}]$ *shown in blue and* $[\mathrm{HbT}]$ *shown in black. The total number of studies (n) reporting each variable is stated next to each graph. Directions of responses are indicated with an arrow or a line if no change; responses with a double arrow indicate a mixed response (both positive and negative changes observed). Size of arrows correspond to occurrence (from de Roever et al. (2018a))*

A summary of the $\Delta[\mathrm{HbO_2}]$ and $\Delta[\mathrm{HHb}]$ reported responses is shown in Figure 2.16. An increase in $\Delta[\mathrm{HbO_2}]$ and decrease or no change in $\Delta[\mathrm{HHb}]$ was observed in 15 studies. An overview of the responses as separated by stimulus type is shown in Figure 2.17. A variation in responses is seen in studies using auditory stimuli which may be due to the higher number of studies that employ this as a stimulus. The most common response in this protocol is an increase in $\Delta[\mathrm{HbO_2}]$ and decrease in $\Delta[\mathrm{HHb}]$ with nine studies reporting this response; two studies observed a varied $\Delta[\mathrm{HHb}]$ response and two studies observed a varied $\Delta[\mathrm{HbO_2}]$. Studies using a visual stimulus also show a variety of responses, with $\Delta[\mathrm{HHb}]$ showing variability or an increase in four out of nine studies. A varied $\Delta[\mathrm{HHb}]$ is also observed in response to a pain stimulus, as identified in one study, with two sensory studies reporting an increase in $\Delta[\mathrm{HbO_2}]$ and decrease in $\Delta[\mathrm{HHb}]$.

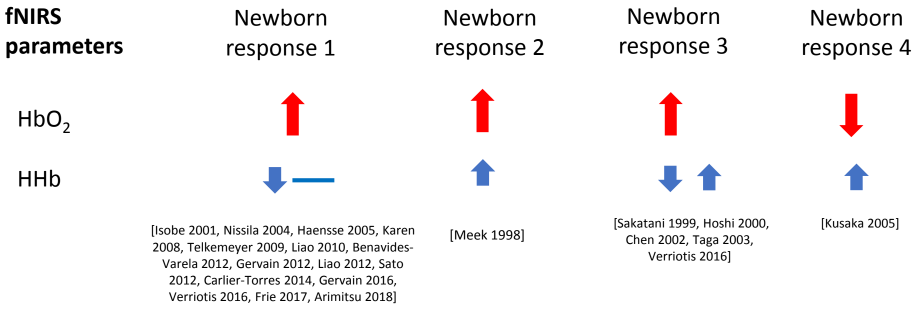

Figure 2.16: Haemodynamic responses to functional activation observed in newborns, with changes in [HbO2] shown in red and [HHb] shown in blue. Data are taken from literature identified in this review paper, and included above only when both variables, Δ[HbO2] and Δ[HHb], have been reported and discussed. The size of the arrows (small and large) relate to the magnitude of the response. Responses with a double arrow indicate a mixed response (both positive and negative changes observed) (from de Roever et al. (2018a))

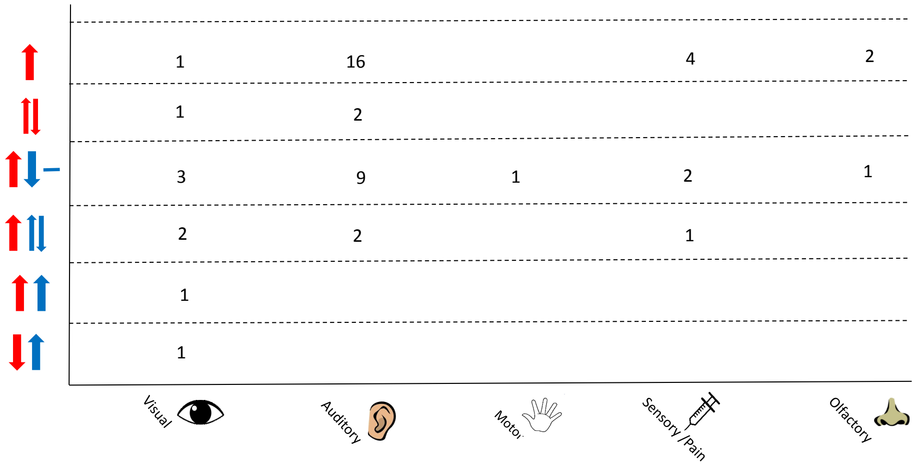

Figure 2.17: Chart showing observed responses separated by stimulus type. Number of studies showing observed response is shown. Directions of arrow indicate whether an increase, decrease, varied response or no change was seen in the NIRS parameter. Δ[HbO_2] is shown in red and Δ[HHb] in blue (from de Roever et al. (2018a))

2.3.4 Interpretation of fNIRS studies in newborns

The majority of studies demonstrated an increase in Δ[HbO_2] with most variation in response arising from Δ[HHb] (see Figure 2.15). No clear association between the reported response and stimulus type, auditory, visual, motor or sensory/pain and olfactory, is observed.

As noted in Section 2.2.4, studies using fMRI BOLD have also observed a heterogeneous response in the newborn brain during functional activation. Care should be taken when interpreting fMRI BOLD studies, as they are often conducted with infants under sedation to prevent movement artifacts. The effect of sedation on the haemodynamic response in human infants has not been investigated; however, in animal studies, sedation did not affect the response of HbO_2 and HHb signals (Sharp et al. (2015)).

A BOLD study by Arichi et al. (2012) looked at the BOLD response from two groups of term infants: one group sedated and one group unsedated. They identified no difference in global CBF between the two groups, suggesting the inverse BOLD response is not as a result of sedation. However, other studies have suggested that sedation may alter the baseline CBF (Seghier et al. (2006)); further investigation into different types of sedation and its effect on the haemodynamic response in newborns is needed. Additionally, since BOLD fMRI detects activated cortical regions via detection of a decrease in Δ[HHb], the presence of an increase in Δ[HHb] may be overlooked unless both an increase and decrease of the fMRI signal are considered.

Functional studies in adults have identified a typical haemodynamic response consisting of an increase in $\Delta[\mathrm{HbO_2}]$ that reaches a peak a few seconds before the peak decrease in Δ[HHb]. Some studies in newborns have shown a slower haemodynamic response compared with adults (~12–16 s peak latency compared with 4–6 s typical peak latency in adults during motor stimulation; Isobe et al. (2001)). The slower response of the neonatal haemodynamic response compared with the adult response may be due to several factors such as sedation (for example, Isobe et al. (2001) monitored sedated newborns), a differing functional organisation of the brain in newborns or ongoing myelin and synapse development and hence a developing NVC mechanism (Kusaka et al. (2011)). It has been suggested that myelination can effect the latency of the haemodynamic response, with increased myelination (such as in the adult brain) leading to a more synchronous synaptic activation (Harris et al. (2011)). MRI studies have shown that visual and auditory sensory regions myelinate faster than motor regions (Welker and Patton (2012)), hence it is plausible that the latency of the haemodynamic response varies according to the stimulus type.

In contrast, Verriotis et al. (2016) identified a faster peak haemodynamic response of 2–4 s for $\Delta[\mathrm{HbO_2}]$ compared with peak latencies of 4–6 s in adults. They suggest this may be the result of differing stimulus durations but alternatively, be related to an immature vascular regulation in newborns that may result in reduced hyperemia and hence a shorter increase in $\Delta[\mathrm{HbO_2}]$.

The majority of studies reported here do not discuss the peak latencies. One study, however, did identify a relationship between the latency of the haemodynamic response to the gestational age of the subject, with significantly shorter latencies for infants with higher gestational age (Kotilahti et al. (2005)), suggesting a variation in the NVC mechanism with age.

Some adult studies have additionally identified an initial dip in the haemodynamic response in the form of an immediate decrease in $\Delta[\mathrm{HbO_2}]$ and increase in Δ[HHb] after onset of the stimulus before the typical oxygen supply to oxygen utilisation ratio is established. The origin of this dip is unknown but has been shown to be localised and may reflect localised neuronal activity (Zaidi et al. (2018)). The majority of fNIRS studies on newborns do not observe this dip that is typical in the adult response. However, from visually inspecting the time-courses of the haemodynamic responses in this review, a dip was identified in some studies (Kotilahti et al. (2010), Liao et al. (2010), Liao et al. (2012), Arimitsu et al. (2011)) although this was not discussed in any of the papers.

The following aspects need to be considered for understanding the fNIRS results: physiological mechanisms, study design, instrumentation and data analysis. Study design aspects such as stimulus choice are important considerations, where stimuli that evoke large haemodynamic changes in extracerebral layers should be avoided. Likewise, the type of instrumentation used is also important as this could have an impact on the haemodynamic response recorded. Hardware aspects such as the number of light sources and detectors, and arrangement of these, as well as methodological techniques applied such as the algorithm to determine $\Delta[HbO_2]$ and $\Delta[HHb]$ all need to be considered. As this chapter is focusing on brain anatomy and function, just the physiological mechanisms are presented here. For further discussion about the other factors that can affect measurements of the haemodynamic response, see the full review paper, de Roever et al. (2018b).

2.3.5 Physiological mechanisms

Several physiological mechanisms have been hypothesised to explain the discrepancy in the newborn haemodynamic response, and in particular to explain the observed increase in $\Delta[HHb]$ reported in some studies (Meek et al. (1998), Sakatani et al. (1999), Hoshi et al. (2000), Chen et al. (2002), Taga et al. (2003), Kusaka et al. (2005), Verriotis et al. (2016)).

Several studies observed an increase in $\Delta[HbO_2]$ and decrease in $\Delta[HHb]$ similar to that observed in the adult brain, suggesting that NVC is intact and functioning in the newborn brain.

However, other studies demonstrated an increase in $\Delta[HHb]$ as well as $\Delta[HbO_2]$, suggesting that the balance between oxygen consumption and oxygen delivery in the neonatal brain differs from the adult brain. Factors that effect NVC include the signaling pathways responsible for dilating blood vessels, which may still be developing and hence alter the expected increase in CBF, and myelination which effects the latency of the response (Harris et al. (2011)).

It has been suggested that the NVC mechanism in the neonatal brain is not yet fully established and can lead to the differing response observed compared with adults, where NVC is well-established (Jasdzewski et al. (2003)). The rapid developmental changes occurring in the newborn brain may affect the coupling between neural activity and blood flow, so fNIRS measurements may reflect the altered functional coupling of the brain (Kozberg et al. (2016)). The increase in oxygen consumption during neuronal activation may not always lead to overperfusion due to the immaturity of the vascular regulation in this cohort of subjects. Additionally, there may be a higher metabolic demand in these subjects compared with adults where metabolic demands in the neonate are still evolving that leads to a reversal of the balance between oxygen supply and consumption (Jasdzewski et al. (2003)). Finally, it may be that NVC matures at different rates depending on the brain region, which may lead to varying responses dependent on functional tasks.

An increase in Δ[HHb] may also be related to venous dilation. Some studies, such as in Hoshi et al. (2000), observed an increase in Δ[HHb] not only with each subject but also within the same subject. An explanation for this may be related to increases of regional CBF which can lead to venous dilation and cause the increase in Δ[HHb] observed. It may be that cerebrovascular reactivity varies with developmental state.

Another possible explanation comes from a blood stealing effect, where regions surrounding the activated region receive reduced blood flow. Hence, an observed decrease in Δ[HbO_2], as sometimes observed, or an increase in Δ[HHb] may be due to the activated region deeper in the brain 'stealing' the blood flow from the fNIRS-measured volume or an activated region close to but not within the fNIRS-measured volume.

Kozberg et al. investigated the haemodynamic response in neonatal rats during electrical hindpaw stimulation reporting an increase in Δ[HHb] (Kozberg et al. (2013)); this inverted response changed as the rats matured, developing to the characteristic haemodynamic response of an increase in Δ[HbO_2] and a decrease in Δ[HHb]. Importantly, they reported increases in systemic blood pressure occurring during stimulation, with their magnitude dependent to the stimulation strength. These systemic blood pressure changes produce fluctuations in haemodynamics and oxygenation in the rat newborn brain that are exaggerated due to the underdeveloped cerebral autoregulation capacity. This acts as a significant confounding factor that can attenuate the haemodynamic response, invert it or even produce one in the absence of evoked neural activity. This physiological phenomenon and issue has been well described and discussed in adult functional activation studies with fNIRS as a major factor in producing false positives and false negatives (see recent review by Tachtsidis and Scholkmann (2016)).

Finally, the waking state of the newborn should be considered as this may affect the response seen to a stimulus. Four studies reported responses in awake newborns (Meek et al. (1998), Bartocci et al. (2000), Nissila et al. (2004), Kotilahti et al. (2005)), nineteen studies reported responses in asleep newborns (see Table 2.2), one study reported responses in sedated newborns (Isobe et al. (2001)) and the remainder of studies reported responses in a mixture of awake/quiet rest and asleep subjects. It is unclear how different arousal states can affect the neurovascular response. The study in the sedated newborns (Isobe et al. (2001)) showed a slower haemodynamic response. Kotilahti et al. (2005) found a diminished response to an auditory stimulus when neonates were in quiet sleep compared with active sleep. Furthermore, Aslin (2012) has suggested that regional differences observed in sleeping neonates may disappear when arousal of the neonate increases and haemodynamic responses increase and could potentially override any regional differences seen.

2.4 Monitoring metabolism using broadband NIRS

An advantage of using broadband NIRS compared with other neuromonitoring techniques is its ability to monitor not just haemodynamic changes occurring in the brain, but also metabolic changes. By using a broadband system, the redox spectrum of the terminal electron acceptor in the ETC, CCO, can be monitored. This provides information about the oxygen utilisation at a cellular level. Monitoring of this chromophore is discussed further in Section 3.1.4.

Only one previous study has used fNIRS to monitor Δ[CCO] in term neonates less than 1 month of age. Zaramella et al. (2001) used an auditory stimulus to monitor $\Delta[\text{HbO}_2]$, Δ[HHb] and Δ[CCO] over the temporal lobe in newborns, aged 1 – 41 days, of which 2/19 were term and the remaining preterm.

An auditory stimulus in the form of a tone of sweeping frequency was presented at 90 dB and data were collected for a median baseline of 4 minutes 40 s, followed by a median of 2 minutes 40 s during exposure to the stimulus and a median of 3 minutes 5 s recovery after the stimulus. Probes were placed over the left or right temporal region and changes in concentration of each chromophore were recorded every 5 s. The cerebral blood volume was also calculated. In general, an increase in $\Delta[\text{HbO}_2]$ and Δ[HbT] was seen with a mixed Δ[HHb] response. Δ[CCO] did not change significantly during functional activation, as shown in Figure 2.18. However, as the cohort of subjects consisted of mainly preterm neonates, results for the term neonates are not explicitly stated so the response from these subjects cannot be identified.

The group used a NIRO 300 to make the measurements, which uses only four wavelengths: 775, 810, 850 and 910 nm. The selection of wavelengths is an important parameter in order to assess changes in Δ[oxCCO] accurately. Later work on monitoring changes in Δ[oxCCO] has suggested that a larger number of wavelengths is required to accurately isolate the spectral components of this chromophore from haemoglobin signals and avoid cross-talk, where changes in one chromophore induce spurious changes in another chromophore. This is discussed further in Section 5.5.1. Briefly, it has been demonstrated that, due to the broad spectral peak of oxCCO and low concentration in-vivo, the selection of wavelengths is important in order to accurately quantify changes in concentration. A higher number of wavelengths has been demonstrated to improve accuracy in the measurement of changes in concentration of oxCCO (Matcher et al. (1995), Arifler et al. (2015)).

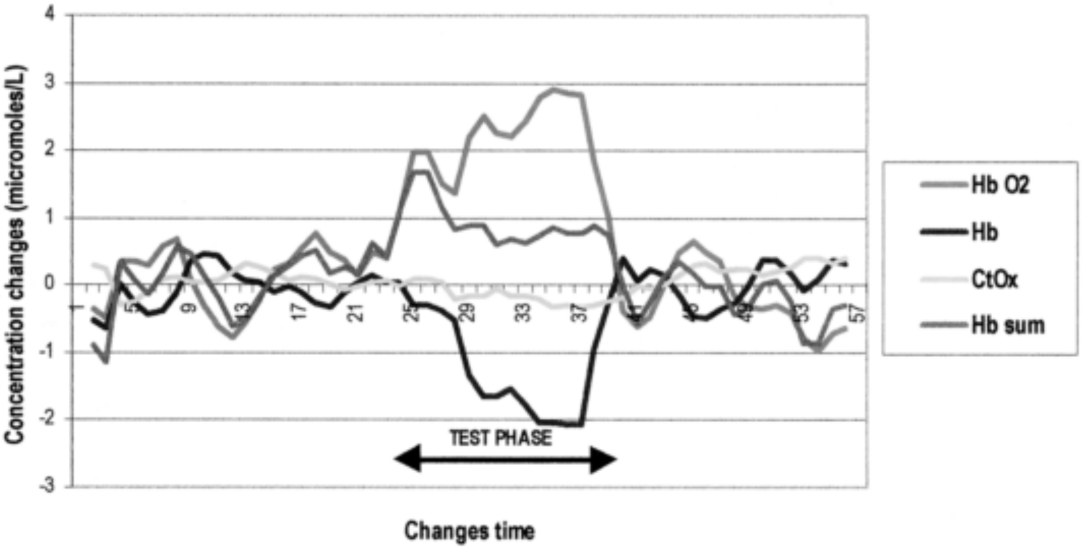

Figure 2.18: Example of functional activation response of a neonate, although it is unclear whether this is for a term or preterm subject. No significant change was seen in CCO during activation (from Zaramella et al. (2001))

2.5 CCO in functional activation

It has been demonstrated that Δ[oxCCO] is a depth-dependent signal, with the concentration of CCO being much higher in cerebral tissue compared with extracerebral tissue. This is likely due to the higher mitochondrial density in tissue with higher metabolic rates such as the brain; this compares with extracerebral tissues with lower metabolic rates. Kolyva et al. (2014) performed systemic hypoxia and hypocapnia (decrease in cerebral oxygen and carbon dioxide), and hyperoxia and hypercapnia (increase in cerebral oxygen and carbon dioxide) in 15 adult healthy volunteers using four source-detector separations 2, 2.5, 3 and 3.5 cm. The authors identified a depth-dependent response of Δ[oxCCO], with a statistically significant increasing amplitude observed with increasing source-detector separations. In contrast, the haemodynamic variables did not show this statistically significant depth gradient.

de Roever et al. (2017) performed continuous frontal lobe NIRS measurements from 17 healthy adult volunteers. Short 1 cm source-detector separation channels were regressed from longer separation channels in order to minimise the extracerebral contribution to standard fNIRS channels (see further discussion of this method in 3.2.4). A significant increase in Δ[oxCCO] was observed only at 3 cm whereas a significant $\Delta[\mathrm{HbO_2}]$ was observed at 1 cm, 2 cm and 3 cm, as shown in Figure 2.19. Regression of the 1 cm channel made no difference to the Δ[oxCCO] response, whereas a functional response not previously seen in the haemoglobin signals at 3 cm is revealed for the right hemisphere. This depth-dependence of Δ[oxCCO] is distinct from haemodynamic signals and suggests its role as a potential alternative and more brain-specific marker of functional activation.

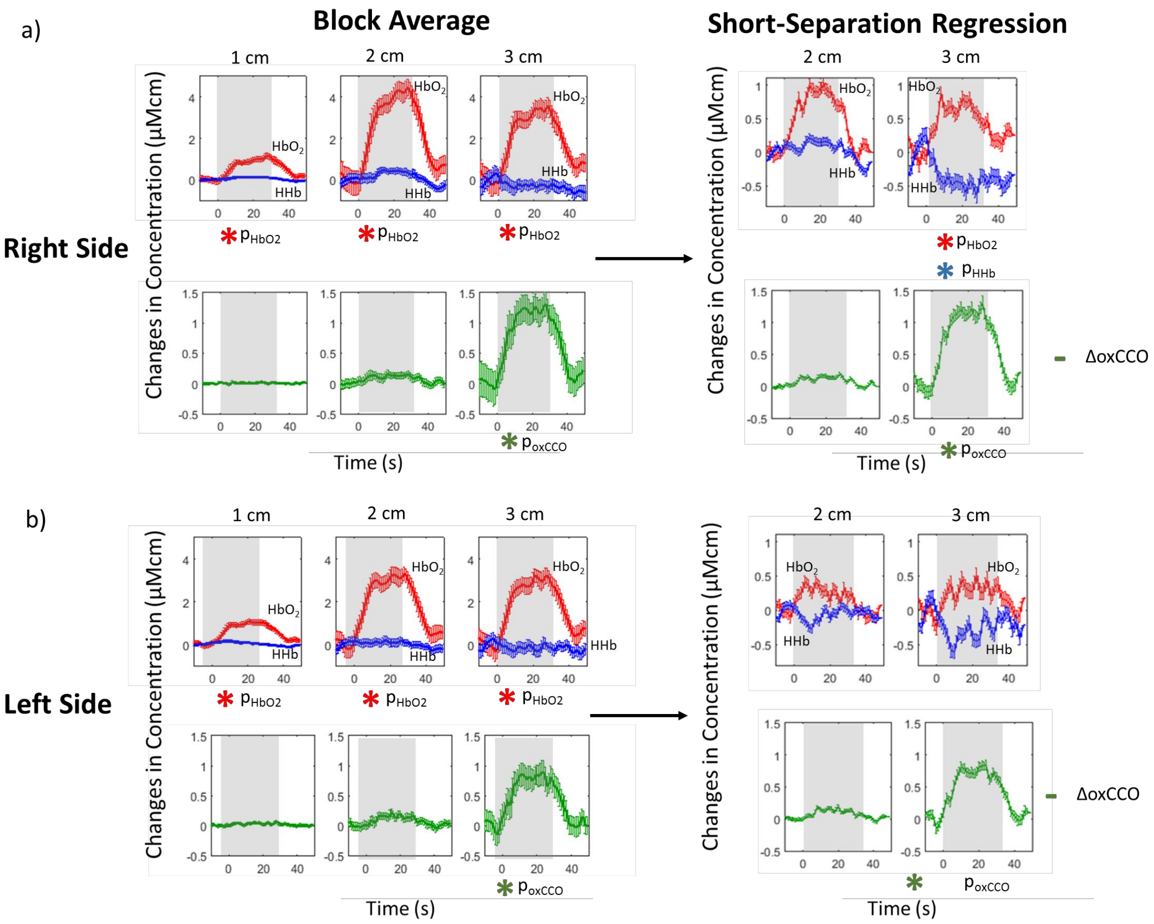

Figure 2.19: Block-average and standard error of mean for 17 subjects during functional activation for left and right sides (a) without regression (b) with short-separation regression. Stimulus period indicated by grey background (from de Roever et al. (2017))

2.5.1 Broadband NIRS in children and adults

Identifying normal developmental patterns in the neonate, as discussed in Section 2.3, has potential use not only in understanding the neurodevelopment in healthy neonates but also in investigating impairment in patients with brain injury. The use of bNIRS enables not only haemodynamic changes to be resolved, as is typical with NIRS systems using a few wavelengths (usually two to four), but it also enables changes in the oxidation state of cytochrome-c-oxidase to be resolved.

Monitoring of this variable informs on the oxygen uptake at the cellular level and hence provides a marker of cerebral metabolism. It has been shown that using a larger number of wavelengths, as with a bNIRS system, reduces the potential noise and cross-talk that oxCCO is susceptible to due to its low concentration in-vivo compared with haemoglobin (Bale et al. (2016)).

This technique can be extended further for use in older children and adults, where the coupling between neuronal activity and changes in haemodynamics and metabolism can provide an assessment of brain function in both healthy and brain-injured subjects. Investigating the metabolic response during brain activity provides an additional dimension to the neurovascular coupling mechanism and provides a more comprehensive overview of the processes occurring during neuronal stimulation.

CHAPTER 3

Broadband near-infrared spectroscopy

This chapter introduces the principles behind NIRS and reviews current instrumentation used for monitoring haemodynamic changes in neonate and infant studies. The concept of monitoring metabolism using NIRS is also introduced and a history of broadband NIRS systems is provided, with the final section describing the components of such broadband systems.

3.1 Near-infrared spectroscopy

NIRS is a non-invasive, optical method to monitor haemodynamic changes in tissue. Tissue is relatively transparent in the NIR region (700 - 1000 nm) and this allows NIR light to pass through tissue and be detected, revealing information about the composition of tissue. Jöbsis (1977) was the first to report that the transparency of brain tissue in the NIR range could be used to monitor real-time blood oxygenation and oxygen sufficiency non-invasively. This technique has since been utilised in many clinical applications.

3.1.1 Absorption

In 1729, Bouguer observed that a monochromatic point source, with initial intensity I_0, travelling through a homogeneous absorbing medium will reduce in intensity, dI, by the same amount per thickness of layer increase, dx (see Figure 3.1).

Hence

$$dI/I = -\mu_{\mathrm{a}} dx \tag{3.1}$$

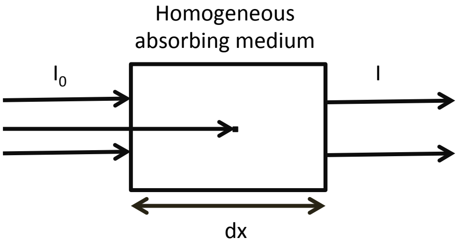

Figure 3.1: Schematic of absorption in a homogeneous medium

where I is the resulting intensity and μ_{a} is a constant indicating the probability over an infinitesimal path that a photon will be absorbed in the medium, also known as the absorption coefficient. It has units of cm^{-1}.

The equation can be integrated to give

$$I = I_0 e^{-\mu_{\mathrm{a}} x} \tag{3.2}$$

where x is the photon pathlength. This is known as Bouguer's law, although it is often attributed to Lambert and known as the Bouguer-Lambert law.

3.1.2 Scattering

Similar to absorption, a homogenous, purely scattering medium will reduce the initial intensity, I_0, by a factor of dI for every increase of thickness layer, dx. This is shown in Figure 3.2. Assuming that attenuation is due soley to scattering, this will be analogous to 3.1 and hence

$$I = I_0 e^{-\mu_{\mathrm{s}} x} \tag{3.3}$$

where μ_{s} is the scattering coefficient of the medium, indicating the probability over an infinitesimal path that a photon will be scattered. It has units of cm^{-1}. It should be noted that this equation is only valid if unscattered light contributes towards the resulting intensity, I. For any highly scattering medium, such as biological tissue with a thickness <1 mm, transmitted light will be scattered multiple times and hence Equation 3.3 does not apply.

Most media, including tissue, is highly scattering. Multiple scattering causes light to rapidly lose its directionality. The direction of this scatter is described by the anisotropy of the medium, g, which describes the degree to which scatter is not equal over all angles. A completely isotropic medium scatters equally in all directions, and has an anisotropy of 0. Tissue is mainly a forward scattering media, and has an anisotropic factor of ~0.7 – 0.98. It is useful to assume a case of

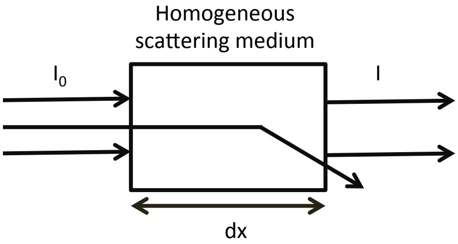

Figure 3.2: Schematic of scattering in homogeneous medium

isotropic scatter, where the scattering coefficient has been reduced by a factor of (1-g); this is known as the transport scattering coefficient, μ_{st}:

$$\mu_{\mathrm{st}} = \mu_{\mathrm{s}}(1 - g) \tag{3.4}$$

3.1.3 Attenuation

The effects of both scattering and absorption is defined by attenuation, A, which is the ratio of incident intensity light to transmitted intensity light, where losses are due to either scattering, absorption or both. The absorption and scattering coefficients, μ_{a} and μ_{s}, can be combined to give the total attenuation coefficient, μ_{t}, giving

$$A = log_{10}(I_0/I) = e^{-\mu_{\mathrm{t}} x} \tag{3.5}$$

where

$$\mu_{\mathrm{t}} = \mu_{\mathrm{a}} + \mu_{\mathrm{s}} \tag{3.6}$$

The total attenuation coefficient, μ_{t} applies to a single scattering event only, where the linearity observed in the attenuation is only applicable to a lightly scattering medium.

3.1.4 Chromophores

There are several absorbing compounds of interest in tissue in the NIR region, known as chromophores. Tissue is composed of 70 – 90 % water; water displays a high absorption in the UV ($\lambda < 400$ nm) and mid-infrared ($\lambda > 5000$ nm) regions, whilst displaying a relatively low absorption in the near-infrared region, a so-called 'window of transparency'. Figure 3.3 shows the absorption spectra of common chromophores in the NIR region.

The main absorbers in the NIR region are oxy- and deoxy- haemoglobin, found only in red blood cells. The two states of haemoglobin, HbO_2 and HHb, have different absorption spectra in this range, as shown in Figure 3.3, and are responsible for arterial blood appearing bright red and venous blood appearing more blue.

Another chromophore found in tissue is melanin, found in the epidermis of skin, and is highly attenuating in the UV region. Lipids are also found in subcutaneous tissue, especially in the brain in the form of myelin. Lipids have a reasonably flat absorption spectra, with their absorption coefficient much lower than the absorption of water, hence, the effects are considered constant.

Finally, cyctochrome-c-oxidase is the terminal electron acceptor in the electron transport chain found in the mitochondrial membrane. It has two haem iron centres, a and a_3, and two copper centres, Cu_a and Cu_b. The dominant NIRS species is the copper centre, Cu_a, and redox state changes that occur when oxygen is reduced to water in the final transfer of the ETC can be detected using NIRS (Mason et al. (2014)). The difference absorption spectrum between the oxidised and reduced forms of CCO is shown in Figure 3.4.

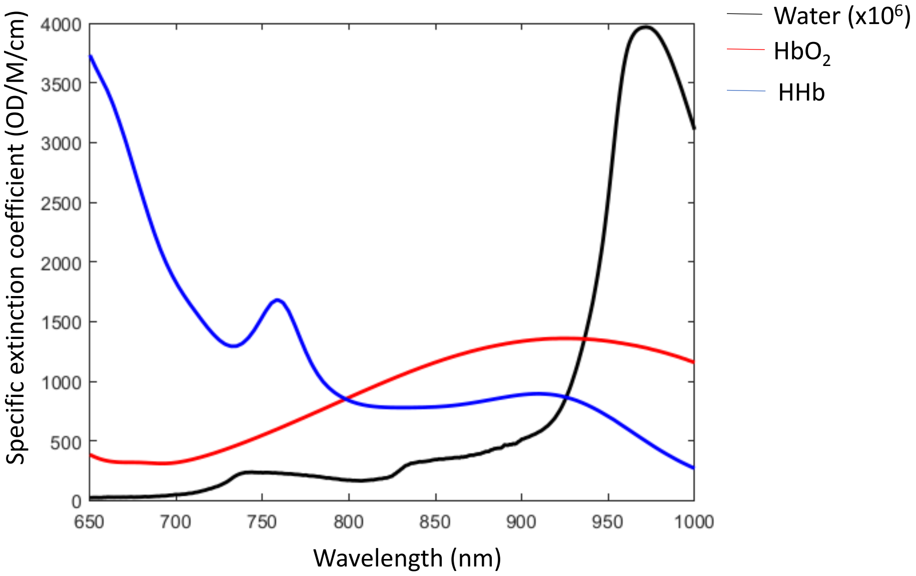

Figure 3.3: Graph showing absorption spectra of common chromophores found in tissue over the NIR region (data from UCL Biomedical Optics Research Laboratory department)

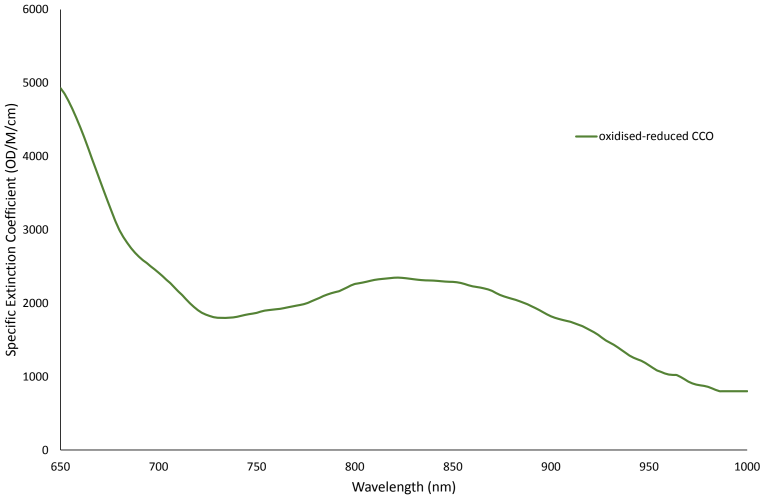

Figure 3.4: Graph showing the difference absorption spectrum between the oxidised and reduced forms of CCO (data from UCL Biomedical Optics Research Laboratory department)

3.1.5 Beer-Lambert Law

In 1852, Beer derived a relationship between the absorption coefficient, μ_{a}, and the absorber concentration, c, where he stated that in a purely absorbing medium, the probability of a photon being absorbed is proportional to the number of absorbers in a given volume (i.e. the concentration), hence

$$\mu_{\mathrm{a}} = \alpha c \tag{3.7}$$

where α is the specific absorption coefficient, with units of molar^{-1}cm^{-1} and c is the concentration in units of molar.

Combining Equation 3.7 with Bouguer-Lambert's law in Equation 3.2, gives the Bouguer-Beer-Lambert law, or Beer-Lambert law for short:

$$I = I_0 e^{-\alpha c x} \tag{3.8}$$

This relates the reduction in intensity of light as it passes through a medium to the concentration of absorbers in the medium and the distance travelled by a photon through this medium.

Combining the Beer-Lambert law in Equation 3.8 with the definition of attenuation in Equation 3.5, gives a relation between attenuation and concentration:

$$A = \frac{\alpha c x}{ln(10)} \tag{3.9}$$

It should be noted that α is defined in terms of natural logarithms; this term can also be defined using logarithms to the base 10, where it is known as the specific extinction coefficient, ϵ. Its relation to α is given by

$$\alpha = \epsilon.ln(10) \tag{3.10}$$

3.1.6 Modified Beer-Lambert law

Taking the Beer-Lambert law and applying it to biological tissue, we can determine an empirical relation between attenuation of light by tissue and concentration of chromophores in tissue. Tissue is a highly scattering medium, so a few changes have to be made to the Beer-Lambert law to account for these effects. This is known as the modified Beer-Lambert law (MBBL), given by:

$$A = (\epsilon_1 c_1 x + \epsilon_2 c_2 x + ...).DPF + G = \sum_{n=1}^{n} \epsilon_{\mathrm{n}}.c_{\mathrm{n}}.x.DPF + G \tag{3.11}$$

where ϵ_{n} and c_{n} represent the extinction coefficients and concentrations for n different absorbing compounds in the material.

The terms G and DPF account for multiple scattering: G is an unknown additive term that takes into account scattering losses and DPF is the differential pathlength factor, a multiplying term that represents the increased optical pathlength of a photon due to scattering.

The DPF is a wavelength-dependent term due to the fact that different wavelengths of light absorb and scatter by different amounts. Hence, the mean effective optical pathlength, taking into account multiple scattering, is given by

$$pathlength_{\mathrm{effective}} = DPF.x \tag{3.12}$$

The DPF is an experimentally measured quantity with different tissue types having different values. The DPF can be found using time-resolved systems, where the time of flight of each photon can be measured and hence an average pathlength factor determined. Studies have determined common DPF values, with a value of 4.99 demonstrated for the neonatal head and 6.26 demonstrated for the adult head (Duncan et al. (1995)). In reality, every subject will have a varying anatomy, with different skull sizes and CSF distribution, all of which can affect the pathlength of the photons. Hence, unless the pathlength is directly measured for each subject, the DPF is only an estimate based on previous empirical evidence.

3.1.7 Differential spectroscopy

The modified Beer-Lambert law is only able to provide information about differential concentrations rather than absolute concentrations. This is because of the unknown value of the scattering coefficient, G. If G is considered constant throughout the measurement period, we can use a differential at two different time points to cancel out the unknown constant G and provide a temporal change in concentration, Δc, from a measured attenuation change, ΔA.

If two chromophores, HbO_2 and HHb, are considered, this is given by

$$\Delta A(\lambda_1) = A(\lambda_1, t_1) - A(\lambda_1, t_0) = (\epsilon_{\mathrm{HbO_2}}(\lambda_1).\Delta c_{\mathrm{HbO_2}} + \epsilon_{\mathrm{HHb}}(\lambda_1).\Delta c_{\mathrm{HHb}}).DPF(\lambda_1).x \tag{3.13}$$

To solve for these two chromophores, a minimum of two wavelengths is needed:

$$\begin{bmatrix} \Delta A(\lambda_1) \\ \Delta A(\lambda_2) \end{bmatrix} = \begin{bmatrix} \epsilon_{\mathrm{HbO_2}}(\lambda_1) & \epsilon_{\mathrm{HHb}}(\lambda_1) \\ \epsilon_{\mathrm{HbO_2}}(\lambda_2) & \epsilon_{\mathrm{HHb}}(\lambda_2) \end{bmatrix} \begin{bmatrix} \Delta c_{\mathrm{HbO_2}} \\ \Delta c_{\mathrm{HHb}} \end{bmatrix} .DPF.x \tag{3.14}$$

The concentration can be solved by rearranging the matrix, such that

$$\begin{bmatrix} \Delta c_{\mathrm{HbO_2}} \\ \Delta c_{\mathrm{HHb}} \end{bmatrix} = \frac{1}{x} \begin{bmatrix} \epsilon_{\mathrm{HbO_2}}(\lambda_1) & \epsilon_{\mathrm{HHb}}(\lambda_1) \\ \epsilon_{\mathrm{HbO_2}}(\lambda_2) & \epsilon_{\mathrm{HHb}}(\lambda_2) \end{bmatrix}^{-1} \begin{bmatrix} \frac{\Delta A(\lambda_1)}{DPF(\lambda_1)} \\ frac\Delta A(\lambda_2)DPF(\lambda_2) \end{bmatrix} \tag{3.15}$$

3.1.8 Broadband near-infrared spectroscopy

To resolve changes in haemoglobin, HHb and HbO_2, it is sufficient to use just two different wavelengths to resolve for the concentration changes of these two unknowns. This is because their absorption spectra are distinct in the NIR region; choosing a wavelength above and below the isosbestic point provides a suitable distinction between the two spectra. Theoretically, it should be possible to distinguish between three different chromophores in tissue, HbO_2, HHb and oxCCO using three wavelengths. However, because the concentration of CCO is much lower than that of haemoglobin, and the oxidised minus reduced CCO spectrum has a broad peak, more wavelengths are needed to accurately resolve attenuation changes that are due to this chromophore.

Broadband NIRS can be used in order to resolve changes in oxCCO, with the gold standard method using over a hundred wavelengths. Taking equation 3.15 and solving for three chromophores using multiple wavelengths gives:

$$\begin{bmatrix} \Delta c_{\mathrm{HbO_2}} \\ \Delta c_{\mathrm{HHb}} \\ \Delta c_{\mathrm{oxCCO}} \end{bmatrix} = \frac{1}{DPF.x} \begin{bmatrix} \epsilon_{\mathrm{HbO_2}}(\lambda_1) & \epsilon_{\mathrm{HHb}}(\lambda_1) & \epsilon_{\mathrm{oxCCO}}\lambda_1) \\ \epsilon_{\mathrm{HbO_2}}(\lambda_2) & \epsilon_{\mathrm{HHb}}(\lambda_2) & \epsilon_{\mathrm{oxCCO}}\lambda_2) \\ . & . & . \\ . & . & . \\ . & . & . \\ \epsilon_{\mathrm{HbO_2}}(\lambda_{\mathrm{n}}) & \epsilon_{\mathrm{HHb}}(\lambda_{\mathrm{n}}) & \epsilon_{\mathrm{oxCCO}}\lambda_{\mathrm{n}}) \end{bmatrix}^{-1} \begin{bmatrix} \Delta A(\lambda_1) \\ \Delta A(\lambda_2) \\ . \\ . \\ . \\ \Delta A(\lambda_{\mathrm{n}}) \end{bmatrix} \tag{3.16}$$

3.2 fNIRS instrumentation

There are several different types of fNIRS instrumentation that have been used to monitor changes in concentration of HbO_2, HHb and oxCCO in neonates and infants. The focus in this section is on continuous-wave (CW) instrumentation, although time-resolved and frequency-domain systems are also briefly discussed.

3.2.1 Frequency-domain systems

Frequency-domain (FD) NIRS systems modulate the intensity of the light source at a certain frequency (typically around 100 MHz). The light attenuation as well as the phase shift are subsequently measured, allowing quantification of the amount of light scatter in the tissue. FD systems are able to determine the mean pathlength light has travelled through tissue and therefore determine the DPF, in contrast to CW systems where the DPF is predicted using previous empirical measurements (Duncan et al. (1995)).

3.2.2 Time-resolved systems

Time-resolved (TR) NIRS systems deliver short pulses of light to the subject, typically in the order of ps. They measure the time-of-flight of photons after they have passed through the tissue and have reached the detector. A histogram of the number of photons and the time of arrival provide information about absorption and scattering of light in the tissue, and a mean pathlength of light through the tissue and hence DPF can be determined for each measurement.

3.2.3 Continuous wave systems

CW NIRS systems use a continuous, constant intensity light source to illuminate the tissue and a detector to measure the resulting intensity of light after it has passed through the tissue. This allows changes in light attenuation to be monitored, which are related to optical changes in the tissue due to varying haemodynamic oxygenation states. Hence, a change in concentration of HbO_2 and HHb can be determined by relating attenuation changes to the absorption spectra of these chromophores (see Section 3.1.6).

3.2.4 Multi-distance methods

One of the main confounding factors in functional experiments are the extracerebral changes that can occur during a functional task that are unrelated to the haemodynamic cerebral changes that indicate brain activity in response to the stimulus. This can lead to false positives, where a positive response is observed where no cerebral response has been induced, and false negatives, where no response is observed in the presence of functional activity. Several methods have been used to account for extracerebral effects including monitoring changes in systemic physiology such as heart rate and respiratory rate in order to identify where large, task-related systemic changes may have confounded a measurement. A review by Tachtsidis and Scholkmann (2016) discusses further the challenges with functional measurements.

Recently, use of short-separation regression methods have been used to account for unrelated extracerebral effects during functional activation tasks (Saager et al. (2011), Gagnon et al. (2012), Goodwin et al. (2014)). Long source-detector separations are more likely to interrogate cerebral tissue due to the longer pathlength taken by photons while photons emitted from short source-detector separations are more likely to be detected before reaching the deeper cerebral tissue. Hence, a short source-detector separation can be used to monitor only the extracerebral layers; this can then be regressed from longer source-detector separations to remove the extracerebral response.

3.2.5 CW fNIRS instrumentation to monitor neonates and infants

The majority of fNIRS studies on neonates and infants use CW systems due to their ease of use, portable nature and relative accessibility in terms of cost. Most CW systems use a few wavelengths (typically 2 to 4 wavelengths) in order to determine the two unknown concentration quantities in tissue: HbO_2 and HHb. Sources usually comprise of either light emitting diodes (LEDs) or lasers, emitting a few discrete wavelengths in the region 600 nm to 980 nm. Sources can be time-multiplexed such that a detector only captures signals from one light source or one wavelength at a time, or frequency multiplexed such that sources are each modulated at a different frequency.

Detectors are usually either photomultiplier tubes (PMTs), silicon p-i-n photodiodes (SPD) or avalanche photodiodes (APD). PMTs work through the photoelectric effect, where an incident photon is absorbed by a photocathode and emits an electron. An electric field accelerates the emitted electron to generate a large number of electrons for every one photon. This amplifying effect provides a good sensitivity to incident photons. SPDs and APDs are sensitive semiconductor devices that work through an internal photoelectric effect: incident photons absorbed by the semiconductor raise electrons to a higher energy level, forming electron-hole pairs and hence a detectable photocurrent. Similar to PMTs, a large electric field is applied to generate an avalanche effect and increase the number of electrons generated from a single photon. SPDs and APDs work similarly in operation, except SPDs can be operated with a reverse voltage above the breakdown voltage to provide a very high gain compared to APDs. This is useful for photon counting.

Optical fibre bundles are typically used to couple the light source and detectors to the subject, although it is possible to couple LEDs or SPDs directly to the subject without the need for optical fibres. Such fibreless systems have the advantage of increased mobility of the patient due to the minimal nature of the source and detectors at the subject-end and an improved optical coupling compared with an optical fibre system, where the added weight of the fibres can increase susceptibility of poor optical coupling. However, optical fibre systems are able to collect a spectrum of light intensity from the tissue making it suitable for a bNIRS system able to monitor metabolic changes. Optical fibres with high numerical apertures maximise the amount of light collected from the tissue, although the added bulk of the fibres at the subject-end can add to patient discomfort, especially in younger patients who are less tolerant to stress. Furthermore, optical fibres are fragile so risk of damage to the instrumentation is increased.

Probe holder designs enable attachment of the source and detector fibre bundles to the subject. For neonate and infant studies, it is desirable to have a design that enables quick placement with minimum discomfort. Depending on the number of source and detector fibre bundles, probe designs can vary from simple flexible holders that can be held to the subject or stuck on using sellotape, to embedded fibre bundles in a cap or band that can be placed relatively quickly to monitor cerebral changes. The headgear of a NIRS system can be one of the most challenging aspects: good and consistent optical coupling is required throughout the measurement period. Factors such as hair can be a big issue as hair is a strong absorber of NIR light and can severely reduce the signal-to-noise of the measurement.

CW NIRS systems are characterised by the number of measurement channels, defined as a source-detector pair. The number of channels affects the level of cortical coverage (this is determined by the number of sources and detectors as well as the source-detector configuration) and the source-detector separations, which determines the depth of light interrogation. A review by Scholkmann et al. (2014) provides a more comprehensive overview of CW NIRS instrumentation.

3.2.6 Commercial fNIRS systems

The use of fNIRS in newborns and infants has been of increasing interest over the years due to the ease of use and portability of such systems, and the ability to monitor the infant in a natural setting making it an ideal neuromonitoring tool to investigate the developing brain.

There have been a number of in-house built fNIRS systems to monitor brain activation in newborns and infants, for example, Nissilä et al. (2003), Karen et al. (2008), Liao et al. (2012). Additionally, a number of commercial systems have been developed over the years to meet the requirements of researchers, neuroscientists and clinicians with an interest in monitoring the young brain. The first functional study in newborns was performed by Meek et al. (1998) using a NIRO 500, developed by Hamamatsu. This system utilises four wavelengths to interrogate the tissue. Since then, a number of companies have developed NIRS technology that has been used in infant studies, including NIRO (Hamamatsu), OMM (Shimadzu), ETG (Hitachi), Omniat Tissue Oxymeter (ISS) and NTS (Gowerlabs Ltd).

As technology has advanced and systems become more sophisticated, the number of source and detector fibre bundles is increasing, enabling larger cortical areas to be monitored with more spatial sensitivity. As a result of this, one of the most challenging aspects of fNIRS in the younger population of newborns and infants is design of a comfortable, light-weight probe holder to couple this large number of source and detector fibre bundles to the head. This younger population is less tolerant to large, bulky designs or discomfort compared with adults. Furthermore, whilst adult subjects can tolerate each source and detector fibre bundle being put on individually, with sufficient hair clearance underneath the probe performed for each fibre bundle put in place, this is not possible to do with infants due to their shorter attention span and lower tolerance levels. Therefore, a design that enables quick and easy placement of a large number of fibre bundles, with good contact to the head to ensure good optical coupling, is desirable. As newborns and infants can become fussy, movement artifacts are also a challenge, with a comfortable and well-fitting piece of head gear helpful to minimise loss of data due to movement.

Another difficulty encountered when monitoring infants with fNIRS is the vast difference in head circumferences over a relatively small age range, due to the rapidly maturing brain. The high curvature of the infant head compared to the adult head makes optimum contact with source and detector fibre bundles to the head more difficult to achieve, and it is important that good optical coupling is maintained throughout the measurement period. Hair is also a strong absorber of NIR and hence can greatly diminish the SNR of the optical signal. Finally, the optimum source-detector separation needs to be determined to ensure the cerebral cortex is being interrogated and to maximise the signal-to-noise ratio. Studies on infants have used separations ranging from 2 cm to 4 cm, with some studies employing additional short source-detector separation channels to account for extracerebral effects (Saager and Berger (2005), Gagnon et al. (2012), Brigadoi and Cooper (2015)).

3.3 Components of a broadband NIRS system

A bNIRS system enables monitoring of not only haemodynamic changes in the form of HbO_2 and HHb, but also of metabolic marker, cytochrome-c-oxidase, providing information about oxygen utilisation at a cellular level. In this section, an overview of the components of a bNIRS system are described, where the term 'broadband' is taken to mean a bandwidth of at least 100 nm.

3.3.1 Light source

In order to reduce the uncertainty in the measurement of changes in concentration of oxCCO, as discussed in Section 3.1.8, a broadband light source with a bandwidth of over 100 nm, with a minimum spectral resolution of the system of 5 nm, is needed. This is required to characterise the broad peak around 835 nm in the CCO-difference extinction spectrum (Tisdall et al. (2008b)). This typically consists of a thermally stable white light source such as a tungsten halogen light bulb, which is filtered to the NIR region using high-pass and low-pass optical filters. A thermally stable source reduces noise in the system and ensures that any intensity changes in the light are from actual physiological changes rather than instrumentation instability. The magnitude of the intensity spectra for each channel are typically between 5000 to 60,000 counts per second. The power of the light source needs to fall within safety limits to prevent any tissue damage but still provide sufficient signal-to-noise.

3.3.2 Optical source and detector fibre bundles

Optical fibre bundles are used in order to transmit the light from the source to the subject (source fibre bundles), and collect the attenuated light from the subject to the detector (detector fibre bundles). The optical fibre bundles consist of a bundle of small glass fibres, typically with diameters in the order of microns for each glass fibre. The bundles are encased in a flexible black tubing to protect the fibres from damage and reduce light contamination from the external environment. The overall bundle size is in the order of mm. It is desirable for detector fibres to have a high numerical aperture to enable a wide angle of light collection and hence increase the sensitivity of the fibres to the tissue.

The ends of the source and detector fibre bundles have to be adapted to the patient-end, where a good contact with the subject is needed in order to reduce light loss. Source and detector fibre bundle heads, referred to as probes, are typically designed to allow fixture to the subject via either a cap or probe holder. They can come vertically out of the fibre bundle or can be designed so that the fibre head is at a right angle to the fibre bundle.

The detector fibre bundles are stacked vertically into a ferrule to allow input to a spectrograph front-end, where the vertical stacking enables light delivery through a spectrograph slit. This enables light from multiple detectors to be simultaneously collected by a camera.

The advantages of optical fibre bundles include the flexibility in the source and detector arrangement and the absence of any electronic parts at the subject-end. The disadvantages are the bulky nature of the fibres, especially when increasing the number of sources and detectors, and their susceptibility to damage due to the fragile nature of the glass fibres.

3.3.3 Probe holders

Probe holders are needed to hold the optical source and detector fibre bundles in place at the subject-end. Configuration of the sources and detectors determines the number of channels in the system; for example, one source and one detector a few cm apart consists of one channel. If multiple detectors surround one source, this increases the number of measuring channels of the system. Probe holders can be designed according to the desired configuration; they also allow a fixed source-detector separation, which determines the brain sensitivity of the measurement. Longer source-detector separations are more likely to penetrate deeper regions of tissue; however, signal-to-noise is a limiting factor. Finally, probe holders need to provide a good optical coupling between the probes and the subject to prevent light loss and ensure a rigid and stable placement of the probes on the head. Any changes in optical coupling during a measurement may manifest

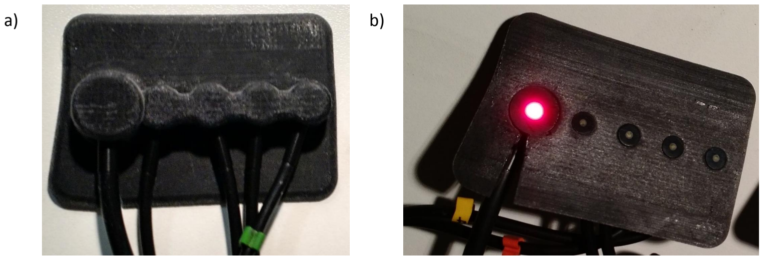

Figure 3.5: An example of a 3D printed, flexible probe holder. a) shows the top side of the probe holder holding a source detector and four detector fibre bundles. b) shows the underneath side of the probe holder that attaches to the subject directly

itself as artefacts in the optical measurements. Figure 3.5 shows an example of a 3D printed probe holder using a flexible, soft material.

3.3.4 Spectrograph

As many wavelengths are being used to interrogate the tissue, a spectrograph is needed to separate the incoming light into its wavelength components before detection by a camera.

A diffraction grating is used to disperse the incoming light. Diffraction gratings consist of a periodic structure of slits; the spacing of the etched grooves are important to the performance of the grating. The light incident on the grating is diffracted to different orders, n, dependent on the wavelength of light, λ, as described by the diffraction grating equation:

$$dsin\theta = n\lambda \tag{3.17}$$

where d is the distance between the slits and θ is the angle of diffraction. A diagram showing this concept is shown in Figure 3.6, where the point of constructive interference represents the light being diffracted to a certain order.

The efficiency of the grating differs for different wavelengths, with the efficiency defined for every order as the fraction of light that reaches that order. The efficiency of the grooves can be optimised using blazing, where the blaze wavelength is the wavelength at which the grating is most efficient.

The spectral resolution is determined by the ability to differentiate between two spectral lines that are close together. Theoretically, the properties of the diffraction grating determine the limit of the diffraction-limited resolution, as described by the resolving power of the grating. This gives the minimum theoretical resolution of the grating. As well as partially determining the spectral resolution of the spectrograph, the diffraction grating additionally determines the wavelength range. The slit width of the spectrograph determines the spectral resolution of the

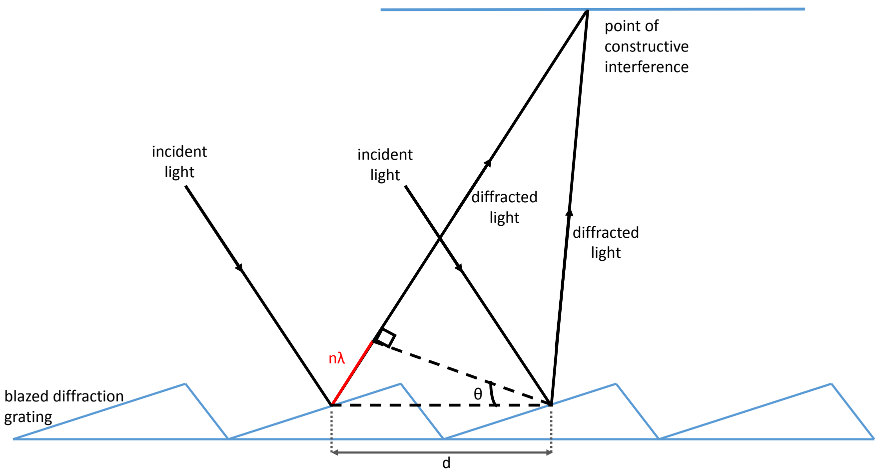

Figure 3.6: Diagram showing how light is diffracted by a blazed diffraction grating, according to the diffraction equation. Constructive interference occurs when the extra distance travelled by the light is equal to $n\lambda$

overall system and controls the amount of light that enters the spectrograph. A trade-off between good light-throughput and spectral resolution needs to be made, with a larger slit width increasing the throughput but at the cost of spectral resolution.

The resolution of a diffraction grating is given by:

$$grating\ resolution = slit\ width\ \times\ grating\ groove\ density \tag{3.18}$$

This is a dimensionless parameter; see Section 4.6.9.

A high through-put and low noise levels are desirable to reduce light loss during this process. The light-throughput can be described by the f-number of the spectrograph, which is related to the top angle of a cone of light the spectrograph can accept.

3.3.5 Charge-coupled device (CCD)

The separated light is directed onto a charge-coupled device (CCD), where a two-dimensional imaging chip captures the light intensity.

A CCD is an integrated circuit etched onto a silicon surface, forming pixels. Pixels are arranged horizontally in rows and vertically in columns. As photons reach the CCD, electrons are generated via the photoelectric effect. This charge can be collected at a positively-held gate in the pixel, with the electric charge proportional to the light intensity. The charge has to be transferred out of the

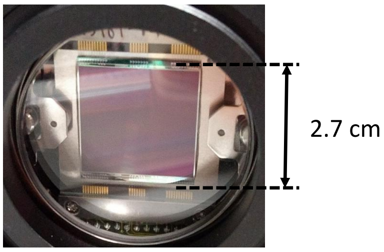

Figure 3.7: Example of a CCD imaging chip

CCD to be read; a control circuit causes the charge in each pixel to transfer to its neighbouring pixel. Charge is transferred one row at a time, down columns, until the final row, known as the readout register, transfers the charge out of the CCD. The final pixel converts this charge into a voltage, so that the array is converted into a series of voltages that can be converted to photon intensities by a computer.

Light is collected in two directions of the imaging array: the x-direction represents the wavelength, where light is separated into its wavelength components in this direction and the y-direction represents the spatial position of each individual detector fibre bundle. Figure 3.7 shows an example of a CCD imaging chip.

There are several sources of noise within a CCD that cause uncertainty in the collected signal. Thermal energy, also known as dark noise, occurs when extraneous thermal electrons in image pixels are generated independent from electrons generated to form the image. Another source of noise comes from photon shot noise, which occurs due to statistical variations in photon arrival time at any given point. Hence, this leads to a statistical variation in photoelectrons generated from incident photons. Photon noise, which follows a Poisson distribution, is found as the square root of the signal and is inherent to the variation of the collected photon flux. Finally, read noise occurs due to inherent electronic noise during the process of converting the signal collected by the CCD to a useable number.

3.4 History of broadband NIRS systems

NIRS as a technique to monitor changes in concentration of oxCCO was first proposed by Jöbsis (1977). Previous commercial systems have been designed to monitor changes in Δ[oxCCO]; however, these systems have only featured a few wavelengths, ranging between 775 nm and 910 nm (for example, Brazy and Lewis (1986), Wyatt et al. (1986), Liem et al. (1997), McCormick et al.

(1993), Grubhofer et al. (1999), Al-Rawi et al. (2001)). One of the first bNIRS systems was developed in UCL in 1995 (see Figure 3.8). There has been some controversy of the origin of the CCO signal over the years; however, recently, improved algorithms and technology has enabled reliable measurement of this metabolic marker with the gold standard method consisting of a bandwidth of over 100 nm. This increased number of wavelengths aids in reducing the uncertainty in the attenuation changes due to CCO and hence provides a reliable method to monitor this variable. A recent review by Bale et al. (2016) on NIRS and the CCO signal outlines the history of this marker and the recent developments that have enabled it to be a reliable and robust marker of metabolic activity.

Table 3.1 shows the evolution of bNIRS systems.

Table 3.1: *Table summarising bNIRS systems to measure oxCCO, used on either adults or neonates*

System (University)	Author (year)	Title	Participants	Wavelength range (nm)	Source-detector separation (cm)
UCL 1	Springett et al. (2000)	Oxygen dependency and precision of cytochrome oxidase signal from full spectral NIRS of the piglet brain	Piglets	650 – 980	3.5
	Tisdall et al. (2007)	Near infrared spectroscopic quantification of changes in hte concentration of oxidized cytochrome oxidase in the healthy human brain during hypoxemia	Adults	650 - 980	3.5
	Tisdall et al. (2008b)	Increase in cerebral aerobic metabolism by normobaric hyperoxia after traumatic brain injury	Adults	650 - 980	3.5

Continued on next page

System, University	Author (year)	Title	Participants	Wavelength range (nm)	Source-detector separation (cm)
UCL1	Tisdall et al. (2008a)	Changes in the attenuation of near infrared spectra by the healthy adult brain during hypoxaemia cannot be accounted for soley by changes in the concentrations of oxy- and deoxy-haemoglobin	Adults	650 - 980	3.5
Humboldt 1	Heekeren et al. (1999)	Noninvasive Assessment of Changes in Cytochrome-c Oxidase Oxidation in Human Subjects During Visual Stimulation	Adults	700 - 1000	Between 2.6 and 3.0

Continued on next page

System, University	**Author (year)**	**Title**	**Participants**	**Wavelength range (nm)**	**Source-detector separation (cm)**
Humboldt 2	Wobst et al. (2001)	Linear Aspects of Changes in Deoxygenated Hemoglobin Concentration and Cytochrome Oxidase Oxidation during Brain Activation	Adults	720 - 920	3
Humboldt 2	Uludag et al. (2004)	Cytochrome-c-oxidase redox changes during visual stimulation measured by near-infrared spectroscopy cannot be explained by a mere cross talk artefact	Adults	720 - 920	2.5

Continued on next page

System, University	**Author (year)**	**Title**	**Participants**	**Wavelength range (nm)**	**Source-detector separation (cm)**
UCL 2 (pHOS)	Tachtsidis et al. (2011)	Analysis of the Changes in the Oxidation of Brain Tissue Cytochrome c Oxidase in Traumatic Brain Injury Patients during Hypercapnoea: a Broadband NIRS Study	Adults	650 - 980	3.5
	Ghosh et al. (2012)	Use of a Hybrid Optical Spectrometer for the Measurement of Changes in Oxidized Cytochrome c Oxidase Concentration and Tissue Scattering During Functional Activation	Adults	740 - 860	3.5

Continued on next page

System, University	Author (year)	Title	Participants	Wavelength range (nm)	Source-detector separation (cm)
UCL 2 (pHOS)	Kolyva et al. (2012)	Systematic investigation of changes in oxidized cerebral cytochrome c oxidase concentration during frontal lobe activation in healthy adults	Adults	740 - 8600	2.0, 2.5, 3.0, 3.5
	Ghosh et al. (2013)	Normobaric Hyperoxia Does Not Change Optical Scattering or Pathlength but Does Increase Oxidised Cytochrome c Oxidase Concentration in Patients with Brain Injury	Adults	780 - 900	3.5
	Kolyva et al. (2014)	Cytochrome c oxidase response to changes in cerebral oxygen delivery in the adult brain shows higher brain-specificity than haemoglobin	Adults	780 - 900	2.0, 2.5, 3.0, 3.5

Continued on next page

System, University	**Author (year)**	**Title**	**Participants**	**Wavelength range (nm)**	**Source-detector separation (cm)**
UCL 2 (pHOS)	Highton et al. (2014)	Analysis of slow wave oscillations in cerebral haemodynamics and metabolism following subarachnoid haemorrhage	Adults	780 - 900	3.5
UCL 3 (CYRIL)	Bale et al. (2014a)	A new broadband near-infrared spectroscopy system for in-vivo measurements of cerebral cytochrome-c-oxidase changes in neonatal brain injury	Neonates (1 - 7 days)	770 - 906	1.0, 1.5, 2.0, 2.5
UCL 4 (Mini CYRIL)	Kaynezhad et al. (2016b)	Optical monitoring of retinal respiration in real time: 670 nm light increases the redox state of mitochondria	Rats	700 – 1100 nm	Adjacent

Continued on next page

System, University	Author (year)	Title	Participants	Wavelength range (nm)	Source-detector separation (cm)
UCL 4 (Mini CYRIL)	Siddiqui et al. (2017)	Non-invasive measurement of a metabolic marker of infant brain function	Infants	780 – 900	2.8
UCL 5	Phan et al. (2016a)	Spatial Distribution Of Changes In Oxidised Cytochrome C Oxidase During VisualStimulation Using Broadband Near Infrared Spectroscopy Imaging	Adults	780 - 900	2.5, 3.78
	Phan et al. (2016b)	Multi-channel multi-distance broadband near-infrared spectroscopy system to measure thespatial response of cellular oxygen metabolism and tissue oxygenation	Adults	780 - 900	2.0, 3.0, 3.5

Continued on next page

System, University	**Author (year)**	**Title**	**Participants**	**Wavelength range (nm)**	**Source-detector separation (cm)**
Ryerson	Nosrati et al. (2016)	Event-related changes of the prefrontal cortex oxygen delivery and metabolism during driving measured by hyperspectral fNIRS	Adults	700 - 900	3

A timeline of bNIRS systems is presented in Figure 3.8. As can be seen, the number of sources, detectors and ultimately channels has increased over the years as improvements in technology have been made. The next few sections will discuss some of the most recent broadband systems developed at UCL, before concluding with the purpose and novelty of the latest iteration of bNIRS system described in this thesis.

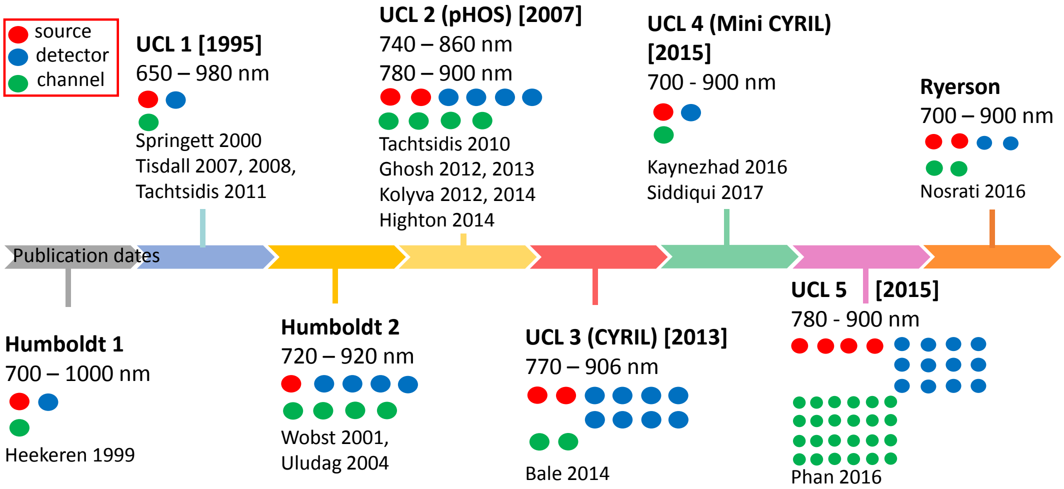

Figure 3.8: Timeline showing history of bNIRS systems to monitor Δ[oxCCO]

3.4.1 CYtochrome Research Instrument and appLication (CYRIL)

CYRIL is a lens-based broadband system developed at UCL to monitor the changes in concentration of HbO_2, HHb and oxCCO in neonates with suspected hypoxic ischaemic encephalopathy in the neonatal intensive care unit (NICU) at UCL Hospital (Bale et al. (2014b)).

A labelled photograph of the set-up is seen in Figure 3.9. It consists of a tungsten-halogen light bulb (ORIEL Fibre Optic Illuminator 77501) filtered to 136 wavelengths, between 770 and 905 nm; a set of bifurcated fibre bundles connect the light source to the patient-end, where a flexible probe holder is used to house the source and detector fibre bundles. The probe holder is fixed on to the head with double-sided tape. Eight detector fibre bundles arranged linearly, with four detectors monitoring the left hemisphere and another four detectors monitoring the right hemisphere, collect light from the tissue at the patient-end to a spectrograph (Acton LS785, Princeton Instruments). The detector fibre bundles are arranged into a ferrule at the system-end and positioned in the spectrograph front-end; here, light is transmitted through a slit into the spectrograph and the incident light from each fibre bundle is separated into its individual wavelength components and collected at a charge-coupled device (CCD) (PIXIS 512f, Princeton Instruments). The CCD displays the spectrum from each fibre bundle, with wavelength along the horizontal axis, and the position of the fibre bundle on the slit along the vertical axis.

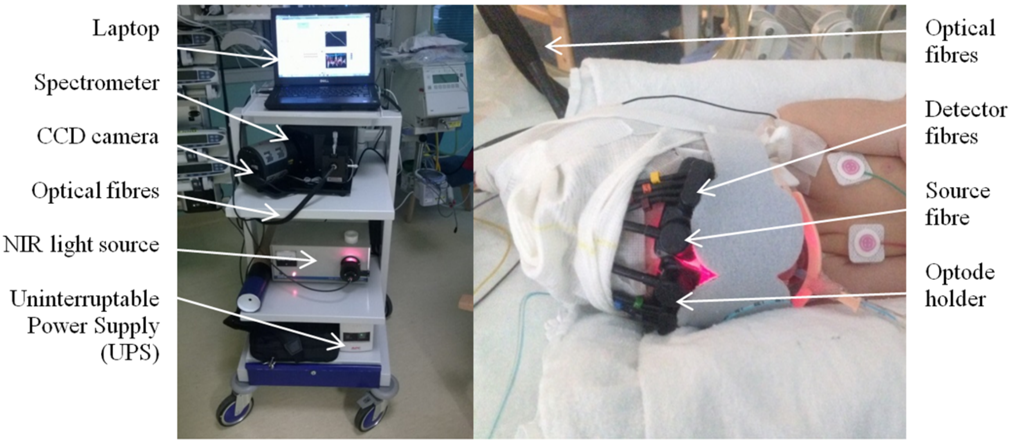

Figure 3.9: Labelled photograph of CYRIL system in NICU. Left hand image shows an image of the individual components and right hand image shows use of the system on a neonate in the NICU (from Bale et al. (2014b))

The system uses LabVIEW (National Instruments) software to convert collected intensity spectra to concentration changes using the UCLn algorithm, in terms of attenuation. From the attenuation changes, the modified Beer- Lambert law is utilised to determine the concentration changes.

CYRIL is able to monitor over two regions of the frontal cortex, with a total of four detectors each on the left and right hand sides of the forehead. The multiple detectors at different source-detector separations enable monitoring of the tissue oxygenation using a technique known as spatially resolved spectroscopy. Tissue oxygenation is defined as the ratio of oxygenated to total tissue haemoglobin and is related to oxygenation status, blood volume, flow changes and oxygen utilisation (Suzuki et al. (1999)).

3.4.2 Mini-CYRIL

A miniature version of CYRIL, named mini-CYRIL, was recently developed at UCL and is a more compact and easily deployable system compared with CYRIL. It has been used to monitor retinal mitochondrial respiration following exposure to 670 nm in aged rats (Kaynezhad et al. (2016b)) and has the potential to be used in a NICU setting to monitor cerebral metabolism in brain-injured neonates.

It is a single-channel system and consists of a small tungsten halogen light source (HL-2000-HP, Ocean Optics) filtered to the NIR region using a 695 nm high-pass filter. An optical source fibre bundle delivers light to the tissue and a detector fibre bundle collects light at the tissue, where it is focused on to the slit of an off-the-shelf miniature broadband spectrograph (Ventana VIS-NIR, Ocean Optics and QE65pro, Ocean Optics). A back-thinned CCD detector with improved etaloning effects enhances the photosensitivity in the NIR region. The system uses MATLAB (MathWorks) code to convert intensity data to concentration changes. Figure 3.10 shows a comparison of the mini-CYRIL system and CYRIL.

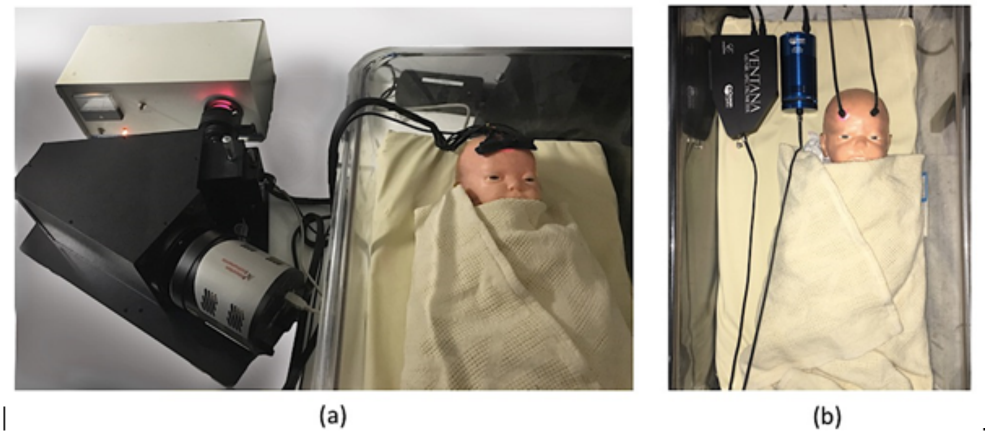

Figure 3.10: Comparison showing size difference between (a) the CYRIL system and (b) the mini-CYRIL system with real size baby model for reference (from Kaynezhad et al. (2016a))

3.4.3 Multi-distance broadband NIRS system

The most recent bNIRS system developed at UCL is described in Phan et al. (2016b) where it was used to monitor cellular oxygen metabolism and tissue oxygenation during functional activation in healthy adults. It has also been used to monitor adults with acute brain injury (Phan (2017)).

The system is comprised of 12 detector fibre bundles and 4 source fibre bundles, forming a multi-channel, multi-distance system for use on the adult brain. It is composed of two lens-based spectrographs and two CCDs (PIXIS: 512f, Princeton Instruments), each with an imaging chip of 512 pixels x 512 pixels. Two 50 W halogen light sources, filtered to 504 − 1068 nm, each connect to a bifurcated fibre bundle. Time-multiplexing capabilities of the light sources allow switching every 1.4 s, leading to a total time of 2.8 s for a single acquisition. Detector bundles house six detector fibre bundles (five with a bundle diameter of 1.5 mm and one with a bundle diameter of 0.6 mm), which connects to the input of the spectrograph. This provides a 24-channel system capable of monitoring at multiple source-detector separations, thus providing a measure of tissue oxygenation index as well as changes in concentration of haemodynamic and metabolic variables. LabVIEW (National Instruments) software is used to convert intensity measurements to concentration changes using the UCLn algorithm between 780 nm to 900nm. Figure 3.11 shows a labelled photograph of the system.

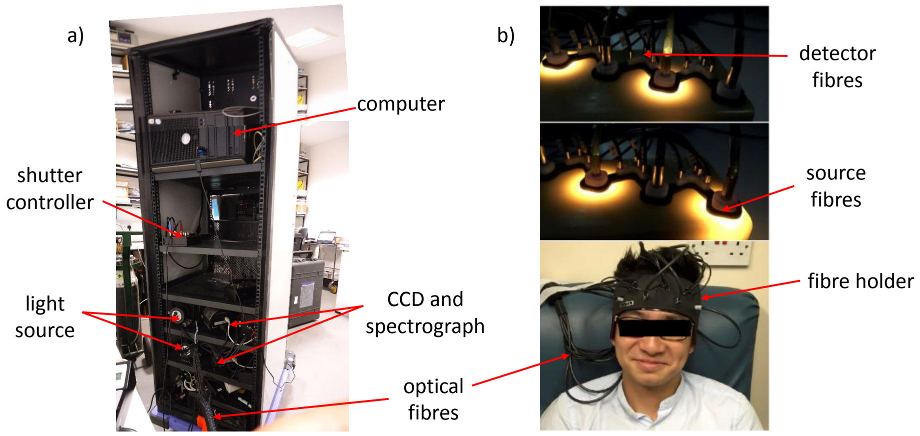
[redacted]

Figure 3.11: Labelled photograph of most recent bNIRS system developed at UCL. a) Image showing the components of the system (own photo). b) Use of the system on an adult volunteer (from Phan et al. (2016b))

3.4.4 Next iteration broadband NIRS device

The aim of this thesis is to develop a new generation bNIRS device in-line with the most recent technology and methods. A compact and simple system that is relatively portable is desirable in clinical settings where there is a need for a real-time brain monitor of metabolism.

The new system uses the latest CCD technology, with the largest imaging chip size currently on the market, with a size of 2.68 cm x 2.60 cm. This will enable a maximum of sixteen detector fibre bundles to be simultaneously imaged onto the chip, reducing the detection components to a single device, as opposed to the system described in Section 3.4.3 where two CCDs and spectrographs are combined in order to deliver the high channel capacity.

Furthermore, a large bandwidth diffraction grating with a bandwidth of 308 nm will enable light collection between 610 nm and 918 nm. Potential future use of accessing this lower wavelength range below 770 nm compared with previous devices will help in determining absolute concentrations of metabolism using second differential techniques.

Smaller, compact light sources that were used in the mini-CYRIL will be utilised and integrated with time-multiplexed switching to maximise the number of available channels. Finally, software will be upgraded and developed to ensure fast handling of data from this large number of channels including real-time visual presentation of the raw intensity data and calculated concentration changes.

The next chapter describes the development of this new device, which represents the next iteration of a multi-channel bNIRS system that is both compact and relatively easy to use.

CHAPTER 4

Development of a multichannel, broadband NIRS system

In this chapter, the development of a bNIRS system to measure changes in concentration of HbO_2, HHb and oxCCO will be discussed. The system consists of two light sources, with bifurcated optical fibre bundles to give a total of four source fibre bundles, and twelve detector fibre bundles, coupled to a spectrograph and CCD, with its operation controlled by LabVIEW (National Instruments) software. The system is a development of a previously designed system named CYRIL, briefly described in Section 3.4.1 and in more detail in Bale et al. (2014a); the new system benefits from a larger bandwidth grating, a more sensitive and larger CCD and an increased number of detector fibre bundles and source fibre bundles with light source switching capabilities.

4.1 Design specifications

The design of the system is motivated by the end-use of the system, to monitor cerebral haemodynamic and metabolic changes in neonates and infants in a clinical environment during a functional activation task. Important considerations are therefore the portability of the device to enable easy transport within the hospital, compactness of the system enabling measurements to be done with minimal interference to standard clinical practice and given the limited space available in the hospital, and small source and detector probes to minimise headgear bulk on such young subjects. Furthermore, expansion of the capabilities of the system is desirable, with time-multiplexed source switching enabling a higher number of channels to provide a larger coverage of brain regions.

The specifications for the system are explored in Table 4.1, where the final specifications of CYRIL, a system also designed to monitor neonates, are compared with the specifications of the new system. Further sections in this chapter also compare the new components of the system with those previously used in CYRIL as both systems have been designed with the infant head in mind.

Table 4.1: Table of previous CYRIL system specifications compared to specifications for new system

	CYRIL Specifications	**Necessity with new system**	**Solution**
Safety	Light intensity within safety levels and does not cause heating	Essential	Optical filters blocking light to the NIR region to minimise heat deposition
	Electrically safe at patient end	Essential	Optical fibres used to avoid any electrical device at the patient end
	Electrically safe at device end	Essential	Isolation transformer to protect the system from the mains supply
Optics	Sensitive to low light levels	Essential	Lens-based spectrometer to maximise light throughput
	Measures oxCCO	Essential	Use of a broadband light source and UCLn algorithm to resolve changes in oxCCO and use of a high signal-to-noise spectrograph

Continued on next page

	CYRIL Specifications	Necessity with new system	Solution
Optics	Measures tissue oxygenation index	Non-essential	Flexible arrangement of source-detector combinations may allow for future implementation of this
	Measures both hemispheres of brain	Essential	This has been upgraded from desirable with the CYRIL system. A larger number of sources and detectors will allow for a larger coverage of the head, enabling multiple regions of the head to be monitored simultaneously
	Insensitive to ambient light	Essential	Blackout fabric placed over the probe holders
	Stable measurements over long periods	Essential	Thermally stable light source and thermoelectrically-cooled CCD ensures minimisation of fluctuations in incident light and detection
	1 Hz sampling frequency	Desirable	High numerical aperture and bundle fibres, high light throughput in spectrograph

Continued on next page

	CYRIL Specifications	**Necessity with new system**	**Solution**
Optics	Flexible detection	Desirable	Separate fibre bundles allows change in configuration via specifically designed 3D printed probe holders
Clinical Practicalities	Probes suitable for neonate	Essential	Light and small custom-built optical fibre bundles with a plastic end and flexible probe holders
	Probes stay on for long studies	Desirable	This has been downgraded from essential. Whilst the probes need to stay attached with little movement, functional activation studies will be shorter with measurement periods of generally less than an hour. Furthermore, the study will be accompanied by a bNIRS technician throughout, who can intervene if a probe holder comes loose
	Compact and portable	Essential	All components fit on a moveable trolley
	Device does not interfere with patient care	Essential	Long fibre bundles of 3 m allow the device to be out of the way of nurses and doctors. Additionally, careful probe holder design to avoid interference with existing monitoring techniques

Continued on next page

	CYRIL Specifications	**Necessity with new system**	**Solution**
Clinical Practicalities	MRI safe	N/A	This has been changed from desirable to not applicable. The functional activation studies will not be performed in conjunction with an MRI machine
	Stable and reproducible data acquisition	Essential	No motorised parts – all operations performed by software
	Easy to use	Essential	A user-friendly LabVIEW graphical user interface
	Continues running in event of power cut	Desirable	This has been downgraded from essential. The use of the system is now for shorter studies during functional activation, rather than long, extended monitoring periods at the cotside
	Simultaneous recording of systemic data	Desirable	This has been downgraded from essential. Whilst it would be advantageous to have simultaneous systemic data, this may be more difficult in situations away from the cot-side as done previously

Additional specifications include

- multiple light sources with time-multiplexed switching between them to increase the number of channels;
- probes easy to attach to enable placement of a large number of fibre bundles relatively quickly;
- increased bandwidth of spectrometer to allow collection at lower wavelengths below 770 nm. This may be of interest in future work to determine absolute concentrations (Matcher and Cooper (1994)).

4.2 Hardware: version 1

As discussed in Section 3.3, the main components of a bNIRS system consist of a broadband light source (typically a tungsten halogen bulb), optical source and detector fibre bundles to transport the light to and from the subject, a spectrograph to separate the wavelength components of collected light and a CCD with a two-dimensional imaging chip to capture the light intensities. Software is able to control these hardware components and process and output the data into a useful format.

Two versions of the system were developed, with the first iteration comprising of one light source with one source fibre bundle and sixteen detector fibre bundles and the second iteration comprising of two light sources and four source fibre bundles and 12 detector fibre bundles. A labelled photograph of the first iteration of the system is shown in Figure 4.1. Below, the hardware and software components for version 1 of the system are discussed.

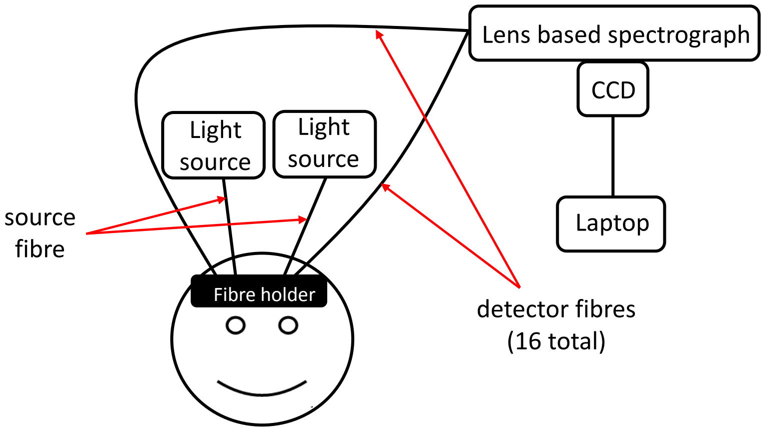

Figure 4.1: Schematic showing the concept of bNIRS measurements for version 1 of the system

4.2.1 Broadband light source

A broadband light source with over a 100 wavelengths is required in order to provide an over-determined matrix (see equation 3.16) that minimises the uncertainty in the oxCCO signal.

The previous light source used in CYRIL was the ORIEL Fibre Optic Illuminator 77501 (see Figure 3.9). It uses a 100 W tungsten halogen light source, and a shutter and iris can be used to block or limit light entering the optical fibre bundle. This light source is no longer in production.

Several light sources were tested as appropriate alternatives, with scope to minimise the size of the source to aid in the development of a compact system and also enable switching of the light source, either via external shutters or internally in the source.

Firstly, the ORIEL 66088 Fiber Optic Illuminator, shown in Figure 4.2, was assessed for its suitability. It uses a 150 W quartz halogen light source with dichroic reflector to focus the light into the fibre bundle. The intensity can be adjusted by changing the voltage via the front panel intensity control knob. An external shutter would be required to enable switching this source on and off, which may add to the complexity of the switching mechanism due to the need for an additional component. This source produced a suitable intensity spectrum through tissue as shown in Figure 4.3.

Figure 4.2: Labelled photograph of ORIEL 66088 light source

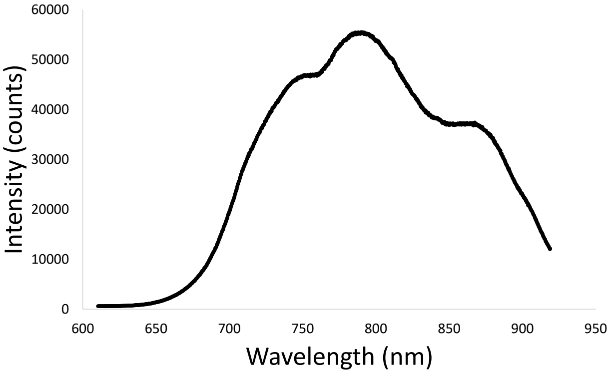

Figure 4.3: Intensity spectrum of ORIEL 66088 light source through tissue

The HL-2000-HP-FHSA (Ocean Optics) light source, shown in Figure 4.4, was also tested. This source is utilised in the mini-CYRIL system discussed in Section 3.4.2. It emits light between 360 - 2400 nm and an integrated fan keeps the light source cool and stable. A built-in filter holder enables use of a 650 nm long-pass filter to remove shorter wavelengths and hence minimise heat deposition and UV exposure when applied to tissue. An internal TTL shutter is incorporated into the design, excluding the need for an external shutter. An additional advantage is the small size of this source aiding in the development of a compact system. The intensity spectrum of this source is shown in Figure 4.5.

Figure 4.4: Labelled photograph of HL 2000 light source

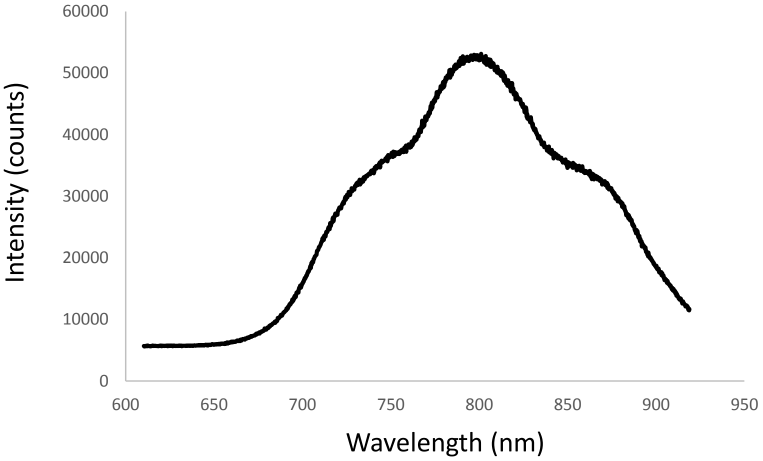

Figure 4.5: Intensity spectrum of HL-2000-HP-FHSA light source through tissue

4.2.2 Optical fibre bundles

Optical fibre bundles were custom-built (Loptek, GmBH) for application with the system. Similar fibre dimensions were used to CYRIL as this has previously been shown to provide optimum light delivery and detection in the neonate head (Bale et al. (2014b)).

Light source fibre bundles deliver light from the source to the tissue. The source fibres consist of a fibre bundle with 30 μm diameter fibres and a high numerical aperture of 0.57. The total source bundle diameter is 1.4 mm, with the optical fibres 3 m in length. The ends consist of a 10 mm diameter plastic head for the subject end. The common side consists of an SMA connection for input into the light source (an adapter was used for the ORIEL 66088 light source). The source fibre bundle is shown in Figure 4.6.

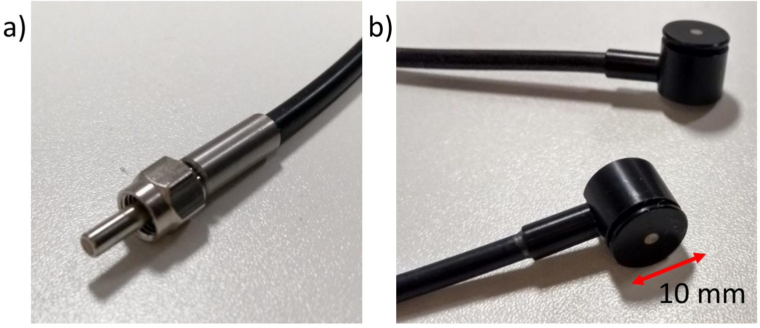

Figure 4.6: Image showing source fibre bundle. a) SMA connector for input into light source. b) Source head at subject-end

Detector fibre bundles collect light that has travelled through the tissue and deliver it to the spectrograph. The detector fibres have a high numerical aperture of 0.57 and core fibre diameter of 30 μm, with each fibre bundle measuring 1 mm in diameter. The initial design of the detector fibre bundles utilised a small plastic head configuration at the subject end, measuring 5 mm diameter by 5 mm height. A small head configuration was chosen to minimise the bulk of the headgear, specially designed with the neonate and infant head in mind, where space is a limiting factor in accommodating a larger number of fibre bundles. Figure 4.7 shows a comparison of these detector fibre bundles with the previous fibre bundles used in CYRIL, where the head height was 10 mm.

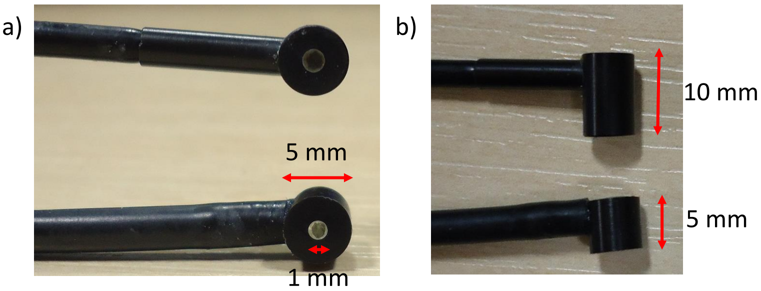

Figure 4.7: Comparison of detector fibre bundles for CYRIL and new system. a) same detector head diameter of 5 mm with fibre bundle diameter of 1 mm b) differing detector head heights of 10 mm (above for CYRIL system) compared with 5 mm (below for new system)

Version 1 of the system consisted of 16 individual detector heads bundled vertically into a metal ferrule at the common side to enable input into the spectrograph front-end. Each fibre bundle in the ferrule is separated by 0.5 mm casing. The total ferrule diameter is 25 mm. The maximum number of detectors is determined by the size of each detector bundle, the spacing between each detector and the size CCD imaging chip; this is discussed in Section 4.6.10

Each fibre bundle is labelled at the detector head end according to its vertical position in the ferrule to enable identification of each detector (see Figure 4.8, where detector 1 is chosen as the top detector and detector 16 as the bottom detector). A comparison of the previous CYRIL ferrule, containing eight detectors, with the larger input ferrule containing sixteen detectors, is shown in Figure 4.8. Figure 4.9 shows the difference in size between the two ferrules from above.

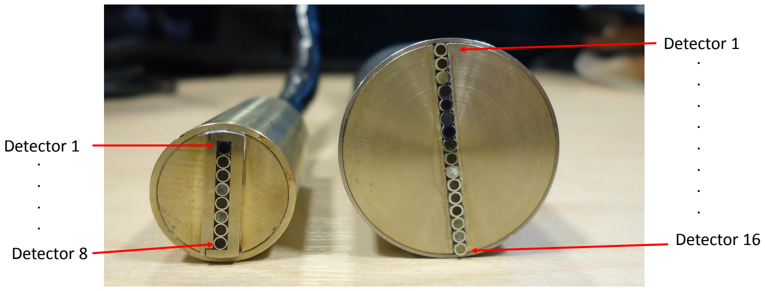

Figure 4.8: Comparison of input ferrule for CYRIL and the new system. Each ferrule contains the detector fibre bundles arranged linearly for input into the slit at the spectrograph front-end. Left hand side shows eight detector fibre bundles in CYRIL system, right hand side shows sixteen detector fibre bundles in new system

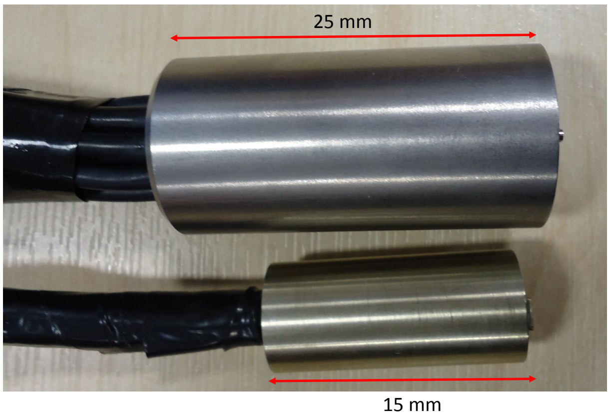

Figure 4.9: Comparison of input ferrule from above for CYRIL and the new system. Bottom shows smaller ferrule size used in CYRIL system, top shows larger ferrule size in new system

4.2.3 Probe holder development

Probe holders are required in order to hold the source and detector fibre bundles on the subject's head, enable easy placement of a large number of fibre bundles and provide a fixed source-detector separation. The design needs to be comfortable, especially for neonates and infants who are less tolerant than adults to bulky or restrictive headgear. Furthermore, clearing the hair and careful placement of each individual fibre bundle, as is sometimes performed in adult studies, is not possible with younger subjects due to the time-consuming nature of this method and the lower level of tolerance of the subjects.

Two different types of probe holder designs were explored: a flexible pad for direct placement on the forehead and integration of the source and detector fibre bundles into a cap for whole head coverage.

Probe holders were designed in Autodesk Inventor and 3D printed; a combination of soft and hard materials were investigated to determine the most appropriate material.

Pad design

For the pad design, a flexible material that moulds to the curvature of the head is desirable. However, due to the intended use of the probe holder, as a reusable holder across multiple subjects, a material that is also strong and hard-wearing is required; by combining a harder material into the 3D printing material, a more durable material can be obtained.

Previous probe holder designs using with CYRIL, shown in Figure 3.9, utilised a flexible holder that held the source and detector fibre bundles in a linear array adjacent to each other to enable measurements of tissue oxygenation index. The aim of the probe holder designs with this system was to provide a wider coverage of the head; therefore, fibre bundles need to be placed further apart from each other in a non-linear configuration. An example of a probe holder design for use on the frontal lobe is shown in Figure 4.10 where the source and detector fibre bundles are placed into a flexible 2D array pad with a source-detector separation of 3 cm. This was printed using TangoBlack, although there were issues with the durability of this material as it was prone to tearing. The shore hardness of TangoBlack could be adjusted to increase the stiffness of the material and hence improve the resilience against tearing; a shore hardness of 50 was found to provide the optimum balance between flexibility and rigidity.

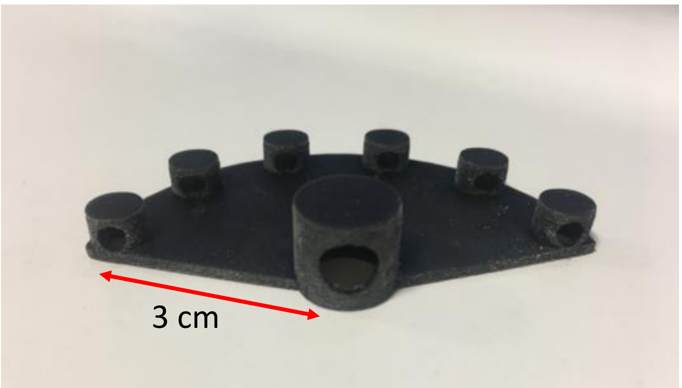

Figure 4.10: Example of 3D printed probe holder in TangoBlack material, holding one source fibre bundle and 6 detector fibre bundles

Cap design

Probe holder designs were additionally developed for incorporation into a cap to allow potential whole-head coverage, or broad coverage of certain cortical regions, with quick and easy placement. A neoprene cap was selected as suitable headgear due to its flexible and stretchy nature, whilst still retaining a certain stiffness for robust source-detector separations.

Initial cap designs were made from TangoBlack; a hole in the cap can be cut to enable the holder to be incorporated into the cap using a ring design to hold it in place. Figure 4.11 shows an example of this initial design. However, it was found that the flexible material was only suitable for one use as it was prone to tearing upon placement and removal of the fibre bundle.

Secondary CAD designs comprised of two parts: a base section that can be inserted into a cap using a wider version of the ring design, and a top section that can be clicked into the base section via an annular snap-fit connection to secure probes in place. Pieces were printed in both VeroClear and in nylon and dyed black; nylon was found to be a more suitable material due to its strong nature and resilience to regular snap-fit mechanisms – for example, the cap clicking in and out when adjusting a fibre bundle. The bases can be incorporated into a cap and probes secured into place with the tops before an experiment, enabling a simple process of fibre bundle placement with a subject. Figure 4.12 shows an example of a nylon base incorporated into a neoprene cap. Figure 4.13 shows an example of the design in VeroClear with a probe held in place.

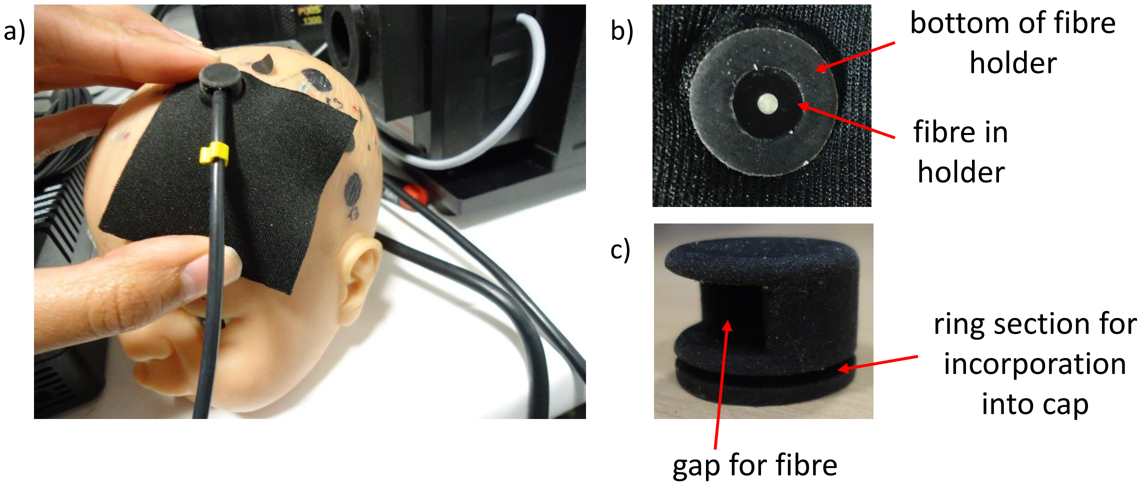

Figure 4.11: Example of 3D printed probe holder in TangoBlack for placement in a cap. a) An example showing how the probe holder can be incorporated into a neoprene material for placement on an infant head. b) The bottom of the fibre bundle and probe holder in the cap. This is the side that is in contact with the subject's head. c) The probe holder before incorporation into a cap. The ring design allows for secure placement in the cap and a gap enables fibre bundle placement and provides an exit for the fibre bundle length

The larger source probes were easier to handle compared with the smaller detector probes, where placement was more difficult due to the small size. Furthermore, design of a probe holder to house such a small head was more difficult, in particular with the clipping mechanism where the tolerance

Figure 4.12: Example of 3D printed probe holder in nylon for placement in a cap

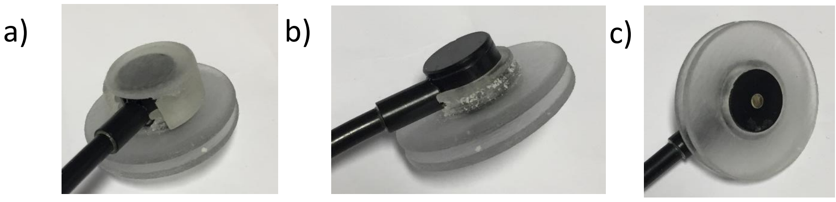

Figure 4.13: Example of 3D printed probe holder in VeroClear. Components consisted of two parts: a base to allow placement into the cap and a top to click into the base and hold the probe in place

for error is smaller; the accuracy of the 3D printed material made this mechanism more prone to error.

An additional challenge encountered with the small detector head design was the small distance between the end of the probe in contact with the tissue and the fibre bundle coming out of the head at 90°. Only neoprene materials of 2 mm thickness were able to be used in combination with this probe as thicker materials would prevent the probe from coming into contact with the subject. This limited the range of suitable materials for development of a cap; thicker neoprene materials were found to provide more rigidity to the source and detector probe positionings, enabling a more fixed source-detector separations whereas thinner materials were easier to handle and place on small subjects.

4.2.4 Spectrograph

The Acton Series LS 785 spectrograph (Princeton Instruments) was used to separate the incoming light into its wavelength components. This was the same spectrograph utilised in CYRIL, although a different diffraction grating was used to expand the wavelength detection of the system.

A labelled photograph of the spectrograph is shown in Figure 4.14. It is a lens-based spectrograph enabling a higher throughput than mirror-based systems. Fast f/2 lenses enable direct fibre optic coupling without the need for f-matching components. Anti-reflective coated lenses provide optimum NIR transmission (between 750 - 1050 nm) of over 99% transmission throughout the working range of the spectrograph.

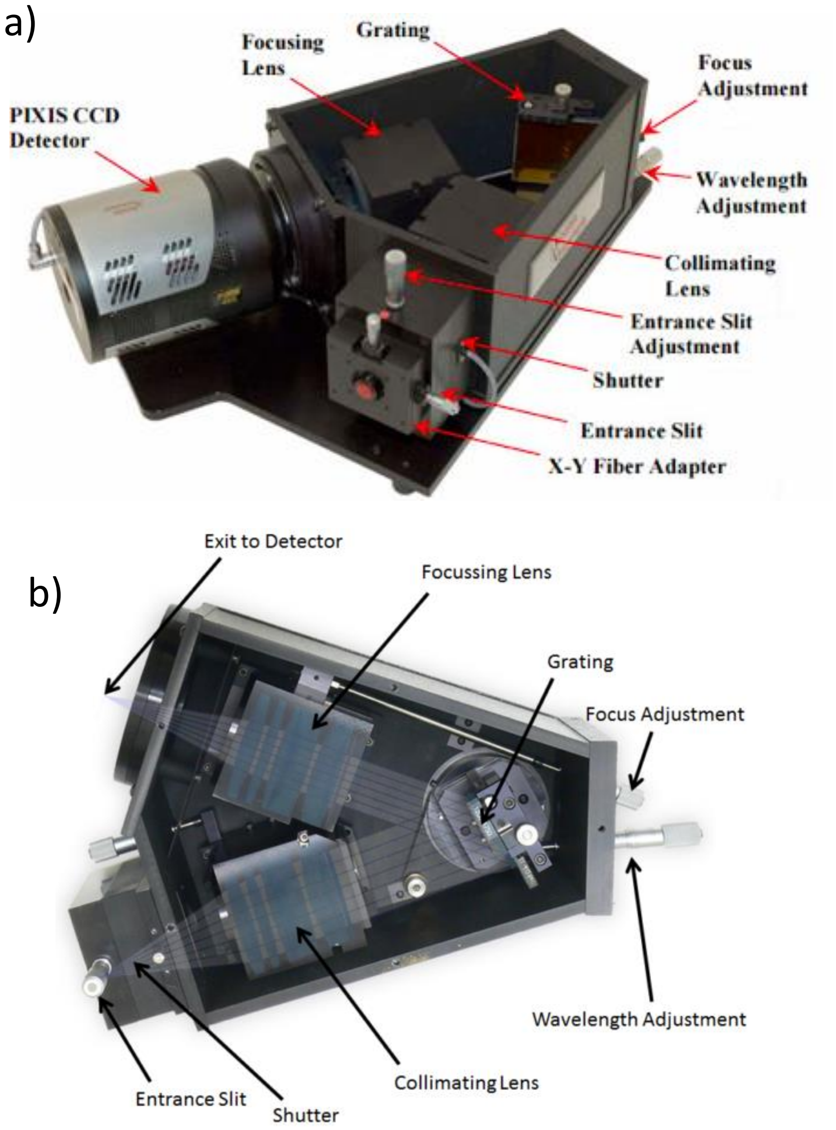

Figure 4.14: Labelled photograph of a) outside of the spectrometer b) inside of the spectrometer (from LS785 manual (Princeton Instruments))

The entrance of the spectrograph comprises an x-y fibre bundle adapter to hold and position the input ferrule, an adjustable slit to prevent overexposure and a shutter to control light input.

Fibre bundle adapter

The x-y fibre bundle adapter had to be modified to be compatible with the larger ferrule size of the new system, as shown previously in Figure 4.8, by increasing the diameter of the input aperture of the adapter. CAD software (Autodesk Inventor) was used to design a new larger aperture adapter and 3D printed with VeroBlack, a solid black material. The design of the 3D-printed adapter and image of the adapter fitted to the spectrograph front-end is shown in Figure 4.15.

The original x-y fibre bundle adapter also consisted of two adjustable micrometer settings that enabled movement of the ferrule horizontally and vertically. This allowed different sections of the CCD to be illuminated. However, due to the larger CCD being utilised in this system (discussed in the next section) and hence larger input ferrule, this component was no longer required due to the maximum size of the CCD imaging array being utilised.

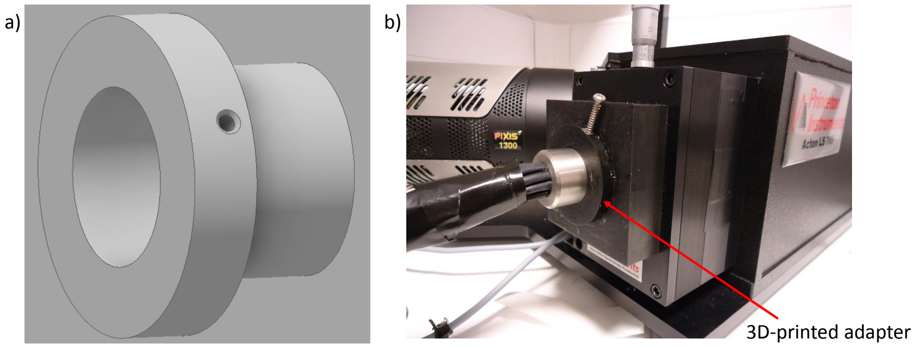

Figure 4.15: a) CAD design of adapter to fit to spectrometer front-end. Design shows increased diameter to accommodate larger ferrule. b) Picture showing 3D-printed adapter fixed to the spectrograph with the ferrule in place. A screw holds the ferrule in the correct position

Slit size

The optimum slit size was found to be 35 μm, to allow sufficient light-throughput without overexposure. Slit sizes larger than this were found to overexpose the CCD. 10 μm was the recommended minimum slit size by Princeton Instruments due to the jaws of the slit not reaching 0 μm to protect the slit from damage in case of over-turning the micrometer to below 0 μm.

Diffraction grating

The diffraction grating inside the spectrograph differs from the original CYRIL system; rather than a bandwidth of 136 nm, between 770 nm and 906 nm, this system has a grating with bandwidth of 308 nm, with a wavelength range between 610 nm and 918 nm. The grating is blazed at 750 nm and has 600 grooves/mm. The grating assembly is aligned by Princeton Instruments to the LS 785. Ability to detect these lower wavelengths below 770 nm could be utilised with future second differential methods to determine absolute concentrations of oxCCO; this method has previously been used to determine absolute concentrations of HHb (Cooper et al. (1996)).

After light has been diffracted at the grating, it is focused onto a CCD detector with an f/2 focusing lens. Focus of the lens can be adjusted to provide optimum focus onto the CCD using the micrometer labelled 'focus adjustment' shown in Figure 4.14. Light can be focused in the y-direction to reduce cross-talk between the different detectors. Wavelength adjustment can also be changed to rotate the grating to a centre wavelength position on the CCD detector.

4.2.5 Charge-coupled device (CCD)

The PIXIS 1300F (Princeton Instruments) is used to detect light from the spectrograph. It is a front-illuminated CCD with a two-dimensional imaging array, with a sensor size of 26.8 mm x 26 mm. This sensor contains a 1340 x 1300 imaging array, hence the pixel size is 20 μm x 20 μm, as shown in Equation 4.1.

$$\begin{gathered} pixel\ height = \frac{26.8}{1340} = 0.02\ mm \\ \\ pixel\ width = \frac{26}{1300} = 0.02\ mm \end{gathered} \tag{4.1}$$

Light is collected in two directions of the imaging array: the x-direction collects light intensities as it is separated into its wavelength components and the y-direction collects light from each individual detector fibre bundle (see the linear detector configuration in Figure 4.8). A labelled photograph of the CCD is shown in Figure 4.16.

This is in comparison with the PIXIS 512F CCD (Princeton Instruments) used in CYRIL, where the sensor size is 512 x 512 pixels (24 μm x 24 μm) on a 12.3 mm x 12.3 mm chip. The PIXIS 1300F provides over double the imaging capacity hence it is expected to be able to fit twice as many detectors on the y-axis (a total of 16 detectors) and over double the wavelength range along the x-axis (a 308 nm bandwidth).

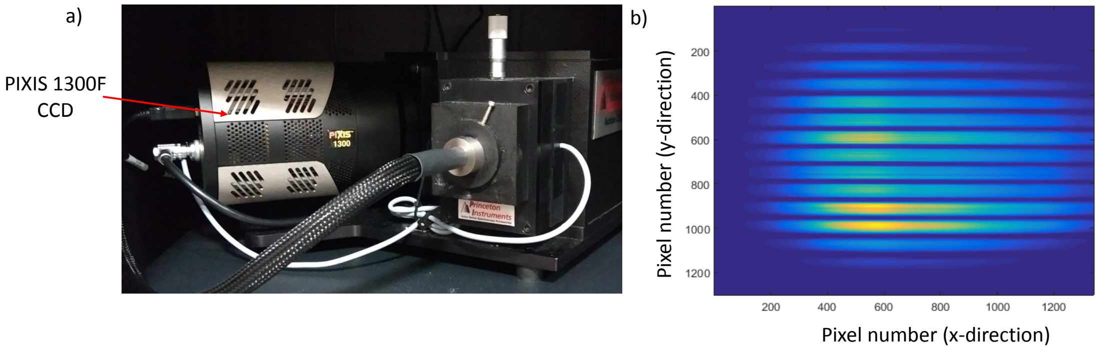

Figure 4.16: a) PIXIS 1300F CCD (Princeton Instruments) connected to spectrograph. b) Example of snapshot showing multiple detector fibre bundles simultaneously captured on CCD imaging array. y-axis corresponds to different detectors and x-axis corresponds to wavelength

The CCD is a 16-bit system and is hence able to handle 2^{16} (65 536) values. The probability of an incoming photon being absorbed in the photosensitive region of the sensor, known as the peak quantum efficiency, lies within the NIR region making it suitable for the application. Furthermore, the front-illuminated design of the CCD means there are no etaloning effects.

Several noise sources within a CCD can cause uncertainty in the collected signal. Thermal energy, also known as dark noise, occurs when extraneous thermal electrons in image pixels are generated independent from electrons generated to form the image. Deep cooling of the system to -65°C reduces thermal noise; the PIXIS-1300F utilises Peltier cooling to reach such low temperatures. The dark current is 0.01 electrons per pixel per second when operated at -60°C.

Another source of noise comes from photon shot noise, which occurs due to statistical variations in photon arrival time at any given point. Hence, this leads to a statistical variation in photoelectrons generated from incident photons. Photon noise is found as the square root of the signal and is inherent to the variation of the collected photon flux.

Finally, read noise occurs due to inherent electronic noise during the process of converting the signal collected by the CCD to a useable number. The PIXIS 1300F contains low noise electronics which make it ideal for low light level applications. The read noise at 100 kHz is 2 electrons root mean square.

4.3 Software: version 1

The hardware components are controlled by software developed in LabVIEW; the original software for CYRIL was modified and adapted to expand the system into a 16 detector system.

The main alterations in version 1 of the software include:

- converting individual detector paths into parallelisable loops to increase efficiency of program and aid in reading of the LabVIEW code;
- adjusting viewable graphs in user interface so data from all detectors are visible. This includes collected intensity data and corresponding calculated concentrations;
- adjusting binning interface of software to include and calculate bins for 16 detectors;
- modifying logic of reference spectra section to enable collection from 16 detectors.

The overall structure of the program, shown in Figure 4.17, remains similar, with the initial section comprising of the settings controlling the camera and graphical user interface (GUI). When the program is first run in LabVIEW, the CCD begins to cool to -65°. Once the initial parameters have been selected by the user in the settings section, the 'start' button can be selected to begin data collection and conversion to concentration data. This is done in a producer-consumer loop in the software. The producer loop collects the intensity data and displays them, and places the intensity values in a data queue, providing data buffering to temporarily store the data. These data are then processed in the consumer loop to calculate and display the changes in concentration. All the data are saved in the consumer loop to individual excel files for each detector concentration values and intensity values, as well as a separate time file. Using the producer-consumer loop allows data collection to continue in the producer loop without having to wait for the consumer loop to process each set of incoming data. Additionally, saving the data to individual excel files line by line prevents data loss should the system crash or there be a power cut.

A flow chart of the overall mechanisms of the software is shown in Figure 4.17.

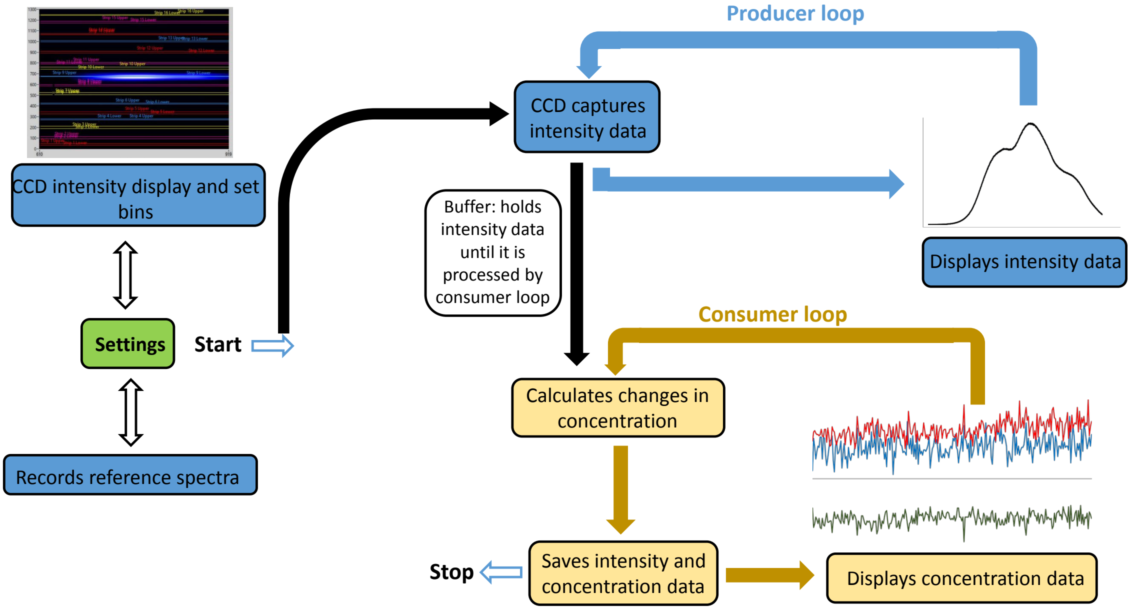

Figure 4.17: Block diagram showing the main functions of the LabVIEW program, version 1

Settings

The setting tab is shown in Figure 4.18. It includes all the parameters that can be defined by the user, with common options set as default upon opening the program. Parameters that can be changed include the DPF and source-detector separation. A drop-down menu allows selection of frequency of data collection, which ranges between 1 Hz and 5 Hz. A 'comments' bar at the top of the tabs section allows the user to send a comment during data collection, which is saved in the time file in the next time point of data collection.

Comment
error

Subject Number
filter

Start time
_180117_140747

Current time
14:07:51.535
18/01/2017

Frequency (Hz)
1

Number of Detectors
16

Optode distance (cm) 1
1.5

Optode distance (cm) 2
2

Optode distance (cm) 3
2.5

Optode distance (cm) 4
3

DPF
4.99

Adult arm: 4.16
Adult head: 6.26
Neonate head: 4.99

Start wavelength (nm)
770

End wavelength (nm)
906

Display Number (s)
500

Saturation limit
65535

Noise limit
0

Figure 4.18: Settings tab in software where user can select parameters before starting measurements

Binning

Binning of the CCD describes the process of adding adjacent rows of pixels in the CCD to form a single row. This can be done for the collected spectrum of each detector to maximise the number of counts without exceeding data limitations in the system. The CCD camera is comprised of a 2D imaging array, as described in 4.2.5. The intensity data from each detector are collected such that the wavelength separation is differentiated in the x-axis, where each pixel corresponds to a wavelength between 610 nm and 918 nm, and the different detectors are separated in the y-direction of the camera array corresponding to the displacement along the entrance slit. The spectrum collected from each detector is distinct and visible in the GUI where the intensity data are collected for each detector; since the CCD is a 16-bit system and only able to handle 65 536 values, binning of the collected spectrum for each detector in the y-direction is necessary to maximise intensity counts whilst preventing overexposure of the CCD. The size of the binning region over the collected spectrum for each detector can be adjusted by the user.

A snapshot can be taken to display the intensities acquired on the whole of the CCD; this allows each exposed detector spectrum to be visible on the CCD and enable a suitable binning range to be selected. An example of this is shown in Figure 4.19. The intensities across the pixels within each detector bin in the y-direction are integrated to provide an intensity spectrum against wavelength for each detector. The binning can therefore be adjusted by the user to increase or decrease the overall photon count of the intensity spectrum.

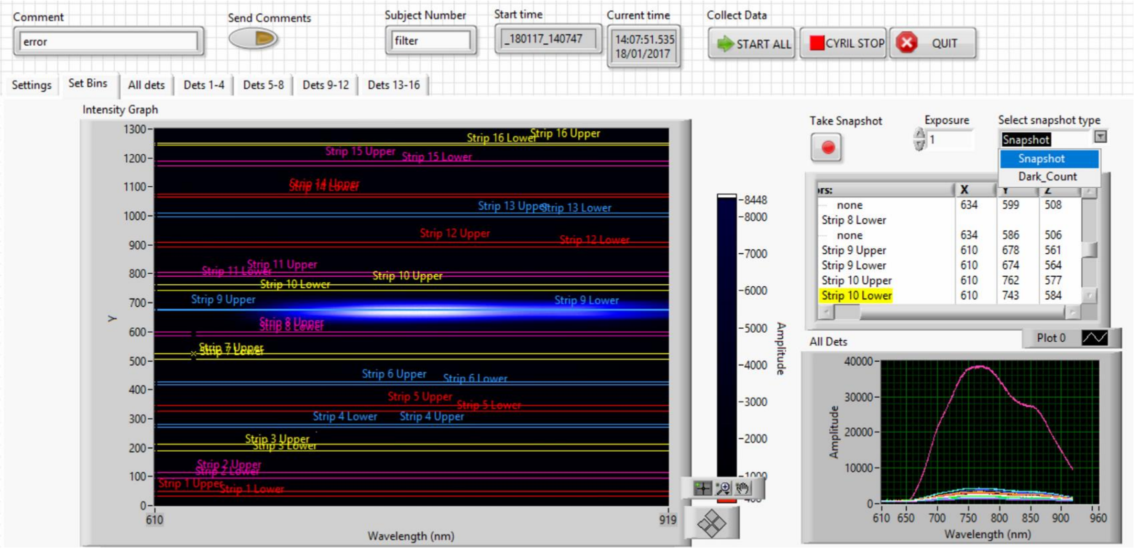

Comment: error

Subject Number: filter

Start time: _180117_140747

Current time: 14:07:51.535 18/01/2017

Exposure: 1

Select snapshot type: Snapshot

rs:	X	Y	Z
none	634	599	508
Strip 8 Lower			
none	634	586	506
Strip 9 Upper	610	678	561
Strip 9 Lower	610	674	564
Strip 10 Upper	610	762	577
Strip 10 Lower	610	743	584

Figure 4.19: Screenshot of software GUI showing binning section, where bins for each detector can be manually altered by the user. A snapshot of the image on the CCD can be obtained and is automatically saved

Intensity data collection

A typical spectrum through an adult head is shown in Figure 4.20 where 42 pixel rows have been binned and integrated to provide a maximum intensity of around 30 000 counts.

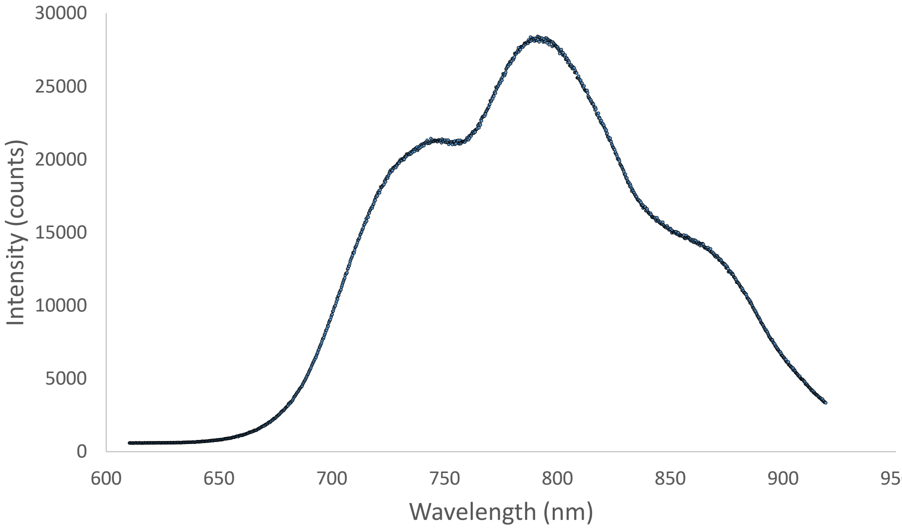

Figure 4.20: Typical reflected intensity spectrum from the adult head. Measurements taken from one detector over frontal lobe with a binning region of 42 pixels

One of the main modifications to the original program involved enabling the software to handle a larger number of detector probes, in both the photon intensity collection from each detector and the conversion of this raw intensity data to changes in concentration. These processes have been modified to run in parallelisable loops rather than as individual pathways for each detector as previously. Parallelisable loops enables iteration of the loop to occur concurrently in multiple cores hence reducing processing time. This also allows the user to select the number of detector fibre bundles they want to utilise.

The user interface has been modified to fewer tabs, to allow easier visualisation of all the detectors. Display of the 16 detector fibre bundles is separated into four tabs, for easy viewing, with the intensity data and concentration data presented in real time.

Snapshot data are now automatically saved with a timestamp in the file name to enable saving of either the dark count of the CCD, or illumination of the detector fibre bundles onto the CCD. This can aid in quality checking of data in the post-processing stage.

Concentration calculation

The concentrations are calculated as with the original software, based on the modified Beer- Lambert law using the UCLn algorithm (Matcher et al. (1995)). The UCLn algorithm is a least-squares fitting procedure to determine the best fit of the chromophore extinction coefficients. The intensity data are converted into a change in attenuation for each pixel; these are then interpolated to 136 wavelengths between 771 nm and 906 nm using spline interpolation. The change in attenuation is divided by the wavelength dependency of the DPF. The psuedo-inverse matrix of the extinction coefficients of the chromophores is multiplied by the change in attenuation, with the DPF, wavelength dependency of the DPF and source-detector separations included in the calculation. This process been modified to run in a parallelisable loop with concentration values displayed in real-time.

Currently, only wavelengths between 771 - 906 nm are being used to calculate concentration changes even though the diffraction grating in the new system has a larger bandwidth than previously.

4.4 Hardware: version 2

The second iteration of the system is comprised of two light sources, with two bifurcated source fibre bundles for each source, resulting in a total of four source fibre bundles. The initial sixteen detector fibre bundles were reduced to twelve detector fibre bundles due to issues with imaging all sixteen fibre bundles on the CCD (this is discussed in detail in Section 4.6.10). Light source switching capabilities are implemented in this version of the system. A labelled photograph of the second iteration of the system is shown in Figure 4.21.

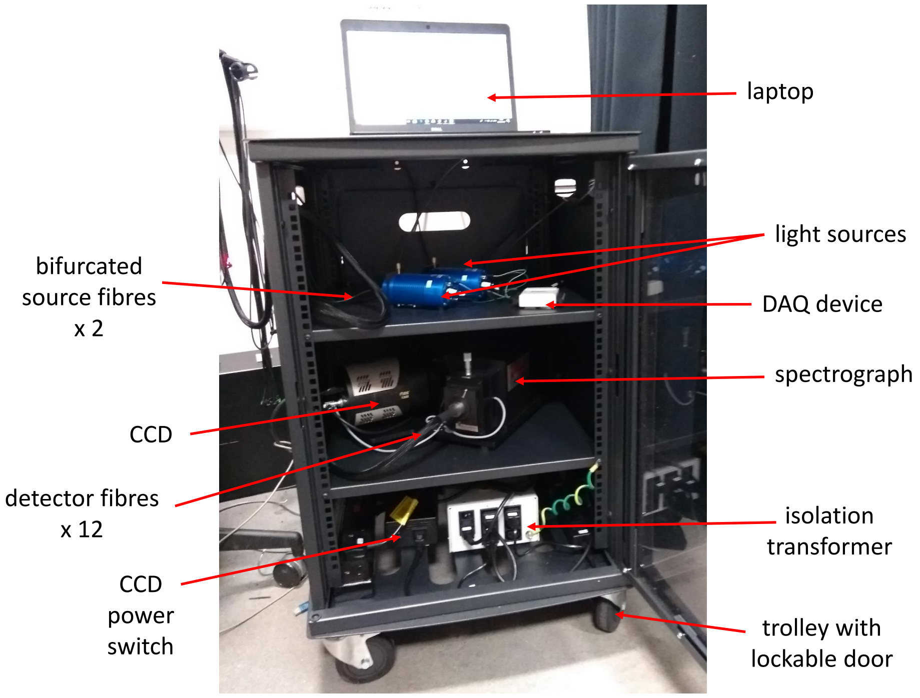

Figure 4.21: Labelled photograph showing the components of the final version of the system. This version has two light sources with a shutter controlled by a DAQ device to incorporate time-multiplexed light switching of the sources. A total of 12 detector fibre bundles collect light from the subject's head and are connected to a spectrograph and CCD camera. LabVIEW software controls the operation of the system

4.4.1 Optical fibre bundles and probe holders

Source fibre bundles were adapted to include a bifurcation at 2.5 m into two separate fibre bundles for 0.5 m; hence, for each light source, there are two source fibre bundles. This is shown in Figure 4.22.

Figure 4.22: Image showing optical source fibre bundle bifurcated after 2 m, with two single fibre bundles for 0.5 m

The detector probes were re-designed as the small size of the ends made incorporation into a cap design for potential whole-head coverage quite challenging, as discussed in Section 4.2.3. In version 2 of the system, these detector probes were altered to match the larger head size of the source detectors to enable a more robust design with relation to the cap.

Additional designs were investigated with these larger probes. The ring mechanism around the bottom of each fibre bundle head, consisting of a gap 1 mm from the end of the head, enabled designs where the probe can be held in place in the holder; these designs have previously been used in infant studies done in Birkbeck Babylab (Lloyd-Fox et al. (2010)). In collaboration with colleagues at Babylab, two methods of utilising the ring mechanism were explored: a clipping mechanism where the probe can be pushed into place in the holder and a sliding mechanism where the probe can be slid into and out of the holder. These mechanisms were tested with different materials to check for robustness. TangoBlack 50shore was found to be a suitable material for the base pad with nylon dyed black the most resilient material for the solid circular holders. Embedding of the solid holders into the softer base pad was plausible, although the VeroBlack used in this printing method was prone to breaking. The optimum solution was to use a glue to adhere the two materials together. A slow cure, high strength glue (Slo-zap) and a curing accelerator (Foam safe kicker, Zap) provided the strongest bond between the two materials. Examples of these mechanisms are shown in Figure 4.23.

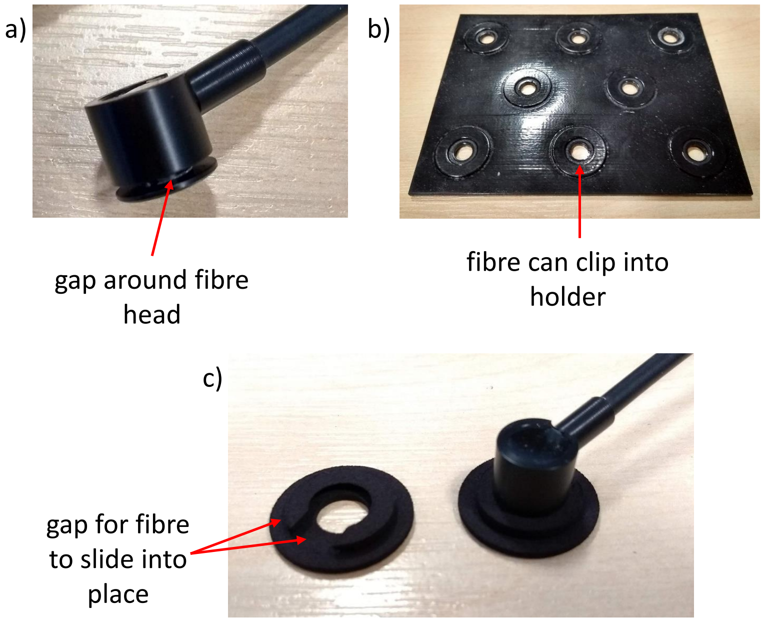

Figure 4.23: a) Image showing probe ring mechanism consisting of a gap 1 mm from the base of the head. b) Example of a flexible base pad printed in TangoBlack with hard, VeroBlack circular holders embedded into base pad. Probes can be pushed into circular holders and are held in place via a clipping mechanism. c) A circular holder printed in nylon and dyed black. A 1 mm gap around the base of the holder with an opening at the front enables probes to be slid into position

4.4.2 Light source

The HL-2000-FHSA-HP (Ocean Optics) has an internal shutter that can be controlled externally. This source was therefore selected as the most suitable light source to incorporate time-multiplexed switching. A National Instruments DAQ device was used to control the TTL input of the source via the DB15 port; one pin connected to ground and a second pin controlled the shutter (5 V to open the shutter and 0 V to close the shutter). The pins that control the shutter are labelled in Figure 4.24. The shutter switch of the light source needs to be operated in the TTL setting to enable external control of the source. Two light sources were used in total, each with a bifurcated set of source fibre bundles, resulting in a total of four source fibre bundles, which can be switched on and off alternately.

Initially, a USB-6229 (National Instruments) device was used to send TTL pulses to the light source. Two BNC to DB15 port cables were made for this use, with the relevant wires from a BNC cable soldered to the corresponding wires of a DB15 cable and heat-shrink used to seal the exposed wires. This set-up worked as required, although the DAQ device used was on the large side.

A USB-6800 (National Instruments) was selected as a suitable alternative device to send TTL pulses to the light source and was chosen due to its small size. Wires at the screw terminal plugs of the DAQ device connected to the ground and shutter control pins of the light source. Both DAQ device set-ups are shown in Figure 4.24.

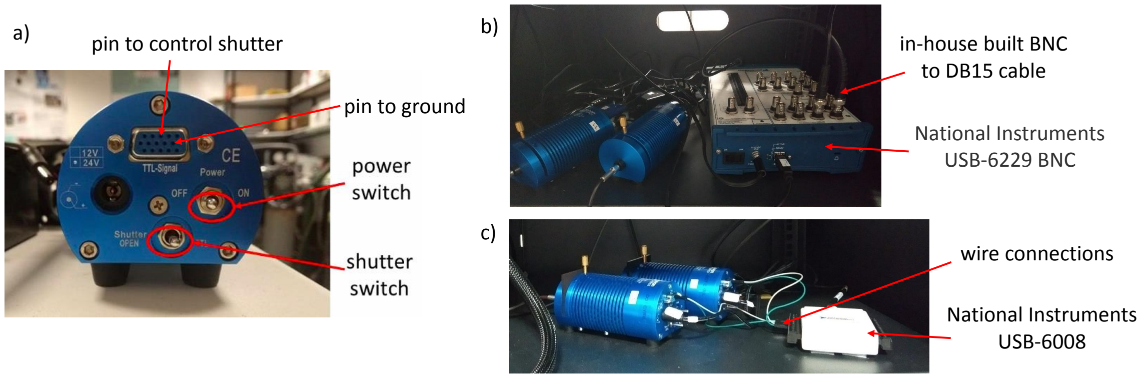

Figure 4.24: a) Back of HL-2000-FHSA-HP light source showing location of pins to control shutter. The shutter switch has to be set to TTL mode. b) Set-up showing first DAQ device, USB-6229 (National Instruments), used to control the shutter settings. c) Set-up showing miniature DAQ device, USB-6008 (National Instruments), used to control the shutter settings

4.5 Software: version 2

Version 2 of the software included time-multiplexing of the sources to alternately switch the sources on and off in order to increase the number of measurement channels of the system. The main alterations compared with version 1 of the software include:

- incorporating switching of light sources, ensuring that data are collected only when the light source is at its peak intensity or when the light source is fully off;
- ensuring that the switching and data collection are kept in synch for the many hours the system may be running;
- adjusting the viewable graphs on the GUI to show the intensities during the switching and amending the concentration calculations such that only every alternate intensity point is used. This ensures a smooth concentration trace is seen on the graphs as this is calculated from only when the source is on.

Figure 4.25 shows a block diagram of the main operations of version 2 of the software.

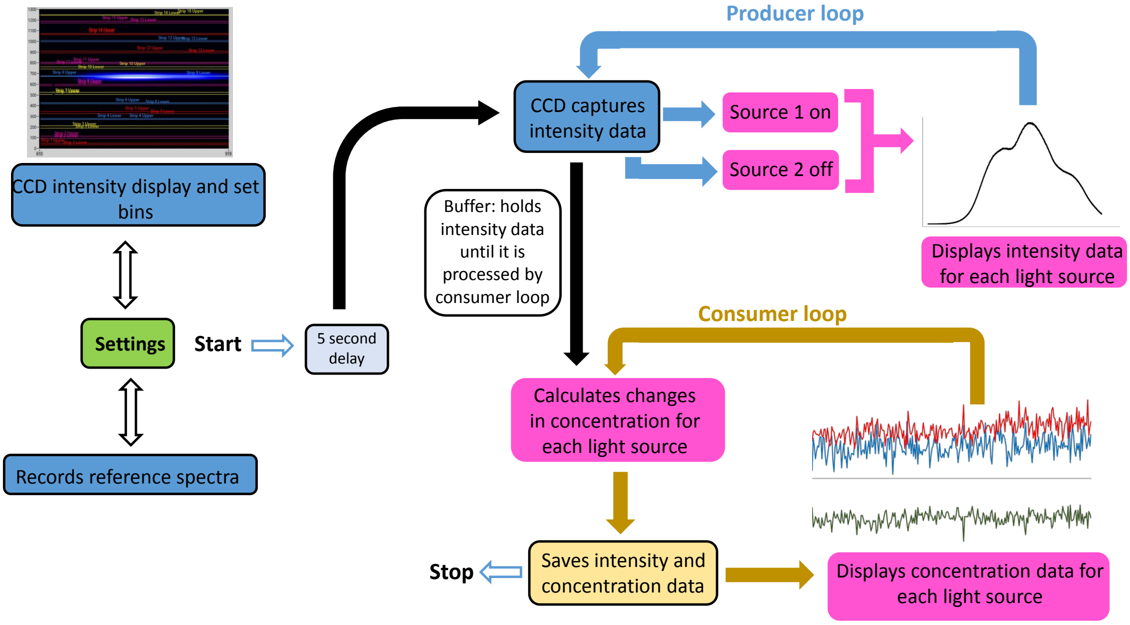

Figure 4.25: Block diagram showing the main functions of the LabVIEW program, version 2. The additional changes compared with version 1 are shown in pink

To ensure robust data collection when incorporating the light switching process within the software, it is essential that the CCD is capturing data at the right time. It takes a finite amount of time to open and close the shutter, hence it takes a certain time for the source to be fully on and fully off. Data should only be collected when the light source is at its highest and lowest intensity. If there is an overlap in the data collection between the light being on and off, then the intensity data collected will not reflect the tissue measurements accurately as the intensity of light will not be stable during the measurement period.

To ensure data were captured when the light source was in a stable on or off state, a counter in the LabVIEW software was added such that whenever new data were captured by the CCD, the counter increased by one and triggered the switching of the light source (either on or off depending on whether the counter was a positive or negative integer). The light sources were connected to a DAQ assistant to control the switching of the light sources. When the counter was even, light source 1 was triggered on (fibre bundles 1 and 3) by sending a 5 V signal to the DAQ assistant and light source 2 was triggered off (fibre bundles 2 and 4) by sending a 0 V signal to the DAQ assistant.

A schematic showing the timing of the light switching and data collection of the CCD is shown in Figure 4.26.

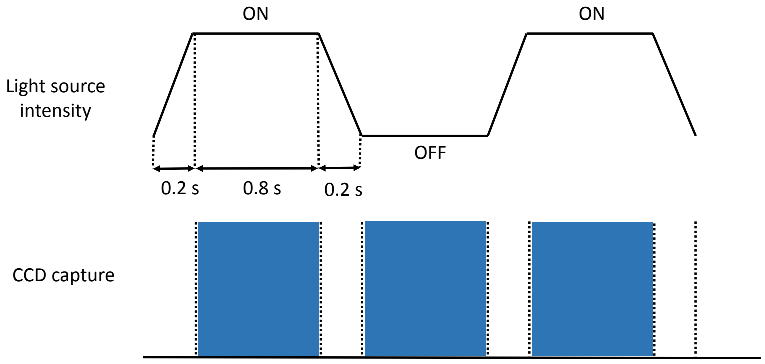

Figure 4.26: Schematic showing timing of the light switching and corresponding CCD data capture

4.6 Preliminary testing of system

Preliminary testing of the system was performed in the laboratory to determine the characteristics of the system. Important aspects to investigate were the safety limits, stability of the measurements, resolution and capacity.

4.6.1 Temperature of source fibre bundles

The heating effect of the light source on the skin needs to be considered as radiated light energy has the potential to cause burns. The two sources of heat come from the radiated NIR light energy absorbed by the skin and the conducted energy from direct contact with the light emitted from the fibre bundle. Light absorption varies depending on the wavelength; light in the UV and microwave range are highly absorbed by tissue.

The temperature rise caused by the light emitted at the source probe was tested in water; water was chosen as a suitable medium due to the high water content of tissue and the high specific heat capacity of water making temperature measurements less susceptible to random thermal fluctuations. A 650 nm long-pass filter was used to reduce thermal effects. The light source probe was placed in a water bath in a flexible bag, with a temperature probe placed directly onto the outside of the flexible bag using double-sided tape (Tape Range Distributors, UK). A fifteen minute baseline was recorded with the light source off and data were collected for a further hour with the light source switched on before the light source was turned off. The temperature profile showed an increase of 1°C, as shown in Figure 4.27.

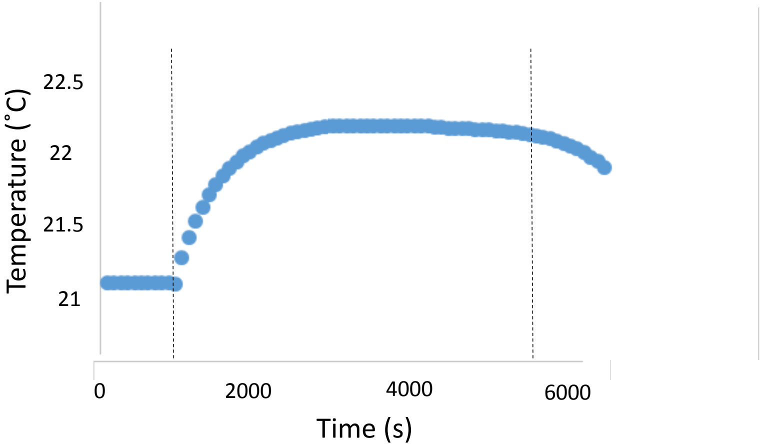

Figure 4.27: Graph of temperature increase observed when source probe was placed in a water bath. Vertical lines indicate the light source switching on (first line) and switching off (second line)

The temperature profile of the ORIEL 66088 was measured for a fifteen minute period. During this time, an increase of 7°C was measured, before measurements were stopped due to a burning smell. This turned out to be due to the filter at the bulb being burned through, as shown in Figure 4.28. This source was no longer used from this point due to the high temperatures of the source, with all subsequent results obtained with the HL 2000. Previous temperature measurements on CYRIL found no thermal effects or damage to the tissue observed in any use of the system (Bale (2016)).

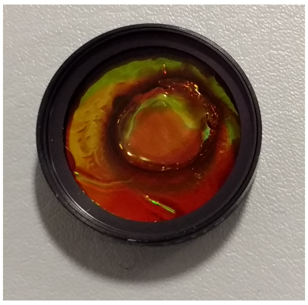

Figure 4.28: Image of high-pass filter burned by ORIEL 66088 light source

4.6.2 Power measurement

A broadband light source produces a divergent beam of light unlike lasers where the light energy is focused in a small area. However, safety limits are still applicable to prevent tissue damage from thermal heating; these limits are lower than for lasers.

An S130C photodiode power sensor (Thorlabs) was used to assess the power output at the end of the source probe of the broadband HL 2000 light source with 650 nm long-pass filter. All measurements were taken in a dark room. A USB4000 spectrometer (Ocean Optics) was used to measure the background noise for a one minute period and the intensity spectrum of the light source for another minute period. The mean of the background spectra was subtracted from the mean intensity spectra. This intensity spectrum was then normalised by dividing the photon count at each wavelength point by the sum of total photons of the spectrum in order to weight the spectrum across wavelength. The sum of all the points therefore added up to one.

This weighted intensity spectrum was multiplied by the electrical current recorded by the S130C when exposed to the light source in order to obtain a weighted current spectrum across all wavelengths. This was then normalised to the responsivity curve of the S130C, in units of A/W, which had a varying response across different wavelengths. Data were interpolated to the wavelengths of the responsivity curve and interpolated values were divided by the responsivity of the power sensor. The power spectrum for one source fibre bundle as detected by one detector fibre bundle is shown in Figure 4.29.

The average power was measured to be 3.2 mW. The area of the source fibre bundles is 6.15 mm^2,hence the power per square millimetre is 0.52 mW/mm^2, which lies within the UK safety standards of a maximum of 2 mW/mm^2.

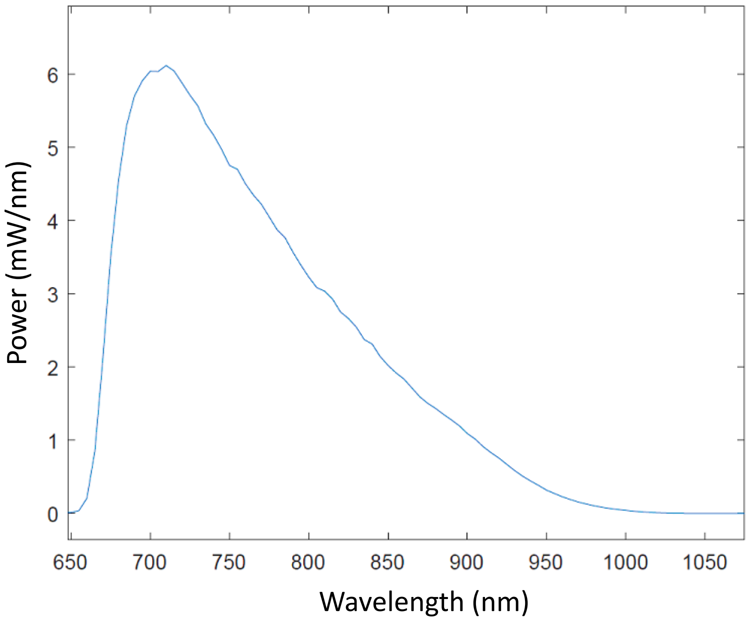

Figure 4.29: Graph showing power spectrum from one light source fibre bundle

4.6.3 Temperature of CCD

Cooling of the CCD reduces thermal noise in the system, as discussed in Section 3.3.5.

The specifications of the PIXIS 1300F state a minimum typical temperature of -65°C and a guaranteed minimum temperature of -55°C. The time for the CCD to cool to its lowest temperature was tested to ensure proper cooling and determine how long after starting the LabVIEW program to wait before measurements can be started.

There were initial problems with the CCD temperature getting to its lowest temperature, with only -30°C reached after around 30 minutes. This was measured using LabVIEW software, where the temperature was set and measured in a separate virtual instrument outside of the main program to minimise risk of error. The LabVIEW software was first checked to see if this was an issue with the software-hardware interaction; this was followed by use of the LightField software (Princeton Instruments). Once it was determined to be a hardware problem, the CCD was sent back to Princeton Instruments where it was found that the Peltier, getter, vacuum chamber and ferrule nut required replacement. Measurements were repeated when the fixed CCD was returned; it was found to cool to a minimum temperature of -55°C.

A graph of the temperature of the CCD from starting cooling to reaching the set temperature is shown in Figure 4.30, where both the initial faulty cooling and the fixed cooling profiles are shown. It takes around 50 minutes for the CCD to cool to the expected minimum temperature. Measurements should be started no sooner than 20 minutes from starting the LabVIEW program to ensure the CCD has cooled sufficiently; at this stage, the intensity spectra look similar to spectra obtained at lower temperatures, where the difference to the quality of the spectra at lower temperatures is more incremental. The average dark count at -30°C was found to be similar to the average dark count at the fully cooled CCD temperature of -55°C, with a value of around 600 counts.

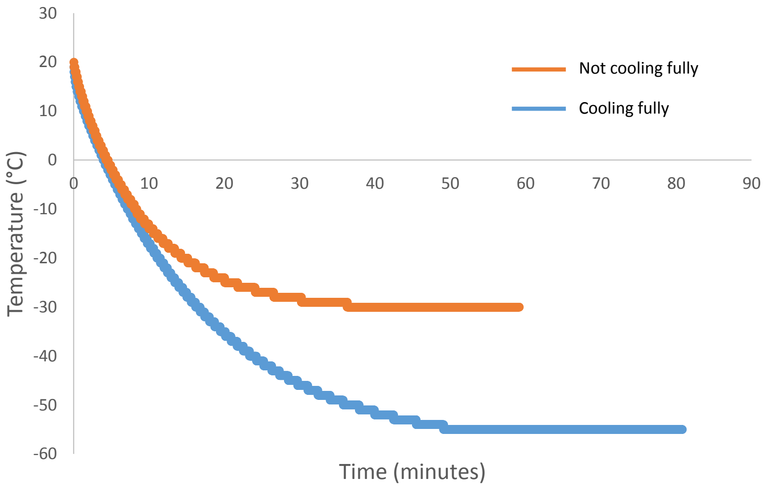

Figure 4.30: Graph showing the temperature of the CCD cooling from starting the program to reaching -55° C

4.6.4 Stability of measurements

The stability of measurements was tested using a solid optical tissue phantom (μ_a = 0.107 mm^{-1} and μ_s = 9.7 mm^{-1} at 830 nm). The light source and sixteen detector probes were placed in a probe holder and attached to a phantom using double-sided tape. Measurements were taken for 19 hours; an example of the results over 5 minutes is shown in Figure 4.31. Relatively stable concentration changes are recorded over the course of 19 hours, with changes in the order of a few nM.

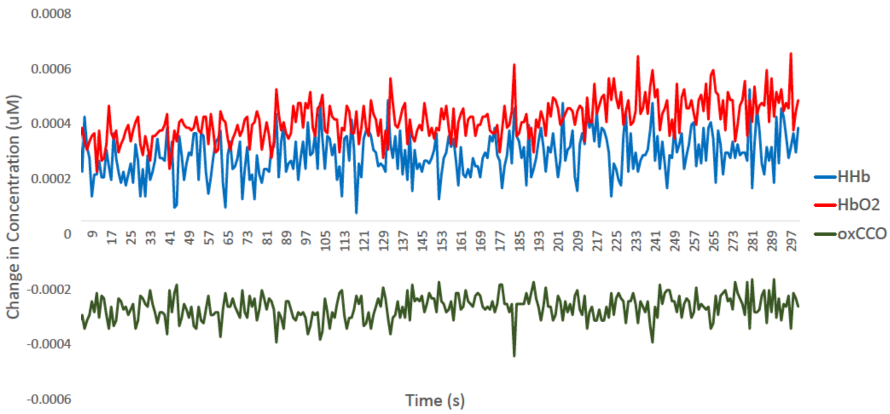

Figure 4.31: Graph showing a 5 minute sample of data collection on a phantom over a 19 hour period

4.6.5 Stability of light switching

It is important for the switching of each light source to be stable over a long period of time to ensure the frequency of switching is consistent and not lagging over long periods. This is to ensure that the CCD data collection and switching of the light sources remain in synch so that the CCD is capturing data at the time when the light source is in a stable on or off period as well as to ensure the calculated concentrations correspond to the expected state of the source (on or off) and that this does drift or swap after a long period of running the software. Figure 4.32 shows the maximum intensity of one detector for a light source switching at 1 Hz when run for 4 hours.

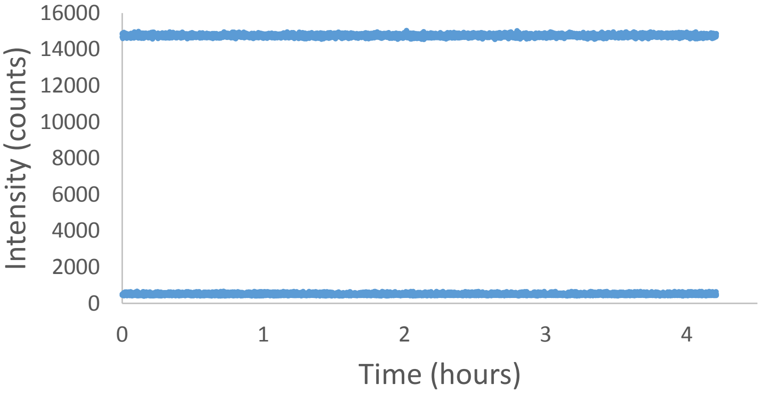

Figure 4.32: Graph showing the maximum intensities over a four hour period as recorded by one detector demonstrating the stability of light source switching

Figure 4.33 shows a 30 second period when the system is running at 5 Hz, the determined maximum frequency of data collection. It can be seen that the peak intensities fall at a minimum and maximum consistently, corroborating the specifications of the light source that the shutter switching capabilities is at least 5 Hz.

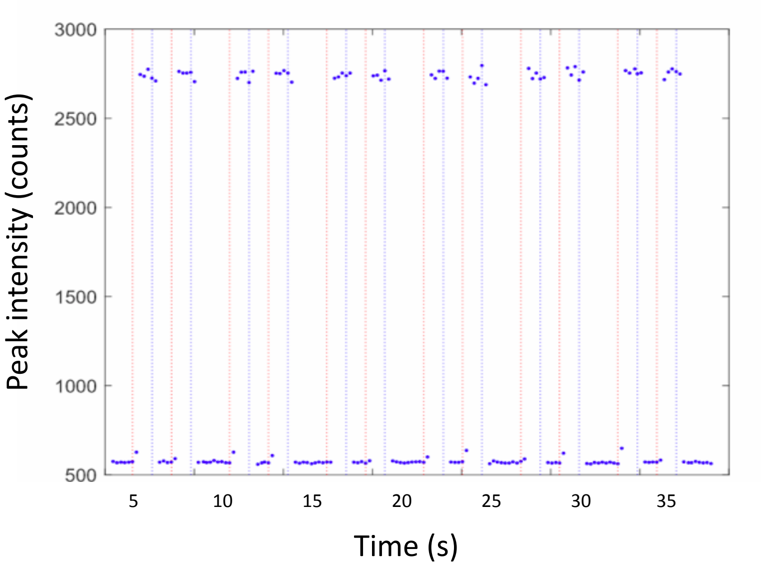

Figure 4.33: Graph showing the maximum intensities over a four hour period as recorded by one detector demonstrating the stability of light source switching and the speed of the switching operation. Red dotted vertical lines show when the shutter is open and blue dotted vertical lines show when the shutter is closed

4.6.6 Dark count

The dark count of the system is the signal measured even when there is no incident light on the detector (see Section 3.3.5). The dark count of the system was measured with the slit set to 0 μm in a dark room with the detectors covered in black-out material. The counts were measured to be around 600 counts per bin with bin settings chosen as a typical setting for the adult head (around 30 pixels in the y-direction of the CCD). The dark count was measured for twenty hours to test the stability of the signal over time. No variation in the average counts was found across this time period with the noise level remaining at around 600 counts; it is therefore an option to remove the dark count from the intensity signals before further processing. This option should be used as standard practice before a measurement period as it can greatly improve the SNR. For example, removal of an average of 600 thermally-induced counts per bin would leave a photon noise of $\sqrt{6000}$, or around 24 counts. For a signal of 6000 counts, this would lead to an SNR of much less than 10% that would be obtained were the dark count not removed. However, it is noted that removal of this measurement is not always possible in a clinical setting, where pressure on time may not allow for such a measurement to be obtained.

4.6.7 Slit width

The width of the entrance slit at the spectrograph front-end can be changed and determines how much light from the detector fibre bundles enters the spectrograph. A wider slit allows a higher amount of input light but reduces the resolution of the system. There is therefore a trade-off between a high signal and a high resolution. Since the dark count was measured to be around 600 counts, it is desirable to have a consistent peak intensity of at least 6000 counts, such that the noise only comprises 10% of the signal. Measurements were made on a solid tissue phantom at a source-detector separation of 3 cm. Raw data were collected over approximately 30 s at varying slit entrance widths ranging from 10 μm to 40 μm; the average results are presented in Table 4.2. A slit width of 35 μm was determined to consistently measure a minimum of 6000 counts. The effect of this width on the optical resolution is presented in Section 4.6.9.

Table 4.2: Average maximum counts for varying entrance slit widths

Slit width (μm)	**Average maximum counts**
10	3187
15	4111
20	5467
25	5257
30	5834
35	8575
40	9749

4.6.8 Wavelength calibration

Every pixel in the x-direction is calibrated to its corresponding wavelength using LightField (Princeton Instruments) acquisition software. Figure 4.34 shows the wavelength calibration of the PIXIS 1300F CCD as measured by this software using a neon-argon calibration lamp, which has distinct peaks at certain wavelengths. The measurement was done with a slit width of 10 μm. Figure 4.35 shows the same calibration spectrum but zoomed in to show the separation of the signal at the peaks at 840.7 nm and 842.4 nm; these peaks are visible and distinct, demonstrating the resolution of the spectrograph is at least 1.7 nm.

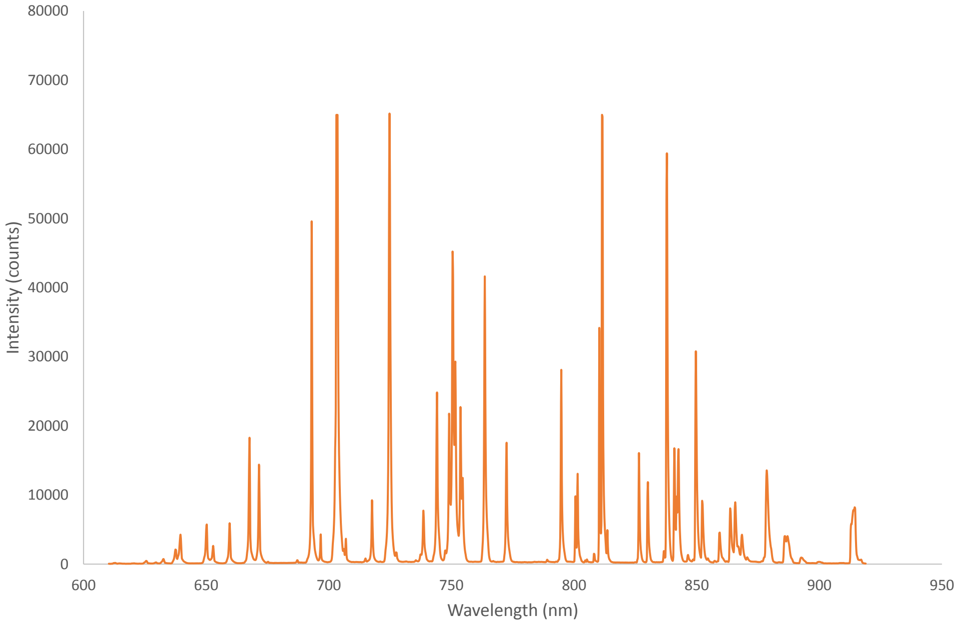

Figure 4.34: Spectrum of wavelength calibration of PIXIS 1300F CCD as measured by LightField (Princeton Instruments) using a neon-argon lamp

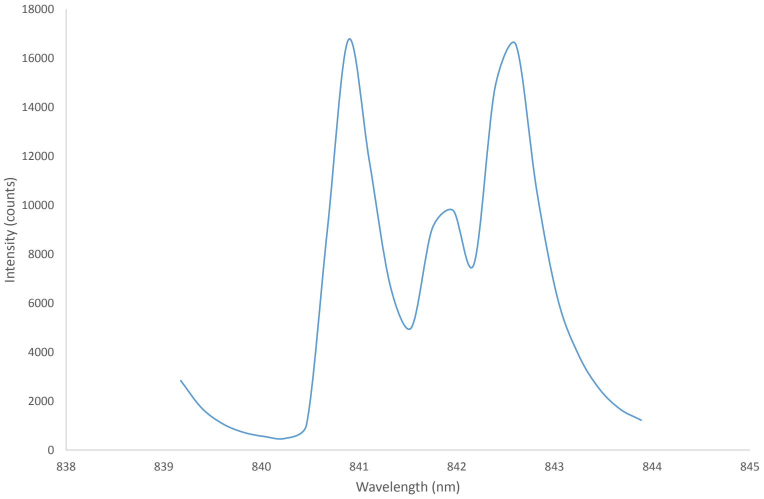

Figure 4.35: Spectrum of wavelength calibration of PIXIS 1300F CCD as measured by LightField (Princeton Instruments) using a neon-argon lamp, zoomed in to show separation between the peaks at 840.7 nm and 842.4 nm

4.6.9 Spectral resolution

The spectral resolution of the system, as defined by the ability of the system to separate adjacent wavelengths, is determined by the groove density of the grating, slit width of the spectrometer and number of CCD pixels. The projected slit width at the detector is larger than the theoretical limiting resolution, therefore the resolution is defined by the practical limitations of the system. In this case, the slit width is larger than the CCD pixel size so the spectral resolution is limited by this slit width. Since each slit width has a pixel resolution value, the spectral resolution of the system can be calculated as below:

$$\begin{aligned} Dispersion &= \frac{Spectral\ range}{Number\ of\ detector\ elements} \\ &= \frac{318\ nm}{1340 pixels} = 0.23\ nm/pixel \end{aligned} \tag{4.2}$$

$$\begin{aligned} Grating\ resolution &= slit\ width\ \times\ grating\ groove\ density \\ &= 35\ \mu m\ \times\ 600\ grooves/mm = 21 \end{aligned} \tag{4.3}$$

$$\begin{aligned} Spectral\ resolution &= dispersion\ \times\ resolution \\ &= 0.23\ nm/pixel\ \times\ 21 = 4.83\ nm \end{aligned} \tag{4.4}$$

The optical resolution of the system is therefore 4.83 nm which is sufficient for resolving changes in oxCCO. A resolution of at least 5 nm is required to characterise the broad peak at 835 nm in the oxidised minus reduced CCO spectrum. Due to the increased width of the slit, the optical resolution measured here is larger than shown in Section 4.6.8.

4.6.10 Detection of all detector fibre bundles

Given the size of each detector fibre bundle of 1 mm and assuming each bundle is separated by 0.5 mm in the ferrule, the expected maximum number of fibre bundles able to be detected can be determined by the size of the CCD chip. The PIXIS 1300F has an imaging area of 26.8 mm x 26 mm, hence the number of fibre bundles that can fit on this chip is given by

$$Maximum\ number\ of\ detectors = \frac{CCD\ size}{fibre\ bundle\ diameter\ +\ fibre\ bundle\ separation} \tag{4.5}$$

$$= \frac{26.8\ mm}{1.5\ mm} = 17\ fibre\ bundles$$

A ferrule housing 16 detectors was decided to be suitable to utilise the size of the CCD imaging area, with the even number of detectors allowing a symmetrical configuration to monitor across cortical regions. The optical fibre bundles are shown in Section 4.2.2.

An image of the intensities from all detectors on the CCD can be seen by using the snapshot button, where the exposure time was set to 1 s. Detector fibre bundles were placed on a solid tissue-like phantom with a source 3 cm away in order to equally illuminate all the detectors. An example of the set-up is shown in Figure 4.36 where a probe holder was 3D printed to enable placement of 8 detectors surrounding one source. Two sets of these probe holders were developed such that all 16 detectors could be illuminated using two source fibre bundles. An example of one detector is shown in the probe holder.

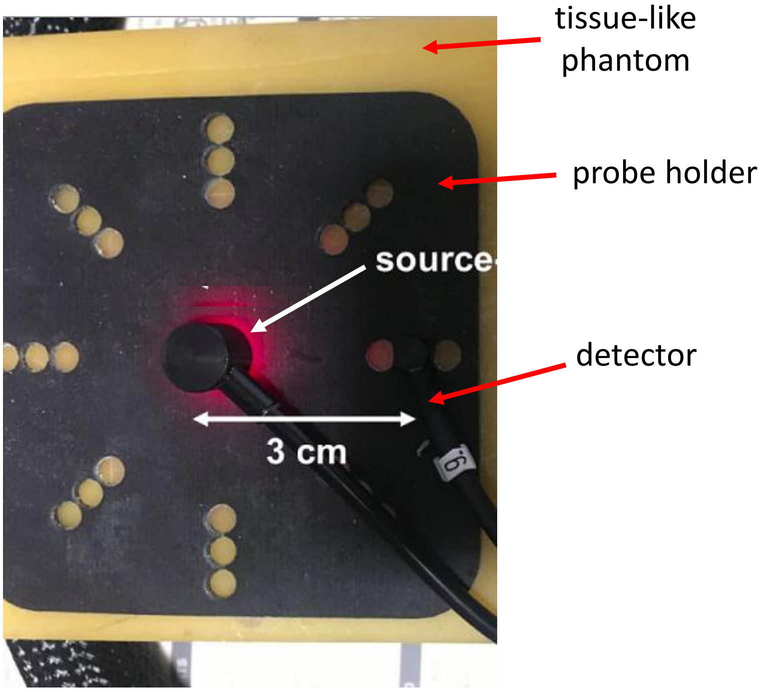

Figure 4.36: Example of experimental set-up to take a snapshot image of illuminated detectors. Detectors can be placed in the probe holder around a source probe such that all detectors are equidistant from the source. The probe holder can accommodate source-detectors separations of 2, 2.5 and 3.0 cm

A snapshot of all the detector fibre bundles illuminated on a solid tissue phantom is shown in

Figure 4.37. Sixteen separate spectra would be expected to be visible on the CCD; however, only 12 distinct spectra of light are visible. Figure 4.37 shows a dark region at the top and bottom of the CCD where no light is reaching the sensor. Each detector was illuminated individually and the two detectors at the top (detectors 15 and 16) and bottom (detectors 1 and 2) of the ferrule were not visible on the CCD. The dark regions correspond to around below 200 pixels and above 1100 pixels on the y-axis.

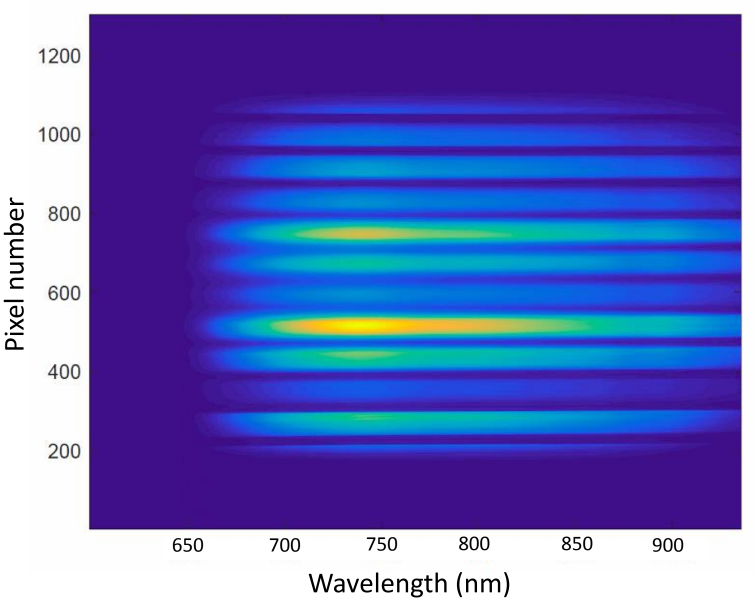

Figure 4.37: Snapshot of CCD when 16 detector fibre bundles are illuminated. Only 12 distinct spectra are seen, rather than the expected 16 distinct spectra. A dark region is seen at the top and bottom of the CCD

There was likely an obstruction in the light path between the spectrograph front-end and the CCD; the optical ray traces through the set-up were unavailable to identify where the obstruction was. In order to investigate this, the shutter, located at the front of the spectrograph behind the slit, was removed to check the size of the aperture was large enough for the ferrule. It was found that the shutter in-front of the spectrograph had a diameter of 23 mm; this compared with the ferrule diameter of 25 mm, with the linear detector array measuring 24 mm long. Hence, part of the top and bottom detectors are obstructed by the shutter, as shown in Figure 4.38. However, this still only accounts for the light path from two detectors being blocked, whereas four detectors in total were not visible on the CCD. It is likely that another aperture within the system is blocking the light pathway. As a result, only 12 detectors are able to be imaged on the CCD.

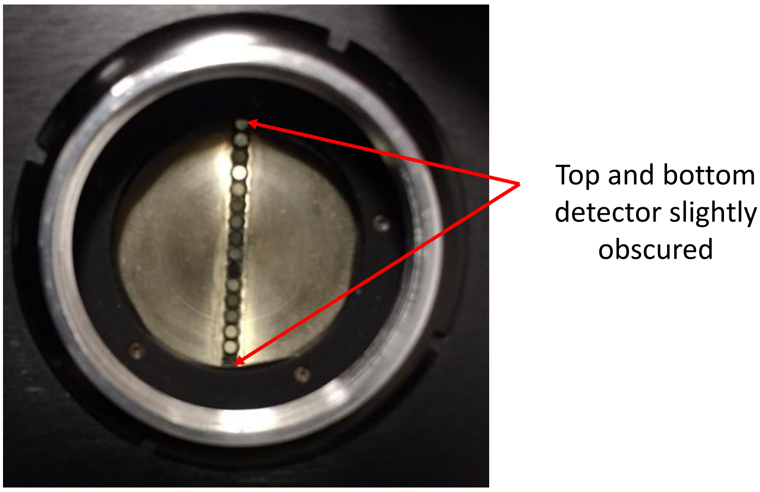

Figure 4.38: Image of ferrule through snapshot aperture showing top and bottom detectors in ferrule being partly obstructed by smaller shutter diameter

4.6.11 Cross-talk

Cross-talk in the CCD occurs when light from one detector is visible in the data collection of another detector. This should not be confused with optical cross-talk, which is discussed in Section 5.5.1.

A snapshot of the image on the CCD can be taken to analyse the light intensities across the 1340 x 1300 pixel imaging array when individual and multiple detector fibre bundles are illuminated. The width of each collected spectrum can be assessed to quantify cross-talk in the system.

Each detector fibre bundle has a diameter of 1 mm. There is no magnification in the system, hence the width of each detector when projected on the CCD is given by

$$\frac{size\ of\ detector\ fibre\ bundle}{size\ of\ pixel} = \frac{1\ mm}{20\ \mu m} = 50\ pixels \tag{4.6}$$

The snapshot of all the detectors shown in Figure 4.37 shows a spread of light from each distinct detector spectrum such that the collected spectrum from each detector is not distinct from the adjacent spectra. This suggests cross-talk is present within the system. An intensity profile of the snapshot along the y-axis can be taken. If no cross-talk is present in the system, the intensity between each detector spectrum should return to baseline values indicating a distinct separation between each detector imaging region. The intensity profile along 820 nm is plotted in Figure 4.39 and shows the intensity between each light spectrum does not return to baseline. The wavelength 820 nm was selected as this is near the peak intensity of a typical spectrum through tissue.

The slit at the spectrometer front-end was identified as the cause of this observed cross-talk due to the large ferrule size not being able to closely come in contact with the slit due to the slit screws

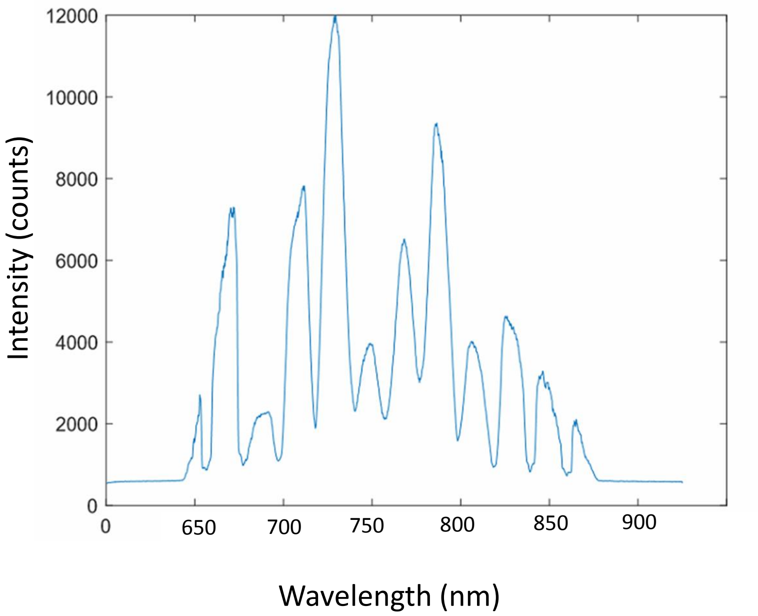

Figure 4.39: Intensity profile of snapshot of CCD for all illuminated detectors at 820 nm. A spread of light in each detector spectrum can be seen. No return of intensity to baseline values can be seen between each detector spectrum, suggesting cross-talk

being in the way. A new slit that used glue to bond it to the spectrometer was used instead of the original screwed slit to enable closer contact between the ferrule and the slit. Figure 4.40 shows the intensity profile of the snapshot of the CCD with the same set-up as previously; as can be seen, each detector spectrum appears more distinctly and a return of intensity values to baseline can be seen.

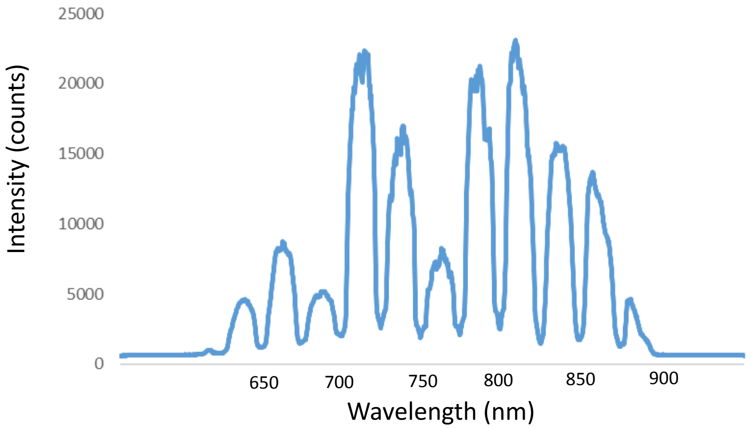

Figure 4.40: Intensity profile of snapshot of CCD for all illuminated detectors with new bonded slit. Collected detector spectra appear more distinct than previously. A return of intensity to baseline values can be seen between detector spectrum, suggesting little cross-talk between adjacent detectors

4.6.12 Optimum focus

Investigation into the source of this cross-talk also looked at the focus of the lens on to the CCD. This could be controlled using a micrometer at the side of the spectrograph. Snapshots were taken at 0.1μm increments from 1.0 μm to 2.0μm to assess the optimum focus of light onto the CCD. 1.7 μm was identified to be the optimum focus, with a clear return to baseline seen between detectors compared with other focus values. Figure 4.41 shows the intensity profile along 820 nm for 1.0 μm and 1.7μm.

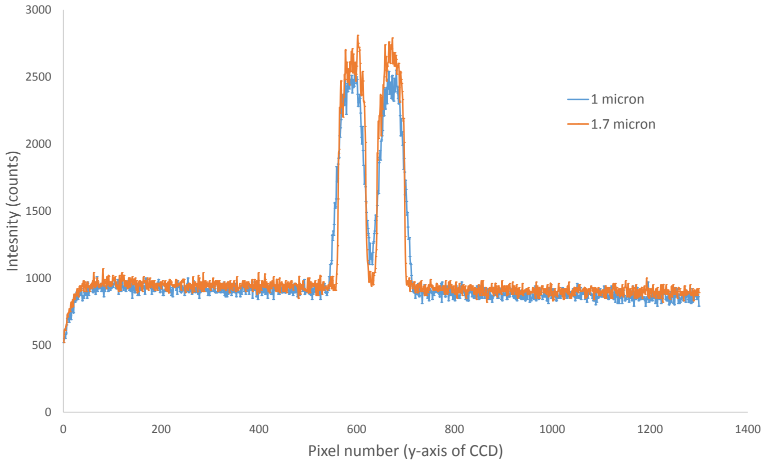

Figure 4.41: Intensity profile of snapshot of CCD for two illuminated detectors. Focus at 1.7 μm shows a closer return to baseline than at 1.0 μm

CHAPTER 5

Using the broadband NIRS system in monitoring the healthy adult brain

The last chapter discussed the development of the next iteration bNIRS device. This chapter investigates the capabilities of this system to monitor multiple regions of the adult head using a functional activation task to stimulate haemodynamic and metabolic changes. Although the system has been developed specifically for the neonate and infant head, the capacity of the system to monitor cerebral changes in the adult head was of interest; firstly as a suitable paradigm to test the capabilities of the system in a laboratory setting before being deployed in a clinical unit and secondly to verify the limits of the system. A visual task inducing changes in the occipital lobe and a Stroop task inducing changes in the prefrontal lobe were both investigated.

5.1 Background

The scope of this chapter is to monitor brain activity in healthy adult volunteers using a functional activation paradigm to induce predictable changes in concentration of HbO_2 and HHb, as well inducing changes in metabolic variable, oxCCO. As discussed in Section 2.1.4, neural acivity can be inferred from haemodynamic changes due to the neurovascular coupling mechanism, which is well-established in adults as an increase in $\Delta[HbO_2]$ and decrease in $\Delta[HHb]$.

Of interest is the response of the cerebral metabolism; whilst changes in the haemodynamics have been widely investigated and are relatively repeatable, changes in oxCCO are not yet established. Studies of changes in oxCCO during functional activation in adults have revealed a mixed response with both increases and decreases seen in this parameter. Kolyva et al. (2012) observed a heterogeneous response in Δ[oxCCO] during frontal lobe activation. The study used an anagram-solving task across 11 volunteers; confounding measurements of Δ[oxCCO] were investigated including wavelength selection, DPF, systemic responses and changes in optical scattering due to the functional response. They concluded that the heterogeneity in the metabolic response was physiological rather than as a result of confounding factors in the measurement technique. Phan et al. (2016b) performed a Stroop task to investigate functional changes in the prefrontal cortex across 9 volunteers. The authors found an increase in Δ[oxCCO] in 5 out of 12 channels; these results are discussed in more detail in Section 5.7. de Roever et al. (2017) used a working memory challenge in the form of either a Stroop task or anagram-solving task to investigate the cerebral metabolic response in 17 healthy volunteers. Short-separation regression was used to account for extracerebral changes; block-averaged results demonstrated an increase of Δ[oxCCO] with significance only observed at the longest source-detector separation of 3 cm. Although an increase was seen in the block-average of the results, a heterogeneous response was seen between individual volunteers with further investigation of this response in adults needed.

Some studies in the occipital lobe have identified consistent increases in Δ[oxCCO]. Uludag et al. (2004) performed a visual stimulus in the form of an annular black and white checkerboard and a radial red and green isoluminant stimulus. Across 14 volunteers, the authors found an increase in the oxCCO response that was not explainable by a cross-talk artefact and hence determined it was as a result of a phsyiological change. Similarly, Phan et al. (2016a) used a checkerboard paradigm to investigate the visual response in the occipital lobe and found a consistent increase in Δ[oxCCO] across 4 volunteers demonstrating a focal localisation of Δ[oxCCO] discrete from the haemodynamic signal.

5.2 Objectives

The aim of this section is to perform a preliminary test using the newly developed system discussed in Chapter 4 to monitor brain activation in healthy adult volunteers in order to:

- demonstrate the capabilities of the system to monitor functional changes in the adult brain and test the limitations of the system;
- design a study protocol based on a functional activation task to monitor changes in concentration of the three parameters, HbO_2, HHb and oxCCO;
- implement methods to extract the haemodynamic response from collected data;

- investigate the response of Δ[oxCCO] compared with the haemodynamic response during functional activation.

A functional task presents a useful testing platform to evaluate the capacity of the system to monitor induced changes. Aims of chapter are to test the capabilities of the system to monitor changes in variables induced by these tasks and to introduce analysis techniques for handling functional data. Two methods to investigate the metabolic response were selected: a visual task and a working memory task. Written informed consent was obtained from each participant before the study and the study was approved by the University College London Ethics Committee.

5.3 Visual activation

A visual task was initially selected as a suitable paradigm to investigate the cerebral response. Visual stimuli are processed in the occipital lobe and involve low-cognitive mechanisms. The haemodynamic response to visual stimulation is well-defined, with large, repeatable changes making it a suitable task to test the ability of the system to monitor this response. Furthermore, the response of Δ[oxCCO] has been previously reported (Heekeren et al. (1999), Uludag et al. (2004), Phan et al. (2016a)), providing a useful comparison for these measurements.

Since visual stimulation is a passive task that does not depend on the attention or concentration of the volunteer, the variation between volunteers due to this is not a confounding factor and simplifies the haemodynamic, and subsequently metabolic, response functions. A passive task is also less likely to induce unrelated physiological changes due to factors such as stress, which means that exctracerebral contamination of the bNIRS signal is less likely.

5.3.1 Visual functional task

A 4 Hz black and white checkerboard with reversal pattern was selected as a suitable stimulus to activate the visual cortex. The protocol consisted of twenty repetitions; rest periods were periodically interspersed between 30 s activation periods. Rest periods ranged from 25 to 35 s to stagger the exposure to the activation period and to reduce anticipation of the task by the volunteer. A computer screen was used to display the checkerboard in full screen. The reversing checkerboard display was run in MATLAB (MathWorks) using Psychtoolbox 3. Rest periods consisted of a black screen with a small white cross in the centre; participants were asked to look at the cross during these rest intervals to ensure consistency across volunteers and keep the volunteer's eyes in focus.

Since the LabVIEW software that runs the bNIRS system is a computationally intensive process, a separate computer was used to run the equally intensive checkerboard pattern protocol. Time synchronisation between the presentation of the stimulus and the data collection are important in order to identify whether functional changes align with the presentation of stimuli. The two computers therefore had to be synchronised. During the protocol, a marker on the computer running the protocol was sent to a timestamp file in MATLAB to indicate the start time of the experiment and timestamps of resting periods and periods of activation. This marker was sent to the laptop of the bNIRS system via the serial port. The system software was amended to incorporate detection of the trigger at the serial port during every loop of data collection; when a trigger was detected, a marker was added to the saved timestamp file during that loop hence enabling synchronicity with the protocol.

5.3.2 Headgear for monitoring occipital region

Headgear was an important consideration, especially with the large number of source and detector fibre bundles where quality-control of the data becomes more difficult. Although a visual stimulus provides a reliable task in terms of predictability and size of response, the occipital lobe at the back of the head is a region covered by hair. Hair is a major issue for NIRS measurements due to its interference with the optical coupling between the probes and the scalp, as well as its strong absorption properties in the NIR region. In order to obtain a good NIRS signal through hair, it is necessary to perform hair clearing at the location of each probe to minimise these obstructive effects.

A symmetrical configuration of the sources and detectors was used with source-detector separations of 3 cm; a central row of the four sources maximised the number of measurement channels. Initial design of the headgear used a neoprene cap to house the source and detector probes. Holes were cut in the cap and 3D printed rings were placed within these holes to hold the probes in place; a clipping mechanism as discussed in Section 4.2.3 was selected to integrate the probes within the cap. However, it was found that even using the smallest cap diameter available, that the fitting of the cap at the back around the occipital region was variable between volunteers; often it was found to be loose in this region due to varying head shapes and sizes. Instead, a band design was developed as this was found to be easier to fit tightly around the rear of the head across various volunteers. In order to increase optical contact of the probes with the scalp, strips of velcro were placed around the band over the top of probes to provide extra pressure.

5.3.3 Experimental set-up

Three volunteers were recruited to participate in this experiment. Around thirty minutes was allocated to the placement of the headgear to ensure as good optical contact was obtained as possible. The band was placed on the volunteer using the inion, a notch at the back of the skull, as a marker for placement; the centre of the band was placed 2 cm above the inion so that the source-detector array covered the occipital lobe. The band was made as tight as was comfortable for the volunteer to prevent movement of the probes during the experiment, although care has to be taken with applying too much pressure as this can cause unwanted flushing that can contaminate the cerebral bNIRS signal. The hair was then cleared from the area where each probe would be placed using a thin implement to move hair and tuck it underneath the edges of the band. Figure 5.1 shows an example of the task and experimental set-up. Experiments were performed in a corner of the laboratory surrounded by a black-out curtain and with the lights switched off to minimise any external contamination of the signal.

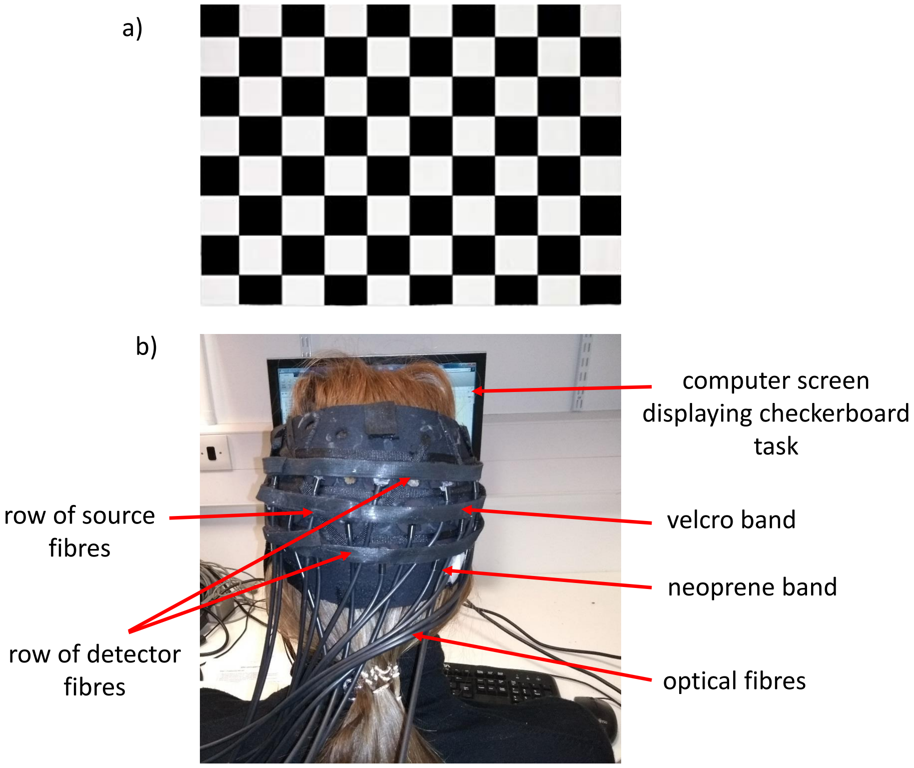

Figure 5.1: a) Example of checkerboard pattern shown to participants. b) Experimental set-up showing headgear covering occipital lobe

5.3.4 Results

It was found that measurements over the occipital cortex were significantly affected by hair. Figure 5.2 shows an example of the intensity spectrum obtained from one detector in a participant, using a CCD integration period of 0.8 s. The peak intensity is very low at only around 1000 counts and the signal appears quite noisy. This protocol was attempted across three volunteers with careful preparation involving hair clearance before each measurement; however, a better signal could not be obtained. The highest quality data were obtained from a participant with fine, blonde hair where the signal was stronger compared with participants with dark hair, although the signal was not of high enough quality to derive concentration changes.

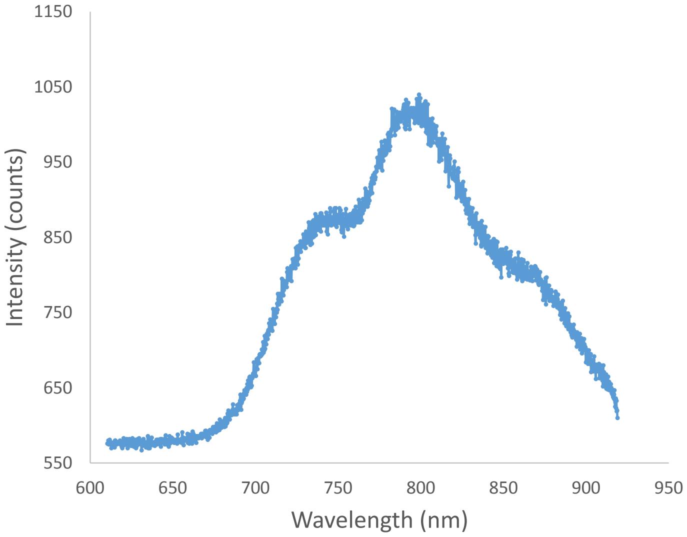

Figure 5.2: Example of intensity spectrum obtained from visual cortex for one detector, with a CCD integration period of 0.8 s

Since the system is specifically designed for use on infants and neonates, the detector fibre bundle diameter is 1 mm. It is possible that this diameter is too small to adequately clear regions of hair and any signal from the scalp is absorbed before it reaches the detectors. It may be that the thinner skull and extracerebral layers in infants would enable sufficient light transmission even through hair. Infants generally have less dense hair coverage, which is an advantage, but hair clearing would not be possible with such young volunteers. Chapter 7 presents an example of bNIRS acquisition over the temporal lobe in an infant.

5.4 Working memory functional task

An alternative functional task that induces changes over a region of the cortex that is not covered by hair is desirable. The frontal lobe is a region where placement of bNIRS probes is relatively easy compared with other regions where hair is dense and a limiting factor. Tasks that induce brain activation in the frontal and prefrontal lobes include working memory challenges such as the Stroop task or anagram-solving.

The Stroop task was selected as a suitable functional stimulus to monitor in healthy adult volunteers; this task has been widely used in previous investigations with a spatial response of Δ[oxCCO] observed (Phan et al. (2016b)) allowing a comparison of the metabolic response and validation of the system functionality. The Stroop task involves presenting participants with a word, such as 'red'; the word is coloured in either red or a different colour. Participants have to name the colour of the word rather than the written word.

While the Stroop task has the advantage of inducing changes over the prefrontal cortex, the disadvantage compared with a visual stimulus is that the response is more variable. Since the task is not a passive one but requires the attention of the participants, there can be more variability in the induced response. Furthermore, the task can be more stressful to participants and is therefore more likely to induce systemic changes in physiology leading to an unwanted extracerebral response that can mask or alter the cerebral signal.

5.4.1 Headgear for monitoring frontal region

A band design was also selected as an appropriate form of headgear to hold the probes over the frontal cortex due to the ease of placement of the band on a volunteer and ability to position the band consistently across volunteers. A neoprene material was adapted to fit around the curvature of the top of the head and velcro was used to secure the band in place. The same 3D printed holders that were described in Section 5.3.2 were used to hold the probes securely in the band.

The source-detector configuration was designed such that a row of four sources in the centre were surrounded by four detectors each. The source-detector separation was 3 cm. Coupled with the time-multiplexing of the light source, this permitted a total of 18 channels. A schematic of the configuration is shown in Figure 5.3 where the measuring channels are shown when the light sources alternate on and off.

In order to ensure the same cerebral region is monitored across volunteers with varying head

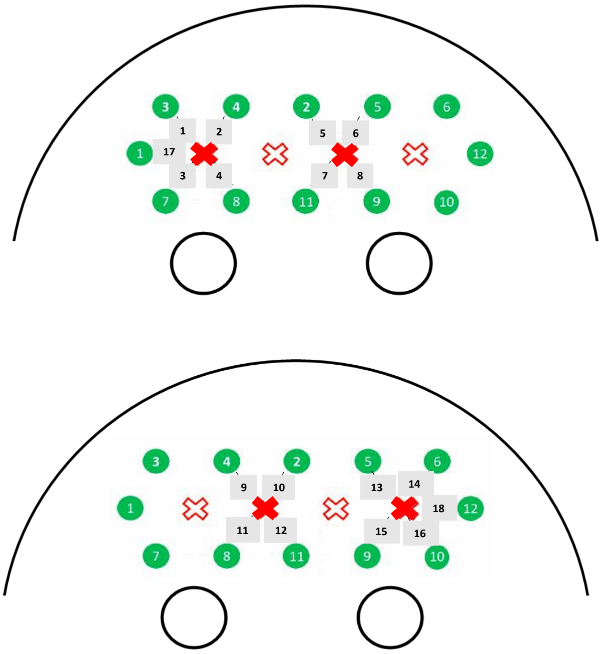

Figure 5.3: Diagram showing source-detector configuration across frontal lobe with time-multiplexed sources. Green circles indicate detectors, grey squares indicate measurement channel and red crosses indicate light sources (solid red is a source that is on, red outline only is a source that is off)

circumferences, a protocol was designed such that placement of the headgear was consistent across volunteers. The band was placed on the head such that the two central sources were directly over the Fp1 and Fp2 points, according to the EEG 10-20 system. The length from the nasion to the inion of each volunteer was measured using a flexible tape measure, ensuring the tape measure was flat. Measurements were taken three times and an average of the nasion-inion measurement taken. The Fp1 and Fp2 points were then located as the points 1 cm either side of the midline and 10% up of the nasion-inion length. Figure 5.4 shows a schematic of the positioning of the probe array on the frontal lobe.

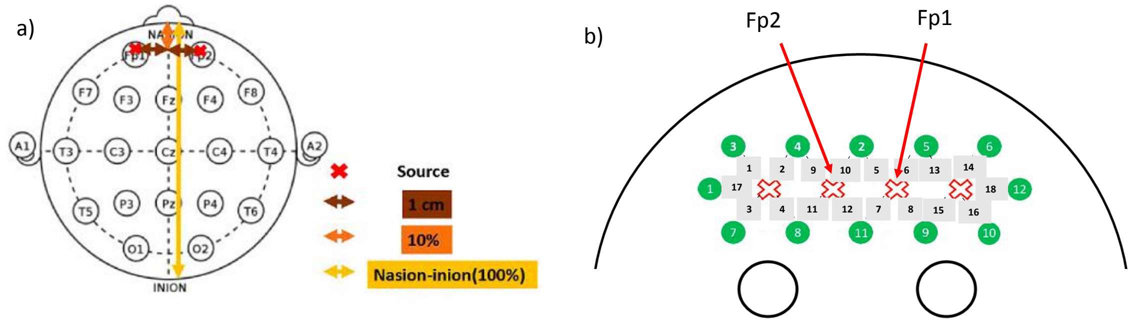

Figure 5.4: a) Diagram showing source placement using 10-20 system. b) Diagram showing positioning of probe array from front

5.4.2 Volunteers

Ten healthy, right-handed healthy adult volunteers were recruited (5 male; mean age 25 years). Written informed consent was obtained from each participant. The study was approved by the University College London Ethics Committee. Data from one participant were excluded due to incorrect performance of the task.

5.4.3 Experimental set-up

Volunteers were monitored in a dark room with black-out curtain to minimise contamination of the bNIRS signal from external light sources. Volunteers were seated in front of a computer screen displaying the task and ergonomic considerations were taken into account to ensure comfort of the participant. The Stroop task was run on a separate computer to the bNIRS system and a trigger was sent at the start of each rest and stimulus period via serial port as discussed in Section 5.3.1.

A 2 minute baseline at the start of the experiment was taken. Stimulus periods were 25 s long interspersed with baseline periods varying between 15 and 30 s to prevent anticipation of the start of the stimulus period. There were 20 repetitions of the stimulus period, resulting in a total experiment time of between 15 and 20 minutes. Participants were asked to look at a blank screen during baseline periods and select relevant keys on the keyboard during the task (for example, the letter 'r' would be selected to answer red). Movement was kept to a minimum by requesting participants to minimise head movements during the task. Figure 5.5 shows an example of the experimental set-up, with a graphic of the Stroop task shown and a participant with the headgear on.

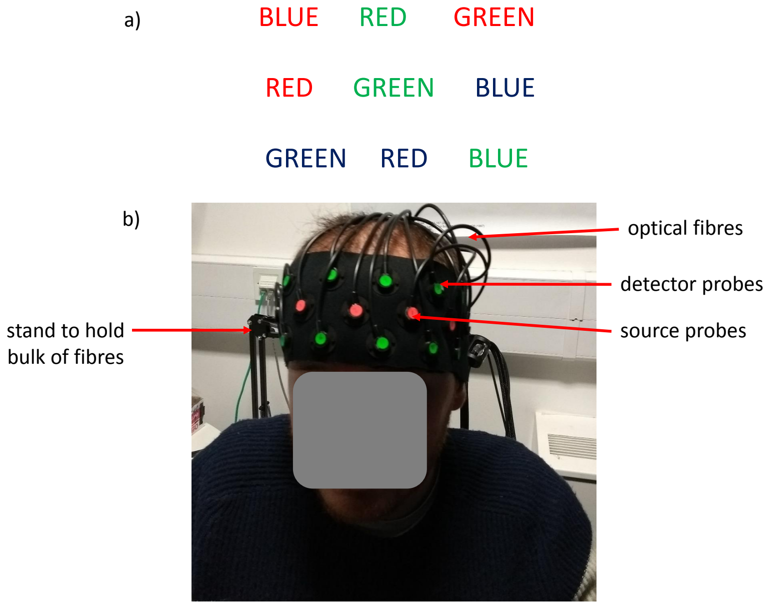

Figure 5.5: a) Example of Stroop task showing written colours appearing in either the same or contradicting colours. b) Example of experimental set-up with frontal headgear in place on a volunteer

5.5 Data analysis

5.5.1 Residual analysis

Parameter cross-talk occurs when spurious concentration changes in one chromophore induce concentration changes in another chromophore. This should not be confused with cross-talk that can appear in the collected CCD image that is discussed in Section 4.6.11. Because the concentration of CCO is much lower than that of haemoglobin, it is more likely that large changes in haemodynamics may mask changes in oxCCO and this signal is more susceptible to cross-talk compared with the haemodynamic signals. One method of assessing whether cross-talk has affected the metabolic signal is to perform residual analysis.

Residual analysis is used here to check that the model used in the linear regression in the MBLL is appropriate. The residual is defined as the difference between the observed value, in this case the attenuation change, and the predicted value, in this case the two- and three- chromophore fit model.

The change in attenuation between the intensity spectra before and during functional activation was used to derive the changes in concentration using two methods: when solving for three chromophores, $\Delta[\mathrm{HbO_2}]$, $\Delta[\mathrm{HHb}]$ and $\Delta[\mathrm{oxCCO}]$, and when solving for only two chromophores,

$\Delta[HbO_2]$ and $\Delta[HHb]$. The attenuation change was then back-calculated from these two concentration changes and the residual differences between the calculated and back-calculated attenuations were investigated.

If all the chromophores contributing to the spectra are accounted for, the residual should look like noise, randomly fluctuating around zero. However, if a chromophore is unaccounted for, then a shape to the spectra will be present.

5.5.2 Extracting the haemodynamic and metabolic responses

Data analysis were performed in MATLAB (Mathworks). Concentration data were bandpass-filtered in the range [0.005 0.3] Hz, using a 5th order Butterworth filter to remove physiological noise. A block-average was taken across all events for all volunteers to isolate stimulus-related activations from uncorrelated haemodynamic trends.

5.5.3 Statistical analysis

All statistical analysis was carried out in SPSS (IBM, USA). A baseline period, defined as the 10 s window immediately prior to activation, and a 10 s activation period defined as a period around the maximum change in the middle of the stimulus period were selected. The response for each volunteer was defined as the difference between activation and baseline. A student's paired t-test was used to compare the response of the activation compared with zero (i.e. no response). Values of $p < 0.05$ were considered statistically significant. Results are presented as mean ± standard error.

5.6 Results

5.6.1 Residual results

An example of the data collected from one volunteer is shown in Figure 5.6, where the raw data in terms of the measured intensity spectra are shown both before and during the presence of a stimulus at 3 cm source-detector separation. Figure 5.6 also shows the resulting attenuation change from these two spectra. The final section of the figure shows the residuals between the measured attenuation and back-calculated attenuation using the two- (HbO_2 and HHb) and three-chromophore (HbO_2, HHb and CCO) fitting methods.

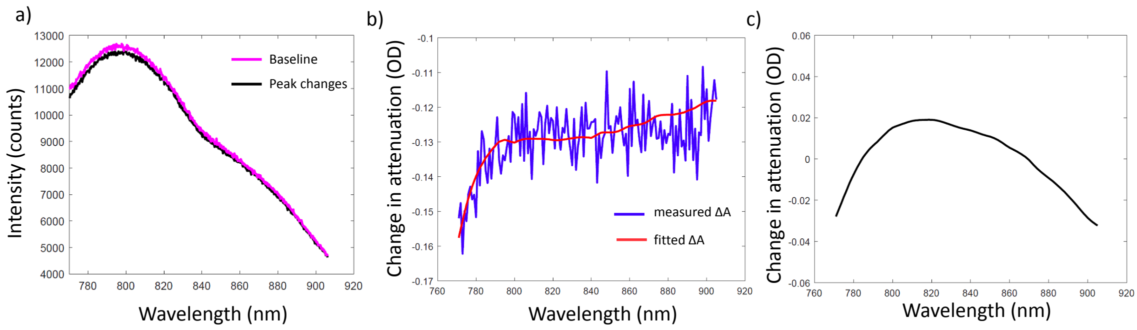

Figure 5.6: An example of raw data obtained from one volunteer. a) shows the measured intensity spectra both before and during presence of a stimulus. b) shows the resulting attenuation change and the fitted attenuation change using a three chromophore model to account for HbO_2, HHb and oxCCO. c) shows the back-calculated change in attenuation from calculated concentration changes. The difference between three- (oxCCO, HbO2, HHb) and two- (HbO2, HHb) chromophore fit is plotted. The shape of the difference spectrum is similar to the oxidised – reduced CCO spectrum

5.6.2 Intensity data

The quality of the raw intensity data were assessed before further analysis to ensure measurements were likely to have come from tissue and were not affected by noise. Two aspects were looked at to ensure high quality data: the peak intensity (with a peak value such that noise only contributes to 10% of the overall signal) and the shape of the spectrum. It is known that a typical spectrum through the adult head has a peak at the isosbestic point at around 800 nm and a secondary peak at around 750 nm due to the HHb peak in the absorption spectrum. A typical spectrum was shown previously in Figure 4.20.

Given these requirements, it is possible to discard any data of poor quality at this stage before further processing. Figure 5.7 shows an example of two intensity spectra of poor quality. The low intensity value indicates that the signal to noise ratio is too low to obtain any useful information relating to concentration changes and the unusual shape of the second spectrum indicates that the signal did not originate soley from tissue but the measured light path is likely to have travelled through other media such as air or the neoprene cap before reaching the detector.

Figure 5.8 shows an example of a good quality intensity spectrum obtained from one channel from a participant, where the peak intensity is at least 10 times the average intensity of the noise. A high peak intensity is seen with the expected shape of the spectrum suggesting it is likely that this signal originates from tissue and contains information about the absorption ratios of HbO_2, HHb and oxCCO.

Channels 17 and 18 were excluded from all volunteers due to the poor intensity data obtained

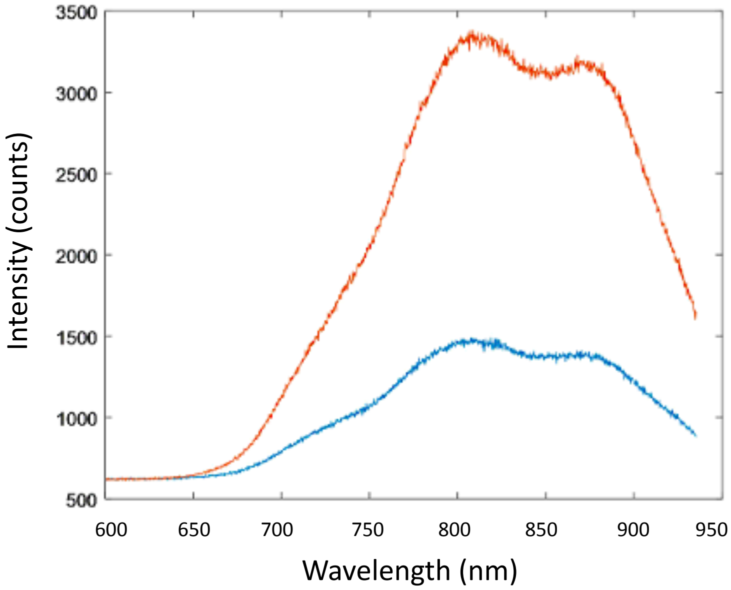

Figure 5.7: Example of poor intensity data collected from a participant. The blue line shows low intensity data and the orange line shows an unusual shape spectra that suggests the light is being distorted by a medium other than tissue

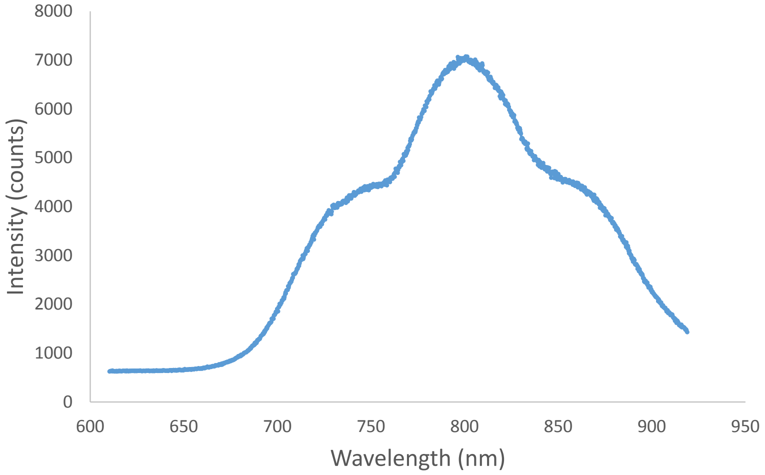

Figure 5.8: Example of good quality intensity data collected from a participant. A high peak intensity is shown with the expected spectra shape from tissue

from these detectors; due to the length of the array, these channels were often positioned over areas of hair and therefore did not obtain a good quality signal. Further channels were excluded from participants based on the data quality criteria described. The locations of these channels differed between volunteers; factors such as the fitting of the band to the head and the size of the participant's head contributed to the quality of the signal.

Since two sources are being used at any one time, it is important to assess the source interference at the detectors. There is a chance that one detector may be collecting light from two light sources.

To investigate the interference due to multiple light sources, measurements were taken on an adult forehead with the headgear positioned over the frontal cortex as described in Figure 5.4. One light source was used to illuminate all the detectors at positions of source 1, 2, 3 and 4 individually and the intensity data at all the positions were recorded for each source translation to ensure a negligible amount of interference occurred.

5.6.3 Concentration changes

Only channels that matched the criteria for good quality data were further analysed. Raw intensity data were converted into changes in concentration using the modified Beer-Lambert law between 770 and 905 nm.

An example of a trace during the Stroop task for one channel from one participant is shown in Figure 5.9 for $\Delta[HbO_2]$ and $\Delta[HHb]$ and in Figure 5.10 for Δ[oxCCO].

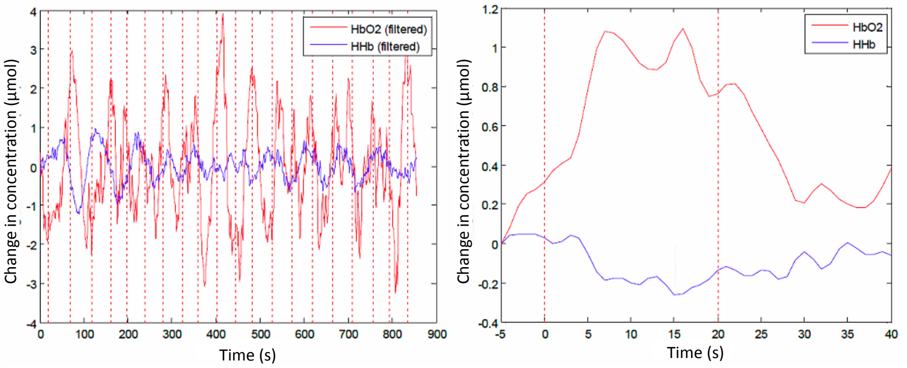

Figure 5.9: Concentration changes obtained from one channel for one volunteer during the Stroop task. a) the filtered $\Delta[HbO_2]$ and $\Delta[HHb]$ traces with dotted vertical lines indicating the task start times. b) The block average across all the stimulus periods

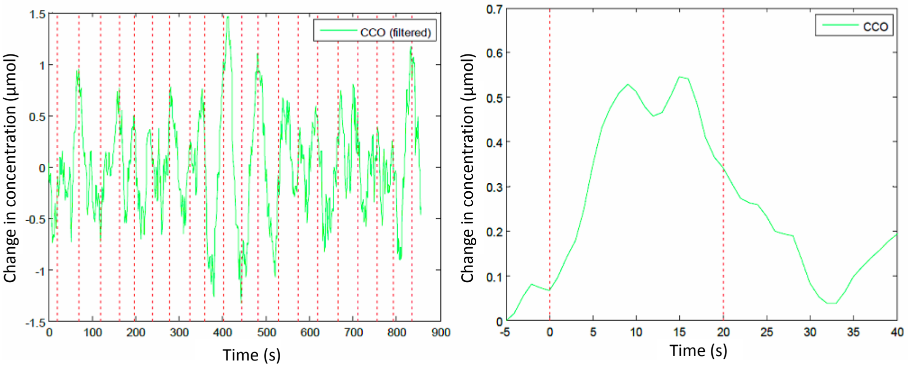

Figure 5.10: Concentration changes obtained from one channel for one volunteer during the Stroop task. a) the filtered Δ[oxCCO] trace with dotted vertical lines indicating the task start times. b) The block average across all the stimulus periods

A block average across all the channels for all participants with the standard error of mean is shown in Figure 5.11. Values of Δ[oxCCO] was multiplied by 10 for ease of visualisation compared with the haemoglobin values. The total number of included volunteers for each channel is indicated in the block average of the results.

Figure 5.12 shows the locations of channels with significant responses in any of the three chromophores. In channels where a typical functional response is observed, with a statistically significant increase in Δ[HbO$_2$] and decrease in Δ[HHb], a significant increase in Δ[oxCCO] was observed in 5 out 10 channels with a maximum amplitudes varying from 0.012 μM (channel 6) to 0.027 μM (channel 14).

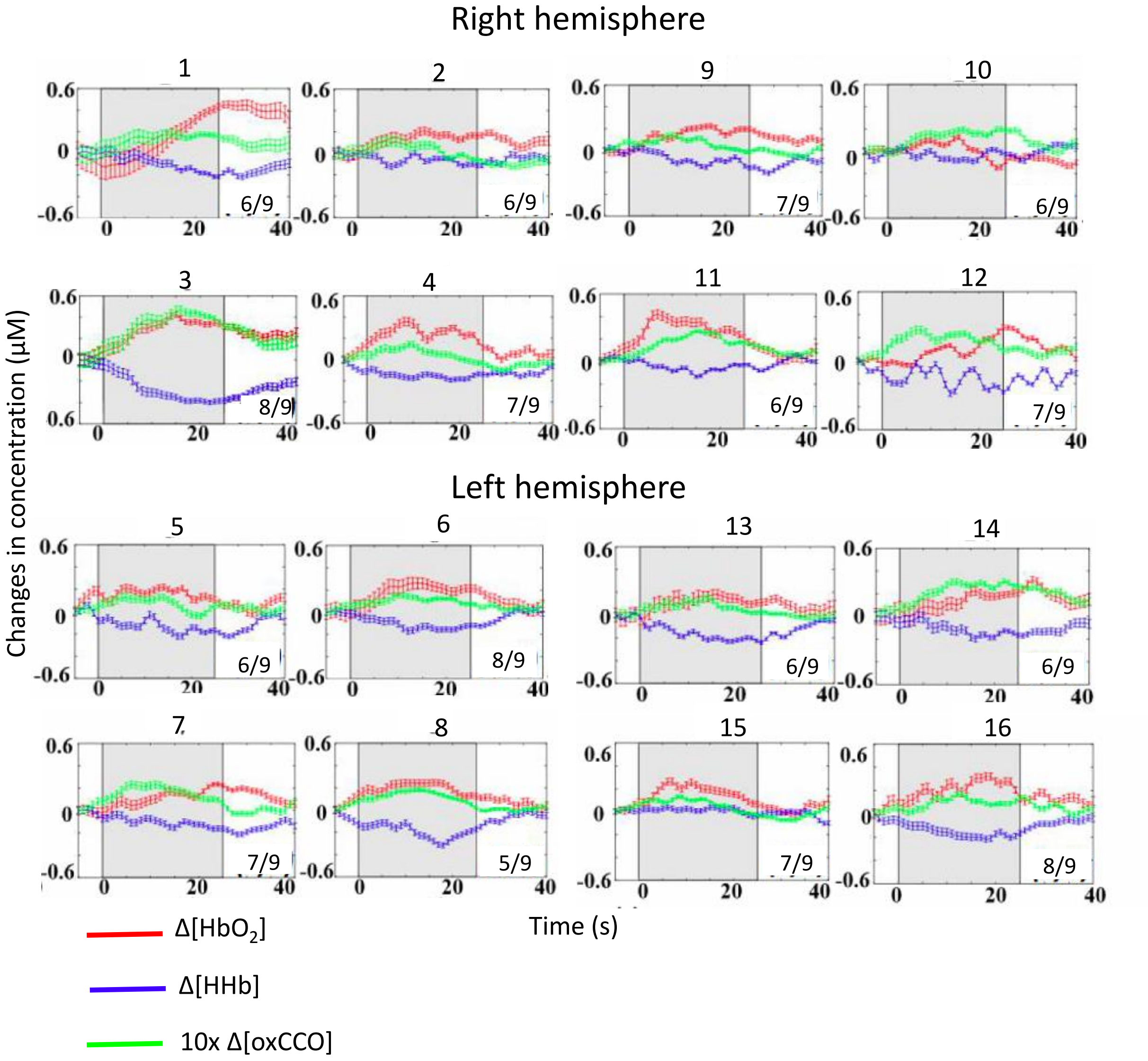

Figure 5.11: Summary of results for the prefrontal cortex. Results are a block average across all nine volunteers. The number of participants included in the block average for each channel is shown

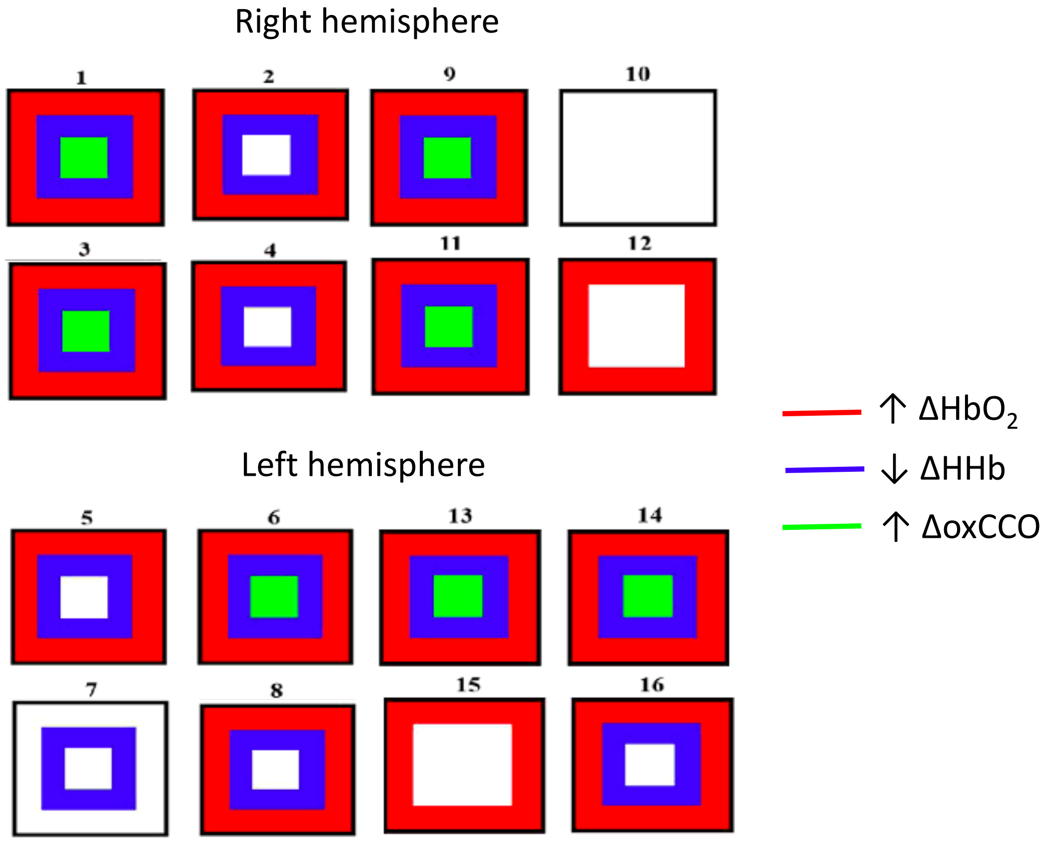

Figure 5.12: Locations of channels with significant responses in $\Delta[HbO_2]$, $\Delta[HHb]$ *and* $\Delta[oxCCO]$

Table 5.1: The mean response in μM across nine volunteers for each chromophore and the corresponding p value in channels with significant changes in Δ[oxCCO]

	Channel 6		Channel 9		Channel 11		Channel 13		Channel 14	
	Mean response (μM)	p	Mean response (μM)	p	Mean response (μM)	p	Mean response (μM)	p	Mean response (μM)	p
$\Delta[HbO_2]$	0.215	0.041	0.192	0.003	0.32	0.048	0.142	0.048	0.198	0.013
Δ[HHb]	-0.119	0.013	-0.129	0.002	-0.075	0.047	0.174	0.003	-0.142	0.011
Δ[oxCCO]	0.012	0.033	0.014	0.04	0.019	0.02	0.014	0.033	0.027	0.022

5.7 Discussion

The difference between the two back-calculated attenuations from the two- and three- chromophore fits reveals a shape in the spectrum similar to the oxidised – reduced CCO spectrum (see Figure 3.4) suggesting that absence of the oxCCO spectrum when calculating concentration changes leaves a chromophore with the spectral features of oxCCO unaccounted for. Therefore, it suggests that the oxCCO signal obtained is a real signal, and not a result of cross-talk.

Investigation showed the interference from multiple sources being used showed little impact on far detectors, with little signal reaching these detectors. This validates the source-detector configuration used in this study, with multiple sources having little impact on the SNR on further detectors.

The group averaged results show a typical functional activation in some channels, with a haemodynamic response showing an increase in $\Delta[\text{HbO}_2]$ and decrease in $\Delta[\text{HHb}]$ in 10/16 channels. Not all the channels exhibited strong activation. A significant response in $\Delta[\text{oxCCO}]$ was seen in 7/16 channels. It has previously been shown that CCO is a more brain-specific marker due to the higher mitochondrial density in the brain compared with extracerebral layers (Kolyva et al. (2014), de Roever et al. (2017)); this makes it a potentially useful signal in functional activation experiments where haemodynamic signals are often contaminated with extracerebral changes and may explain the discrepancy between the number of channels with observed significant changes seen here.

It has previously been shown that the Stroop task activates the dorsolateral prefrontal cortex (Banich et al. (2000)). It may be that the positioning of the probe array was lower on the head with only the top row of channels covering the dorsolateral prefrontal cortex and the bottom row of channels extending into the orbitofrontal prefrontal cortex. This matches with the significant $\Delta[\text{oxCCO}]$ responses, which are seen mainly in the upper row of the probe array. Using such a large number of source and detector fibre bundles over such a small area of the head presents the problem of choosing a suitable configuration that enables all the fibre bundles to be utilised. The geometric layout of the probes also resulted in a poor quality signal at detectors 1 and 12, located at the outer edge of the headgear. The low intensity counts from these two detectors can be attributed to these probes being positioned over hair due to the long length of the array configuration. Furthermore, the probe design was not tailored for use on the adult head and therefore an array can not easily or efficiently be placed to cover the frontal lobe. A more suitable probe design for this paradigm would consist of straight optical fibre bundles with no 90° bend as is currently used for use in infants and young children.

A significant response in Δ[oxCCO] was seen in seven (44%) out of sixteen channels, with the mean response varying from 0.012 μmol to 0.027 μmol. Significant changes in Δ[oxCCO] occurred in the presence of significant haemodynamic changes in these seven channels (channel 1, 3, 6, 9, 11, 13, 14). The variation in the amplitude changes agree with previous work from Phan et al. (2016b) who looked at 24 measurement channels to monitor frontal activation NIRS concentration changes. Results from Phan et al. (2016b) observed a mean variation in response between 0.024 μmol and 0.033μmol with the maximum concentration changes of Δ[oxCCO] compared with Δ[HbO_2] varying between 13.0% and 18.8%. This is in contrast with this study where the maximum concentration changes in Δ[oxCCO] response varied between 5.6% and 13.6% of that of the maximum changes in HbO_2. The amplitude changes in Δ[HbO_2] observed in this study are generally similar to those observed in the study by Phan et al. (2016b), although the observed changes in oxCCO are smaller in this study. This study used a source-detector separation of 3.0 cm, whereas Phan et al. (2016b) used a longer separation of 3.5 cm; it may be that the smaller amplitude changes in Δ[oxCCO] observed here are due to a smaller percentage of the cerebral cortex being interrogated compared with a longer separation of 3.5 cm. This depth-dependence of the oxCCO signal at increasing source-detector separations has previously been observed (Kolyva et al. (2012)).

Significant changes in Δ[HbO_2] and Δ[HHb] was seen in fourteen and thirteen channels, respectively (88% and 81%) out of sixteen channels for both variables, although only twelve channels showed simultaneous significant responses in these haemodynamic variables.

No significant changes in Δ[oxCCO] were observed in five channels where a significant haemodynamic response was observed (31%). It may be that these channels are showing significant responses due to systemic changes in physiology resulting in large haemodynamic changes in the extracerebral layers independent of cerebral activation, hence no significant response in Δ[oxCCO] is observed. Monitoring of systemic variables such as heart rate and blood pressure is needed to corroborate this. Large extracerebral fluctuations have been shown to contribute to false positives and negatives (Tachtsidis and Scholkmann (2016)); a marker independent of extracerebral fluctuations is desirable to avoid this.

Using the CCO signal in addition to the traditional haemodynamic signals enables a more specific localisation of functional activation and may provide a more brain-specific marker of functional activation independent of extracerebral changes. This protocol on healthy adult volunteers has demonstrated the capability of this bNIRS system to measure induced concentration changes in both haemodynamics and metabolism in regions where hair is not present. To optimise the use of the system in the adult head, a tailor-made probe design for this application has to be used consisting of a larger optical fibre bundle area to enable enough light to penetrate through the hair and be detected. A larger detector fibre bundle diameter would mean fewer detectors are able to fit onto the CCD imaging array, thereby reducing the number of channels of the system.

5.7.1 Summary

The system was used to record functional activation-induced changes of $\Delta[\text{HbO}_2]$, $\Delta[\text{HHb}]$ and $\Delta[\text{oxCCO}]$ in 16 channels in nine healthy adult volunteers across the prefrontal cortex and identified channels with significant changes in $\Delta[\text{HbO}_2]$, $\Delta[\text{HHb}]$ and $\Delta[\text{oxCCO}]$. The limits of the system were reached when attempting to monitor changes in the occipital lobe; hair was found to be a significant factor in the quality of the bNIRS signal obtained and therefore it was not possible to monitor regions covered by hair. This limits use of the system in adults to the frontal and prefrontal cortex. Adaptation of the optical fibre bundles of the system for application in adult studies is possible with the design of an optical fibre bundle with a larger diameter to enable a signal to be obtained through hair. However, this would reduce the number of detector fibre bundles incident on the CCD imaging array thereby reducing the total number of channels of the system.

CHAPTER 6

Monitoring infants with seizures using the broadband NIRS system

The capabilities of the multi-channel bNIRS system to monitor changes in cerebral haemodynamics and metabolism across multiple brain regions has been demonstrated in the previous chapter using a functional activation paradigm to monitor changes in the healthy adult brain.

This aim of this chapter is to demonstrate the capability of the bNIRS system to monitor regional variations in brain injury in a clinical setting, specifically in infants and children with epilepsy in conjunction with electrical recordings of brain activity using EEG. Children with epilepsy were monitored for up to a few hours simultaneously with EEG.

There are various challenges in performing simultaneous EEG and bNIRS measurements and when performing studies in a clinical environment. This chapter begins with an introduction to seizures and the rationale for monitoring cerebral oxygenation and metabolism in this cohort of patients. The experimental protocol is discussed and results from twelve epilepsy patients are presented.

6.1 Introduction

Epilepsy is a relatively common and potentially devastating neurologic condition. The prevalence of infantile epilepsy in the UK is 0.7 people per 1000 (Eltze et al. (2013)) and between 40 and 100 per 100,000 in children and adolescents (Hauser (1995)) and is often associated with poor long-term neurological function and development. Epilepsy is characterised by frequent, recurring seizures, or ictal events, where abnormal and excessive neuronal discharges occur. These bursts of electrical activity cause temporary disruption of the brain's normal functioning and are usually accompanied by clinical manifestations such as uncontrollable movement of limbs or loss of consciousness. EEG is the standard method of monitoring electrophysiological patterns in the brain that can help diagnose epilepsy, with the majority of patients demonstrating characteristic EEG alterations during a seizure (St. Louis et al. (2016)).

Periods between seizures, known as interictal periods, often show abnormal EEG traces with brief paroxysmal discharges, called interictal epileptiform discharges (IEDs), occurring. These IEDs include spike ($<$70 s duration), spike and wave, or sharp-wave (70–200 s duration) discharges (St. Louis et al. (2016)). These waveforms are not associated with seizure symptoms and are known as subclinical seizures. The interictal period corresponds to the majority of a patient's life (i.e. the time periods when the patient is not having a seizure).

Seizures can be broadly classified as either generalised or partial; in generalised seizures, the seizures begin in both cerebral hemispheres simultaneously whereas partial seizures originate in one or more localised foci and can spread to affect the entire brain. Epilepsies are a heterogeneous disorder, with the majority due to genetic predispositions. Although the pathways to seizure disorders have been extensively studied (Steinlein (2008)), it is still unclear why there is such variability in cognitive impairment. There is some evidence suggesting that the seizure events themselves may contribute to a worst cognitive outcome (Korman et al. (2013)).

It is not known whether the neurovascular coupling mechanism during abnormal physiological events, such as during seizures, remains intact. NVC in a healthy brain involves an increase in CBF to meet the energy demand during neuronal activation. However, the high stress of a sudden increase in metabolic rate of oxygen during ictal periods may lead to a local tissue ischaemia, where the increase in cerebral blood flow typically seen with neuronal activity may not be sufficient to meet the increased metabolic demand of the tissue (Schwartz (2007), Wallois et al. (2009)). This potential hypoxia during ictal and interictal events may be responsible for cell death associated with epilepsy.

6.1.1 NIRS as a neuromonitoring tool in seizures

Techniques such as NIRS are promising tools to investigate this type of brain injury. There have been a few studies that have looked at characterising changes in NIRS parameters during epileptic activity in neonates and children. For example, focal seizures have been associated with increases in cerebral blood volume in convulsive seizures in patients aged between 1.5 months to 16 years old (Haginoya et al. (2002)) and decreases in Δ[HHb] and increases in $\Delta[\mathrm{HbO_2}]$ have been observed during generalised absence seizures in patients between 1 to 16 years old (Roche-Labarbe et al. (2008)). Neonatal seizures have shown an increase in Δ[HbO_2] and Δ[HHb] (Wallois et al. (2010)). More recently, diffuse optical tomography images during seizures were presented in an infant following HIE showing haemodynamic changes across the whole head (Singh et al. (2014)). A biphasic haemodynamic response was identified with increases in Δ[HbO_2], Δ[HHb] and ΔHbT prior to seizure onset before a decrease below baseline. Spatial variation in the haemodynamic response to seizures was observed despite generalised EEG activity.

Changes using broadband-measured Δ[oxCCO] has recently been studied in a newborn with repeated seizures following HIE (Mitra et al. (2016)). A rapid increase in Δ[oxCCO] was observed at the onset of seizures with a rise in the baseline of amplitude-integrated EEG. Cerebral oxygenation and cerebral blood volume, as measured by Δ[HbD] and Δ[HbT] respectively, fell before seizure onset before recovering to baseline during seizures. However, a progressive fall in the baseline of Δ[oxCCO] was observed, indicating a decrease in mitochondrial oxidative metabolism (Mitra et al. (2016)). This might explain the exacerbation of brain injury after repeated or prolonged seizures.

Children with epilepsy are often impaired in their development and neurological function but it is unclear how paroxysmal events are related to this. Broadband NIRS could provide a useful tool in monitoring cerebral changes in such patients due to its non-invasive nature. Measuring the energy consumption of the brain might be able to provide an insight into how traumatic seizure events are for the brain. Furthermore, monitoring regional changes in both haemodynamics and metabolism during a functional task in epilepsy patients may be able to inform on cognitive function in individual patients. The metabolic state of the brain during seizures may help clinicians to determine specific cortical locations of abnormal brain function that may predict abnormal neurodevelopmental patterns in patients.

6.2 Challenges and objectives

The aim of this study was to perform simultaneous bNIRS and EEG measurements in children with epilepsy to monitor changes in haemodynamics and metabolism in the brain before and during clinical and subclinical epileptic events. Simultaneous EEG and video-EEG monitoring will enable identification of movement artifacts and epileptic events that will then enable analysis of bNIRS signals to identify changes associated from baseline periods. The combined EEG and bNIRS modalities will provide a more robust overview of the cerebral response in epilepsy patients than just one technique alone.

This is the first time that a multi-channel, bNIRS system has been used simultaneously with EEG in a clinical environment to monitor cerebral oxygenation, haemodynamic and metabolism changes in epilepsy patients in young infants and children.

There were several challenges that had to be overcome to enable successful measurement in this patient cohort:

- Recruitment of patients to take part in the study. This involved speaking to parents about the study over telephone before their routine appointments and obtaining informed consent from them on the day of their visit. This required close collaboration with a clinical colleague at the hospital who was responsible for regularly monitoring for potential patients and contacting parents as and when appropriate.
- Using the system in a clinical environment. This required close collaboration with the EEG team on the ward who were responsible for the routine EEG monitoring of patients. As the study was taking place across several different clinical wards, it was essential to work closely with a number of EEG neurophysiologists. This increased awareness of the study amongst the ward staff across the different units, who were then able to help with the combined EEG and bNIRS headgear application such that the disruption to the normal EEG monitoring was minimal.
- Design of a suitable headgear to enable simultaneous bNIRS and EEG monitoring in a broad population cohort. This involved close collaboration with researchers from Babylab at Birkbeck University who have previous experience in EEG-bNIRS monitoring in infants. Using their experience, the ideas and designs then had to be expanded to apply to a variety of different age groups, from infants to older children. Additionally, the practicalities of simultaneously monitoring of bNIRS and EEG had to be taken into account: there could be no disruption to the usual routine EEG recordings whilst still maintaining a good quality bNIRS signal from all channels.
- Careful study design to minimise disruption to routine clinical care. Flexibility in study design was essential to cope with changing conditions in a clinical environment. The design of the system was considered early on such that its portable size enabled easy manoeuvring of the system around established hospital equipment. Furthermore, design of the study had to work around a busy clinical environment with routine assessments from staff such as physiotherapists and consultants regularly taking place. The timing of when studies took place was kept flexible to enable this.

Given these challenges, the objectives for the study were to:

- demonstrate the ability of the system to robustly monitor cerebral changes in oxygenation, haemodynamics and metabolism in a clinical setting in patients with epilepsy of different age groups;
- simultaneously monitor cerebral changes using both EEG and bNIRS; synchronisation of these two modalities enables comparison and identification of seizure events from the EEG that can be related to simultaneous changes in bNIRS measurements;
- investigate the metabolic spatial response during seizure events in order to provide further insight into how seizure events affect the brain.

6.3 Study development and challenges

Ethical approval was obtained from London Bloomsbury Research Ethics Committee. Before being used on the unit, the bNIRS system had an electrical safety check to ensure it was safe to use. This is especially important when using a device that is directly in contact with the patient.

Recruitment was undertaken from two main units at GOSH: the telemetry ward (Koala ward) and the rapid assessment neurology unit (Starfish ward). Patients were eligible for recruitment if they had epilepsy with ongoing daily seizures and written informed parental consent was taken for all patients taking part in the study. A total of 14 patients were recruited as part of this study, with 2 patients excluded prior to data collection due to intolerance of the headgear. A full list of patients is included in Section 6.3.4.

6.3.1 Challenges encountered

There were some initial challenges encountered during the early periods of the study that had to be overcome. This resulted in some deviations from the original study design; these challenges and adaptations are outlined in this section.

Patient recruitment

The focus of this work was originally on monitoring oxygenation, haemodynamic and metabolic changes simultaneously with electrical brain activity in infants with epilepsy under 2 years of age. Oxygenation and metabolic changes in the temporal lobe were of interest to assess differences between the two hemispheres of the brain. This target age range was chosen to reduce the complexity in study design and allow easier comparison across patients within this limited age range. Additionally, young infants were deemed as suitable patients to monitor temporal regions due to the smaller head size enabling a higher signal to be obtained in these regions, with a source-detector separation of 2.5 cm selected. Initial assessment of prior patient profiles before the start of the study identified this as a suitable target; it was predicted that around 1–2 patients per month could be recruited.

Upon starting the study, few patients within this target age range were identified, so the target population was increased to include older children up to 14 years of age. Since hair is a major factor in obtaining a good quality signal, the frontal lobe rather than the temporal lobe was monitored in this new target cohort to ensure a good quality bNIRS signal could be obtained. Frontal bands were designed to hold the bNIRS probes in place on the head with a source-detector separation of 3 cm chosen to ensure good depth penetration in older children. The number of channels was reduced by half compared with the temporal band as this was sufficient to provide full coverage of the frontal lobe. Design of the frontal headgear is discussed in more detail in Section 6.3.2.

The original objective was also to use a functional task in patients under 2 years of age where tolerated to induce controlled haemodynamic changes. A social task was selected as a suitable paradigm, where previous work on healthy infants has already been investigated (Lloyd-Fox et al. (2009), Siddiqui et al. (2017)). However, as a result of the patient inclusion criteria expanding, the functional activation task was no longer appropriate for older children and hence the experimental design had to be adapted to incorporate the inclusion of a larger age group. A task in the form of a hyperventilation (HV) task was identified to induce controlled cerebral haemodynamic changes in this broader patient cohort.

Simultaneous monitoring of EEG and bNIRS

Multimodal monitoring using simultaneous EEG and bNIRS modalities provided another challenge, with the quality of both EEG and bNIRS signal being the most important factor. As the EEG monitoring was as part of routine clinical care, it was vital that any addition of the bNIRS modality did not affect the quality of the EEG signal. It was also necessary to work closely with the neurophysiologists to ensure good placement of the bNIRS and EEG probes. As standard care, the EEG was placed in a 10-20 configuration and the bNIRS probes therefore had to be placed around existing EEG locations. It was important for the bNIRS probes to be placed such that they maintained symmetry between the two cerebral hemispheres to enable comparison between similar locations between the two sides.

Furthermore, to obtain a good quality bNIRS signal it is necessary to maintain constant optical coupling between the skin and the optical fibre bundle. A sufficient amount of space between the EEG electrodes and bNIRS probes was therefore required to prevent interference of the electrodes with the contact of the bNIRS probes. As space on the patient's head is limited, careful consideration of the configuration of the bNIRS channels was needed. Design of the headgear to overcome these challenges is discussed in Section 6.3.2.

The optimum EEG and bNIRS set-up was identified through trial and error as the studies progressed, with some studies achieving a better quality bNIRS signal compared with others. EEG electrodes were typically placed according to the 10-20 system, with a glue sometimes used to hold the electrodes in place. White tape was placed over the top of each electrode to reduce movement of the electrodes, before a stretchy net hat was placed over the top of the electrodes, covering the head, to prevent the electrodes being pulled off by the patient.

The highest signal quality was obtained if the following steps were followed:

- No tape was used on the EEG electrodes nearest to the bNIRS probes. The tape covered a large area on the frontal part of the head and was found to reduce the intensity of the bNIRS signal;
- Frontal EEG electrodes were moved slightly upwards to allow more room for the bNIRS probes. This enabled better contact of the bNIRS probes with the head as the electrodes were far enough away so as not to interfere whilst still maintaining the integrity of the EEG signals required by clinicians;
- EEG electrodes and the bNIRS headgear were placed on the patient at the same time. This minimised disruption to patients and enabled more optimum placement of the two modalities to maximise the signal quality.

These steps were only possible to implement if the EEG neurophysiologist working on the ward was available to help with the placement of the bNIRS probes and potential relocation of nearby EEG electrodes. Close collaboration with the patient's neurophysiologist enabled optimisation of the set-up for each patient. It was found that simultaneous EEG and bNIRS placement delivered the highest quality signals; however, this was not always possible if the patient was coming in for multi-day monitoring. If this was the case, the EEG netting would have to be cut away to allow the bNIRS device to be placed. Depending on the age and temperament of the patient, this could cause stress and discomfort, which also affected the quality of the bNIRS signal due to restlessness of the patient causing movement artifacts and increased difficulty in securely attaching the head gear.

6.3.2 Design of headgear

Headgear was designed with the infant head in mind in collaboration with researchers from Babylab at Birkbeck University, due to their experience with headgear designs for infants under 9 months of age. An additional consideration in design of the headgear was the simultaneous recording of the EEG with the bNIRS. An integrated EEG-bNIRS cap was considered to allow the EEG and bNIRS probes to be placed on the head with relative ease. However, clinical protocols of EEG electrode placement restricted redesign of EEG application through incorporation of the EEG electrodes into a cap, hence it was decided that the most suitable approach would be to place the bNIRS probes around the EEG electrodes. A band design was thus deemed most suitable for this purpose as it would be easier to place on the patient around the existing EEG electrode set-up.

Due to the initial target range of infants under 24 months of age, two different headgear designs were developed based on head circumference rather than age of the patient. A list of head circumferences from the last twenty patients under 24 months of age were collected in order to aid in the development of the designs. Two bands were developed based on this prior patient population; one for head circumferences up to 46.5 cm and one for head circumferences greater than 46.5 cm. A source-detector separation of 2.5 cm chosen as an appropriate separation to monitor cerebral changes in infants up to 2 years old (Anderson et al. (2017), Gervain et al. (2011)).

The source and detector configuration was designed such that each source was surrounded by four detectors in order to maximise the number of channels available. An example of the source-detector configuration is shown in Figure 6.1 where red circles represent the sources and blue circles represent the detectors.

The band was made of a black plastic material with a rigid inner membrane to maintain its shape and maintain a rigid source-detector separation. Holes were punched into the material when a configuration was decided upon. The black colour is able to to block out any ambient light with one side of the material having a slightly sticky surface to prevent movement of the band when in contact with skin.

Figure 6.1 shows the designs of the frontal and temporal bands. The channel configuration for each band was designed such that the scalp regions monitored were mirrored in both hempispheres. A red marker on each band indicated the centre-line to enable symmetric placement. A source-detector separation of 3 cm was used for the frontal band as this was intended for use in older children, while the temporal bands had a source-detector separation of 2.5 cm for patients under 2 years old. The frontal band allowed 8 channels to be monitored, while the temporal band enabled a total of 16 channels to be monitored (8 channels from the left hemisphere and right hemisphere respectively).

The region covered by the bNIRS probes was assessed for each patient, based not only on the patient's age but also the location and type of seizures. An example of the bNIRS set-up on a patient is shown in Figure 6.2.

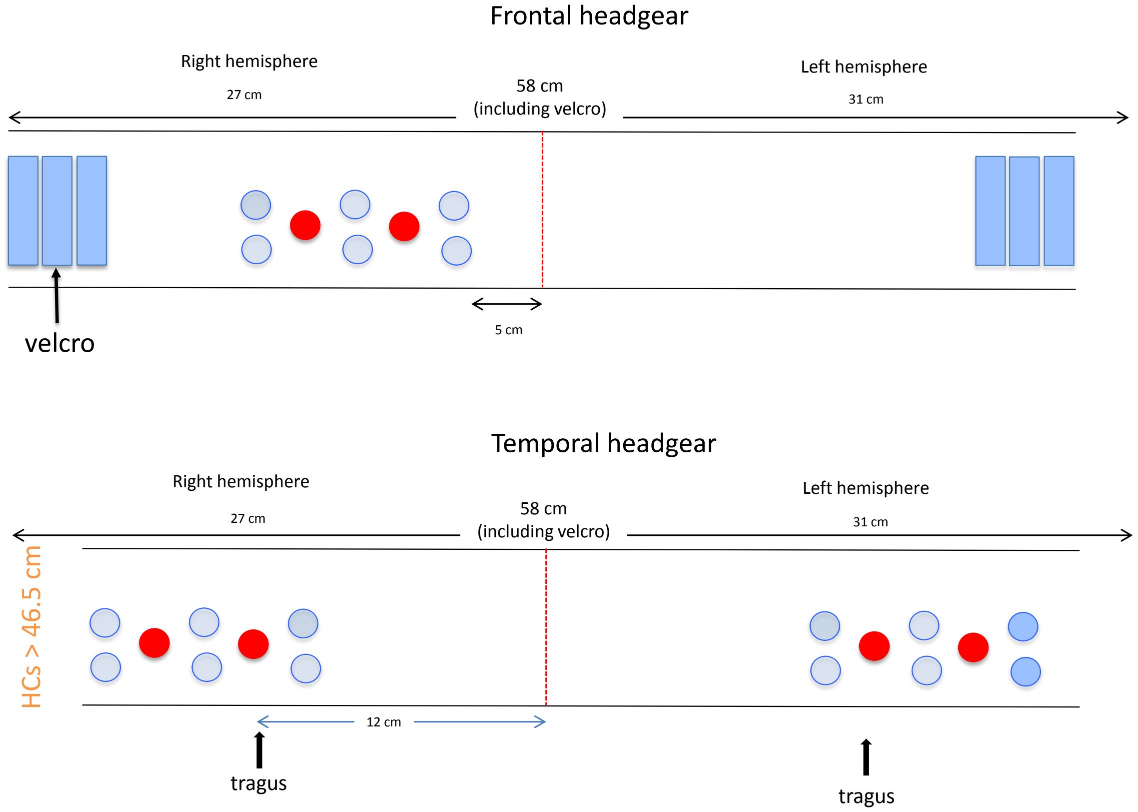

Figure 6.1: Diagram showing source-detector configuration of the frontal and temporal bands. Only the larger temporal band is shown here; a similar band for head circumferences less than 46.5 cm was also produced, with a total band length of 56 cm and distance of 10 cm from the centre line to the tragus

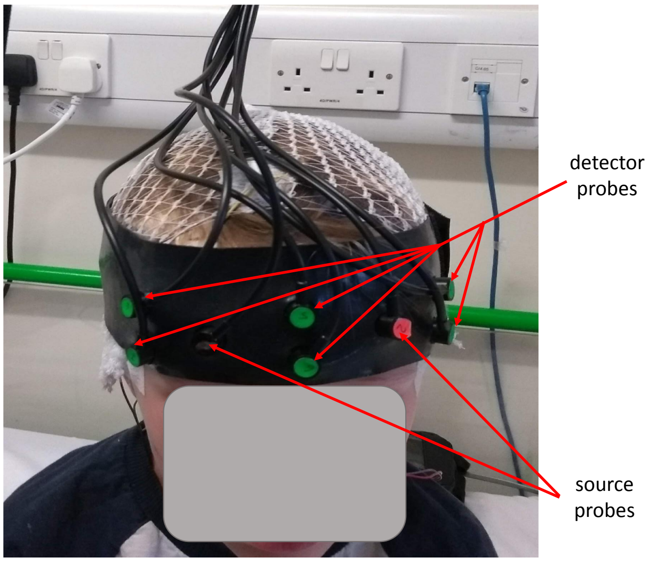

Figure 6.2: Image showing bNIRS frontal band on a patient. The band was placed such that the two centre pair of detectors was align centrally on the head, enabling a symmetric configuration across the frontal lobe and ensuring consistency in placement across subjects

Patients were monitored for between half and hour to two hours, depending on comfort level and tolerance to the headgear, to maximise chances of capturing a paroxysmal event.

6.3.3 Protocol

Infection control was important to maintain when bringing the bNIRS system into a clinical setting. Probes were cleaned and disinfected regularly using alcohol wipes and the system unit and its components regularly wiped down. When the system was not in use, it was stored in a clean and dry environment to maintain cleanliness.

Continuous monitoring of EEG and bNIRS was recorded. Patients admitted to the rapid assessment unit had suspected absence seizures and a HV task was performed as part of usual procedure if the patients were old enough and willing. This involved the patient blowing for between $1-2$ minutes to keep a pinwheel spinning continuously; the start and end points of this period were marked on the EEG by the neurophysiologist. Hyperventilation is often routinely performed to attempt to activate epileptiform activity and absence seizures. A prominent slow wave build-up response is frequently elicited. Photic stimulation is also routinely used to elicit a posteriorly predominant driving response (St. Louis et al. (2016)), although bNIRS measurements were stopped during the photic stimulation as the light was found to interfere with the bNIRS signal.

6.3.4 Patients

Table 6.1 shows the patients recruited, number of good quality recording channels obtained, whether the patient had any seizure events, whether they took part in the HV task and their medical notes. No good quality data were obtained from two of the patients. A common reason patients were admitted was for suspected absence seizures, a generalised onset seizure that causes the patient to momentarily lose attention. These seizures usually only last a few seconds. A brief summary of the clinical notes for the most recently observed seizure for each patient is presented in the table.

One 3 year old patient with focal seizures originating in the left hemisphere was selected as a suitable candidate for the temporal band. The temporal band was also attempted on Patient 6 but the dark hair of the patient prevented a good bNIRS signal to be obtained, hence frontal monitoring was performed instead.

Table 6.1: Table showing details of recruited patients. Note that two of the patients had no channels with good quality bNIRS signals

Patient number	**Date**	**Gender**	**Age (years)**	**Good quality bNIRS channels**	**Hyperventilation**	**Seizures**	**Clinical notes**
1	13/04/2018	F	14	6/8	Y	N	Vacant episodes occurring several time a day
2	13/04/2018	M	5	6/8	Y	N	Mixed atypical absence seizures and generalised seizures triggered by flashing lights
3	09/05/2018	M	6	8/8	N	Y	Type 1, myoclonic jerks accompanied with arms going out and eyes rolling. Can cluster over a few minutes and at times associated with absences. Type 2, potential complex partial seizures that occur during sleep Type 3: Atonic drops and head drops, occurring every 6 months
4	16/05/2018	F	3	8/16	N	Y	Recurring seizures accompanied with heart rate dropping, eyes flickering and head twitching
5	31/05/2018	M	6	6/8	Y	Y	No clinical notes available
6	17/07/2018	F	23 months	6/8	N	Y	Frequent daily seizures, up to 25 a day, accompanied with head nods, stiffness and extension of right arm for around 20 s. Impaired awareness and intermittent jerking with maintained awareness for around 1 minute

8	24/07/2018	F	7	8/8	Y	N	Frequent nocturnal episodes accompanied with alertness from sleep, sitting up and looking around the room and slow repetitive movement of arms
9	01/08/2018	M	4	0/8	Y	Y	Absence seizures accompanied with abrupt behavioural arrest, eyes rolling up and some eyelid twitching
10	07/08/2018	M	11	0/8	N	Y	Type 1, myoclonic absence seizures accompanied with abrupt loss of responsiveness. Average of 20–30 times a day. Type 2, tonic seizures with sudden onset stiffening. Type 3, nocturnal tonic-clonic seizures accompanied with stiffening and jerking
12	15/08/2018	M	1.5	2/8	N	Y	Gelastic seizures that can occur in a cluster accompanied with bursts of laughing or crying, sometimes slow blinking
13	23/08/2018	M	6	6/8	N	Y	Around 5 seizure a day accompanied with sudden loss of tone and falling forwards. Stiffening occurs and appears to stop breathing for around 15 s

14	19/09/2018	F	7	8/8	Y	Y	Type 1, left focal seizures accompanied with slowly dropping to the floor, eyes rolling up and to the left, excessive drooling and hiccoughing sounds, twitching of the left side of the face. Occurs around once per week. Type 2, jerks accompanied with brief jerking of the left arm. Type 3, absence seizures accompanied with behavioural arrest, eyes rolling up and to the left. Occur around once per week for a few seconds

6.3.5 Data processing

Simultaneous monitoring of the EEG and bNIRS requires synchronisation in order to compare the two sets of data within the same time-frame. In order to do this, a marker was simultaneously sent to the EEG recording device and bNIRS programme at the start and end of the measurement period data to time-lock these two signals. bNIRS signals were saved as .csv files and imported into MATLAB for data processing. EEG data and corresponding timestamps were exported from Natus Neuroworks and imported into MATLAB. Synchronisation was then performed afterwards using a program developed in MATLAB (MathWorks, USA).

Concentration changes were calculated using the UCLn algorithm and re-sampled to 1 Hz using spline interpolation.

In order to analyse and extract useful insights from the datasets, data were initially visualised at each location of each bNIRS channel and any variation in bNIRS signals across these different channels, the corresponding EEG trace (selected as the nearest electrode to the bNIRS channels) and any events such as the start and end of the HV task or the start and end of any seizure events. Data were grouped according to the suspected cause of seizure events and whether patients performed the HV task.

6.4 Results

This section presents the results from the studies performed on infants and children with epilepsy. Due to the broad population investigated and the absence of a suitable task appropriate across this broad population, group analysis is inappropriate. Hence, results are presented as individual case studies, with results from similar paradigms presented together.

6.4.1 Examples of data

This section presents some examples of the data collected in this study, showing examples of good quality and poor quality data.

Figure 6.3 shows an example from Patient 3, a 6 year old male patient monitored over a 40 minute period. Figure 6.3a shows a plot of the raw intensity data collected against wavelength for both the beginning of the measurement period and in the middle of the measurement period for one detector. The spectra demonstrate an example of a good quality raw data set, with the expected shape after light has passed through tissue and a sufficient number of counts. Furthermore, the spectrum changes are small between the beginning and middle of the measurement period suggesting a stable and good contact has been established between the bNIRS probes and the skin. Figure 6.3b shows the corresponding concentration changes in HbO_2, HHb and oxCCO as calculated from the raw intensity spectra using the modified Beer-Lambert law.

Figure 6.4 shows an example from Patient 9, a 4 year old male patient monitored over a 50 minute period. The raw intensity data for this patient are shown in Figure 6.4a from one detector. The spectrum at the beginning of the measurement period shows an expected shape of light after it has passed through tissue, similar to that shown in Patient 3 in Figure 6.3. However, the spectrum in the middle of the measurement period, shown in orange, shows a very different shape to that expected, with a strong peak seen at around 860 nm, creating an unnaturally broad peak across 760 nm (where the peak of the HHb absorption spectrum appears) to 860 nm. The corresponding concentration changes are shown in Figure 6.4b, where the traces for HbO_2, HHb and oxCCO look very different to the traces shown in Figure 6.3, with a much flatter trace intercepted with sharp spikes showing a much more disjointed trace.

Reasons for the variance in quality of intensity data have been discussed previously in Section 6.3.1 but briefly include poor contact of bNIRS probes with the skin, due mainly to the interference of EEG electrodes or electrode tape, and movement of the patient. The best protocol for putting on the bNIRS headgear to enable simultaneous, good quality collection with EEG is presented in Section 6.3.1.

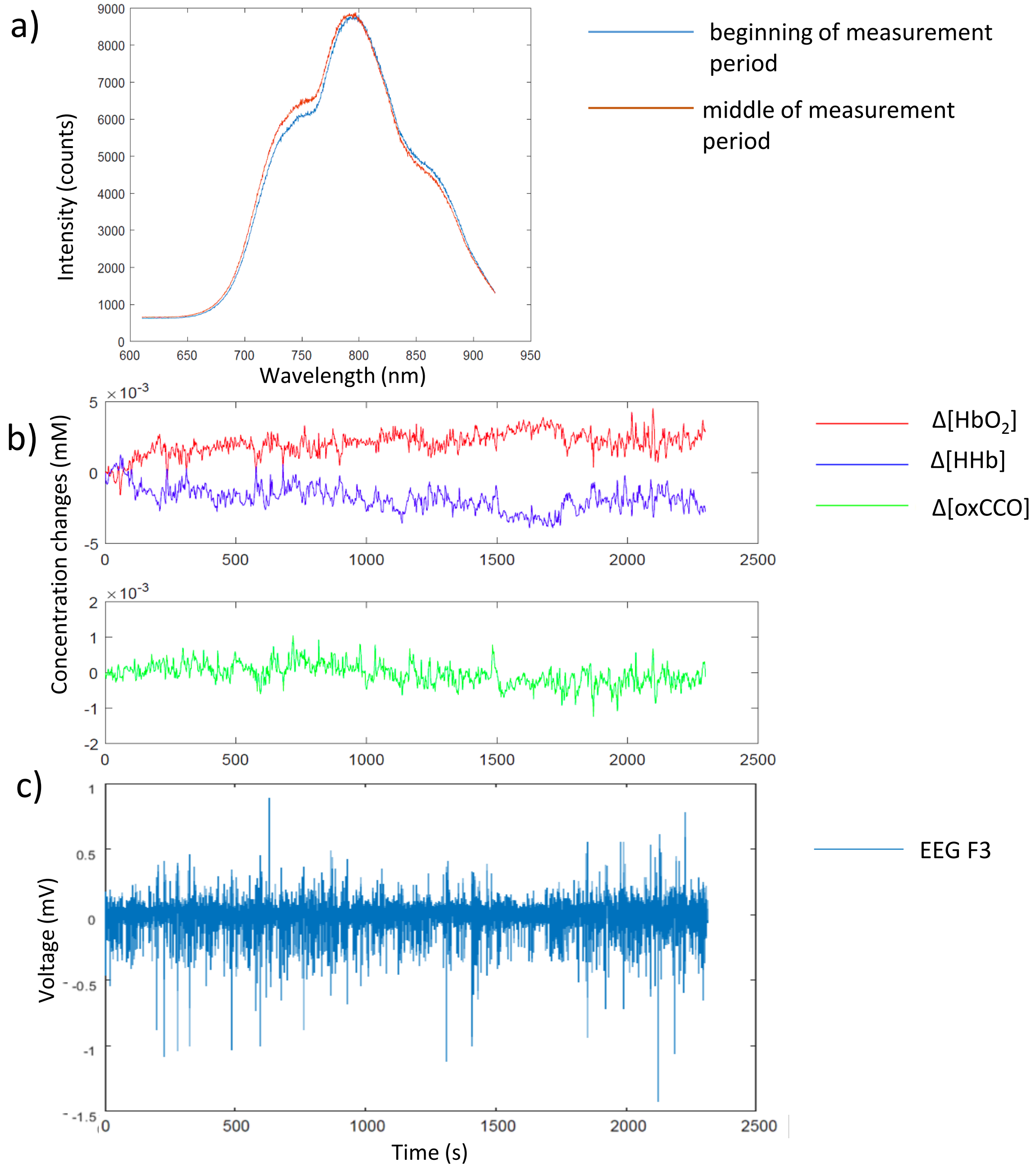
a)
Intensity (counts)
9000
8000
7000
6000
5000
4000
3000
2000
1000
0
600
650
700
750
800
850
900
950
Wavelength (nm)
beginning of measurement period
middle of measurement period
b)
Concentration changes (mM)
× 10^-3
5
0
-5
0
500
1000
1500
2000
2500
Δ[HbO2]
Δ[HHb]
Δ[oxCCO]
× 10^-3
2
1
0
-1
-2
0
500
1000
1500
2000
2500
c)
Voltage (mV)
1
0.5
0
-0.5
-1
-1.5
0
500
1000
1500
2000
2500
Time (s)
EEG F3

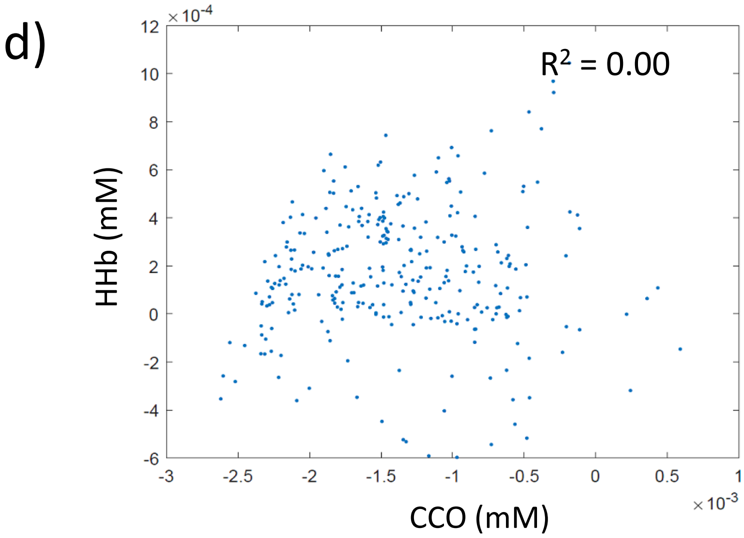

Figure 6.3: Example of good quality data from Patient 3. a) Raw data showing shape of spectra at the beginning of the measurement period (blue) and the middle (orange) for comparison. b) Corresponding concentration traces across the measurement period showing changes in $\Delta[HbO_2]$ *(red),* $\Delta[HHb]$ *(blue) and* $\Delta[oxCCO]$ *(green). c) Synchronised EEG trace over region FP1. d) A plot of* $\Delta[HHb]$ *against* $\Delta[oxCCO]$ *for a 3 minute period in the middle of the measurement period*

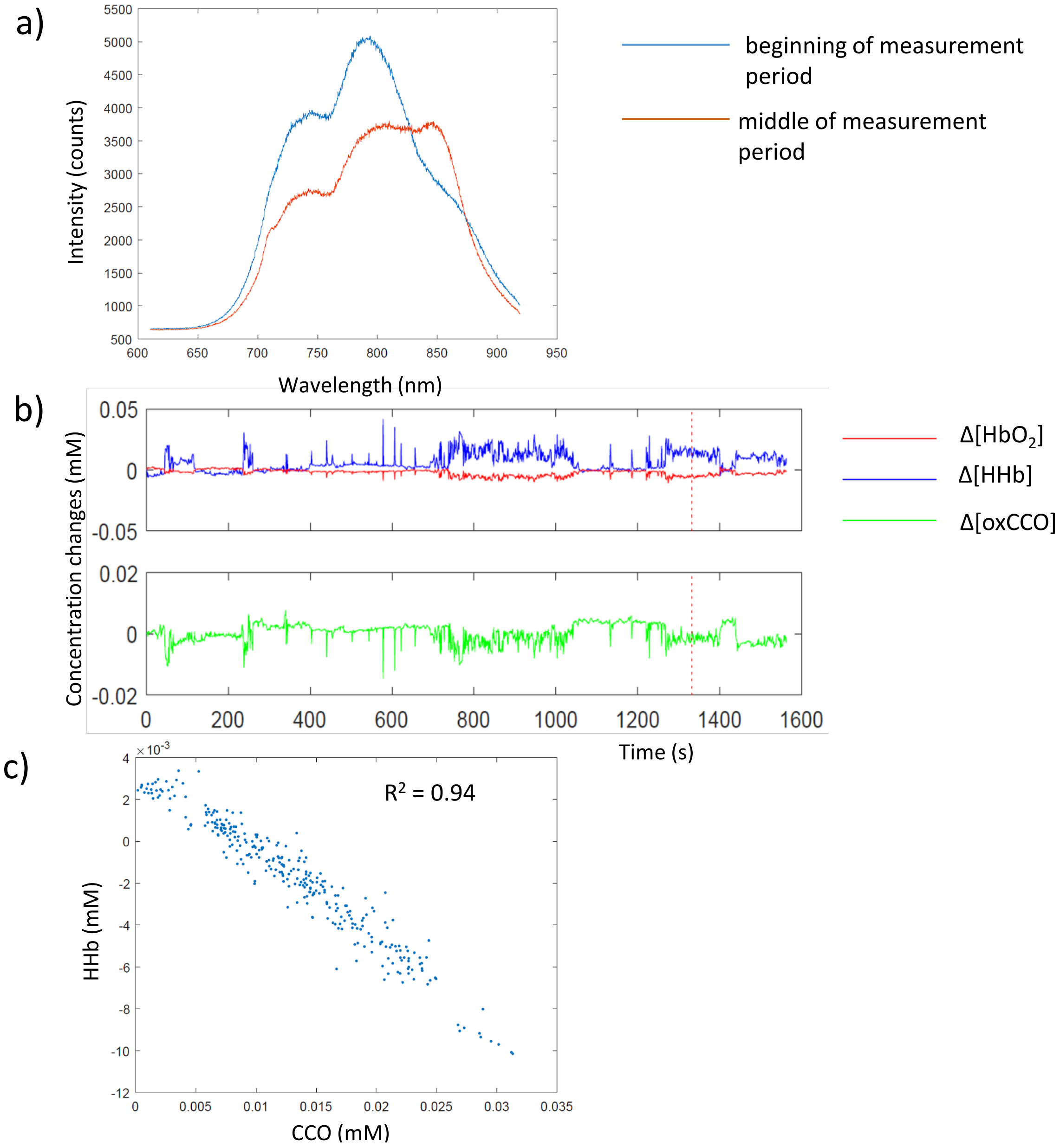

Figure 6.4: Example of poor quality data from Patient 9. a) Raw data showing shape of spectra at the beginning of the measurement period (blue) and the middle (orange) for comparison. b) Corresponding concentration traces across the measurement period showing changes in Δ[HbO$_2$] (red), Δ[HHb] (blue) and Δ[oxCCO] (green). c) A plot of Δ[HHb] against Δ[oxCCO] for a 3 minute period in the middle of the measurement period

6.4.2 Hyperventilation task

A total of 6 patients performed the HV task, consisting of blowing continuously to keep a pinwheel spinning for 1 – 2 minutes. Figures 6.5, 6.6, 6.7, 6.8 and 6.9 show the bNIRS datasets collected, with solid vertical lines indicating the start and end of the HV periods and dotted lines indicating a seizure, as identified by the EEG.

It should be noted that Patients 1 and 2 were the first two patients recruited for the study. As they were older than initially expected (14 years and 6 years old respectively), the temporal band was used to monitor the frontal lobe. This had a source-detector separation of 2.5 cm; future studies on children above 3 years old used a source-detector separation of 3 cm as this is more likely to reflect cerebral changes in this older age range.

Haemodynamic changes can be seen during the HV period in some of the patients: 1, 5, 8 and 14 (data for Patient 14 are shown zoomed in around the HV period for easier visualisation in Figure 6.10. No clear changes are seen in Patient 2 during the HV period, with channels L3 and R3 appearing quite noisy.

The observed bNIRS changes are summarised in Table 6.2. Three of the patients showed a similar haemodynamic response, but the metabolic response differed in all three patients. An increase in $\Delta[\mathrm{HbO_2}]$ and a decrease in Δ[HHb] was observed in Patients 1, 8 and 14 during the HV period in some of the channels. Patient 1 showed little change in oxCCO, with the shift observed in channel R1 likely a movement artifact due to the sudden shift from baseline in all the parameters at this time point. No unusual changes were seen in the EEG for this Patient. Patient 8 showed a corresponding decrease in Δ[oxCCO] alongside the haemodynamic changes. An abnormal EEG was collected in this patient. The drop in metabolism during the HV period indicates a mismatch between the oxygen supply, which is readily available, and uptake of oxygen by the cells, which is falling despite the increase in $\Delta[\mathrm{HbO_2}]$. Patient 14 showed a sudden drop in Δ[oxCCO] immediately after the HV start, which is not indicative of a movement artifact as the haemodynamic signals do not show this same shift, suggesting the change is physiological. This sudden drop was followed by a steady increase to above baseline levels; however, a large drop in Δ[oxCCO] to values much lower than the initial baseline is observed around 100 s after the end of the HV. No obvious changes in haemodynamics are observed at this same time period in the majority of channels.

In contrast, Patient 5 shows an increase in Δ[HHb] and decrease in $\Delta[\mathrm{HbO_2}]$ in channels R1 and R3, with changes delayed from the start of the HV period and continuing after the end of the HV period before a return to baseline. A steady increase in Δ[oxCCO] is seen during the haemodynamic changes. This patient did have brief seizure events during the HV period, lasting only a few seconds. Other channels for this patient show sudden spikes in concentration data, which suggests that these channels may have been affected by movement artifacts.

Table 6.2: Table summarising the bNIRS changes observed across patients during the HV period; Y = yes, N = no

Patient number	**HV changes seen?**	Δ[**HbO$_2$**]	Δ[**HHb**]	Δ[**oxCCO**]
1	Y	Increase	Decrease	No change
2	N	No change	No change	No change
5	Y	Decrease	Increase	Increase
8	Y	Increase	Decrease	Decrease
14	Y	Increase	Decrease	Initial drop followed by steady increase. Delayed drop to below baseline 100 s after end of HV period

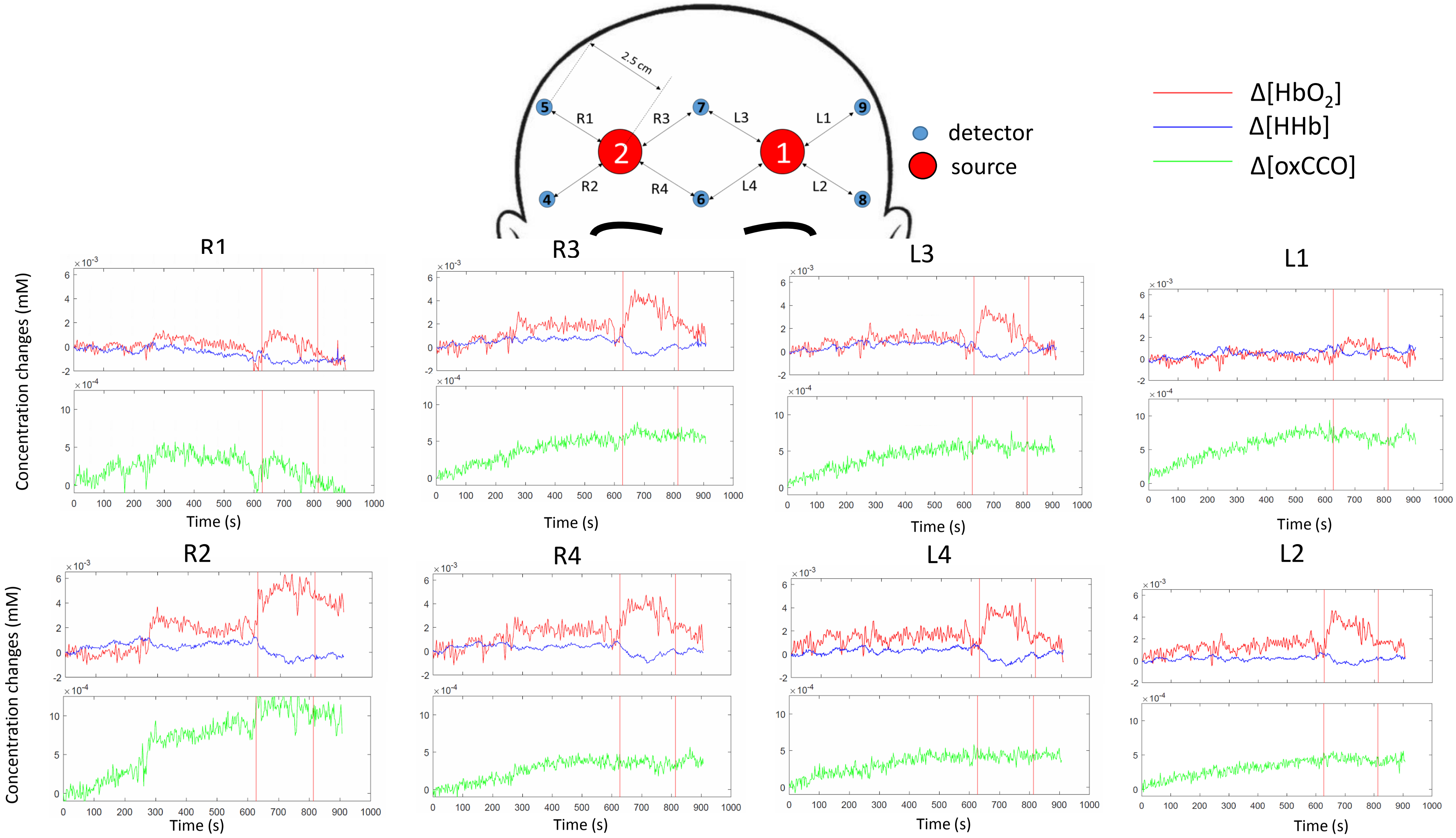

Figure 6.5: Summary of bNIRS data from Patient 1

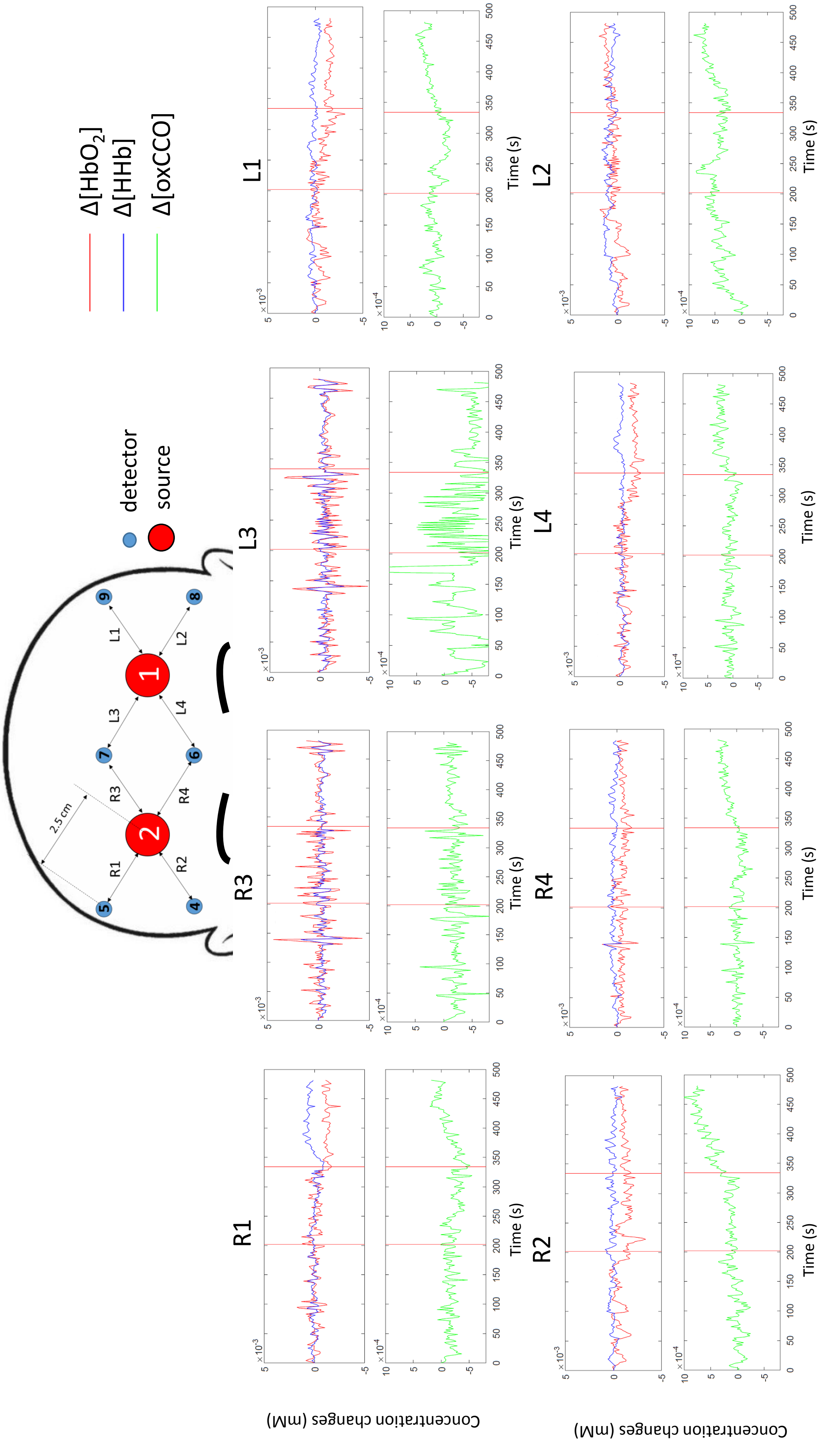

Figure 6.6: Summary of bNIRS data from Patient 2

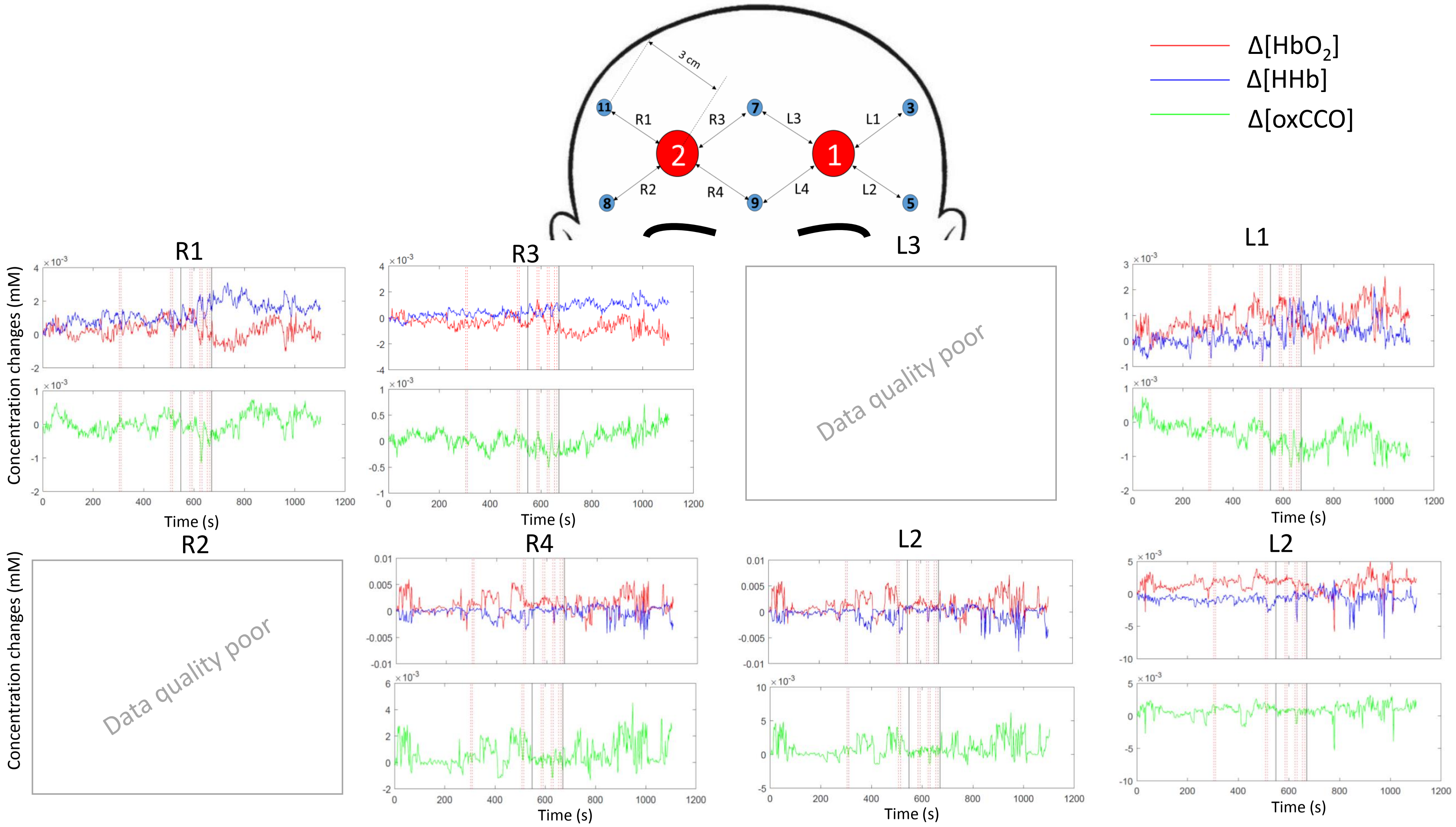

Figure 6.7: Summary of bNIRS data from Patient 5

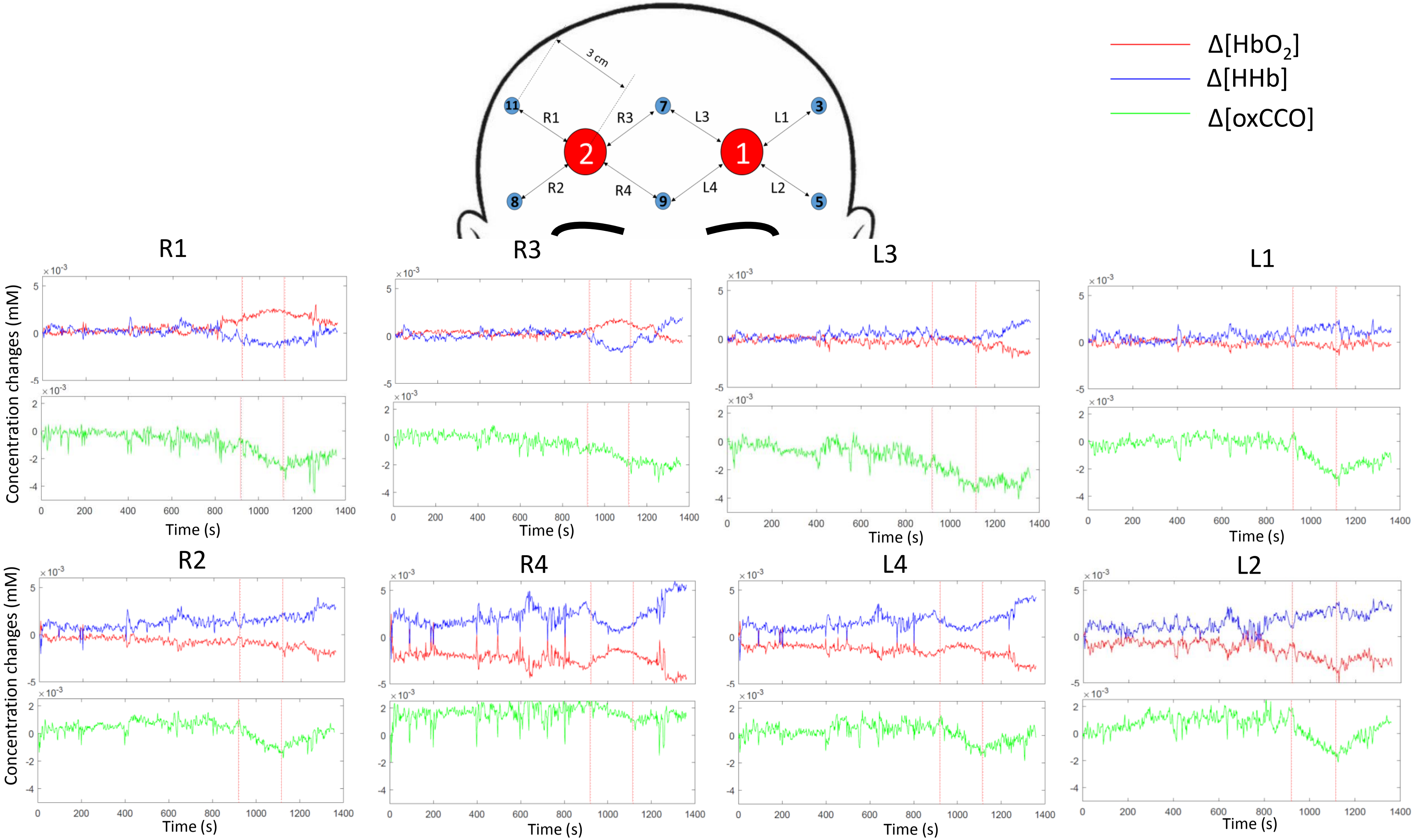

Figure 6.8: Summary of bNIRS data from Patient 8

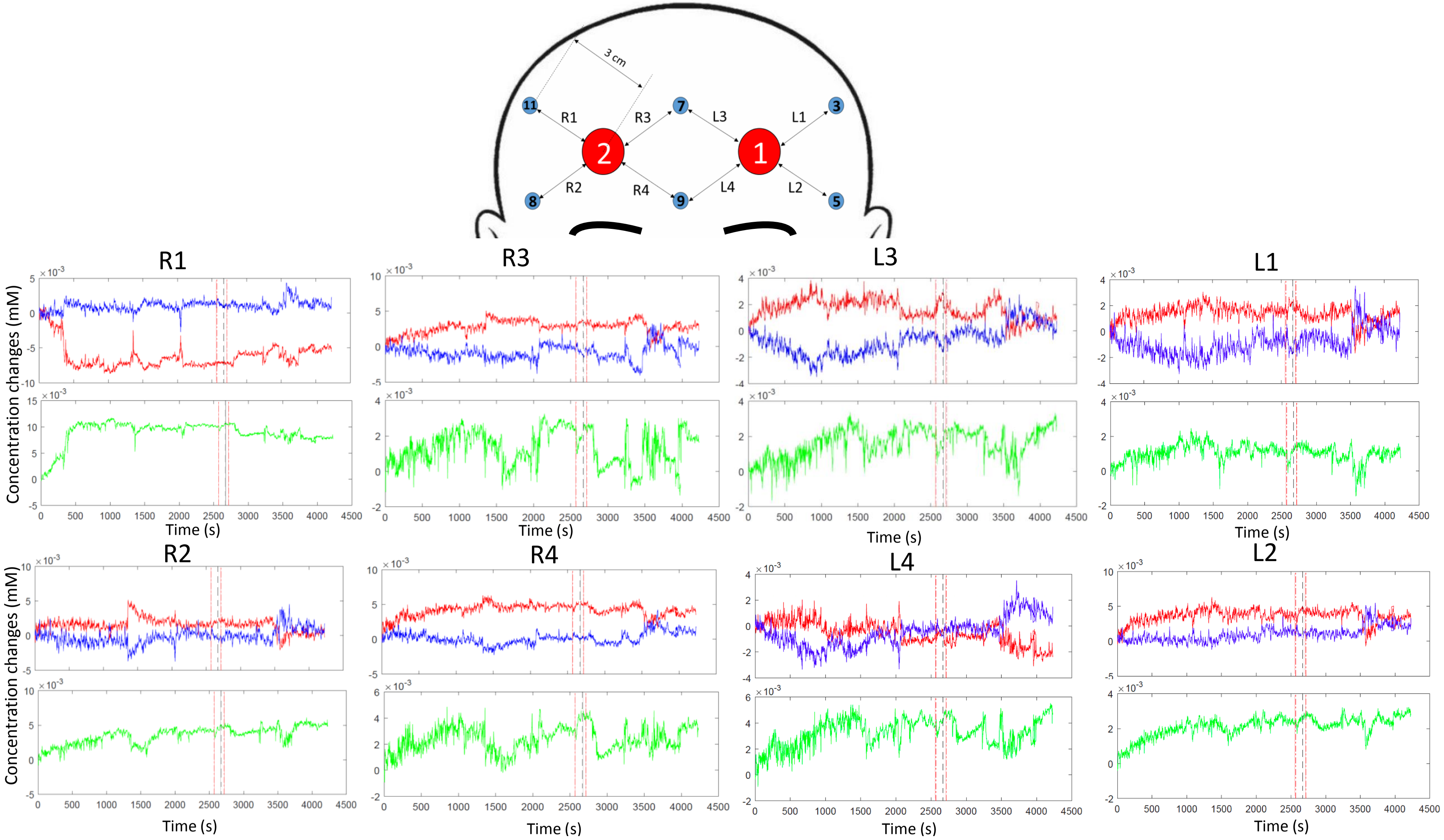

Figure 6.9: Summary of bNIRS data from Patient 14

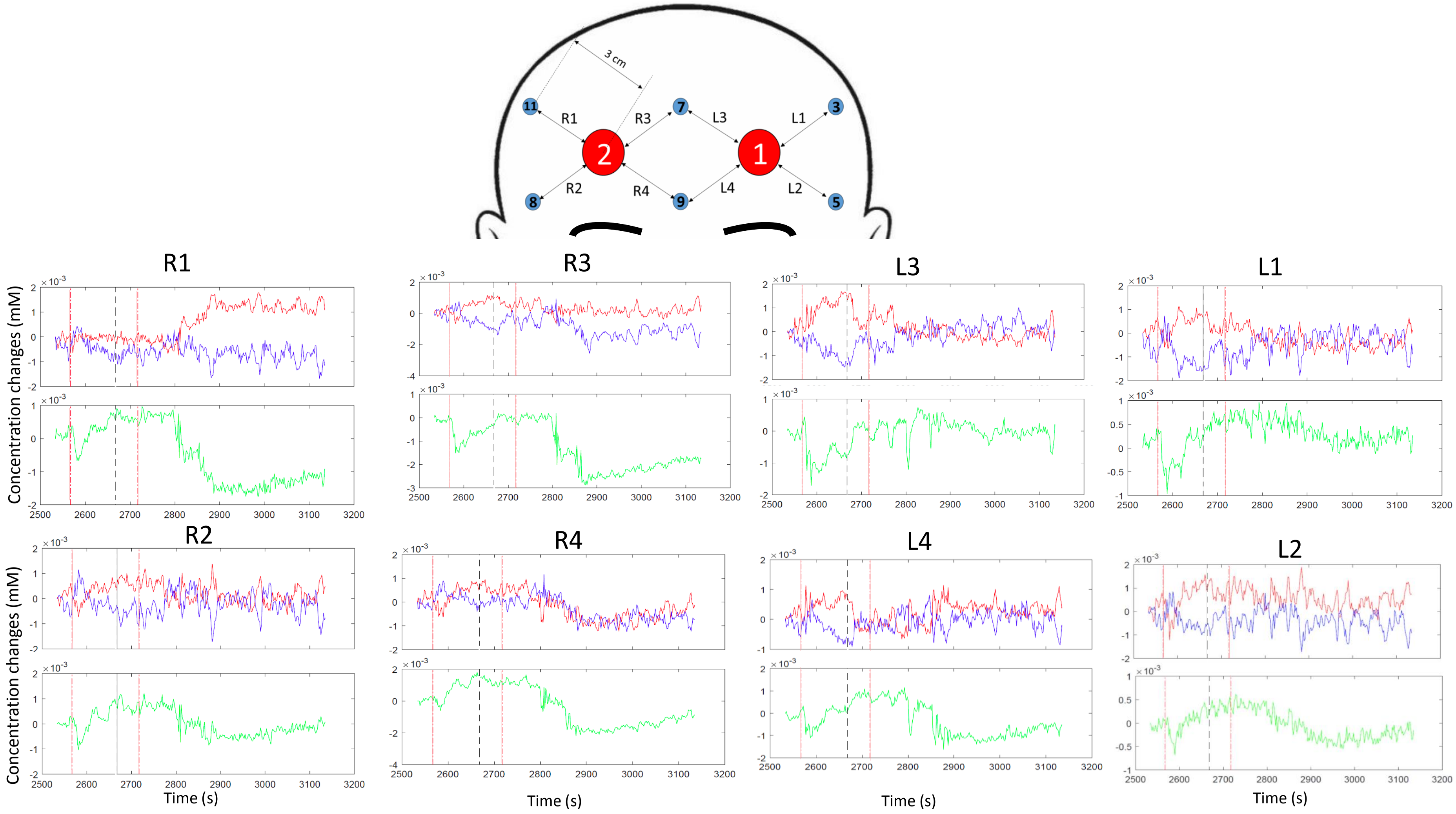

Figure 6.10: Summary of bNIRS data from Patient 14, zoomed in around the HV period

The hyperventilation was difficult to quantify therefore induced changes are variable. Unlike in the laboratory, where adult volunteers are able to sustain longer periods of effort during such a task, in the clinic, the level of hyperventilation varied due to the age of the patient and tolerance of the task. Ideally, an additional monitor of CO_2 would have to be introduced to enable comparison between patients. Hence, no further analysis is performed during these HV periods, although it is noted that interesting differences are observed in the metabolic response between patients suggesting potential for a similar, more rigorous paradigm to be used. It has been demonstrated that monitoring such induced cerebral changes using such a task across a variety of age ranges in young patients in a clinical environment is possible.

6.4.3 Seizures

Seizures were captured during monitoring in a total of seven patients. Figures 6.11, 6.12, 6.13 and 6.14 show the traces from patients where seizures were captured. Seizures were also captured in Figures 6.7 and 6.9 presented in the previous section additional to the HV task. Each dotted vertical line indicating the seizure start and end. All seizures captured were of short duration, lasting only a few seconds. It is noted here that the seizures in Patient 4 are not displayed here but are looked at as a separate case study in the next chapter.

The seizures presented in this chapter did not show any changes in the haemodynamic or metabolic traces in the bNIRS signal, which is likely due to the short duration of the disruption in electrical brain activity not being translated to changes in the slower haemodynamic response function in the brain. An example is presented in Figure 6.15, where the bNIRS traces and corresponding EEG trace from location FP1 is shown for a seizure identified in Patient 3. It is plausible that such short activity does not induce haemodynamic changes. However, again the system demonstrated capabilities in monitoring a broad patient range for up to several hours, long enough to capture a seizure event in some patients.

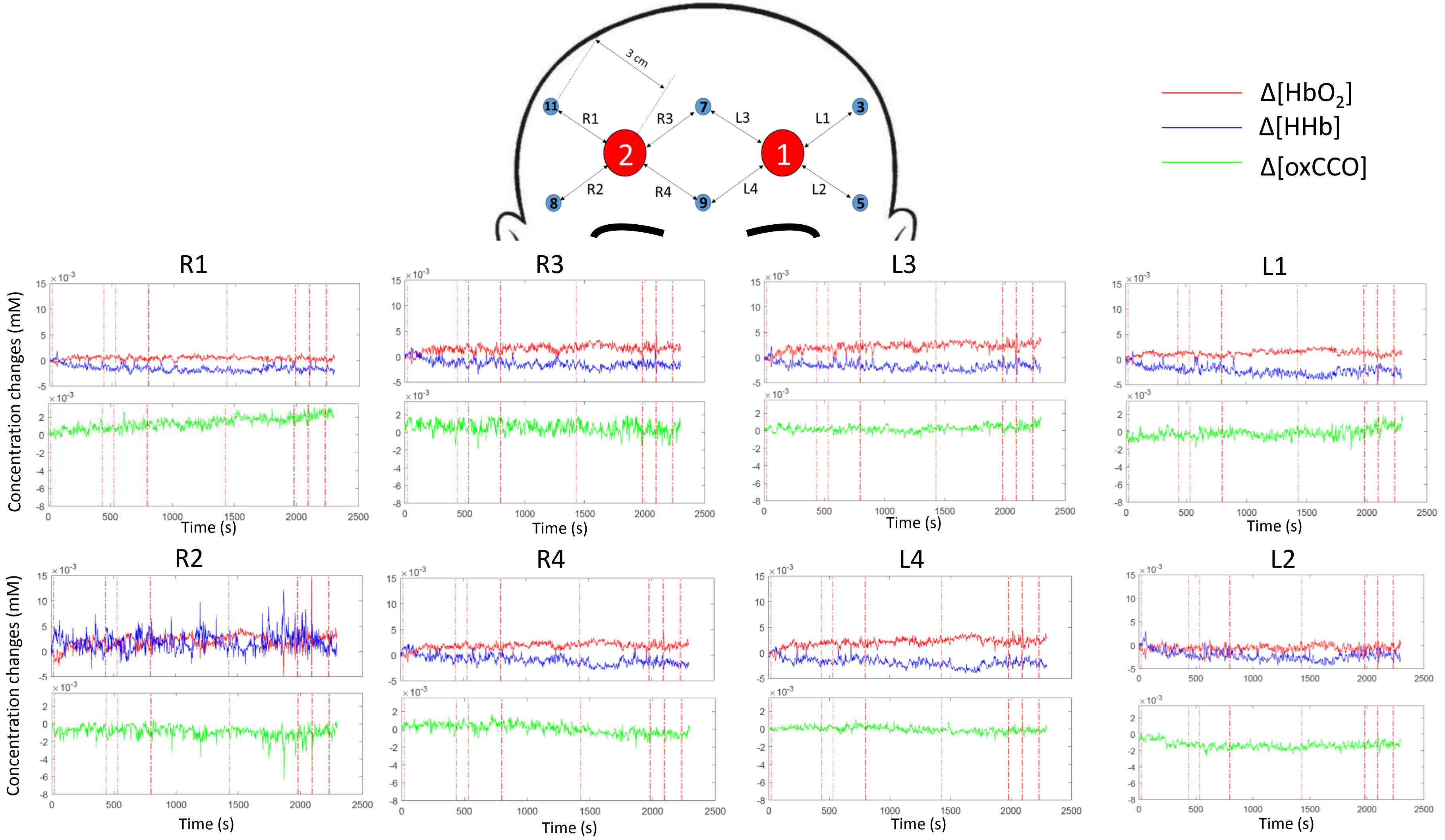

Figure 6.11: Summary of bNIRS data from Patient 3

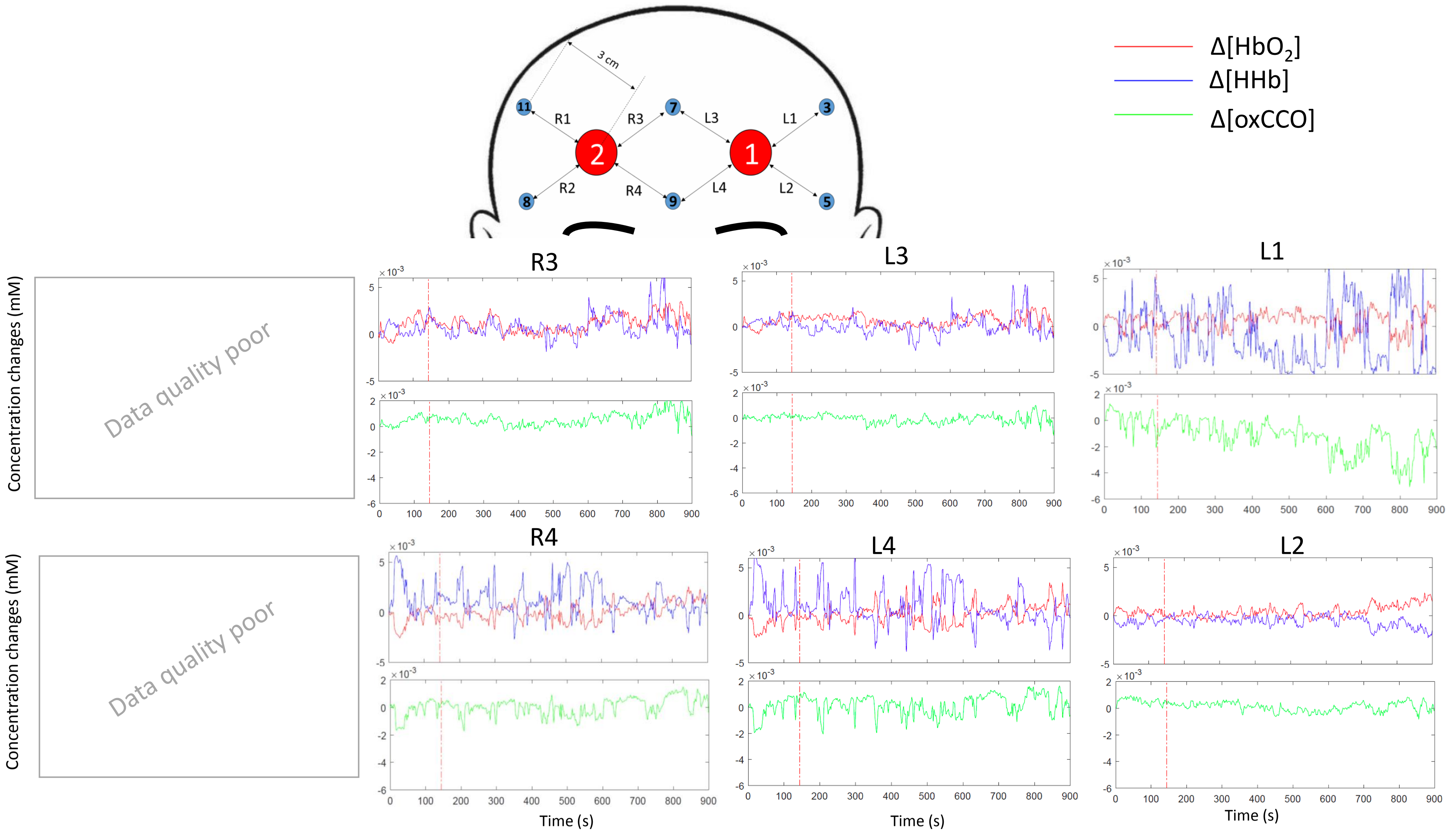

Figure 6.12: Summary of bNIRS data from Patient 6

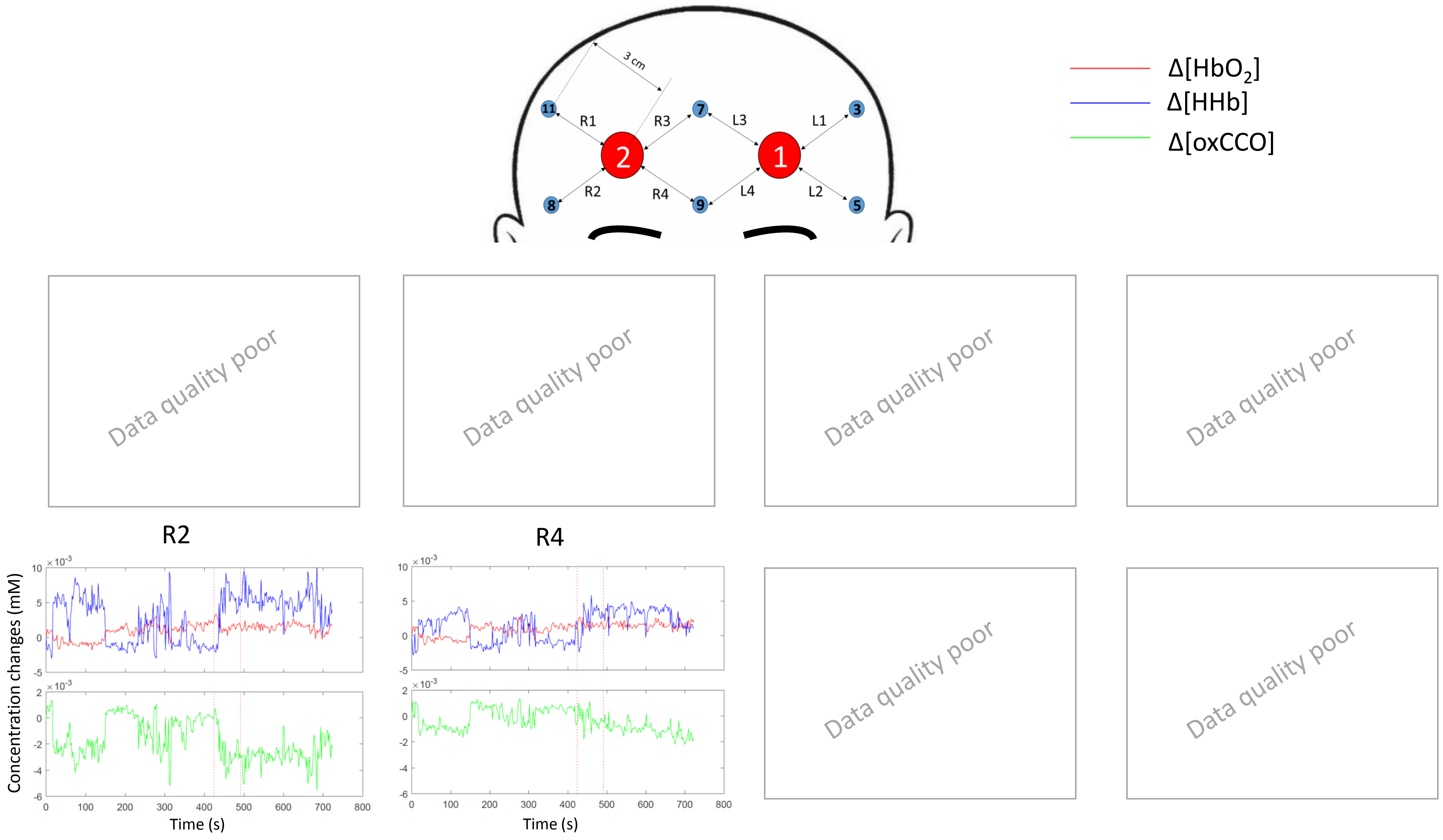

Figure 6.13: Summary of bNIRS data from Patient 12

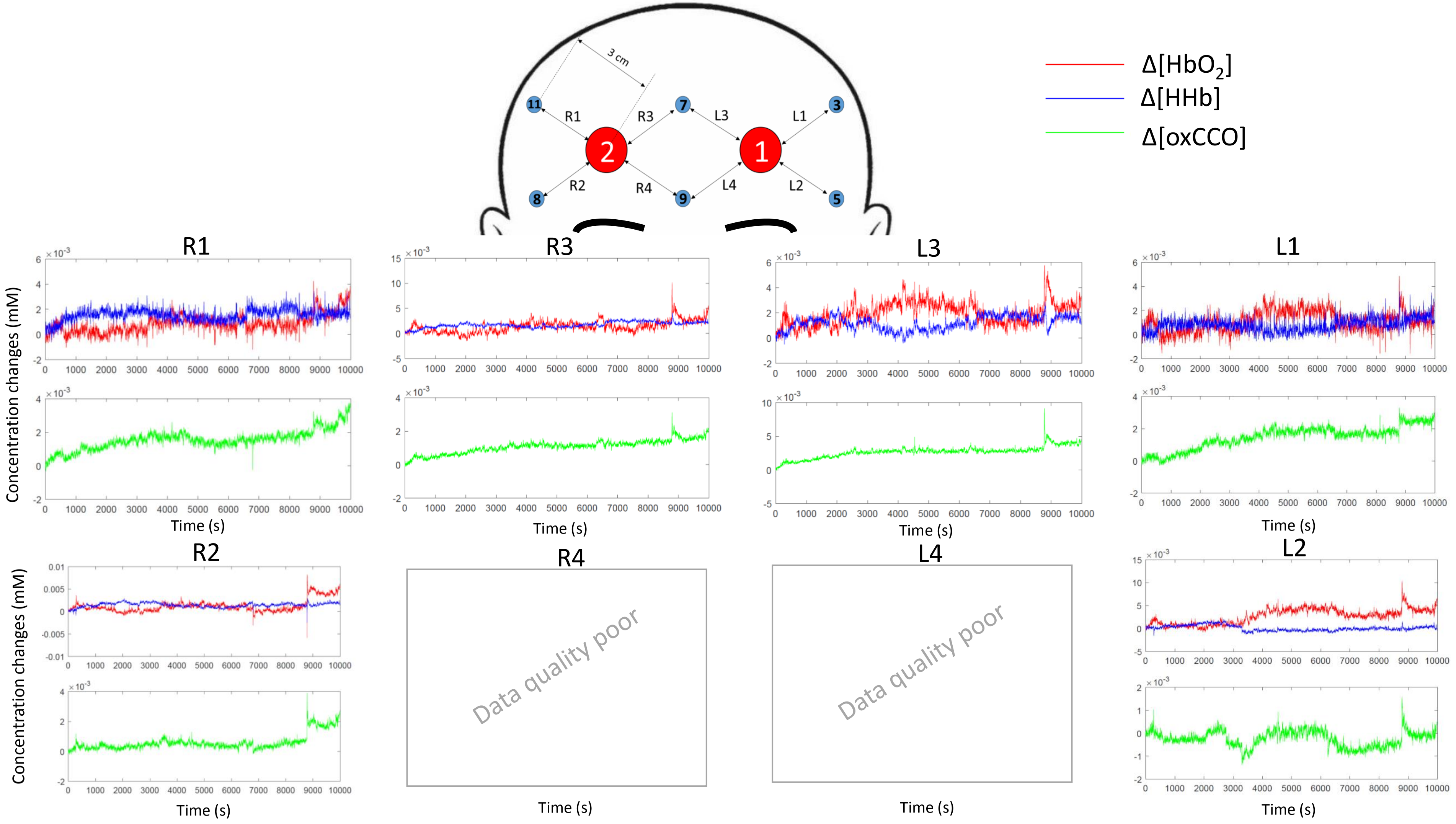

Figure 6.14: Summary of bNIRS data from Patient 13

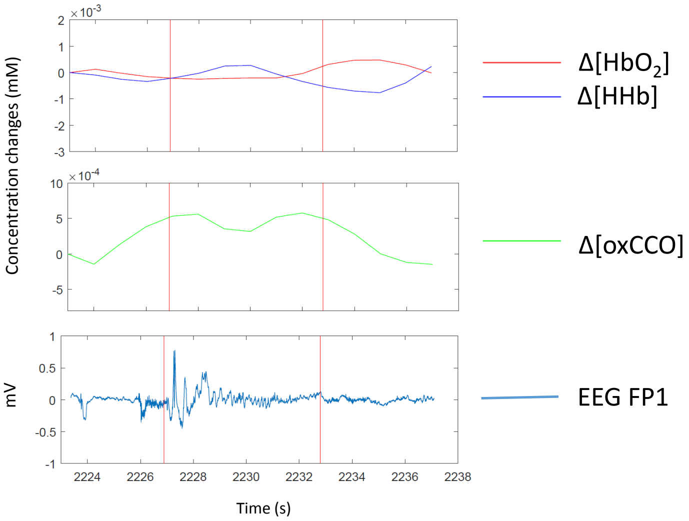

Figure 6.15: Example data showing a seizure from Patient 3. The bNIRS traces are shown alongside the EEG trace at FP1, with vertical lines indicating the seizure start and end

6.4.4 Summary

The bNIRS system demonstrated its capabilities to monitor cerebral changes in oxygenation, haemodynamics and metabolism simultaneously with routine EEG monitoring on children with epilepsy in a clinical environment. This chapter has demonstrated the plausibility of obtaining both a good quality bNIRS signal without disruption of routine clinical electrical EEG measurements; a guide in obtaining the highest quality bNIRS signal was developed through experience over the course of the study. It was also possible to capture seizure events over a relatively short monitoring period through careful patient recruitment as well as induce cerebral changes using a hyperventilation task in some patients. Finally, it is possible to not only monitor electrical and haemodynamic changes but also metabolic changes in epilepsy patients, providing further insight into the functioning of the brain in this patient cohort.

CHAPTER 7

Case study

The previous chapter presented the data from a multitude of epilepsy patients as monitored using simultaneous bNIRS and EEG. This chapter focuses on the analysis of the data from one patient in particular who had recurrent seizures over a short measurement period. Unlike some of the previous data collected, clear changes in the bNIRS parameters can be seen during the seizure events. The combined optical and electrical measurements are presented here with investigation of the relationship between the haemodynamics, metabolism and EEG response during seizures. Regional changes in metabolism and oxygenation are observed demonstrating the potential of the system to provide an insight into the spatial metabolic response of the brain during seizure events.

7.1 Introduction

The previous chapter has shown bNIRS changes from many different epilepsy patients. The majority of seizures only lasted a few seconds as identified by the clinical EEG and therefore were not of sufficient duration to induce a cerebral haemodynamic response. Hence, few or no changes were seen in the bNIRS parameters. This chapter focuses on the analysis from one patient with recurrent seizures, where clear changes in the bNIRS parameters can be seen. This allows for further analysis of the response of the brain during these events.

7.1.1 Aim

In this observational study, the aim was to characterise changes in cerebral metabolism, as measured by changes in concentration of oxCCO, and haemodynamics, as measured by changes in concentration of HbO_2 and HHb, during seizures in relation to EEG-measured electrophysiological changes.

The aims of the study were to:

- quantify metabolic changes during seizures;
- identify any changes specific to localisation of the channels, for example, whether there are any hemispheric differences;
- look at the relationship between EEG and bNIRS signals.

7.2 Study details

7.2.1 Patient

The patient was a three year old girl with drug resistant epilepsy due to an extensive left sided cortical malformation. The patient had a normal term birth and normal early development until seizure onset at 4 months with hypotonia, eye rolling and stiffening of the right side; similar clusters were observed every 2–3 weeks. Seizure frequency increased dramatically in April 2018, when the study was performed. At the time of the study, the patient had multiple seizures per hour whilst on phenytoin, phenobarbitone, sodium valproate and topiramate. Her MRI showed an extensive malformation of cortical development in the left parietal and occipital lobe.

The EEG was recorded over 1.5 hours and captured multiple habitual seizures characterised by eye flickering evolving to facial twitching with subtle head jerks to the right and then stiffening/twitching of the right arm. Fast activity was seen in the EEG over the left parietal region evolving to widespread sharp and slow waves over the left hemisphere. In between episodes, she had very little movement in her right arm or leg. The interictal EEG showed continuous sharpened components over the left posterior quadrant. Numerous electroclinical seizures were captured, lateralising to the left hemisphere with localisation to the posterior quadrant.

7.2.2 Protocol

This study was approved by London Bloomsbury Research Ethics Committee. Informed written parental consent was obtained before the study.

Due to the young age of the patient and the fact that the seizures originated focally from the left posterior hemisphere, it was decided to use the temporal bNIRS band to monitor both left and right hemispheres over the temporal region. The bNIRS and EEG were put on simultaneously; this enabled careful placement of the EEG electrodes around the bNIRS probes and hence enabled a higher quality bNIRS signal to be obtained, as found in Section 6.3.1. The placement of the bNIRS probes to maximise signal quality was especially important using the temporal band due to the added complication of hair, which can significantly attenuate the bNIRS signal.

The bNIRS probe array was initially held against the side of the head as a guide and EEG electrodes were glued to the head in a symmetric configuration according to the 10-20 EEG system. The EEG electrode positions are shown in Figure 7.1 where the electrodes used in this study are shown circled in green.

The bNIRS headband was placed on after the EEG such that the front light source was located above the tragus on both sides. A source-detector separation of 2.5 cm was used. Monitoring was done for an hour with no intervention. Figure 7.2 shows the location of the bNIRS array overlaid on an image of a toddler's brain.

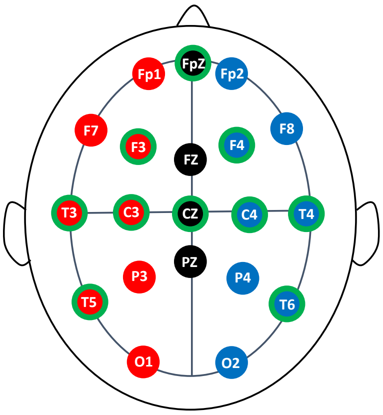

Figure 7.1: Diagram showing EEG electrode locations with the electrode positions used in this study circled in green

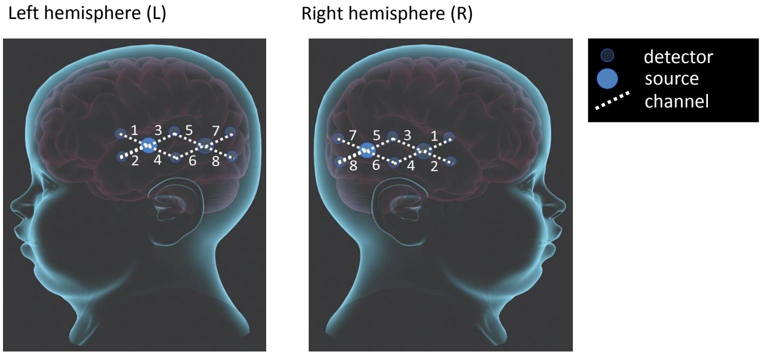

Figure 7.2: Diagram showing bNIRS channel locations across the left and right temporal lobes

7.2.3 Data pre-processing

The quality of the bNIRS data were initially assessed before further analysis was performed, including assessment of the raw intensity spectra and the implementation of residual analysis to check the validity of using the three-chromophore fit model to derive concentration changes. Eight channels were discarded from further analysis. Changes in concentration of HbO_2, HHb and oxCCO were calculated using the UCLn algorithm between 770–906 nm, with the wavelength dependency of the DPF applied. A DPF of 5.15 was used based on the calculation from Duncan et al. (1996) at 807 nm where the age of the subject is taken into account. bNIRS data were resampled to 1 Hz using spline interpolation.

EEG data were sampled at 256 Hz and filtered to reduce low frequency noise such as movement artifacts and high frequency components such as electromyography signals. A filter constructed from a second order Butterworth filter and a zero phase filter was used and applied in cascade to promote filter stability. First a 35 Hz low-pass filter was used followed by a 0.5 Hz high-pass filter. Use of a zero phase filter helped preserve features without distorting the temporal components of the signal.

A clinical neurophysiologist reviewed the EEG data offline after acquisition using Natus NeuroWorks software and marked the start of each generalised seizure by looking at the change in the EEG activity from baseline; in this patient, even when she was not having a seizure, there were ongoing left-sided discharges. The same neurophysiologist looked at the whole EEG dataset and therefore the method of detection of the start of seizure events is consistent for this dataset. Synchronisation of the two monitoring modalities was performed as described in Section 6.3.5 and hence, the timings of the start of each generalised seizure event as identified by the EEG was used to mark the start of seizure events in the bNIRS data.

7.2.4 Analysis

Visualisation of data

The multimodal data were first assessed through visualisation of all the data. This allows the many data channels (multiple bNIRS and EEG channels) and the many seizures identified (17 during the duration of the study) to be summarised and therefore enables easier interpretation of the optical and electrical response to seizures across the brain.

To extract useful insights into the collected dataset, several analysis methods were investigated to assess the spatial heterogeneity in the cerebral response as well as looking at the relationship between the bNIRS and EEG data.

Amplitude analysis

An estimate of oxygen delivery to the tissue can be derived by looking at the mismatch between the oxygenated and deoxygenated states given by the difference between the two haemoglobin states, $\mathrm{HbD} = \mathrm{HbO_2}\text{–}\mathrm{HHb}$. Likewise, a sum of the two haemoglobin states provides a surrogate measure of the total blood volume, HbT ($\mathrm{HbO_2} + \mathrm{HHb}$). ΔHbD and ΔHbT were selected as suitable bNIRS parameters to investigate as a more intuitive representation of the physiology compared with $\Delta[\mathrm{HbO_2}]$ and Δ[HHb].

A 50 s window around the start of each generalised seizure was selected with the 20 s period before and the 30 s period after the seizure start time selected. Traces of the bNIRS parameters, ΔHbD, ΔHbT and Δ[oxCCO] for all channels were plotted during this window for each seizure. To analyse changes during seizure events, the minimum and maximum amplitudes of each bNIRS signal during this window was plotted across each channel, and times to these amplitudes from the seizure onset were assessed. This allowed the data across many channels and many seizures to be summarised to investigate any patterns that may be seizure- or location-dependent.

Spectrograms

Spectral analysis is a useful tool for characterising the frequency components of a signal whilst maintaining the dynamics. It may reveal features in the frequency domain that are not obvious in the time domain and provide additional insight into the characteristics of the signals. A spectrogram enables visualisation of the spectral components and dynamics of the signal; it is a 3D array of frequency against time, with colour denoting the power/frequency.

Correlation between bNIRS and EEG

EEG and bNIRS provide complementary data about the electrophysiological and haemodynamic and metabolic changes occurring in the brain. Correlation analysis was performed to investigate how the bNIRS and EEG are correlated during seizures.

Pearson correlation coefficients (ρ) were computed comparing the mean filtered EEG data with Δ[HbO$_2$]. A moving average filter was applied to the mean filtered EEG data followed by the area under the curve of the absolute EEG values. A correlation was performed with EEG area under the curve values per second and changes in [HbO$_2$] per second. A window of 13 s was used to determine the correlation relative to the detection time. This analysis was done for one location, L2, where the haemodynamic response was fairly consistent across each seizure and this was compared with the EEG nearest to this bNIRS location, F3. Δ[HbO$_2$] was selected as a comparator due to the repeatable increase identified in L2.

7.3 Results

A total of 17 generalised seizures were collected over the 1 hour measurement period. The mean seizure length was 81 seconds, with a standard deviation of 37 s. Good quality bNIRS data were obtained from 8 out of 16 channels: L1, L2, L3, L4 and R1, R2, R3 and R5. The other channels were excluded from further analysis.

7.3.1 Residual analysis

Figure 7.3 shows an example of the intensity data from channel L1 before and during a seizure event and the resulting measured attenuation change. A reduction in the intensity across the spectrum can be seen during the peak change in the seizure due to the increase in total blood volume in this period. The resulting attenuation change corresponds to Δ[HbO$_2$] of $\sim 5\mu$M, Δ[HHb] of $\sim 4\mu$M and Δ[oxCCO] of ~ 0.7 μM. The red line overlayed on the measured attenuation change shows the fitted attenuation change using the 3-component model (including HbO$_2$, HHb and oxCCO). The fitted change in attenuation matches the measured change in attenuation quite closely confirming the validity of using the three component model accounting for changes in oxCCO rather than just haemoglobin changes.

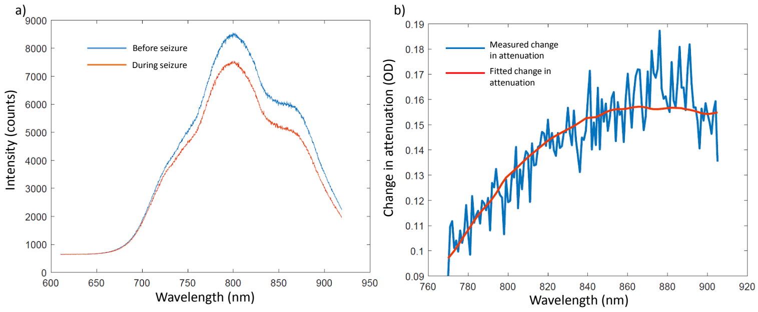

Figure 7.3: a) The measured raw intensity before the seizure and at the peak change during the seizure from channel L1 for seizure 3. A reduction in intensity across the spectrum is observed. b) The resulting measured attenuation change shown in blue with the red line showing the fitted attenuation changes using the 3-component fitting procedure

7.3.2 Summary of data collected

An overview of the bNIRS concentration changes, $\Delta[HbO_2]$, $\Delta[HHb]$ and $\Delta[oxCCO]$, for all the channels during the 1 hour monitoring duration is shown in Figure 7.4. The bNIRS data shown are unfiltered; note the different scales on the y-axis to enable changes to be clearly seen. The vertical lines represent the start of a generalised seizure, with 17 seizures observed in total, as identified from the EEG data.

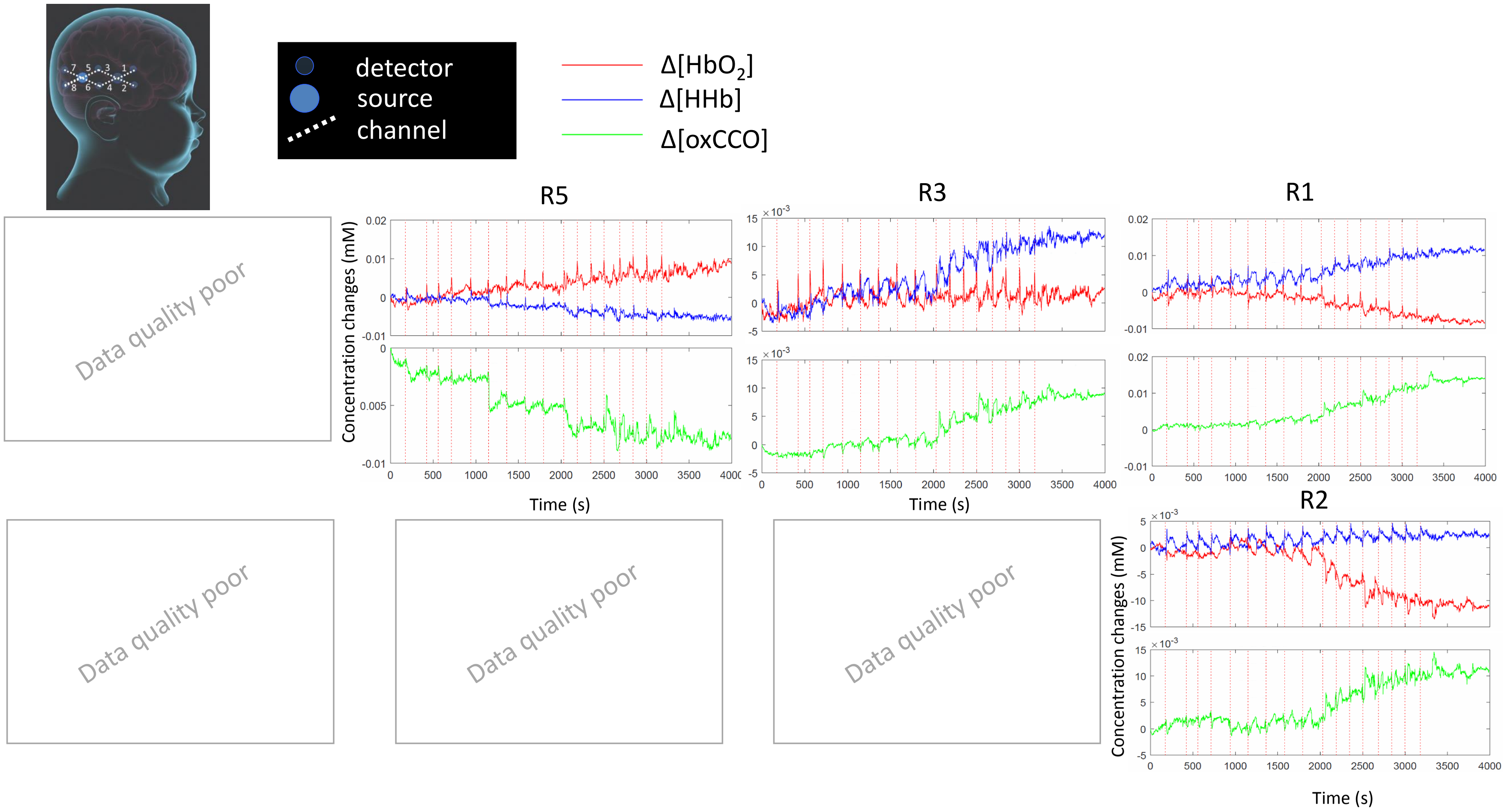
7 5 3 1
8 6 4 2
detector
source
channel
Δ[HbO₂]
Δ[HHb]
Δ[oxCCO]
R5
R3
R1
R2
Concentration changes (mM)
Time (s)
× 10⁻³
0.02
0.01
0
-0.01
0.005
15
10
5
-5
-10
-15
500
1000
1500
2000
2500
3000
3500
4000
Data quality poor
Data quality poor
Data quality poor
Data quality poor

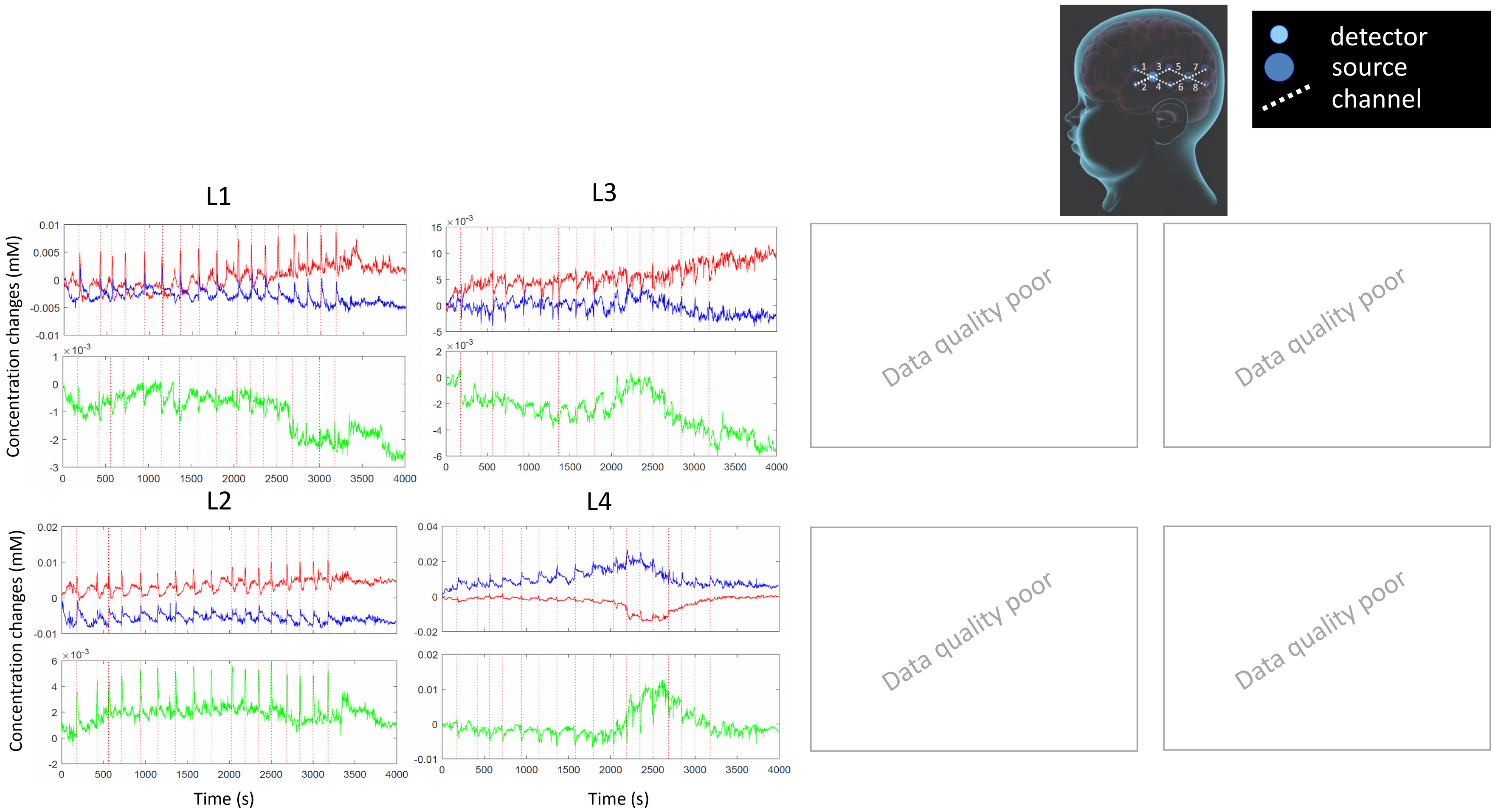

Figure 7.4: Concentration changes in $\Delta[HbO_2]$, $\Delta[HHb]$ and $\Delta[oxCCO]$ during the 60 minute monitoring duration for all channels are shown here. Vertical lines indicate the start of a generalised seizure as identified by the EEG. Each channel location is shown overlayed on a diagram of a child's head; a symmetric configuration was used such that channel 1 on the right hemisphere (R1) and channel 1 on the left hemisphere (L1) correspond to the same location on each hemisphere

An overview of the EEG changes is shown in Figure 7.5. The closest four EEG electrodes to the 8 bNIRS channels, F3, F4, C3 and C4, are displayed here and selected for further analysis. The locations of these electrodes are shown circled in green in the diagram of the electrode configuration. The filtered EEG is shown with vertical lines representing the start of a seizure.

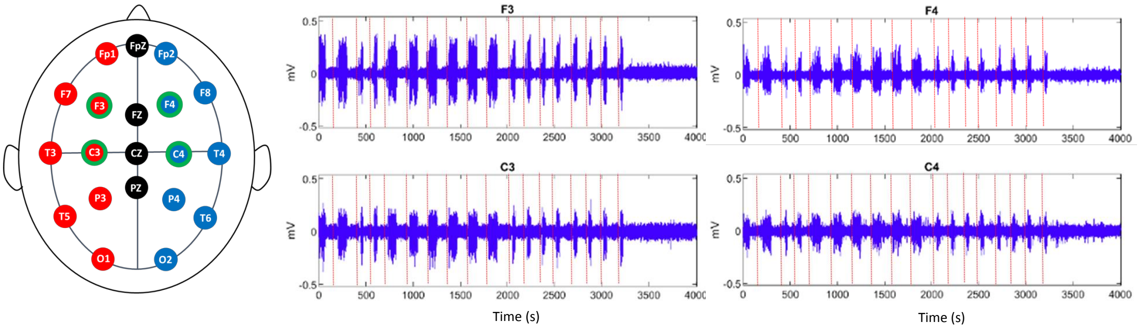

Figure 7.5: Graph showing the filtered EEG traces over the duration of the study. Vertical lines indicate start of generalised seizure events as identified by the neurophysiologist

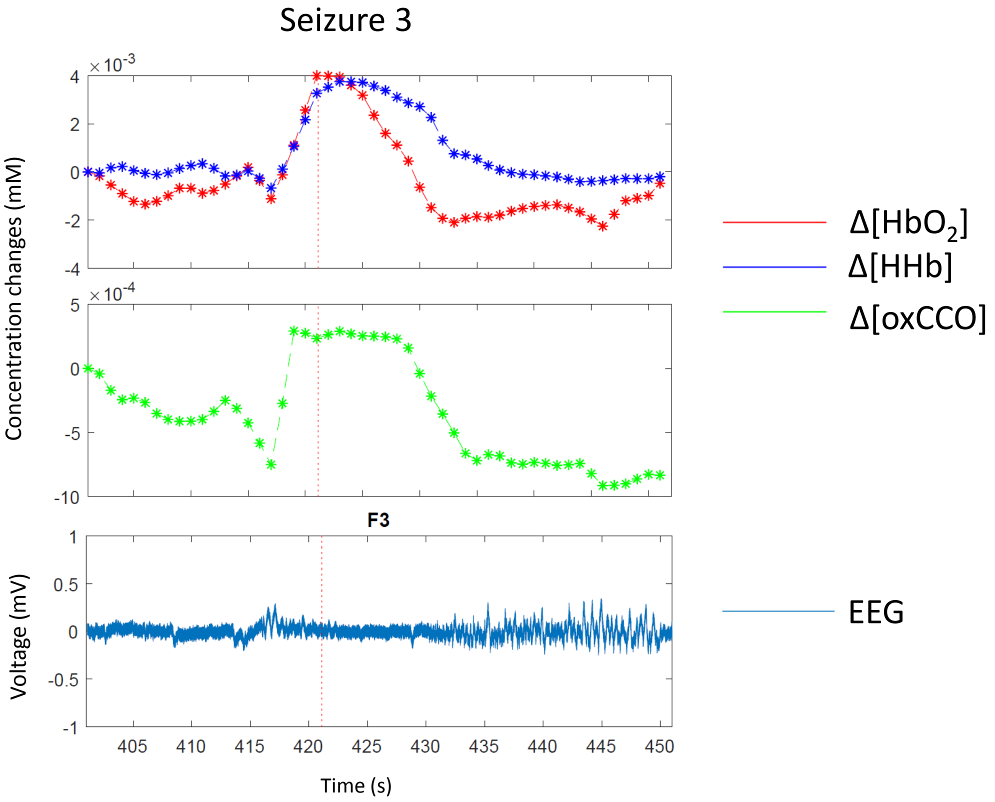

Figure 7.6: Graph showing a portion of the collected NIRS and EEG data from seizure 3. Top panel shows $\Delta[HbO_2]$ in red and $\Delta[HHb]$ in blue, middle panel shows $\Delta[oxCCO]$ in green and bottom panel shows the EEG trace over region F3. Vertical lines indicate start of generalised seizure events as identified by the neurophysiologist

7.3.3 Amplitude analysis

An example of the data for one seizure is shown in Figure 7.7 where a 50 s window showing changes in ΔHbD, ΔHbT and Δ[oxCCO] is shown as well as EEG data from electrode F3. The bNIRS data are shown separated by left and right hemispheres. Changes in HbD are fairly consistent between the hemipsheres with an increase initially seen at the onset of the seizure followed an undershoot before a return to baseline. Changes in HbT show a less consistent response compared with HbD with some variation in the amplitudes between the different channels although the trend of the signal appears similar between hemispheres. A difference in the oxCCO response can be seen between the two hemispheres for some of the channels, with both positive and negative responses observed.

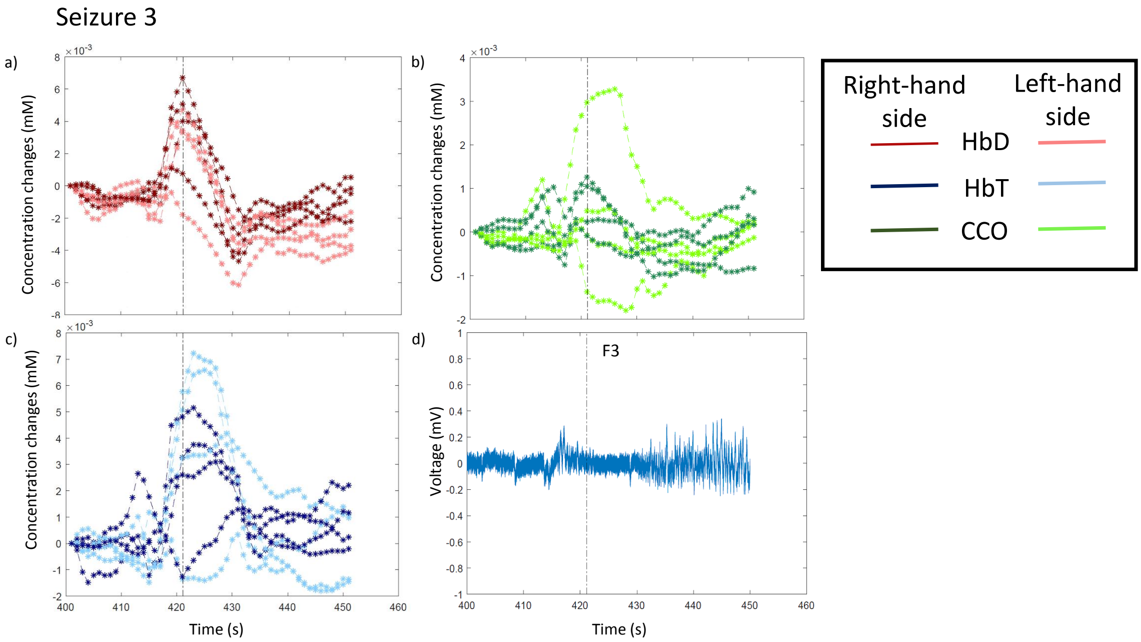

Figure 7.7: Example of traces showing a) ΔHbD, b) ΔHbT and c) Δ[oxCCO] for all channels in seizure 3. Right hemisphere and left hemispheres traces are shown in dark and light shades respectively d) Example of EEG trace from position F3 during the same time period. The vertical line indicates the start of the seizure event as identified by the EEG

Data for all seizures were plotted as in Figure 7.7 and the minimum and maximum amplitudes were identified for each channel. Figure 7.8 and 7.9 shows the minimum and maximum amplitudes identified with respect to bNIRS channel with data from each seizure plotted separately. Data are separated by right and left hemispheres. It is noted that the EEG detection time, as identified by the neurophysiologist, appears a few seconds after an initial increase in the EEG that appears to align with the start of the changes in the bNIRS data. Identifying the start of a seizure from an EEG trace is complex and can be variable; it depends on a multitude of factors such as spike-waves, slow waves, fast activity and rhythmic activity, and also depends on the patient and type of seizure. For this patient, the start of the fast rhythmic activity was used to identify the seizure start time.

Data for the minimum amplitudes for ΔHbD show a reasonably consistent range of amplitudes across channels. The largest magnitude change is seen at L4, with a minimum of -12.9 μM. A small and consistent range in amplitudes is seen for ΔHbT. Δ[oxCCO] show a fairly small range in amplitudes across the channels and also across the seizures with the exception of channel L4, where the amplitudes range from -1.8 μM to -8.9 μM. This suggests that the minimum metabolic response at L4 differs from the other spatial locations, indicating an energetic deficiency at this location. This region corresponds to the left cortical maformation as identified in the MRI.

Data for the maximum amplitudes show a more consistent response for certain channels compared with the minimum amplitudes. For ΔHbD, the range of amplitudes across seizures is fairly consistent with some variation in amplitude occurring across channel location. However, the response appears to be consistent across channel location, with a maximum amplitude of 8.7 μM. Maximum amplitudes for ΔHbT show quite a small range in amplitudes across seizures. This is particularly evident in channels R1, R2, L1, L2 and L3 indicating a consistent peak blood volume across these different locations. A larger range in maximum amplitudes is seen for Δ[oxCCO] for the right hemisphere compared with the left hemisphere. Two seizures have much larger amplitudes at L4 compared with other seizures at this location indicating the variability between seizure events.

The time to minimum and maximum amplitudes from the seizure start was also assessed but is not shown here. No pattern in the time to amplitudes was seen although it is noted that times were both positive and negative as peak changes were seen both before and after the seizure start time.

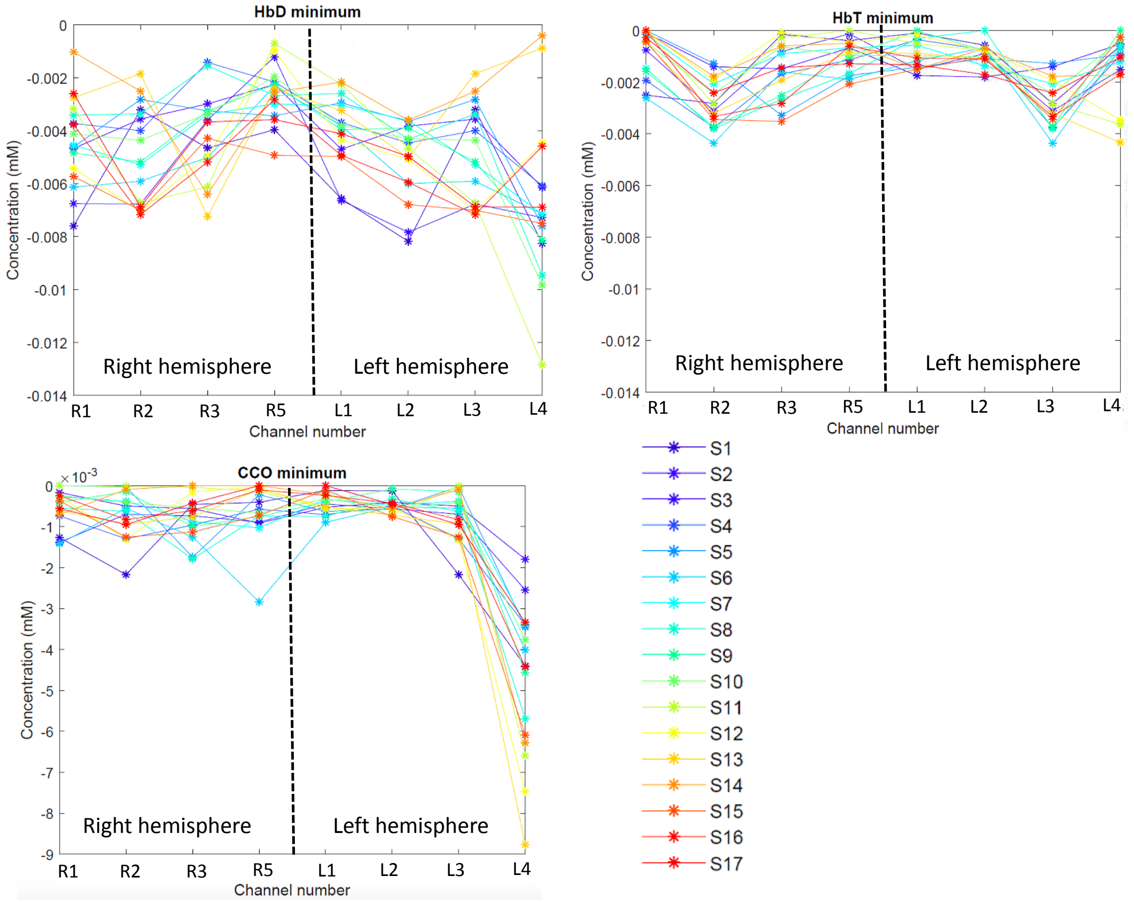

Figure 7.8: Graphs showing minimum amplitudes during 50 second seizure period for each channel, separated by left and right hemispheres. Each seizure number is shown in a different colour

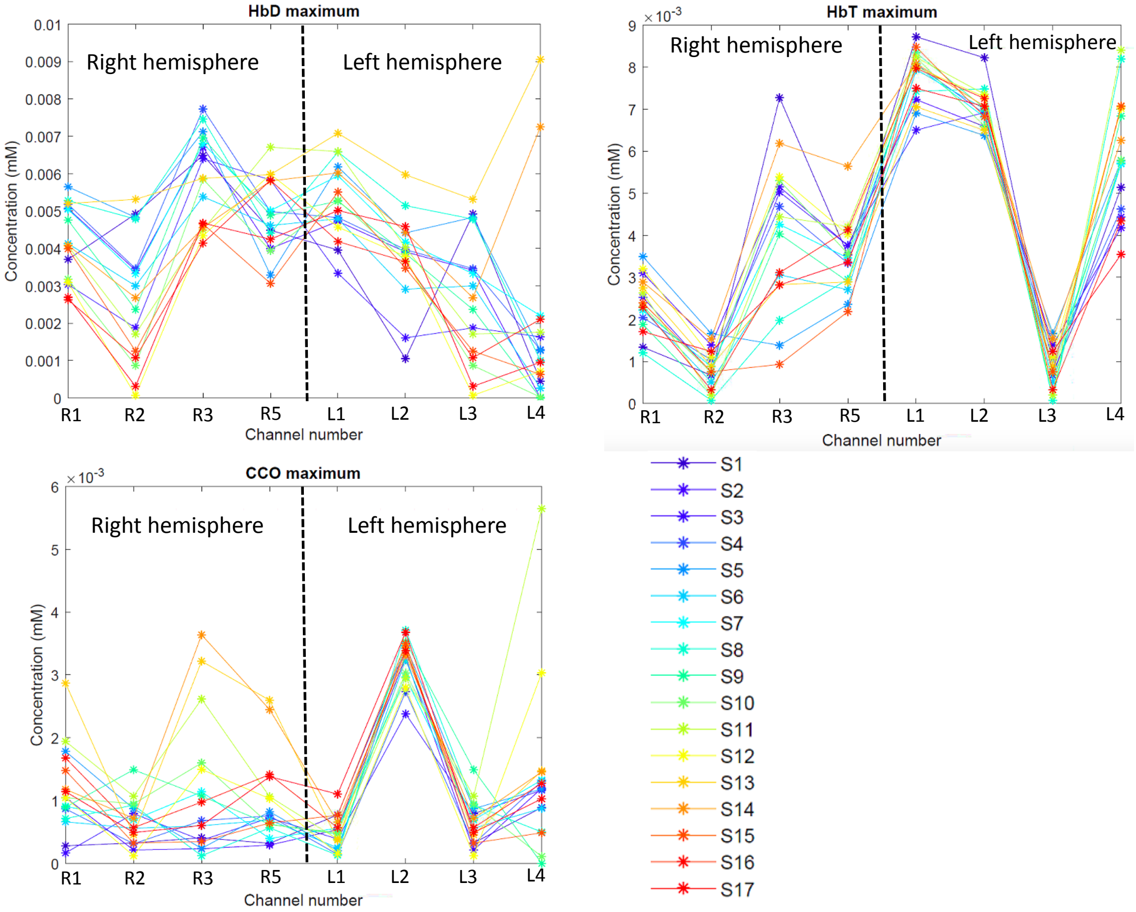

Figure 7.9: Graphs showing maximum amplitudes during 50 second seizure period for each channel, separated by left and right hemispheres. Each seizure number is shown in a different colour

7.3.4 Spectrogram analysis

For the further analyses presented, bNIRS data were filtered in order to eliminate the drift seen in Figure 7.4 and reduce noise while maintaining trends. A band pass filter was used between 0.02 Hz to reduce very slow drifts and 0.5 Hz to reduce low frequency drift and cardiac oscillations. Figure 7.11 shows the filtered $\Delta[\text{HbO}_2]$, Δ[HHb] and Δ[oxCCO] showing the overall features maintained, with the peaks at the seizures still visible.

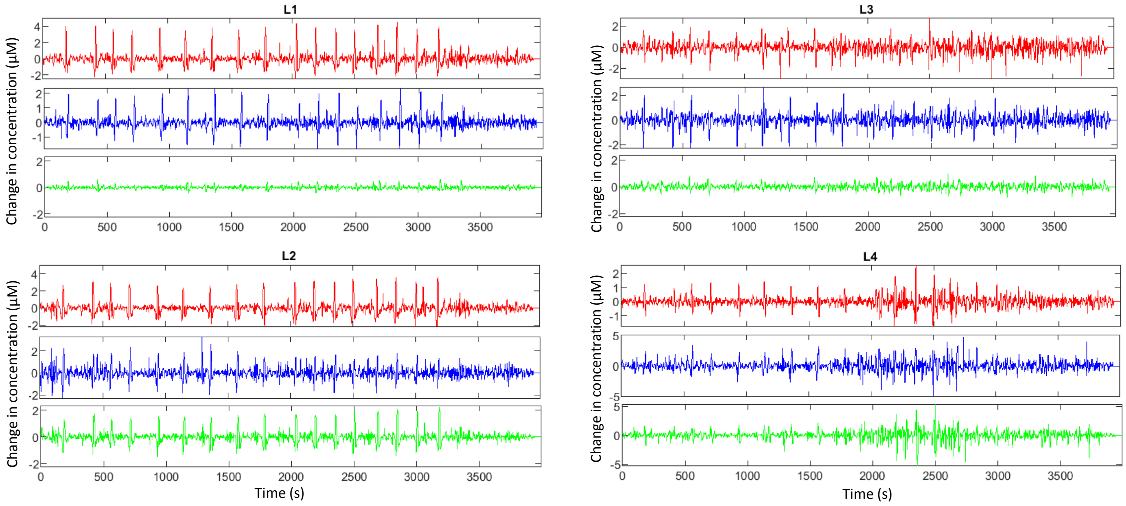

Figure 7.10: Filtered bNIRS data showing channels from the left hemisphere for regions L1, L2, L3 and L4. $\Delta[HbO_2]$ is shown in red, $\Delta[HHb]$ in blue and $\Delta[oxCCO]$ in green

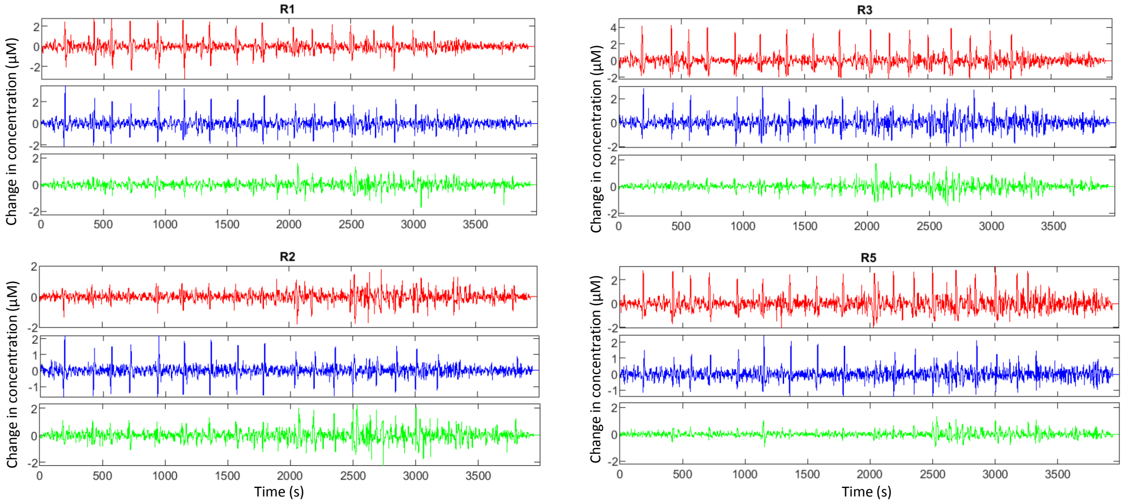

Figure 7.11: Filtered bNIRS data showing channels from the right hemisphere for regions R1, R2, R3 and R5. $\Delta[HbO_2]$ is shown in red, $\Delta[HHb]$ in blue and $\Delta[oxCCO]$ in green

The spectrograms for the four EEG electrodes nearest to the bNIRS channels is shown in Figure 7.12. The power/frequency (dB/Hz) appears greater at F3 than at other locations as indicated by the yellow regions, which correspond to higher power. The seizure periods can be seen in electrode F3, denoted by the low frequency, distinct yellow triangles. These high power bursts depicting each seizure event can also be seen at other EEG locations, although they are not always prominent for every seizure.

The spectrograms for the bNIRS channels are shown for $\Delta[\mathrm{HbO_2}]$ and $\Delta[\mathrm{oxCCO}]$ in Figures 7.13 and 7.14. The EEG electrode at F3 is nearest to bNIRS channels L1 and L2 hence it is expected that these channels should be under more stress. This can be seen for the $\Delta[\mathrm{HbO_2}]$ spectrogram at these positions where high power regions are distinct, indicative of each seizure. Similar distinct regions can be seen in channels R1 and R3 where the number of seizures can be counted looking at the high power yellow peaks. Other channels such as L4 show a large proportion of the total distinct regions and 12/17 seizures can be identified here. Similarly, looking at the $\Delta[\mathrm{oxCCO}]$ spectrogram, the 17 seizures can easily be identified at channels L1 and L2, suggesting a greater metabolic demand of the tissue in these locations compared with other bNIRS locations.

Overall, it appears that the seizures are more visible in the bNIRS $\Delta[\mathrm{HbO_2}]$ spectrograms compared with the EEG spectrograms, indicating the potential for bNIRS as a method for detecting seizures. This is of interest in certain populations, such as neonates, where seizures can be clinically difficult to identify and clinical manifestations of seizures may not be obvious (Hellström-Westas (2018)). Furthermore, there have been instances where clinical seizures do not have corresponding electrographic seizure activity and subtle seizures may pass undetected (Pinto and Giliberti (2001)).

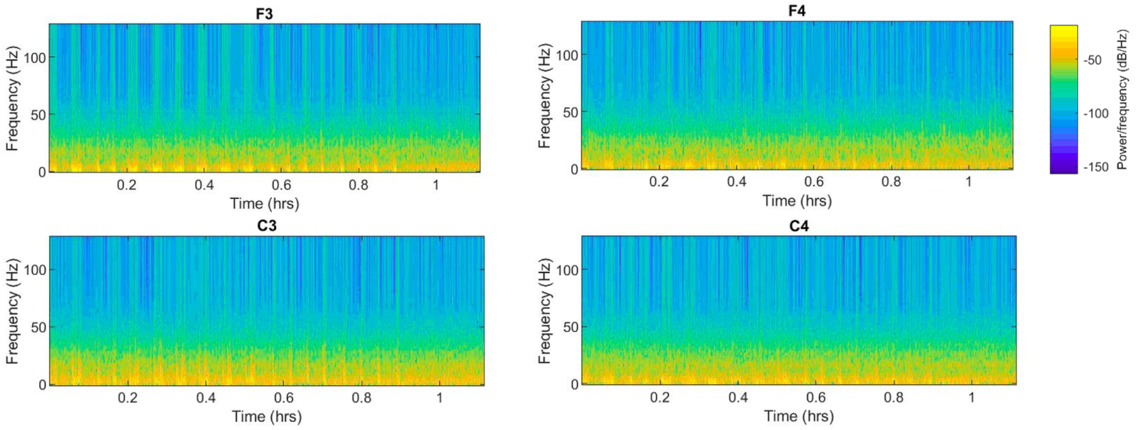

Figure 7.12: Spectrograms for the EEG at locations F3, C3, F4 and C4 over the monitoring period

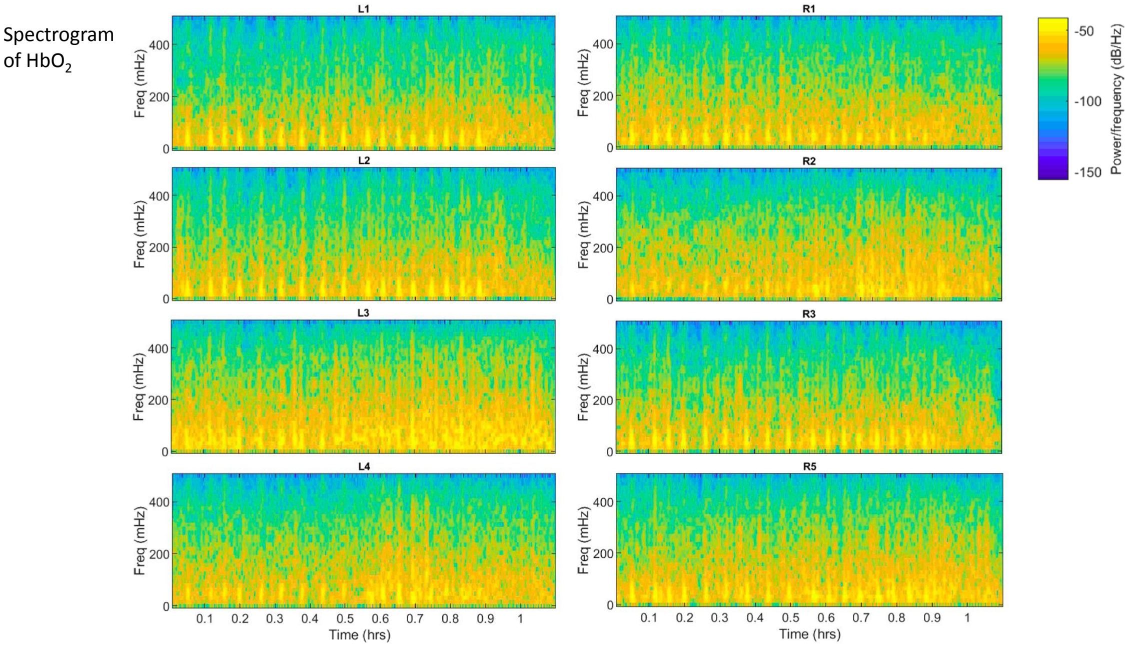

Figure 7.13: Spectrograms for bNIRS-monitored Δ[HbO$_2$] at all channels over the monitoring period

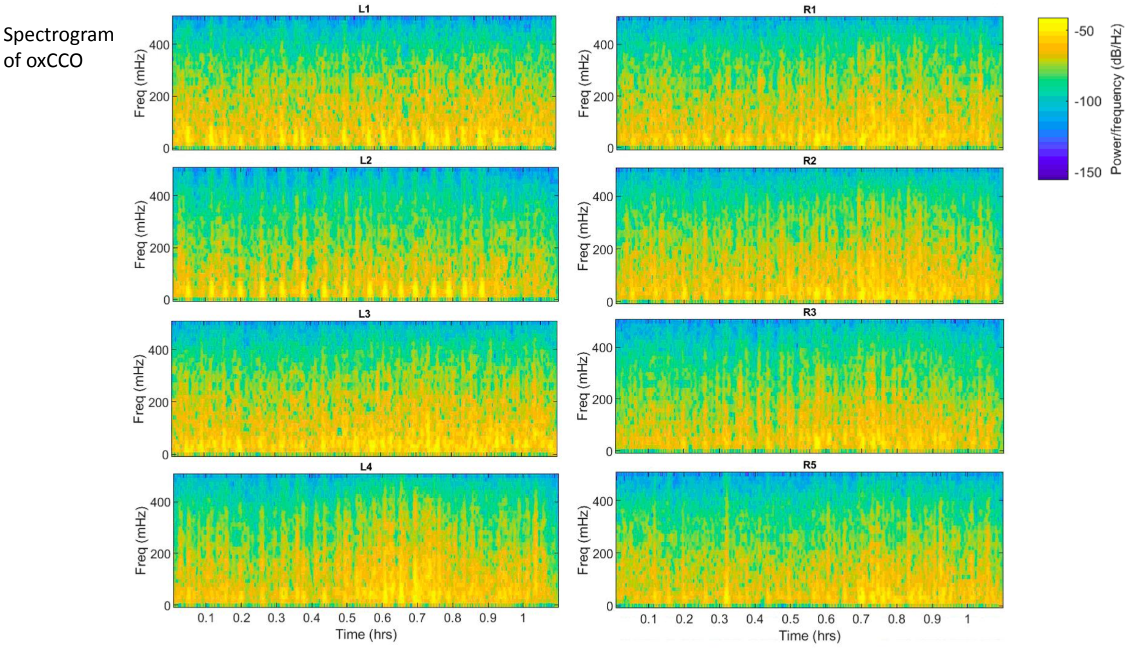

Figure 7.14: Spectrograms for bNIRS-monitored Δ[oxCCO] at all channels over the monitoring period

7.3.5 Correlation analysis

Figure 7.15 shows the results of the correlation analysis between the absolute area under the curve of the EEG at F3 and the Δ[HbO$_2$] trace at L2. The relationship between ictal electrical activity and cerebral haemodynamics remains unclear. It can be seen from the EEG-identified seizure events that there are temporally matching bNIRS changes, with clear changes in the bNIRS parameters observed around the start of the seizure events. With simultaneous EEG and bNIRS recording, the signal correlation provides a method to robustly detect neural processes such as during a seizure as a correlation between electrical and haemodynamic changes is expected.

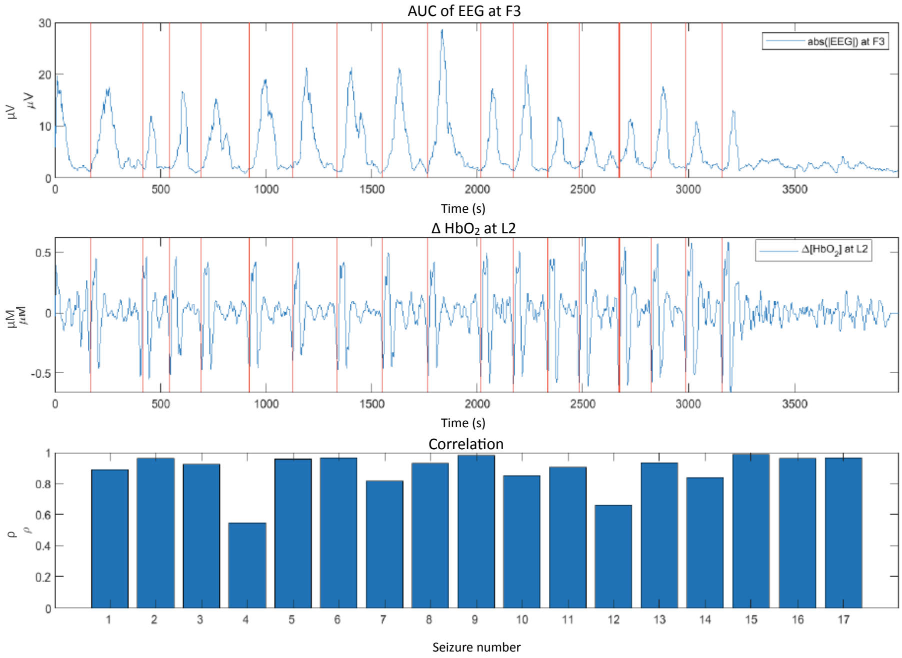

Figure 7.15: Correlation of EEG at F3 with bNIRS-measured $\Delta[HbO_2]$ at L2. a) The absolute area under curve of the electrical signal as measured by the EEG at F3. b) The bNIRS-measured change in concentration of HbO_2 at location L2. c) The correlation between the EEG at F3 and $\Delta[HbO_2]$ at L2 as determined using a Pearson coefficient across each seizure

7.3.6 Discussion and conclusion

In this chapter, a multi-channel bNIRS system developed as part of this PhD was used in a clinical setting. Data from one patient with recurrent seizures are presented here together with EEG, a complementary neuromonitoring technique that is part of standard routine monitoring for epilepsy patients. The use of the system in this clinical environment was demonstrated as a feasible method to monitor brain injury in a child, where observable changes in the haemodynamics and metabolism during seizures were identified. Multiple channels enabled variations in these parameters to be observed at different cerebral locations, which is of particular relevance in this patient where the seizures focalised in the left hemisphere before generalising to across the brain. A large decrease in metabolism was observed in location L4, in the left posterior region, the same region as the cortical malformation seen in the MRI. This large metabolic decrease was not observed at other spatial locations, suggesting an energetic deficiency in this region. Furthermore, simultaneous monitoring with EEG provided additional information that enabled a better understanding of these two combined neuromonitoring techniques and the correlation between the electrical, haemodynamic and cellular responses to seizure events. A number of different methods of analysis were used to explore the regional heterogeneity of the haemodynamic and metabolic response during seizures.

EEG is used as a standard part of routine care in patients with epilepsy. However, NIRS is able to provide complementary and additional information to EEG alone as it provides an insight into the haemodynamic response of the brain to seizures. Furthermore, use of a broadband NIRS systems enables monitoring of the metabolic response during seizures, which provides further information in how the brain is coping with such seizure events. The relation between cerebral oxygenation and oxygen utilisation may be able to predict outcome by assessing the capacity of the brain to buffer such sudden bursts of activity and identify seizures that may be exacerbating brain injury. The combined use of bNIRS and EEG may therefore be a useful tool in monitoring brain injury in epilepsy patients.

CHAPTER 8

Conclusion

This thesis has presented the development of the next-generation broadband NIRS device and demonstrated the use of the system in healthy adult volunteers and in the clinic to monitor seizures in children with epilepsy. This chapter will summarise the work presented in this thesis and suggest future areas of research that have arisen from this work.

8.1 Summary

This thesis has presented the development of a multi-channel broadband NIRS system capable of monitoring changes in concentration of HbO_2, HHb and oxCCO with the aim of using it to monitor cerebral changes in infants and young children.

8.1.1 Development of instrumentation

The development of the instrumentation consisted of upgrading the hardware to the latest available technology and software to integrate further functionality into the device. Two miniature light sources with time-multiplexed switching capabilities were utilised to maximise the number of available channels, providing four source fibre bundles. A spectrograph with a 308 nm bandwidth was used with a CCD with an imaging chip size of 26.8 mm x 26 mm, enabling a wavelength range between 610 nm − 918 nm and a total capacity of imaging 12 detector fibre bundles simultaneously. A variety of probe holders were designed to house the optical fibre bundles across different subjects and experimental conditions. Software was upgraded to handle the larger number of fibre bundles without losing data, implement the switching mechanism and calculate and display the concentration changes in real time. Several issues were encountered during the development of the system that had to be overcome: the hardware affecting the cooling of the CCD was fixed, the cross-talk between adjacent detector fibre bundles was reduced and hardware modifications were made to adapt to the reduced expected capacity of the the CCD imaging array. Overall, the system has been used to monitor the frontal cortex of young children and adults with 8 channels and the temporal lobe of an infant 3 years of age with up to 16 channels. The configuration of the large number of source and detector fibre bundles can be adapted to maximise the number of channels across the head. The frequency of collection is 0.5 Hz.

8.1.2 Functional activation studies in adults

The system was used in healthy adult volunteers to test the capacity and limitations of the system in measuring cerebral changes in the adult head. A visual task monitoring changes over the occipital lobe was used to produce repeatable and large induced physiological changes; however, it was found that the impact of hair was significant and a good quality optical data could not be obtained even in the patients with very light coloured hair. A secondary task to monitor the response of Δ[oxCCO] over multiple channels in the prefrontal cortex during a Stroop task was also used. The advantage of monitoring over the frontal lobe is the lack of hair in this region, enabling a good quality optical signal to be obtained. A significant increase in Δ[oxCCO] was seen in five of 16 channels alongside the typical haemodynamic response of an increase in $\Delta[HbO_2]$ and decrease in Δ[HHb]. This corroborates recent work by Phan et al. (2016b) who saw an increase in Δ[oxCCO] at certain locations suggesting the spatial variation in the response of this chromophore. Although the development of this system was aimed towards younger subjects, there is potential to utilise this device to monitor changes in the frontal lobe, where the response of Δ[oxCCO] is of particular interest during functional activation as a potentially more robust, brain specific marker of functional activation (Kolyva et al. (2014), de Roever et al. (2016)).

8.1.3 Monitoring epilepsy patients in the clinic

The system was deployed at Great Ormond Street Hospital to monitor young children with epilepsy who were experiencing daily seizures. This collaborative work between BORL and clinicians at GOSH enabled data collection from a total of 12 patients with 8 channels, with the majority of changes monitored in the frontal lobe. This was to demonstrate the viability of the system in a clinical setting alongside simultaneous and complementary monitoring with EEG. The majority of patients had absence seizures, lasting only a few seconds, and were therefore not of long enough duration to induce haemodynamic changes. One patient had multiple recurrent seizures where clear changes in the NIRS and EEG data were observed. Furthermore, this patient was monitored over the temporal lobes and allowed monitoring close to the focal origin of the seizures on the left posterior hemisphere. Spectrographic analysis showed clear changes in $\Delta[\mathrm{HbO_2}]$ during each seizure, which were clearer than the spectrographic images of the EEG, suggesting the potential of NIRS as a detection tool for seizures. A number of analysis techniques were applied to investigate the response of Δ[oxCCO] during seizures across multiple locations in this patient to showcase the potential of such a device to monitor cerebral metabolism during seizures. This marker of metabolism may be able to provide additional insight into the impact of seizures on the brain and how the brain is coping with repeated and prolonged seizures.

8.1.4 Discussion

The broadband, multi-channel NIRS device developed as part of this thesis has demonstrated a number of applications in monitoring induced functional changes in the healthy adult brain as well as changes during seizures in children with epilepsy, revealing the response in brain-injury. Not only can the vascular, haemodynamic changes be monitored, leading to information about changes in cerebral oxygenation, HbD, and blood volume, HbT, the cellular activity due to changes in metabolic marker, CCO, can be monitored allowing insight into oxygen utlisation at a cellular level. This is of particular interest in cases of brain injury, where oxygen supply and use can indicate the functioning of the brain and may be able to provide information on overall brain health in individual patients.

8.2 Further work

This thesis has described the application of the system in healthy adult volunteers and in young children with epilepsy. There are several avenues of further work that have arisen as a result of the work presented in this thesis, with additional analysis techniques and clinical applications that can be explored.

8.2.1 Image reconstruction methods

As this system has two sets of switching sources and multiple detectors, there is capacity for the system to be used with image reconstruction techniques so that the spatial changes in haemodynamics and metabolism can be visualised in a three-dimensional image. This method for utilising multiple channels is known as diffuse optical tomography and has the advantage of enabling clear visualisation of spatially resolved changes that is easier to understand than channel-wise analysis, which becomes increasingly complicated for increasing channel number. Diffuse optical tomography consists of modelling the transport of light in tissue, based on the optical properties of the tissue and, from this, predicting the distribution of light in the subject being monitored. This produces a sensitivity matrix of light which can be used in solving the inverse problem, where these model parameters are used to back-calculate the image of the distribution of chromophores. These images can provide information about localised changes in physiological parameters and can provide a different approach for analysing NIRS parameters.

8.2.2 Further investigation into monitoring seizures in epilepsy

This system has been developed for neonates and young children and has potential use in various clinical applications. In this thesis, it has been demonstrated in children with epilepsy. Whilst absence seizures did not show any obvious haemodynamic and metabolic changes, one patient with recurrent seizures that lasted longer than a few seconds did induce visible changes in the NIRS parameters. Variable changes were seen between the hemispheres, with some interesting changes in cerebral metabolism observed at some spatial locations. Further investigation of this response across multiple locations is desirable to enable comparison of this response between subjects, which may provide further insight into the potential of NIRS-measured Δ[oxCCO] as an indicator of brain health in these brain-injured patients. It is predicted that prolonged or repeated seizures may cause further brain injury; investigation of the metabolism during these seizures may provide useful information to how the brain is coping during these events in individual seizures.

8.2.3 Applications in patients with hypoxic ischaemic encephalopathy (HIE)

Another avenue of further work is in patients with hypoxic ischaemic encephalopathy. HIE is a condition that affects 1–2 per 1000 live births and occurs when there is a restriction of blood and therefore oxygen to the brain. The use of broadband NIRS has been demonstrated in this cohort during spontaneous oxygen desaturation events where a consistent negative change in cerebral oxygenation, Δ[HbD], and metabolism, Δ[oxCCO], was found and an increase in total blood volume, Δ[HbT] (Bale et al. (2014b)). The results showed interesting results between mild and severe HIE; however, a disadvantage is the random and spontaneous nature of the events. Furthermore, the study only looked at two locations over the frontal lobe. A study that uses a repeatable, controlled event such as the induced changes as a result of a functional stimulus, would allow the responses across subjects to be compared with less heterogeneity than with spontaneous events. Functional studies in neonates have previously shown a mixed haemodynamic response. It may be that monitoring changes in oxCCO, a more brain-specific marker, can reveal additional information into the mechanisms behind this heterogeneous response in this cohort. Investigation into the functional response following perinatal brain injury may relate to injury severity and future outcome. Furthermore, monitoring across the entire head could be performed with the current system to investigate the role of CCO in the assessment of brain health. The system is set to go to UCL hospital later this year to start on these studies.

Bibliography

Abboub, N., T. Nazzi, and J. Gervain
2016. Prosodic grouping at birth. *Brain Lang.*, 162:46–59.

Al-Rawi, P. G., P. Smielewski, and P. J. Kirkpatrick
2001. Evaluation of a near-infrared spectrometer (NIRO 300) for the detection of intracranial oxygenation changes in the adult head. *Stroke*, 32(11):2492–2500.

Anderson, A. A., E. Smith, F. A. Chowdhry, A. Thurm, E. Condy, L. Swineford, S. S. Manwaring, F. Amyot, D. Matthews, and A. H. Gandjbakhche
2017. Prefrontal hemodynamics in toddlers at rest: A pilot study of developmental variability. *Front. Neurosci.*, 11(MAY):1–10.

Anderson, A. W., R. Marois, E. R. Colson, B. S. Peterson, C. C. Duncan, R. A. Ehrenkranz, K. C. Schneider, J. C. Gore, and L. R. Ment
2001. Neonatal auditory activation detected by functional magnetic resonance imaging. *Magn. Reson. Imaging*, 19(1):1–5.

Aoyama, S., T. Toshima, Y. Saito, N. Konishi, K. Motoshige, N. Ishikawa, K. Nakamura, and M. Kobayashi
2010. Maternal breast milk odour induces frontal lobe activation in neonates: A NIRS study. *Early Hum. Dev.*, 86(9):541–545.

Arichi, T., G. Fagiolo, M. Varela, A. Melendez-Calderon, A. Allievi, N. Merchant, N. Tusor, S. J. Counsell, E. Burdet, C. F. Beckmann, and A. D. Edwards
2012. Development of BOLD signal hemodynamic responses in the human brain. *Neuroimage*, 63(2):663–673.

Arichi, T., A. Moraux, A. Melendez, V. Doria, M. Groppo, N. Merchant, S. Combs, E. Burdet, D. J. Larkman, S. J. Counsell, C. F. Beckmann, and A. D. Edwards
2009. Somatosensory cortical activation identified by functional MRI in preterm and term infants. *Neuroimage*, 49(3):2063–2071.

Arifler, D., T. Zhu, S. Madaan, and I. Tachtsidis

2015. Optimal wavelength combinations for near-infrared spectroscopic monitoring of changes in brain tissue hemoglobin and cytochrome c oxidase concentrations. *Biomed. Opt. Express*, 6(3):933.

Arimitsu, T., Y. Minagawa, T. Yagihashi, M. Uchida-ota, A. Matsuzaki, K. Ikeda, and T. Takahashi

2018. The cerebral hemodynamic response to phonetic changes of speech in preterm and term infants: The impact of postmenstrual age. *NeuroImage Clin.*, 19(October 2017):599–606.

Arimitsu, T., M. Uchida-Ota, T. Yagihashi, S. Kojima, S. Watanabe, I. Hokuto, K. Ikeda, T. Takahashi, and Y. Minagawa-Kawai

2011. Functional hemispheric specialization in processing phonemic and prosodic auditory changes in neonates. *Front. Psychol.*, 2(SEP):1–10.

Aslin, R. N.

2012. Questioning the questions that have been asked about the infant brain using near-infrared spectroscopy. *Cogn. Neuropsychol.*, 29(1-2):7–33.

Azevedo, F. A. C., L. R. B. Carvalho, L. T. Grinberg, J. M. Farfel, R. E. L. Ferretti, R. E. P. Leite, W. J. Filho, R. Lent, and S. Herculano-Houzel

2009. Equal numbers of neuronal and nonneuronal cells make the human brain an isometrically scaled-up primate brain. *J. Comp. Neurol.*, 513(5):532–541.

Bale, G., C. E. Elwell, and I. Tachtsidis

2016. From Jöbsis to the present day: a review of clinical near-infrared spectroscopy measurements of cerebral cytochrome-c-oxidase. *J. Biomed. Opt.*, 21(9):091307–1 – 091307–18.

Bale, G., S. Mitra, J. Meek, and N. Robertson

2014a. A new broadband near-infrared spectroscopy system for in-vivo measurements of cerebral cytochrome-c-oxidase changes in neonatal brain injury. *Biomed. Opt. Express*, 5(10):663–676.

Bale, G., S. Mitra, J. Meek, N. Robertson, and I. Tachtsidis

2014b. CP: In-vivo measurements of cerebral changes in cytochrome- c-oxidase using broadband near-infrared spectroscopy in perinatal hypoxic-ischaemic encephalopathy. In *Biomed. Opt.*

Bale, G. M.

2016. *Development of Optical Instrumentation and Methods to Monitor Brain Oxygen Metabolism : Application to Neonatal Brain Injury.* PhD thesis, UCL.

Banich, M. T., M. P. Milham, R. Atchley, N. J. Cohen, A. Webb, T. Wszalek, A. F. Kramer, Z. P.

Liang, A. Wright, J. Shenker, and R. Magin

2000. fMri studies of Stroop tasks reveal unique roles of anterior and posterior brain systems in attentional selection. *J. Cogn. Neurosci.*, 12(6):988–1000.

Bardouille, T., L. Bailey, and C. Group

2019. NeuroImage Evidence for age-related changes in sensorimotor neuromagnetic responses during cued button pressing in a large open-access dataset. *Neuroimage*, 193:25–34.

Bartocci, M., J. Winberg, C. Ruggiero, L. L. Bergqvist, G. Serra, and H. Lagercrantz

2000. Activation of olfactory cortex in newborn infants after odor stimulation: A functional near-infrared spectroscopy study. *Pediatr. Res.*, 48(1):18–23.

Beckman, A.

2016. Diffuse Optical Spectroscopy and Imaging Lab.

Bembich, S., R. Davanzo, P. Brovedani, A. Clarici, S. Massaccesi, and S. Demarini

2013. Functional neuroimaging of breastfeeding analgesia by multichannel near-infrared spectroscopy. *Neonatology*, 104(4):255–259.

Benavides-Varela, S., D. M. Gómez, and J. Mehler

2011. Studying neonates' language and memory capacities with functional near-infrared spectroscopy. *Front. Psychol.*, 2(APR):1–5.

Benavides-Varela, S., J.-R. Hochmann, F. Macagno, M. Nespor, and J. Mehler

2012. Newborn's brain activity signals the origin of word memories. *Proc. Natl. Acad. Sci.*, 109(44):17908–17913.

Biallas, M., I. Trajkovic, C. Hagmann, F. Scholkmann, J. Carmen, L. Holper, and A. Beck

2012. Multimodal recording of brain activity in term newborns during photic stimulation by near-infrared spectroscopy and electroencephalography. *J. Biomed. Opt.*, 17(8):086011.

Blackwood, D. H. and W. J. Muir

1990. Cognitive brain potentials and their application. *Br. J. Psychiatry*, 157(DEC. SUPPL. 9):96–101.

Blum, T., E. Saling, and R. Bauer

1985. First magnetoencephalographic recordings of the brain activity of a human fetus. *Br. J. Obstet. Gynaecol.*, 92:1224–1229.

Born, P., H. Leth, M. Miranda, E. Rostrup, A. Stensgaard, B. Peitersen, H. Larsson, and H. Lou

1998. Visual Activation in Infants and Young Children Studied by Functional Magnetic Resonance Imaging. *Paediatr. Res.*, 44:578–583.

Born, P., E. Rostrup, H. Larsson, H. Leth, B. Peitersen, and H. Lou

1996. Changing pattern of visually induced fMRI response during human development. *Int. Soc. Magn. Reson. Med. Sci. Meet. Exhib. York, New York.*, (April 27-May 3):1860.

Boto, E., N. Holmes, J. Leggett, G. Roberts, and M. Brookes

2018. Moving magnetoencephalography towards real-world applications with a wearable system. *Nat. Lett.*, 555:657–661.

Bouchon, C., T. Nazzi, and J. Gervain

2015. Hemispheric asymmetries in repetition enhancement and suppression effects in the newborn brain. *PLoS One*, 10(10):1–17.

Braeutigam, S.

2013. Magnetoencephalography: Fundamentals and Established and Emerging Clinical Applications in Radiology. *ISRN Radiol.*, 2013:1–18.

Brazy, J. E. and D. V. Lewis

1986. Changes in cerebral blood volume and cytochrome aa3 during hypertensive peaks in preterm infants. *J. Pediatr.*, 108(6):983–987.

Brigadoi, S. and R. J. Cooper

2015. How short is short? Optimum source–detector distance for short-separation channels in functional near-infrared spectroscopy. *Neurophotonics*, 2(2):025005.

Carlier-Torres, M. E. M., T. Harmony, J. Ricardo-Garcell, J. L. Marroquín, and M. Colmenero

2014. The hemodynamic response to acoustically modified syllables in premature and full term newborn infants acquired by near infrared spectroscopy. *Acta Colomb. Psicol.*, 17(34487):13–21.

Chen, S., K. Sakatani, W. Lichty, P. Ning, S. Zhao, and H. Zuo

2002. Auditory-evoked cerebral oxygenation changes in hypoxic-ischemic encephalopathy of newborn infants monitored by near infrared spectroscopy. *Early Hum. Dev.*, 67(1-2):113–121.

Cheung, J.

2011. Neurons, Nerve Tissues, & the Nervous System.

Chudler, E.

2015. Action Potential.

Chugani, H. T., M. E. Phelps, and J. C. Mazziotta

1987. Positron emission tomography study of human brain functional development. *Ann. Neurol.*, 22(4):487–497.

Cooper, C. E., C. E. Elwell, J. H. Meek, S. J. Matcher, J. S. Wyatt, M. Cope, and D. T. Delpy
1996. The Noninvasive Measurement of Absolute Cerebral Deoxyhemoglobin Concentration and Mean Optical Path Length in the Neonatal Brain by Second Derivative Near Infrared Spectroscopy. *Pediatr. Res.*, 39:32–38.

Coulter, J.
2017. Acoustic Neuroma.

Courtney, Chelsea, Morgan, GSchilbeG, and Tessa
2013. Pyruvate Oxidation and the Krebs Cycle.

Cristia, A., Y. Minagawa, and E. Dupoux
2014. Responses to vocalizations and auditory controls in the human newborn brain. *PLoS One*, 9(12):1–23.

Cui, X., S. Bray, D. M. Bryant, G. H. Glover, and A. L. Reiss
2012. A quantitative comparison of NIRS and fMRI across multiple cognitive tasks. *Neuroimage*, 54(4):2808–2821.

de Roever, I., G. Bale, R. J. Cooper, and I. Tachtsidis
2016. Cytochrome-C-Oxidase Exhibits Higher Brain-Specificity than Haemoglobin in Functional Activation. *Oxyg. Transp. to Tissue XXXIX.*

de Roever, I., G. Bale, R. J. Cooper, and I. Tachtsidis
2017. Functional NIRS Measurement of Cytochrome-C-Oxidase Demonstrates a More Brain-Specific Marker of Frontal Lobe Activation Compared to the Haemoglobins. *Adv. Exp. Med. Biol.*, 977:141–147.

de Roever, I., G. Bale, S. Mitra, J. Meek, N. J. Robertson, and I. Tachtsidis
2018a. Investigation of the Pattern of the Hemodynamic Response as Measured by Functional Near-Infrared Spectroscopy (fNIRS) Studies in Newborns, Less Than a Month Old: A Systematic Review. *Front. Hum. Neurosci.*, 12(October).

de Roever, I., G. Bale, S. Mitra, J. Meek, N. J. Robertson, and I. Tachtsidis
2018b. Investigation of the Pattern of the Hemodynamic Response as Measured by Functional Near-Infrared Spectroscopy (fNIRS) Studies in Newborns, Less Than a Month Old: A Systematic Review. *Front. Hum. Neurosci.*, 12(October).

Doyle, L., C. Nahmias, G. Firnau, D. Kenyon, E. Garnett, and J. Sinclair
1983. Regional cerebral glucose metabolism of newborn infants measured by positron emission tomography. *Dev. Med. Child Neurol.*, 25(2):143–151.

Duncan, A., J. Meek, M. Clemence, C. Elwell, P. Fallon, L. Tyszczuk, M. Cope, and D. Delpy
1996. Measurement of Cranial Optical Path Length as a Function of Age Using Phase Resolved Near Infrared Spectroscopy. *J. Pharm. Pharmacol.*, 45(1996):595–602.

Duncan, a., J. H. Meek, M. Clemence, C. E. Elwell, L. Tyszczuk, M. Cope, and D. T. Delpy
1995. Optical pathlength measurements on adult head, calf and forearm and the head of the newborn infant using phase resolved optical spectroscopy. *Phys. Med. Biol.*, 40(2):295–304.

Dunn, K., N. Reissland, and V. M. Reid
2015. Developmental Cognitive Neuroscience The functional foetal brain : A systematic preview of methodological factors in reporting foetal visual and auditory capacity. *Accid. Anal. Prev.*, 13:43–52.

Eltze, C. M., W. K. Chong, T. Cox, A. Whitney, M. Cortina-Borja, R. F. Chin, R. C. Scott, and J. H. Cross
2013. A population-based study of newly diagnosed epilepsy in infants. *Epilepsia*, 54(3):437–445.

Ferry, A. L., A. Fló, P. Brusini, L. Cattarossi, F. Macagno, M. Nespor, and J. Mehler
2016. On the edge of language acquisition: Inherent constraints on encoding multisyllabic sequences in the neonate brain. *Dev. Sci.*, 19(3):488–503.

Frie, J., M. Bartocci, H. Lagercrantz, and P. Kuhn
2017. Cortical Responses to Alien Odors in Newborns: An fNIRS Study. *Cereb. Cortex*, 28(November):3229–3240.

Gagnon, L., R. J. Cooper, M. a. Yücel, K. L. Perdue, D. N. Greve, and D. a. Boas
2012. Short separation channel location impacts the performance of short channel regression in NIRS. *Neuroimage*, 59(3):2518–2528.

Gervain, J., I. Berent, and J. F. Werker
2012. Binding at Birth : The Newborn Brain Detects Identity Relations and Sequential Position in Speech. *J. Cogn. Neurosci.*, 24(3):564–574.

Gervain, J., F. Macagno, S. Cogoi, M. Peña, and J. Mehler
2008. The neonate brain detects speech structure. *Proc. Natl. Acad. Sci. U. S. A.*, 105(37):14222–14227.

Gervain, J., J. Mehler, J. F. Werker, C. A. Nelson, G. Csibra, S. Lloyd-Fox, M. Shukla, and R. N. Aslin
2011. Near-infrared spectroscopy: A report from the McDonnell infant methodology consortium. *Dev. Cogn. Neurosci.*, 1(1):22–46.

Gervain, J., J. F. Werker, A. Black, and M. N. Geffen

2016. The neural correlates of processing scale-invariant environmental sounds at birth. *Neuroimage*, 133:144–150.

Ghosh, A., I. Tachtsidis, C. Kolyva, C. E. Cooper, M. Smith, and C. E. Elwell

2012. Use of a hybrid optical spectrometer for the measurement of changes in oxidized cytochrome c oxidase concentration and tissue scattering during functional activation. *Adv. Exp. Med. Biol.*, 737:119–124.

Ghosh, A., I. Tachtsidis, C. Kolyva, D. Highton, C. Elwell, and M. Smith

2013. Normobaric Hyperoxia Does Not Change Optical Scattering or Pathlength but Does Increase Oxidised Cytochrome c Oxidase Concentration in Patients with Brain Injury. *Oxyg. Transp. to Tissue XXXIV*, 765:67–72.

Goksan, S., C. Hartley, F. Emery, N. Cockrill, R. Poorun, F. Moultrie, R. Rogers, J. Campbell, M. Sanders, E. Adams, S. Clare, M. Jenkinson, I. Tracey, and R. Slater

2015. fMRI reveals neural activity overlap between adult and infant pain. *Elife*, 2015(4):1–13.

Goodwin, J. R., C. R. Gaudet, and A. J. Berger

2014. Short-channel functional near-infrared spectroscopy regressions improve when source-detector separation is reduced. *Neurophotonics*, 1(1):015002.

Grubhofer, G., W. Tonninger, P. Keznicki, and A. Lassnigg

1999. A comparison of the monitors INVOS 3100 and NIRO 500. *Acta Anaesthesiol. Scand.*, 43:470–475.

Haensse, D., P. Szabo, D. Brown, J.-C. Fauchère, P. Niederer, H.-U. Bucher, and M. Wolf

2005. A new multichannel near infrared spectrophotometry system for functional studies of the brain in adults and neonates. *Opt. Express*, 13(12):4525–38.

Haginoya, K., M. Munakata, R. Kato, and K. Iinuma

2002. Ictal cerebral haemodynamics of childhood epilepsy measured with near-infrared spectrophotometry. *Brain*, 125:1960–1971.

Hall, C. N., C. Reynell, B. Gesslein, N. B. Hamilton, A. Mishra, B. A. Sutherland, F. M. O'Farrell, A. M. Buchan, M. Lauritzen, and D. Attwell

2014. Capillary pericytes regulate cerebral blood flow in health and disease. *Nature*, 508(7494):55–60.

Harris, J. J., C. Reynell, and D. Attwell

2011. The physiology of developmental changes in BOLD functional imaging signals. *Dev. Cogn. Neurosci.*, 1(3):199–216.

Hauser, W.

1995. Epidemiology of Epilepsy in Children. *Neurosurg Clin N Am*, 6(3):419–428.

Heekeren, H. R., M. Kohl, H. Obrig, R. Wenzel, W. von Pannwitz, S. J. Matcher, U. Dirnagl, C. E. Cooper, and A. Villringer

1999. Noninvasive assessment of changes in cytochrome-c oxidase oxidation in human subjects during visual stimulation. *J. Cereb. Blood Flow Metab.*, 19(6):592–603.

Hellström-Westas, L.

2018. Amplitude-integrated electroencephalography for seizure detection in newborn infants. *Semin. Fetal Neonatal Med.*, 23(3):175–182.

Highton, D., A. Ghosh, I. Tachtsidis, C. Elwell, and M. Smith

2014. Analysis of Slow Wave Oscillations in Cerebral Haemodynamics and Metabolism Following Subarachnoid Haemorrhage. *Adv. Exp. Med. Biol.*, Pp. 195–201.

Hoehl, S. and S. Wahl

2012. Recording infant ERP data for cognitive research. *Dev. Neuropsychol.*, 37(3):187–209.

Holland, S. K., E. Plante, A. Weber Byars, R. H. Strawsburg, V. J. Schmithorst, and W. S. Ball

2001. Normal fMRI brain activation patterns in children performing a verb generation task. *Neuroimage*, 14(4):837–843.

Hoshi, Y., S. Kohri, Y. Matsumoto, K. Cho, T. Matsuda, S. Okajima, and S. Fujimoto

2000. Hemodynamic responses to photic stimulation in neonates. *Pediatr. Neurol.*, 23(4):323–327.

Huotilainen, M., A. Kujala, M. Hotakainen, A. Shestakova, E. Kushnerenko, L. Parkkonen, V. Fellman, and R. Näätänen

2003. Auditory magnetic responses of healthy newborns. *Neuroreport*, 14(14):1871–1875.

Igou, S.

2014. Symptoms of Brain Injury.

Irani, F., S. M. Platek, S. Bunce, A. C. Ruocco, and D. Chute

2007. Functional near infrared spectroscopy (fNIRS): an emerging neuroimaging technology with important applications for the study of brain disorders. *Clin. Neuropsychol.*, 21(1):9–37.

Isobe, K., T. Kusaka, K. Nagano, K. Okubo, S. Yasuda, M. Kondo, S. Itoh, and S. Onishi

2001. Functional imaging of the brain in sedated newborn infants using near infrared topography during passive knee movement. *Neurosci. Lett.*, 299(3):221–224.

Issard, C. and J. Gervain

2017. Adult-like processing of time-compressed speech by newborns: A NIRS study. *Dev. Cogn. Neurosci.*, 25:176–184.

Jackson, A. F. and D. J. Bolger

2014. The neurophysiological bases of EEG and EEG measurement : A review for the rest of us. *Psychophysiology*, 51:1061–1071.

James, A. and V. Patel

2014. Hypoxic ischaemic encephalopathy. *Paediatr. Child Health (Oxford).*, 24(9):385–389.

Jasdzewski, G., G. Strangman, J. Wagner, K. K. Kwong, R. A. Poldrack, and D. A. Boas

2003. Differences in the hemodynamic response to event-related motor and visual paradigms as measured by near-infrared spectroscopy. *Neuroimage*, 20(1):479–488.

Jöbsis, F. F.

1977. Noninvasive, infrared monitoring of cerebral and myocardial oxygen sufficiency and circulatory parameters. *Science (80-.).*, 198(4323):1264–1267.

Karen, T., G. Morren, D. Haensse, A. S. Bauschatz, H. U. Bucher, and M. Wolf

2008. Hemodynamic response to visual stimulation in newborn infants using functional near-infrared spectroscopy. *Hum. Brain Mapp.*, 29(4):453–460.

Kaynezhad, P., I. de Roever, G. Bale, and I. Tachtsidis

2016a. Optical monitoring of neonatal brain injury: towards the development of compact clinical systems. *Electro Opt.*

Kaynezhad, P., I. Tachtsidis, and G. Jeffery

2016b. Optical monitoring of retinal respiration in real time: 670 nm light increases the redox state of mitochondria. *Exp. Eye Res.*, 152:88–93.

Khan, S.

2016. Glycolysis.

Klingberg, T., H. Forssberg, and H. Westerberg

2002. Increased brain activity in frontal and parietal cortex underlies the development of visuospatial working memory capacity during childhood. *J. Cogn. Neurosci.*, 14(1):1–10.

Kolyva, C., A. Ghosh, I. Tachtsidis, D. Highton, C. E. Cooper, M. Smith, and C. E. Elwell

2014. Cytochrome c oxidase response to changes in cerebral oxygen delivery in the adult brain shows higher brain-specificity than haemoglobin. *Neuroimage*, 85:234–244.

Kolyva, C., I. Tachtsidis, A. Ghosh, T. Moroz, C. E. Cooper, M. Smith, and C. E. Elwell
2012. Systematic investigation of changes in oxidized cerebral cytochrome c oxidase concentration during frontal lobe activation in healthy adults. *Biomed. Opt. Express*, 3(10):2550 – 2566.

Korman, B., P. Krsek, M. Duchowny, B. Maton, E. Pacheco-Jacome, and G. Rey
2013. Early seizure onset and dysplastic lesion extent independently disrupt cognitive networks. *Neurology*, 81(8):745–751.

Kotilahti, K., I. Nissilä, M. Huotilainen, R. Mäkelä, N. Gavrielides, T. Noponen, P. Björkman, V. Fellman, and T. Katila
2005. Bilateral hemodynamic responses to auditory stimulation in newborn infants. *Neuroreport*, 16(12):1373–1377.

Kotilahti, K., I. Nissila, T. Nasi, L. Lipiainen, T. Noponen, P. Merilainen, M. Huotilainen, and V. Fellman
2010. Hemodynamic responses to speech and music in newborn infants. *Hum. Brain Mapp.*, 31(4):595–603.

Kozberg, M. G., B. R. Chen, S. E. DeLeo, M. B. Bouchard, and E. M. C. Hillman
2013. Resolving the transition from negative to positive blood oxygen level-dependent responses in the developing brain. *Proc. Natl. Acad. Sci. U. S. A.*, 110(11):4380–5.

Kozberg, M. G., Y. Ma, M. A. Shaik, S. H. Kim, and E. M. C. Hillman
2016. Rapid Postnatal Expansion of Neural Networks Occurs in an Environment of Altered Neurovascular and Neurometabolic Coupling. *J. Neurosci.*, 36(25):6704–6717.

Kujala, A., M. Huotilainen, M. Hotakainen, M. Lennes, L. Parkkonen, V. Fellman, and R. Näätänen
2004. Speech-sound discrimination in neonates as measured with MEG. *Neuroreport*, 15(13):2089–92.

Kusaka, T., K. Isobe, T. Miki, M. Ueno, K. Koyano, S. Nakamura, M. Nakamura, Y. Konishi, T. Kuboi, I. Kato, K. Okubo, S. Yasuda, T. Nishida, and S. Itoh
2011. Functional lateralization of sensorimotor cortex in infants measured using multichannel near-infrared spectroscopy. *Pediatr. Res.*, 69(5 PART 1):430–435.

Kusaka, T., K. Isobe, K. Okubo, S. Yasuda, K. Kawada, and S. Itoh
2005. Activation of the visual cortex in infants during natural sleep using multichannel near-infrared spectroscopy. *Adv Exp Med Biol*, 25:368.

Liao, S. M., S. L. Ferradal, B. R. White, N. Gregg, T. E. Inder, and J. P. Culver
2012. High-density diffuse optical tomography of term infant visual cortex in the nursery. *J. Biomed. Opt.*, 17(8):081414.

Liao, S. M., N. M. Gregg, B. R. White, B. W. Zeff, K. a. Bjerkaas, T. E. Inder, and J. P. Culver
2010. Neonatal hemodynamic response to visual cortex activity: high-density near-infrared spectroscopy study. *J. Biomed. Opt.*, 15(2):026010.

Liem, K. D., J. C. W. Hopman, B. Oeseburg, A. F. J. De Haan, and L. A. A. Kollée
1997. The effect of blood transfusion and haemodilution on cerebral oxygenation and haemodynamics in newborn infants investigated by near infrared spectrophotometry. *Eur. J. Pediatr.*, 156(4):305–310.

Lloyd-Fox, S., A. Blasi, and C. E. Elwell
2010. Illuminating the developing brain: The past, present and future of functional near infrared spectroscopy. *Neurosci. Biobehav. Rev.*, 34(3):269–284.

Lloyd-Fox, S., A. Blasi, A. Volein, N. Everdell, C. E. Elwell, and M. H. Johnson
2009. Social perception in infancy: A near infrared spectroscopy study. *Child Dev.*, 80(4):986–999.

Macvicar, B. A. and E. A. Newman
2015. Astrocyte regulation of blood flow in the brain. *Cold Spring Harb. Perspect. Biol.*, 7(5):1–15.

Mason, M. G., P. Nicholls, and C. E. Cooper
2014. Re-evaluation of the near infrared spectra of mitochondrial cytochrome c oxidase: Implications for non invasive in vivo monitoring of tissues. *Biochim. Biophys. Acta - Bioenerg.*, 1837(11):1882–1891.

Matcher, S. J. and C. E. Cooper
1994. Absolute quantification of deoxyhaemoglobin concentration in tissue near infrared spectroscopy. *Phys. Med. Biol.*, 39(8):1295–312.

Matcher, S. J., C. E. Elwell, C. E. Cooper, M. Cope, and D. T. Delpy
1995. Performance comparison of several published tissue near-infrared spectroscopy algorithms.

May, L., K. Byers-Heinlein, J. Gervain, and J. F. Werker
2011. Language and the newborn brain: Does prenatal language experience shape the neonate neural response to speech? *Front. Psychol.*, 2(SEP):1–9.

May, L., J. Gervain, M. Carreiras, and J. F. Werker
2018. The specificity of the neural response to speech at birth. *Dev. Sci.*, 21(3):1–9.

Maynard, D., P. F. Prior, and D. F. Scott
1969. Device for continuous monitoring of cerebral activity in resuscitated patients. *Br. Med. J.*, 4(5682):545–546.

McCormick, D. C., A. D. Edwards, J. S. Wyatt, A. Potter, M. Cope, D. T. Delpy, and E. O. R. Reynolds

1993. Effect of indomethacin on cerebral oxidised cytochrome aa3 concentration in preterm infants. *Pediatr. Res.*, 33(6):603–608.

Meek, J., M. Firbank, C. Elwell, J. Atkinson, O. Braddick, and J. Wyatt

1998. Regional haemodynamic responses to visual stimulation in awake infants. *Pediatr. Res.*, 43(6):840–843.

Minagawa-Kawai, Y., A. Cristia, I. Vendelin, D. Cabrol, and E. Dupoux

2011. Assessing signal-driven mechanisms in neonates: Brain responses to temporally and spectrally different sounds. *Front. Psychol.*, 2(JUN):1–12.

Mitra, S., G. Bale, S. Mathieson, C. Uria-Avellanal, J. Meek, I. Tachtsidis, and N. J. Robertson

2016. Changes in Cerebral Oxidative Metabolism during Neonatal Seizures Following Hypoxic–Ischemic Brain Injury. *Front. Pediatr.*, 4(August):1–7.

Muramoto, S., H. Yamada, N. Sadato, H. Kimura, Y. Konishi, K. Kimura, M. Tanaka, T. Kochiyama, Y. Yonekura, and H. Ito

2002. Age-dependent change in metabolic response to photic stimulation of the primary visual cortex in infants: functional magnetic resonance imaging study. *J. Comput. Assist. Tomogr.*, 26(6):894–901.

Naoi, N., Y. Fuchino, M. Shibata, F. Niwa, M. Kawai, Y. Konishi, K. Okanoya, and M. Myowa-Yamakoshi

2013. Decreased right temporal activation and increased interhemispheric connectivity in response to speech in preterm infants at term-equivalent age. *Front. Psychol.*, 4(March):1–13.

Natzke, L.

1998. Hemoglobin.

Nishitani, N., A. Ikeda, T. Nagamine, M. Honda, N. Mikuni, W. Taki, K. J., and S. H.

1999. The role of the hippocampus in auditory processing studied by event-related electric potentials and magnetic fields in epilepsy patients before and after temporal lobectomy. *Brain*, 122(4):687–707.

Nissila, I., K. Kotilahti, M. Huotilainen, R. Makela, L. Lipiainen, T. Noponen, N. Gavrielides, R. Naatanen, V. Fellman, and T. Katila

2004. Auditory hemodynamic studies of newborn infants using near-infrared spectroscopic imaging. In *Annu. Int. Conf. IEEE Eng. Med. Biol. Soc.*, volume 2, Pp. 1244–1247.

Nissilä, I., K. Kotilahti, T. Noponen, M. Huotilainen, R. Näätänen, and T. Katila
2003. Optical topographic studies of adults and neonates. *Opt. Tomogr. Spectrosc. Tissue V*, 4955:134–144.

Nosrati, R., K. Vesely, T. A. Schweizer, and V. Toronov
2016. Event-related changes of the prefrontal cortex oxygen delivery and metabolism during driving measured by hyperspectral fNIRS. *Biomed. Opt. Express*, 7(4):151–163.

Ogawa, S. and T. Lee
1990. Brain magnetic resonance imaging with contrast dependent on blood oxygenation. *Proc. NatI. Acad. Sci.*, 87(24):9868–72.

Ozawa, M., K. Kanda, M. Hirata, I. Kusakawa, and C. Suzuki
2011a. Effect of gender and hand laterality on pain processing in human neonates. *Early Hum. Dev.*, 87(1):45–48.

Ozawa, M., K. Kanda, M. Hirata, I. Kusakawa, and C. Suzuki
2011b. Influence of repeated painful procedures on prefrontal cortical pain responses in newborns. *Acta Paediatr. Int. J. Paediatr.*, 100(2):198–203.

Pasley, B. and R. Freeman
2008. Neurovascular Coupling.

Peña, M., A. Maki, D. Kovacić, G. Dehaene-Lambertz, H. Koizumi, F. Bouquet, and J. Mehler
2003. Sounds and silence: an optical topography study of language recognition at birth. *Proc. Natl. Acad. Sci. U. S. A.*, 100(20):11702–11705.

Peterson, E. C., Z. Wang, and G. Britz
2011. Regulation of cerebral blood flow. *Int. J. Vasc. Med.*, 2011.

Phan, P., D. Highton, S. Brigadoi, I. Tachtsidis, M. Smith, and C. Elwell
2016a. Spatial Distribution Of Changes In Oxidised Cytochrome C Oxidase During Visual Stimulation Using Broadband Near Infrared Spectroscopy Imaging. *Adv. Exp. Med. Biol.*, Pp. 0–5.

Phan, P., D. Highton, J. Lai, M. Smith, C. Elwell, and I. Tachtsidis
2016b. Multi-channel multi-distance broadband near-infrared spectroscopy system to measure the spatial response of cellular oxygen metabolism and tissue oxygenation. *Biomed. Opt. Express*, 7(11):4424.

Phan, P. T.
2017. *spectroscopy system to investigate the spatial variation in cellular oxygen metabolism in the healthy and injured.* PhD thesis.

Phelps, M. E., E. J. Hoffman, N. A. Mullani, and M. M. Ter-Pogossian
1975. Application of annihilation coincidence detection to transaxial reconstruction tomography. *J. Nucl. Med.*, 16(3):210–24.

Pinto, L. and P. Giliberti
2001. Neonatal seizures: background EEG activity and the electroclinical correlation in full-term neonates with hypoxic-ischemic encephalopathy. Analysis by computer-synchronized long-term polygraphic video-EEG monitoring. *Epileptic Disord. Int. Epilepsy J. Videotape*, 3(3):125–132.

Remsen, S.
2013. Oxidative Phosphorylation.

Roche-Labarbe, N., B. Zaaimi, P. Berquin, A. Nehlig, R. Grebe, and F. Wallois
2008. NIRS-measured oxy- and deoxyhemoglobin changes associated with EEG spike-and-wave discharges in children. *Epilepsia*, 49(11):1871–1880.

Rod, K.
2015. Brain Diagram Cerebrum.

Rutherford, M.
2002. *MRI of the Neonatal Brain*, 4th edition. Saunders Ltd.

Saager, R. B. and A. J. Berger
2005. Direct characterization and removal of interfering absorption trends in two-layer turbid media. *J. Opt. Soc. Am. A. Opt. Image Sci. Vis.*, 22(9):1874–1882.

Saager, R. B., N. L. Telleri, and A. J. Berger
2011. Two-detector Corrected Near Infrared Spectroscopy (C-NIRS) detects hemodynamic activation responses more robustly than single-detector NIRS. *Neuroimage*, 55(4):1679–1685.

Saito, Y., S. Aoyama, T. Kondo, R. Fukumoto, N. Konishi, K. Nakamura, M. Kobayashi, and T. Toshima
2007a. Frontal cerebral blood flow change associated with infant-directed speech. *Arch. Dis. Child. Fetal Neonatal Ed.*, 92:F113–F116.

Saito, Y., T. Kondo, S. Aoyama, R. Fukumoto, N. Konishi, K. Nakamura, M. Kobayashi, and T. Toshima
2007b. The function of the frontal lobe in neonates for response to a prosodic voice. *Early Hum. Dev.*, 83(4):225–230.

Sakatani, K., S. Chen, W. Lichty, H. Zuo, and Y. P. Wang
1999. Cerebral blood oxygenation changes induced by auditory stimulation in newborn infants measured by near infrared spectroscopy. *Early Hum. Dev.*, 55(3):229–236.

Sato, H., Y. Hirabayashi, H. Tsubokura, M. Kanai, T. Ashida, I. Konishi, M. Uchida-Ota, Y. Konishi, and A. Maki

2012. Cerebral hemodynamics in newborn infants exposed to speech sounds: A whole-head optical topography study. *Hum. Brain Mapp.*, 33:2092–2103.

Schneider, U., E. Schleussner, J. Haueisen, H. Nowak, and H. J. Seewald

2001. Signal analysis of auditory evoked cortical fields in fetal magnetoencephalography. *Brain Topogr.*, 14(1):69–80.

Scholkmann, F., S. Kleiser, A. J. Metz, R. Zimmermann, J. Mata Pavia, U. Wolf, and M. Wolf

2014. A review on continuous wave functional near-infrared spectroscopy and imaging instrumentation and methodology.

Schwartz, T. H.

2007. Neurovascular coupling and epilepsy: hemodynamic markers for localising and predicting seizure onset. *Curr. Rev. Clin. Sci.*, 7(99):91–94.

Seghier, M. L., F. Lazeyras, and P. S. Huppi

2006. Functional MRI of the newborn. *Semin. Fetal Neonatal Med.*, 11(6):479–488.

Sharp, P. S., K. Shaw, L. Boorman, S. Harris, A. J. Kennerley, M. Azzouz, and J. Berwick

2015. Comparison of stimulus-evoked cerebral hemodynamics in the awake mouse and under a novel anesthetic regime. *Sci. Rep.*, 5(July).

Shi, Y., R.-b. Jin, J.-n. Zhao, S.-f. Tang, H.-q. Li, and T.-y. Li

2009. Brain positron emission tomography in preterm and term newborn infants. *Early Hum. Dev.*, 85(7):429–432.

Shibata, M., Y. Fuchino, N. Naoi, S. Kohno, M. Kawai, K. Okanoya, and M. Myowa-Yamakoshi

2012. Broad cortical activation in response to tactile stimulation in newborns. *Neuroreport*, 23:373–377.

Siddiqui, M. F., S. Lloyd-Fox, P. Kaynezhad, I. Tachtsidis, M. H. Johnson, and C. E. Elwell

2017. Non-invasive measurement of a metabolic marker of infant brain function. *Sci. Rep.*, 7(1):1–6.

Singh, H., R. J. Cooper, C. Wai Lee, L. Dempsey, A. Edwards, S. Brigadoi, D. Airantzis, N. Everdell, A. Michell, D. Holder, J. C. Hebden, and T. Austin

2014. Mapping cortical haemodynamics during neonatal seizures using diffuse optical tomography: A case study. *NeuroImage Clin.*, 5:256–265.

Sofroniew, M. V. and H. V. Vinters

2010. Astrocytes: biology and pathology. *Acta Neuropathol.*, 119(1):7–35.

Springett, R., J. Newman, M. Cope, and D. T. Delpy

2000. Oxygen dependency and precision of cytochrome oxidase signal from full spectral NIRS of the piglet brain. *Am. J. Physiol. Heart Circ. Physiol.*, 279(5):H2202–H2209.

St. Louis, E., L. Frey, J. Britton, J. Hopp, P. Korb, M. Koubeissi, W. Lievens, and E. Pestana-Knight

2016. *Electroencephalography (EEG): An Introductory Text and Atlas of Normal and Abnormal Findings in Adults, Children, and Infants.*

Steinlein, O. K.

2008. Genetics and epilepsy. *Dialogues Clin. Neurosci.*, 10:29–38.

Suzuki, S., S. Takasaki, T. Ozaki, and Y. Kobayashi

1999. A tissue oxygenation monitor using NIR spatially resolved spectroscopy. *Proc. SPIE*, 3597(January 1999):582–592.

Tachtsidis, I. and F. Scholkmann

2016. False positives and false negatives in functional near-infrared spectroscopy : issues, challenges, and the way forward. *Neurophotonics*, 3(3):030401–1 – 030401–6.

Tachtsidis, I., M. M. Tisdall, and C. Pritchard

2011. Analysis of the Changes in the Oxidation of Brain Tissue Cytochrome-c-Oxidase in Traumatic Brain Injury Patients during Hypercapnoea. *Adv. Exp. Med. Biol.*, 701:9–14.

Taga, G., K. Asakawa, K. Hirasawa, and Y. Konishi

2003. Hemodynamic responses to visual stimulation in occipital and frontal cortex of newborn infants: A near-infrared optical topography study. *Pathophysiology*, 10(3-4):277–281.

Telkemeyer, S., S. Rossi, S. P. Koch, T. Nierhaus, J. Steinbrink, D. Poeppel, H. Obrig, and I. Wartenburger

2009. Sensitivity of newborn auditory cortex to the temporal structure of sounds. *J. Neurosci.*, 29(47):14726–33.

Tisdall, M., I. Tachtsidis, T. Leung, C. Elwell, and M. Smith

2008a. Changes in the attenuation of near infrared spectra by the healthy adult brain during hypoxaemia cannot be accounted for solely by changes in the concentrations of oxy- and deoxy-haemoglobin. *Adv. Exp. Med. Biol.*, 614:217–225.

Tisdall, M. M., I. Tachtsidis, T. S. Leung, C. E. Elwell, and M. Smith

2007. Near-infrared spectroscopic quantification of changes in the concentration of oxidized cytochrome c oxidase in the healthy human brain during hypoxemia. *J. Biomed. Opt.*, 12(2):024002.

Tisdall, M. M., I. Tachtsidis, T. S. Leung, C. E. Elwell, and M. Smith
2008b. Increase in cerebral aerobic metabolism by normobaric hyperoxia after traumatic brain injury. *J. Neurosurg.*, 109(3):424–432.

Uludag, K., J. Steinbrink, M. Kohl-Bareis, R. Ü. Wenzel, A. Villringer, and H. Obrig
2004. Cytochrome-c-oxidase redox changes during visual stimulation measured by near-infrared spectroscopy cannot be explained by a mere cross talk artefact. *Neuroimage*, 22(1):109–119.

van Rooij, L. G., M. C. Toet, A. C. van Huffelen, F. Groenendaal, W. Laan, A. Zecic, T. de Haan, I. L. van Straaten, S. Vrancken, G. van Wezel, J. van der Sluijs, H. Ter Horst, D. Gavilanes, S. Laroche, G. Naulaers, and L. S. de Vries
2010. Effect of treatment of subclinical neonatal seizures detected with aEEG: randomized, controlled trial. *Pediatrics*, 125(2):e358–66.

Vannasing, P., O. Florea, B. González-Frankenberger, J. Tremblay, N. Paquette, D. Safi, F. Wallois, F. Lepore, R. Béland, M. Lassonde, and A. Gallagher
2016. Distinct hemispheric specializations for native and non-native languages in one-day-old newborns identified by fNIRS. *Neuropsychologia*, 84:63–69.

Verma, U. L., F. Archbald, N. A. Tejani, and S. M. Handwerker
1984. Cerebral function monitor in the neonate. I: Normal patterns. *Dev Med Child Neurol*, 26(2):154–161.

Verriotis, M., L. Fabrizi, A. Lee, R. J. Cooper, M. Fitzgerald, and J. Meek
2016. Mapping cortical responses to somatosensory stimuli in human infants with simultaneous near-infrared spectroscopy and event-related potential recording. *eNeuro*, 3(April):1–15.

Volpe, J. J., P. Herscovitch, and M. E. Raichie
1983. Positron Emission Tomography in the Newborn: Extensive Impairment of Regional Cerebral Blood Flow with Intraventricular Hemorrhage and Hemorrhagic Intracerebral Involvement. *Pediatrics*, 72(5).

Wallois, F., A. Patil, and R. Grebe
2010. EEG-NIRS in epilepsy in children and neonates EEG-SPIR chez les patients épileptiques. *Clin. Neurophysiol.*, 40:281–292.

Wallois, F., A. Patil, G. Kongolo, S. Goudjil, and R. Grebe
2009. Haemodynamic changes during seizure-like activity in a neonate : A simultaneous AC EEG-SPIR and high-resolution DC EEG recording Modifications hémodynamiques au cours d ' activités critiques chez un. *Clin. Neurophysiol.*, 39:217–227.

Welker, K. M. and A. Patton

2012. Assessment of Normal Myelination with Magnetic Resonance Imaging. *Semin. Neurol.*, 32:15–28.

Wobst, P., R. Wenzel, M. Kohl, H. Obrig, and a. Villringer

2001. Linear aspects of changes in deoxygenated hemoglobin concentration and cytochrome oxidase oxidation during brain activation. *Neuroimage*, 13(3):520–530.

Wyatt, J. S., M. Cope, D. T. Delpy, S. Wray, and E. O. Reynolds

1986. Quantification of cerebral oxygenation and haemodynamics in sick newborn infants by near infrared spectrophotometry. *Lancet*, 2(8515):1063–1066.

Yamada, H., N. Sadato, Y. Konishi, K. Kimura, M. Tanaka, Y. Yonekura, and Y. Ishii

1997. A rapid brain metabolic change in infants detected by fMRI. *Neuroreport*, 8(17):3775–8.

Zaidi, A. D., N. Birbaumer, E. Fetz, N. Logothetis, and R. Sitaram

2018. The hemodynamic initial-dip consists of both volumetric and oxymetric changes correlated to localized spiking activity. *bioRXiv*, Pp. 1–19.

Zaramella, P., F. Freato, A. Amigoni, S. Salvadori, P. Marangoni, A. Suppiej, A. Suppjei, B. Schiavo, and L. Chiandetti

2001. Brain auditory activation measured by near-infrared spectroscopy (NIRS) in neonates. *Pediatr. Res.*, 49(2):213–9.

Zhang, D., Y. Zhou, X. Hou, Y. Cui, and C. Zhou

2017. Discrimination of emotional prosodies in human neonates: A pilot fNIRS study. *Neurosci. Lett.*, 658(August):62–66.